Dynamics of Dispersive Boundaries: The Determination of Spatial Hydrographic-Parameter Maps from Optical Sea-Surface Image Sequences

Dissertation zur Erlangung des Doktorgrades
am Fachbereich Informatik der Universität Hamburg

vorgelegt von

Christian M. Senet
aus Merseburg

Hamburg 2004

.

Genehmigt von Fachbereich Informatik der Universität Hamburg

auf Antrag von

Prof. Dr.-Ing. Bärbel Mertsching (Universität Paderborn),
Prof. Dr. Bernd Jähne (Universität Heidelberg)
und Prof. Dr. Bernd Neumann (Universität Hamburg)

Hamburg, den 15. Juli 2004

Prof. Dr. H. Siegfried Stiehl (Dekan)

Zusammenfassung

Wellen an physikalischen Grenzflächen werden mit Dispersionsrelationen beschrieben, die Wellenzahlen beziehungsweise -längen und Wellenfrequenzen miteinander verknüpfen. Konkreter Untersuchungsgegenstand dieser Arbeit sind Wellenfelder an der Grenzfläche Wasser–Luft. Das Ausbreitungsverhalten und damit die Dispersionsrelation von Wasseroberflächenwellen hängt unter anderen von den Parametern Wassertiefe und Oberflächenströmung ab. Diese Abhängigkeit wird in dieser Arbeit verwendet, um räumliche Karten der Wassertiefe und der Strömung aus optischen Bildfolgen der dynamischen Wasseroberfläche zu bestimmen. Die optischen Bildfolgen wurden mit einem Bilderfassungssystem, im wesentlichen bestehend aus CCD-Kamera, Computer und Beleuchtungseinheit, an hydraulischen Wellentanks aufgenommen. In hydraulischen Wellentanks, die im allgemeinen für wasserbauliche und ozeanographische Fragestellungen Verwendung finden, können Wellenfelder unter kontrollierten Bedingungen erzeugt werden. Im Rahmen der Arbeit wird ein Verfahren zur Bestimmung von Karten der hydrographischen Parameter Wassertiefe und Strömung eingeführt. Die optischen Bildfolgen werden von Bild- in Weltkoordinaten überführt und im weiteren mit einer dreidimensionalen Fast Fourier Transformation in den spektralen dreidimensionalen Wellenzahl–Frequenz-Raum überführt. Im Wellenzahl–Frequenz-Raum wird eine Dekomposition des Wellenfeldes in einzelne Komponenten durchgeführt. Hierfür werden zwei Alternativkonzepte eingeführt: die Zerlegung in Dispersions–Frequenz–Richtungs-Bins und eine Zerlegung mittels einer signaladaptiven Gaborfilterbank. Die spektralen Einzelkomponenten werden mittels einer zweidimensionalen inversen Fast Fourier Transformation in Einkomponentenbilder überführt. Aufgrund der Zerlegung können nun für jedes der Einkomponentenbilder räumliche Karten von lokalen Wellenzahlenvektoren beziehungsweise -längen bestimmt werden. Für die lokale Wellenzahlbestimmung wird ein Regressionsverfahren verwendet. Die Komposition lokaler Wellenzahlen und gegebener Frequenzen ergibt lokale Spektren. Die Funktion der Dispersionsrelation für Wasserwellen wird zur Bestimmung der Wassertiefe und der Oberflächenströmung regressiv an das lokale Spektrum angepasst; Ergebnisse sind lokale Karten der Wassertiefe und der Strömungsvektoren. Das eingeführte Verfahren ist prinzipiell durch Anpassung oder Ersetzung der von Dispersionen für die Analyse von Wellenphänomenen an beliebigen dynamischen Grenzflächen erweiterbar.

Summary

The propagation of waves at physical interfaces are described by dispersion relations, concatenating wave frequencies and wavenumbers. In this thesis the concrete subject of interest is the air–water interface. The propagation and therefore the dispersion of water-surface waves are depending among others on the water depth and on the surface current. This dependency here is utilised to retrieve spatial maps of water depth and of surface current from optical image sequences of the dynamic water surface. For the acquisition of the image sequences a device essentially consisting of a Charged-Coupled-Device video camera, a personal computer and an illumination unit has been applied. Experiments have been performed in hydraulic wave tanks under controlled conditions; these tanks in general are used in regard to coastal engineering or oceanographic examinations. A method to determine local maps of the hydrographic parameters water depths and surface current is introduced within the scope of the present work. The optical image sequences are transformed from image coordinates to world coordinates and are subsequently transformed to the spectral threedimensional wavenumber–frquency domain by a threedimensional Fast Fourier Transformation. The wave field now is decomposed in the spectral domain. For this purpose two alternative decomposition method are introduced: a decomposition into dispersive direction–frequency bins and a decomposition utilising a adaptive Gaborfilter bank. The spectral single components are transformed back to the spatial domain by a twodimensional inverse Fast Fourier Transform yielding one-component images. From the one-component images local wavenumbers are retrieved by a regression method. The composition of local wavenumbers and given frequencies results in local spectra. By fitting the dispersion relation to these local spectra the local distribution of the hydrographic parameters water depth and surface current vector are determined. In principle, the introduced method is extensible to other dynamic interfaces by usage and adaption of their individual dispersion may resulting in a broad variety of determinable parameter maps.

Contents

1 Introduction

Image analysis for the examination of static patterns and image-sequence analysis for the examination of dynamic processes have evolved from the stage of qualitative treatment a few decades ago to the present-day stage of quantitative inspection.

Task ▷ Examination of dynamic processes: the sea surface

A method for determining quantitative physical parameters from image sequences is proposed in this thesis. The subject is the analysis of image sequences of the moving sea surface to determine hydrographic parameters. Surface waves (Fig. 1) in general are periodic deformations of an interface. In oceanography, surface waves are elongations of the sea surface (i.e. the ocean–atmosphere boundary). These deformations propagate with the phase speed of waves, while the particles themselves oscillate at particle speed and remain at a constant position on average. Sea-surface waves are classified in several ways. Typically they are classified by their generation or their restoring forces. A sea surface, composed from the superposition of plane waves in the ocean over a certain area, $X \otimes Y$ (box), in a certain time interval, T (chunk), is called a wave field.

Each wave of a wave field propagates dispersively. For a freely propagating plane wave at the ocean–atmosphere boundary, the dispersion describes the relation of the wavelength, λ (wavenumber, $k = 2\pi\lambda^{-1}$), to the wave period, τ (or frequency, $\omega = 2\pi\tau^{-1}$).

Image sequences ▷ complete description of processes

Dynamical processes at the sea surface have to be measured in space and time when a complete description of a wave field is required. Therefore systems which acquire image sequences of the sea surface, are promising measurement tools to detect hydrographic parameters influencing the dynamics. The general aim of the analysis of sea-surface image sequences is to give

Figure 1: Sea-surface waves photographed in the Norwegian Sea, (source: author, 1995).

oceanographers or coastal and offshore engineers a tool to measure and analyze multidirectional complex wave fields in hydraulic models as well as in nature.

At the GKSS Research Center nautical radars and CCD (**C**harge-**C**oupled **D**evice) cameras are used to acquire image sequences of the sea surface. Radars are installed on ship- or land-based stations. CCD cameras are mounted in hydraulic wave tanks, which are used to create artificial wave fields under controlled laboratory conditions.

Image sequences ▷ Advantages

Classical instruments such as waverider buoys, laser wave gauges or wire wave gauges normally only deliver time series. Therefore these instruments suffer in their unability to resolve the directionality of a wave field. Satellite-based radars are also used to observe ocean waves, normally delivering single images. A single image may contain the information regarding the directionality of a wave field, but suffer from the so-called 180° ambiguity of direction. In a single image one cannot distinguish whether a wave propagates in a certain direction or in the opposite (180°) direction. For single images this ambiguity has to be resolved by the addition of external information, for example, the wind direction acquired at a coastal meteorological station. An image-sequence acquisition system enables the recovery of a wave-field measurement containing the fully unambiguous directionality. The different sampling approaches are illustrated in Fig. 2.

Nautical radar ▷ Ocean measurements

Directional ocean-wave fields can be measured with nautical radars. This sensor is a standard industrial product. Based on a nautical radar, at the GKSS Research Center the **Wa**ve **Mo**nitoring **S**ystem (WaMoS) has been devoloped. WaMoS, now in the second generation renamed WaMoS II, is a commercial product which has been proved to be reliable on board research vessels, offshore platforms, and land-based stations [RBD99] [RHBD99] [Dit99]. This imaging sensor resolves the spatial and temporal structure of a wave field.

Optical Sensors ▷ Advantages

A nautical radar is limited in regard to its spatial and temporal sampling resolution. A typical nautical radar has a spatial sampling resolution of 5 m – 10 m and a temporal sampling resolution of ca 2 s. Therefore small-scale and as well short-scale processes at the air–sea boundary are not in the scope of a nautical radar.

To overcome this limitation, optical imaging sensors can be used to observe water waves. For this purpose the acquisition and analysis of image sequences using CCD video cameras is an appropriate and promising technique. The advantages of CCD video cameras are the low system price, small size of the sensor, and variable lens mountings. In addition to acquire image sequences, a computer fast enough and equipped with an adequate amount of memory is required. Such an image-sequence acquisition system is a flexible tool for examining dynamical processes.

Optical Images ▷ Brief description of diverse techniques

CCD video image-sequence measurements from offshore stations [IGB86], coastal stations [Jan97], airplanes [DSFF96] and hydraulic tanks [JW89] have been performed by several authors. The photographs in Fig. 3 illustrate the variety of possible platforms suitable for mounting an image-sequence acquisition sensor. Several spatio-temporal- and spectral-analysis techniques

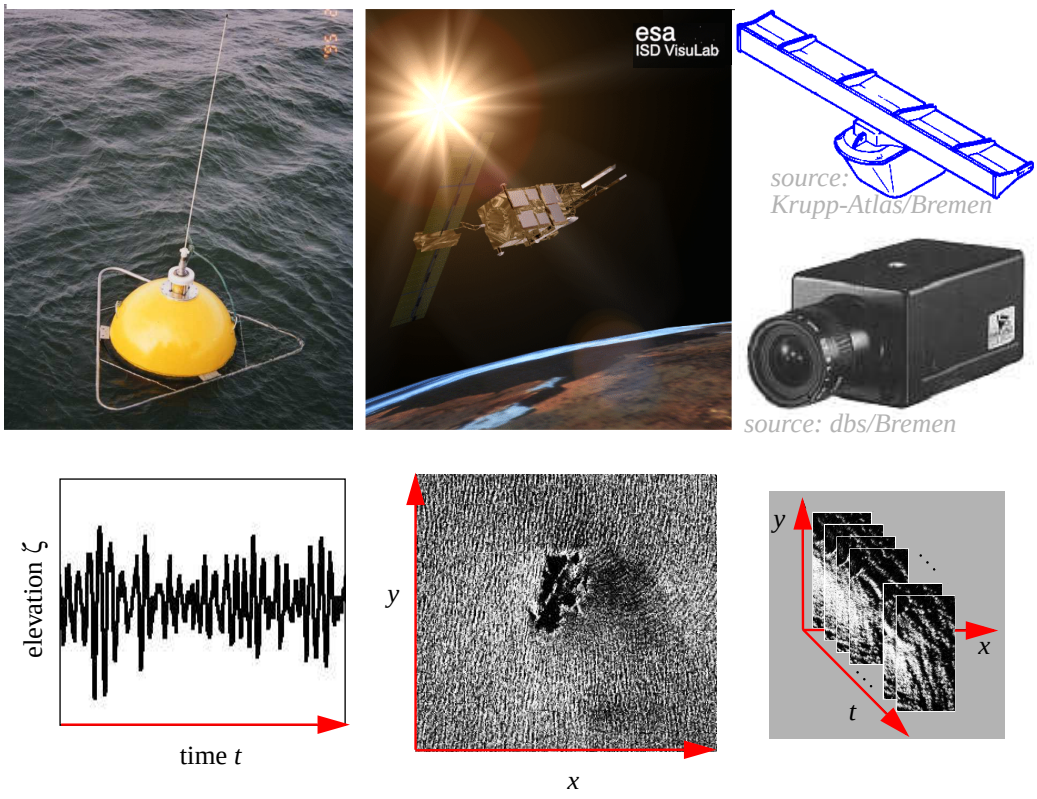

Figure 2: Wave measurements (from left to right): buoy measurements (image source: F. Ziemer, GKSS) yield time series of the sea-surface elevation (temporal 1D measurements) (source: GKSS), satellite-based radar (here taken from a **S**ynthetic **A**perture **R**adar (SAR)) (source: DLR, Oberpfaffenhofen) images yield spatial measurements (spatial 2D measurements), nautical radars (image source: STN Atlas Elektronik, Germany) or CCD cameras (image source: DBS, Bremen) yield spatio-temporal measurements (spatio-temporal 3D measurements).

have been developed to retrieve hydrographic parameters from optical images of the sea surface; one topic of interest is devoted to air-sea interaction. The small-scale roughness of the sea surface, especially microbreaking directly influences the rate of gas exchange at the air-sea interface [DDSW01]. In addition, the small-scale roughness – mainly induced by the local wind field – results in diffusive scatter of microwaves, leading to an increase of radar backscatter. Therefore, for the field of radar remote sensing, there is an urgent need for laboratory and field measurements of the sea surface with high spatio-temporal resolution. For a high-resolution surface reconstruction, the ISG (**I**maging **S**lope **G**auge) method, which bases on the principle of shape from refraction under controlled diffusive illumination conditions has been developed. This method is characterized by only slight nonlinearities of the imaging process. A brief comparsion between the ISG method and the approach to measure in reflection follows below.
Alternatively, shape-from-reflection based methods have been utilized. The approaches of these methods can be distinguished according to the type of

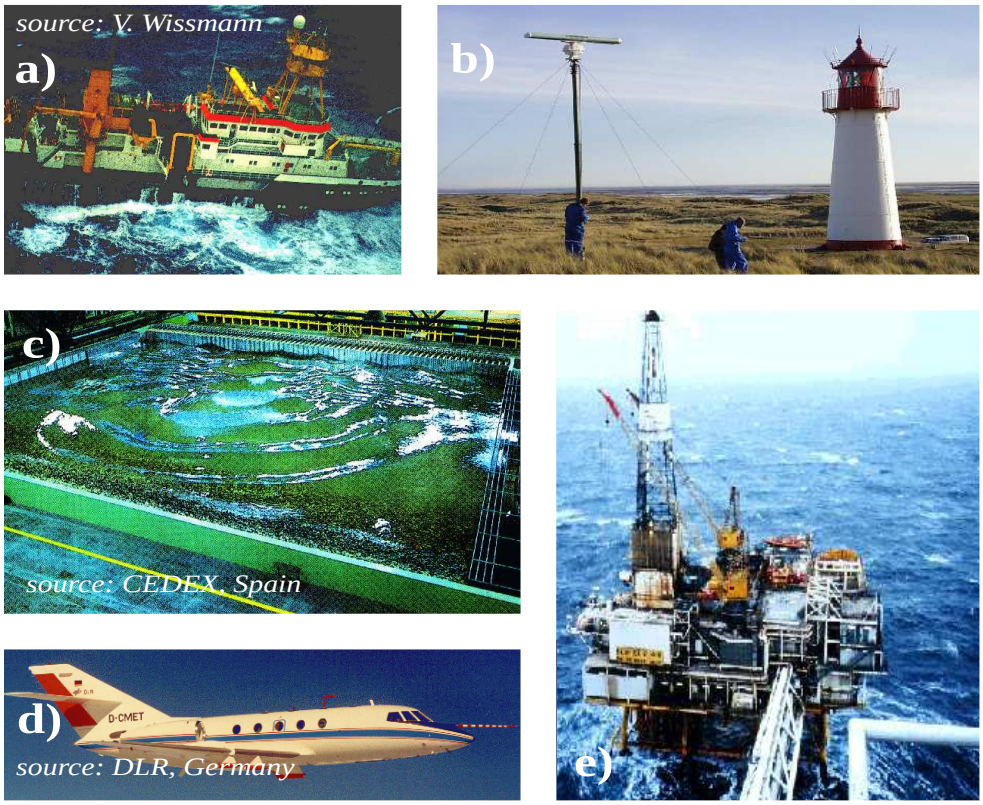

Figure 3: Platforms for image-sequence sensors. For the installation of nautical radar, **a)** ships (image source: V. Wissmann, University of Hamburg), **b)** coastal stations (image source: G. Schymura, GKSS), and **e)** offshore platforms (image source: F. Ziemer, GKSS) are suitable for CCD cameras, as well as **b)** and **e)**, **c)** hydraulic wave tanks (image source: CEDEX, Spain) and **d)** airplanes (image source: DLR, Oberpfaffenhofen) are used to observe the sea surface.

illumination.
In field experiments, sun light is a natural source of illumination. The light field, reflected at the sea surface is called sun glitter. The size of the sun glitter spot depends on the slope distribution of the sea surface. This relation has been used, in the classical approach of Cox and Munck [CM54a] [CM54b], to retrieve one reliable measurements of surface-slope distributions.
According to the hydrodynamic modulation theory, the mean-square wave slope is affected by the submarine bathymetry. It has been shown [HMM94], that a characterization of the submarine bathymetry can be retrieved from the areal sun-glitter patterns. A first skylight-illumination approach has been developed by Stilwell Jr. [Sti69]; here directional wave spectra have been deduced from photographs of the sea surface taken at skylight illumination. The optical imaging process, especially the nonlinearities, have been examinated by Peppers and Ostrem [PO78], and Monaldo and Kasevich [MK81].
Stereo experiments have been untertaken to measure larger-scale surface

waves, but for a specularly reflecting surface the correspondence and resolution problems poses severe limitations, discussed among others in a theoretical review of the diverse optical imaging processes of short ocean waves [JWK92].
Firstly Gotwols and Irani [GI80] [GI82] have deduced the dynamics of sea surface waves from optical image sequences. The fundamental-mode dispersion shell and its harmonics resulting from the strong nonlinearity of the imaging process have been identified.

Image Slope Gauge ▷ Ocean Refraction Measurements

The **I**mage **S**lope **G**auge technique (ISG) determines the local slope of the water surface using a defined light source beneath the water surface. The calibration procedure to determine the local slope is based on a shape-from-shading technique. The principle method was outlined in [Kli96]. The light source is mounted as a spatially extended area. The illumination gradients of the light source are pre-defined and calibrated in two spatial dimensions. The CCD camera is located above the water level and acquires image sequences of the water surface. The variation of the local slopes at the water surface leads to a modulation of the light field due to the optical process of light refraction. Using a colour wedge, three different illumination gradients can be generated simultaneously. The redundancy of one colour channel can be used for normalization of the incident light field. 1D slope measurements can be achieved by a gray-value wedge with a 1D illumination gradient (see Fig. 4 a). By the optical laws of Snellius and Fresnel, the 2D slopes are calculated from the imaged gray values.
On one hand an ISG delivers precise 2D spatial slope maps; on the other hand it is limited by the spatial dimensions of the required light source. Another limitation of an ISG is the necessity for a translucent water body, so that the transmitted light can pass through to reach the camera.

Optical measurements in Reflection ▷ Advantages

To overcome these limitations the light field, reflected at the water surface can be used for imaging. Here camera and light source are both located above the water surface (Fig. 4 b). The proposed method has aims not to retrieve spatial-slope maps as the ISG does, but to retrieve hydrographic parameters by analyzing complex-valued and variance spectra of image sequences, using the dispersion relation of sea-surface waves as additional information to 'interpret' the image sequences on a local spatial scale.

Global method ▷ for stationary and homogeneous processes Method DiSC ▷ New approach for stationary and inhomogeneous processes

From the acquired image sequences, hydrographic parameters, such as the near-surface current-velocity vector [SSZ97] [SSZ01], the water depth [Out98] and the calibrated full-directional wave spectra [SZS97] [See97], are determined. The method used up to now, here called the 'global method', is based on the analysis of gray-level variance spectra calculated by the squared modulus of a 3D Fast-Fourier Transformation (3D FFT) performed on the image sequences. The 3D FFT in terms of image processing is a global operator. Therefore stationarity and homogeneity of the wave field must be fulfilled.
As a first step in the present work the global method, developed for nautical radars, has been adapted to be used with CCD cameras. An example will be presented later; it shows the application of the method in calculating the surface current from optical image sequences.
This thesis is mainly concerned with the presentation of a newly developed

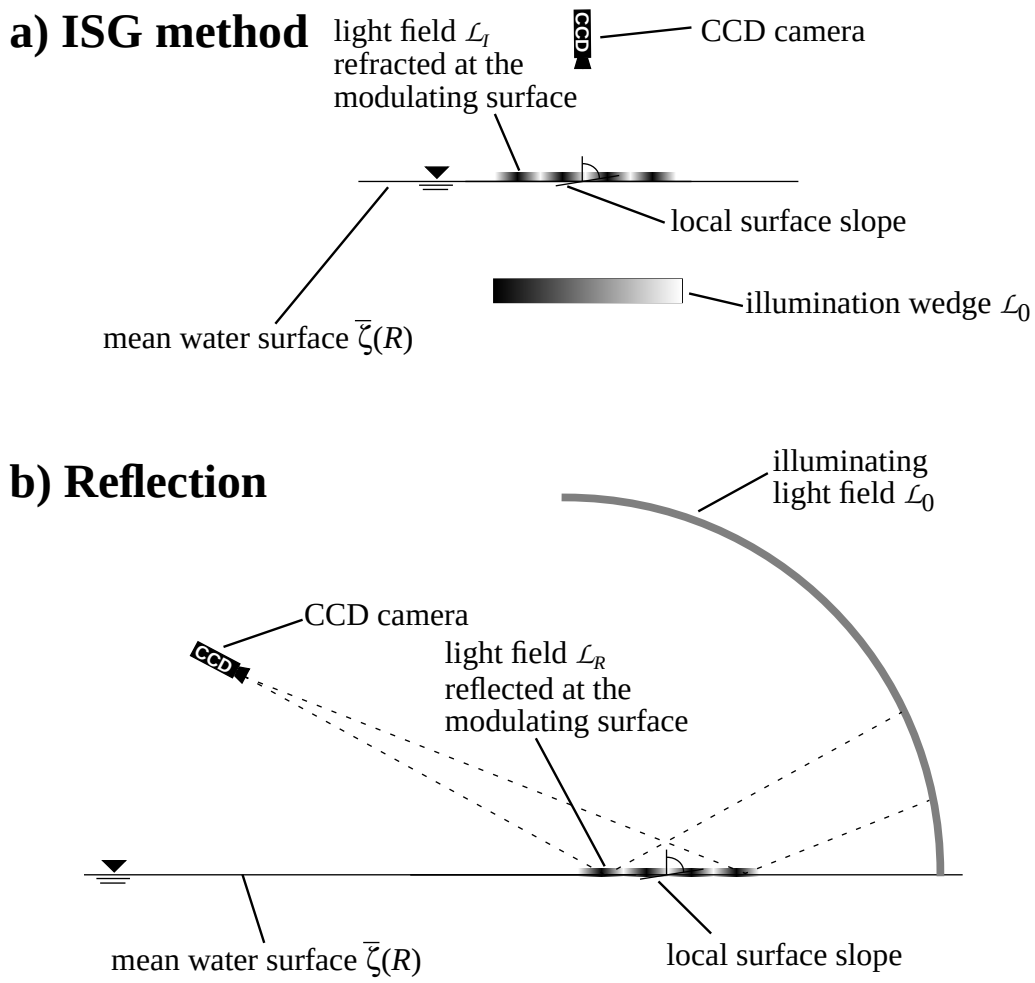

Figure 4: Principal scheme of the optical wave-field measurement **a)** with refraction (ISG: image slope gauge) and **b)** with reflection.

algorithm [SSSZ00] [SSZ00b], which analyses image sequences of dynamic dispersive boundaries, used to determine physical parameters on a local spatial scale. The local analysis method, which allows the analysis of inhomogeneous image sequences of a dynamic and dispersive surface has been labeled **DiSC** (**Di**spersive **S**urface **C**lassificator). In contrast to the global method, DiSC is based on

- preservation of the complex-valued 3D FFT image spectrum,
- filtering techniques to separate the wave signal from noise,
- directional and dispersion separation of the complex-valued spectrum into spectral bins at 2D wavenumber planes of constant frequency,
- 2D inverse Fast Fourier Transformation (2D FFT^{-1}) of the spectral bins, yielding complex-valued, one-component spatial maps in the spatio-frequency domain,

- calculation of spatial maps of local wavenumbers from the one-component images of constant frequency,
- composition of the one-component local wavenumber maps of constant frequency to local 3D spectra and
- calculation of spatial hydrographic-parameter maps from the local 3D spectra.

Here DiSC is applied to image sequences of water waves in hydraulic wave tanks, acquired by CCD cameras [SBL+99a] [SBL+99b] [SSD+99b] [SSZ00d] [SSZ00c]. The algorithm delivers results in form of spatial hydrographic-parameter maps (i.e. spatial maps of the water depth and the near-surface current).
In addition to being used on optical image sequences, DiSC is applied to nautical-radar image sequences acquired from land-based stations [SSD+99a] [SSW+00] [SSWZ00] [SSZ00a]. An overview of the imaging and the image-sequence processing chain is given in Fig. 5.

Method DiSC ▷ ... in context to the scientific field of image processing

In the scientific field of image processing the method DiSC matches to the context of multidimensional texture analysis. Regarding either natural objects or processes, machine vision systems, as well as the human visual system have to be able to cope with inhomogeneous and instationary scenes. Therefore algorithms, which should hold this criterion, should characterize the texture by its spatio-temporal wavenumber-frequency content. If a scene is composed of a few number of spatio-temporally locally regular patterns then it can be assumed that the scenes are described by a superposition of locally coherent modes. A model, which combines these requirements is the AM-FM (**A**mplitude **M**odulation - **F**requency **M**odulation) image representation [HHB96]. Here the mode functions are retrieved by decomposing the images with Gabor filters, composing a filter bank. Gabor filters are used, because they are optimally localized in both the spatio-temporal and the wavevenumber-frequency domain, because the Gabor filters minimize the uncertainty relation. For a general approach of texture analysis, an a priori knowledge about the composition of the texture cannot be assumed. Therefore, the filter bank has to cover the wavenumber-frequency domain completely (see Fig. 6 **a)**). From the Gabor channels, in the spatio-temporal domain, a nonlinear demodulation algorithm is used to obtain the AM-FM model parameters, i.e., the spatio-temporal localized amplitude and wavenumber-frequency vector.
The object of examination in the frame of this study, the dynamic texture of the sea surface, has some special properties, which can be included to the texture analysis algorithm, presented here. For a short period of time a sea-surface gravity wave field is assumed to be stationary. For this reason, a Gabor analysis is not necessary in the frequency domain. In complement to the AM-FM decomposition, the method DiSC combines a Fourier decomposition of the stationary signal in the frequency domain and decomposition in the 2D wavenumber domain using 2D Gabor filters.

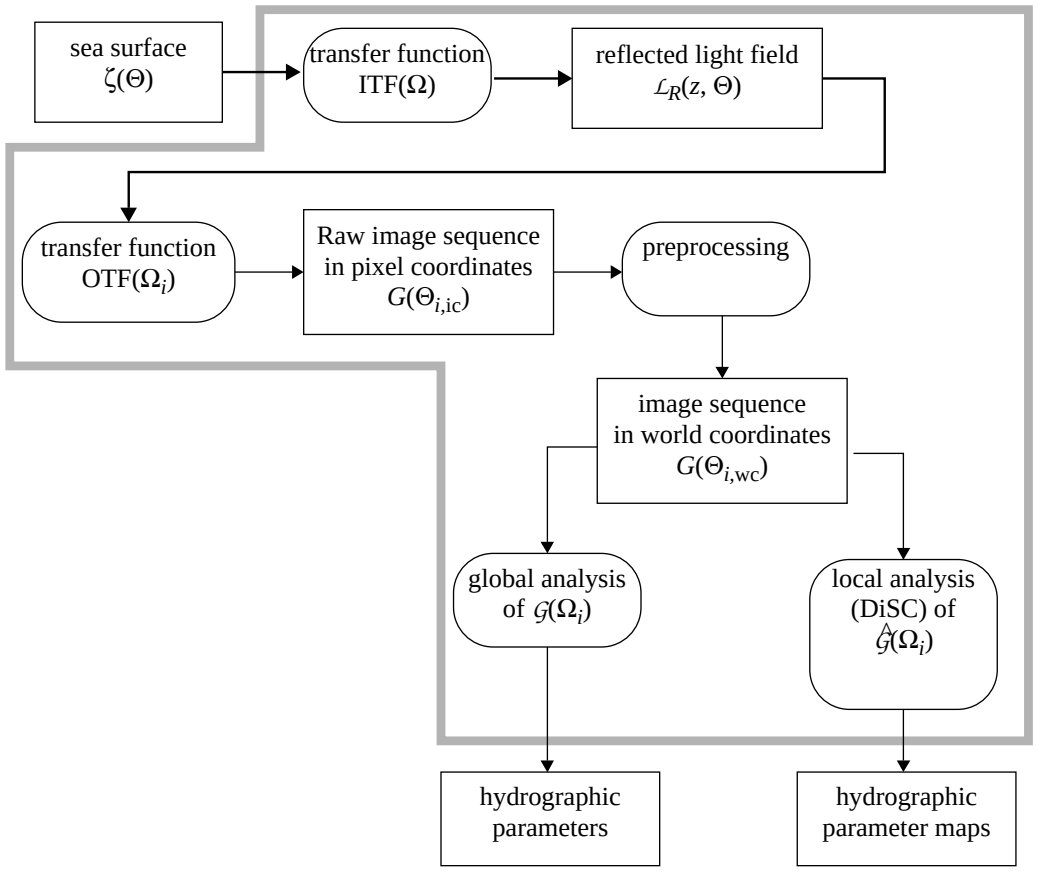

Figure 5: Overview scheme: the relation between the continuous spatio-temporal sea-surface elevation, $\zeta(\Theta)$, and the reflected light field, $\mathcal{L}_R(z, \Theta)$, can be described by a spectral image transfer function, $\mathrm{ITF}(\Omega)$. If $\mathcal{L}_R$ is imaged by a CCD camera, this imaging process and the discretization is described by an optical transfer function, $\mathrm{OTF}(\Omega_i)$. The sensor yields image sequences in camera-pixel or image coordinates, $G(\Theta_{i,\mathrm{ic}})$. The discrete raw-image sequences are geometrically transformed to image sequences given in world coordinates, $G(\Theta_{i,\mathrm{wc}})$ (i.e. the mean sea surface). To retrieve global hydrographic parameters the global analysis is performed on the discrete 3D gray-level variance spectra, $\mathcal{G}(\Omega_i)$, of the image sequences. For spatial hydrographic parameter maps, the local method DiSC is performed on discrete complex-valued 3D spectra, $\hat{\mathcal{G}}(\Omega_i)$, whereby the phase information the spatial structure of the images sequences is preserved.

For the special case of the analysis of the dynamic sea-surface texture the physical behaviour can be modeled by the dispersion relation, yielding the frequency as a function of the wavenumber vector. Because of the validity of the dispersion relation, for each frequency mode only a subregion of the wavenumber domain is occupied by the spectral signature. Only to these subregions the Gabor filters are adapted (see Fig. 6 **b)**). In contrast to a general texture analysis task, the wavenumber-frequency vector is not the target parameter. In an additional step, the hydrographic parameters water

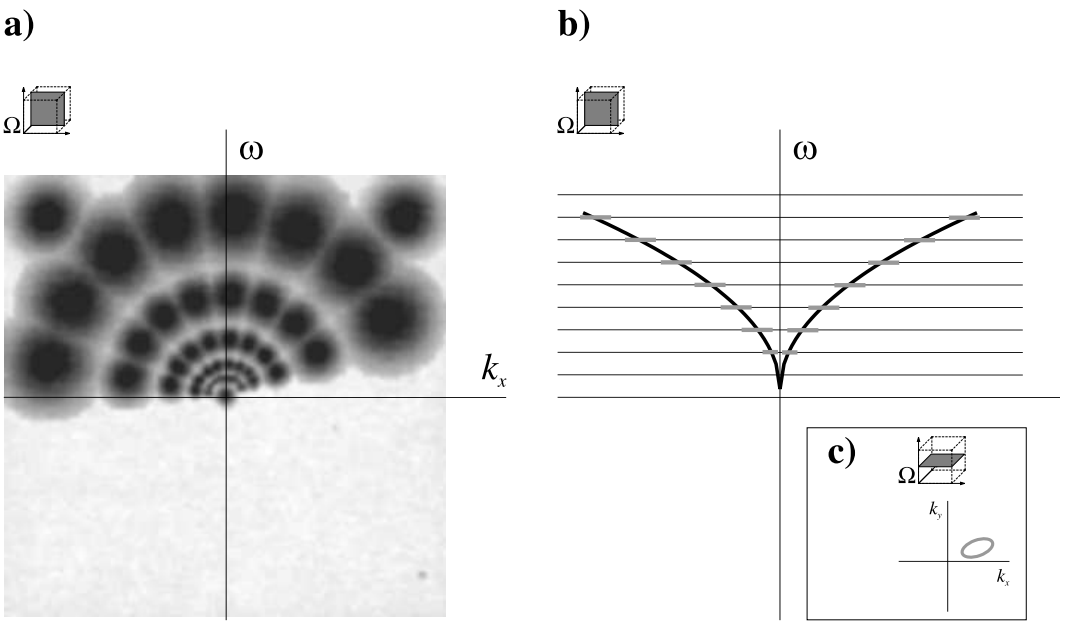

Figure 6: General approach and specialized approach of DiSC: **a)** Gabor-filter bank (underlying Gabor-filter bank image is taken from [HHB96], p. 362) diagrammed in a 2D wavenumber-frequency k_x–ω section of the 3D wavenumber-frequency domain Ω composed of 3D Gabor filters covering one half of the spectral domain completely (general approach); **b)** Gabor-filter bank composed of 2D Gabor filters diagrammed in a 2D k_x–ω section of the 3D spectral domain; the locations of the Gabor filters are attached to the dispersion relation (thick solid line); in **c)** the 2D orientation of a 2D Gabor filter is illustrated in the wavenumber k_x–k_y section of the 3D spectral domain (**b)** and **c)**: specialized approach of DiSC).

depth and current are deduced from the texture parameters wavenumber and frequency using the dispersion relation (which is a function of the free parameters water depth and current) as a physically motivated regression model.

This thesis ▷ brief description of content

The characteristics and the theoretical background of the description of a sea surface, $\zeta(\Theta)$ (or wave field), with surface elevation ζ, 3D spatio-temporal domain Θ, two spatial components x, y, and time t is described in Sec. 2.
The imaging of the sea surface by modulating the incident light field, which is reflected at the sea surface, is described in Sec. 3. This physical relation is parameterized by an image-transfer function, ITF(Ω).
The reflected light field, $\mathcal{L}_R(z, \Theta)$, is observed by a CCD camera. The result is a discrete optical-image sequence. The instrumentation used to retrieve image sequences and an optical transfer function, OTF(z, Θ), describing the imaging properties of the optical image-sequence acquisition system used, are explained in Sec. 4.
The pre-processing steps, the global analysis method and the newly developed local-analysis method are introduced in Sec. 5.
Two experiments are presented in Sec. 6. The first experiment was carried out at the Wind-Wave Tank of the University of Hamburg in order to apply

and test the global-analysis method for optical image sequences. The second experiment was conducted at the Multidirectional-Wave Facility of the Spanish harbour authority CEDEX (Centro de Estudios y Experimentación de Obras Publicas) in Madrid (Spain) a) to demonstrate the ability of the global-analysis method in resolving the multidirectionality of wave fields and b) to apply and test the local-analysis method, DiSC.
The results are presented in Sec. 7 and are discussed in Sec. 8.
A summary and the outlook concerning the future potential of this work to the field of oceanography and coastal engineering is given in Sec. 9. In physics, geophysics, material sciences and others, dispersion relations are often used to characterize physical properties of the observed object. At the end of this work, a strategy is proposed by which DiSC may be applied to solid-matter physics.

2 Dispersive Boundaries: The Sea Surface

2.1 Dispersive Surfaces

The states of aggregation (i.e./ gaseous, liquid and solid) of material and the molecular structure of an individual material allows a broad variety of possibilities for waves to propagate in the inner body or at a boundary. Examples are sound or light waves (propagating also in vacuum) or mechanical surface waves at solid or liquid surfaces. The relation between the spatial and temporal wave parameters wavelength, λ, and waveperiod, τ, is a function of parameters describing matter, such as density, elasticity, plasticity and surface tension. The function describing the relation between λ and τ depending on the free physical parameters is a dispersion relation.
Generally, mechanical waves are an oscillation of material around a rest position. If the particles oscillate around the rest position into the wave-travel direction they are called longitudinal waves (e.g. sound waves).
In solid bodies the molecules are bonded to their neighbours. The characteristics of the material are dependent on the type of molecular bonding. The bonding determines physical parameters such as elasticity and plasticity and therefore the conditions for wave propagation. In contrast in gaseous and liquid medias the molecules move freely. The molecules are not bonded to their neighbours (or bonded for a short residual time in clusters).
Gases have high potential energies, resulting from weak cohesive forces, allowing free motion and a completely random molecular distribution. In gaseous media the type of compression waves is the prior type. The viscosity of gases is lower and the compressibility is higher than for liquid media. Therefore shear waves can hardly develop. An exception can be found at inner atmospheric boundaries, where two types of adjacent air masses meet. Strong vertical temperature gradients generate a vertical density gradient. The boundaries can be assumed to be an interface that allow waves to develop. At the atmospheric interface (e.g. a cold layer beneath a warm layer) shear-wave cloud patterns can be observed (see Fig. 7).
Liquids have moderate cohesive forces. Therefore, liquids have not the orderliness of solid matter or the random behaviour of a gas. The molecules of a liquid do not move unrestrictedly through the total volume. The molecules reside whithin a radius of a few molecules. Water and liquids in general are almost incompressible. Thus hydrodynamic equations the compressibility is neglected normally for transport problems.

2.2 Sea-Surface Waves

Ocean-surface waves move at speeds varying from ca 0.23 ms^{-1} at length scales of millimeters for ripples (capillary waves) up to 290 ms^{-1} for tsunamis (ocean-surface waves created by seaquakes) at length scales up to 200 km. The energy distribution versus length scale is given in Fig. 8. Ocean-surface waves can be classified by their driving forces or their restoring forces. Generation forces are

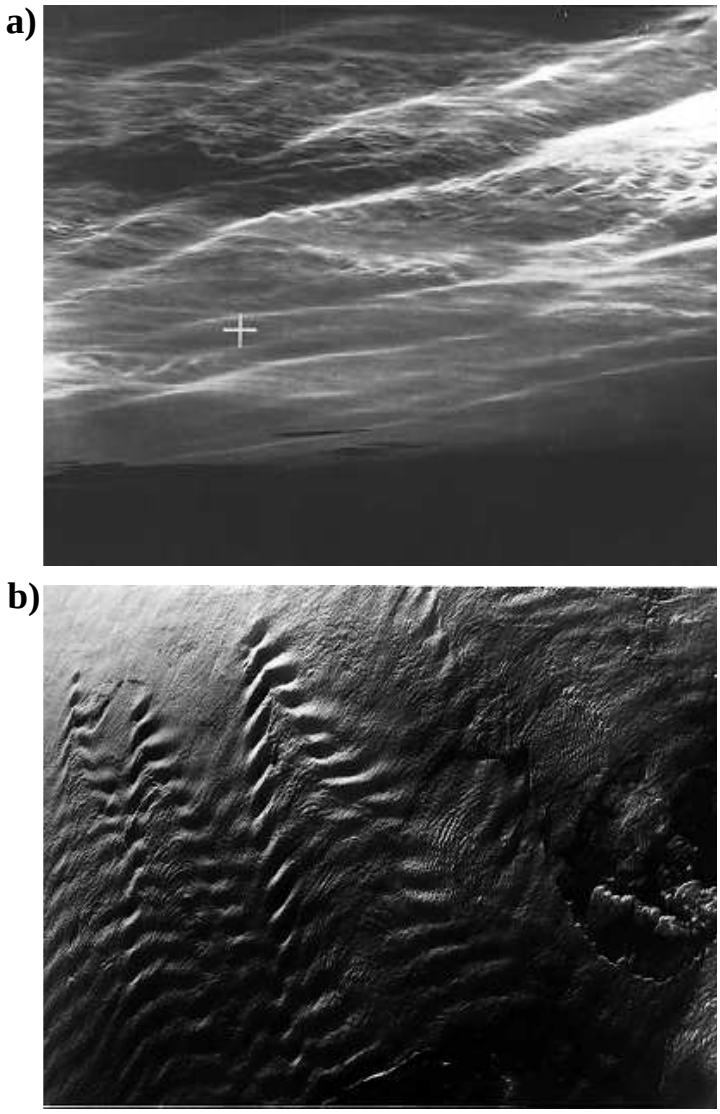

Figure 7: Atmospheric waves: **a)** noctilucent (night luminous) cloud photographed over Scandinavia (source: [Wit57]); **b)** view of cloud-covered mountainous terrain captured by cameras aboard the Space Shuttle (image courtesy of NASA).

- wind (wind sea and swell),
- tidal forces of moon, sun and planets (tidal waves),
- seaquakes (tsumamis) and
- meteorological pressure variabilities.

Restoring forces are

- surface tension (short capillary waves),
- gravition (gravity waves),

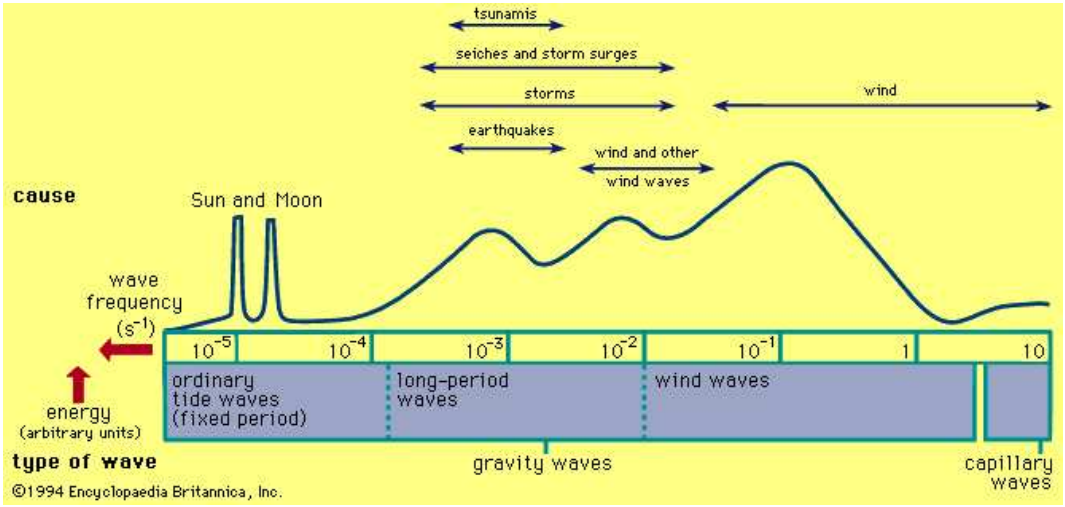

Figure 8: Ocean waves: energy distribution versus wavelength (source: www.brittanica.com).

- Coriolis parameter describing the deflecting force of the earth rotation (Kelvin waves),
- latitude dependence of the Coriolis parameter (planetary Rossby waves) and
- bathymetric variations leading to a deflection of shallow-water waves (topographic Rossby waves).

In addition to wind-generated waves, tidal waves generated by the gravitational forces of the moon, the sun and the solar planets; tsunamis created by seaquakes; and seiches created by natural (or eigen) oscillations in semi-enclosed or closed sea basins are observed in the oceans. These waves are not considered in this thesis. Here wind-generated waves, and in hydraulic wave tanks also mechanically generated waves, with the restoring forces gravity and surface tension are treated.
If wind skims along the water surface, small perturbations of the near-boundary atmospheric pressure field lead to small pertubations of the water surface. The distorted surface allows viscous or turbulent energy transport, leading to the growth of waves.
The formation of a wind sea and the reshaping of the directional and frequency spectra of energy ultimately has not yet been clarified. A first approach to explain the formation and development of wind sea is the instability theory [Tho71], leading to an exponential growth of waves until nonlinear effects become dominant. Kelvin's theory cannot explain the growth of a wind sea at wind speeds lower than 6.5 ms^{-1}. However, observations show that a wind sea already starts to form at a wind speed of 1.1 ms^{-1}.
The sheltering theory [Jef24] is based on the assumption that wind does not pass an irregularly-shaped wave in a laminar flow, but rather becomes turbulent. At the wave's lee side (wave front turned away from wind) vortices are generated, leading to a pressure gradient between luff (wave back, directed

toward the wind) and lee side of the wave. If the wind speed is higher than the wave's phase speed, energy is transported from the atmosphere to the water body leading to wave growth.
Statistical principles were introduced in [Phi57]. The theory is based on the assumption that wind always shows a certain degree of turbulence. This turbulence implies pressure gradients deforming the water surface. In contrast to the sheltering theory, here the turbulence is independent from the actual shape of the surface ('frozen' turbulence). A combined theory [SC66] using the theory of Phillips and Miles [Mil75] – presuming the existence of small waves, leading to pressure pertubations and thus wave growth – shows that Phillips' theory describes the initial state well and that Miles' theory becomes dominant with increasing sea-state energy.
The temporal evolution of wind sea energy is generally described by

$$\frac{\partial \mathcal{E}}{\partial t} + C_G \cdot \nabla \mathcal{E} = \mathcal{S}_{\mathrm{atm}} + \mathcal{S}_{\mathrm{nl}} + \mathcal{S}_{\mathrm{diss}}, \tag{2.1}$$

with energy E, density action (or source term) $\mathcal{S}$, time t, group phase speed C_G, atmospheric source term, $\mathcal{S}_{\mathrm{atm}}$, nonlinear source term, $\mathcal{S}_{\mathrm{nl}}$, and source term of dissipation due to wave breaking, turbulence, bottom friction, etc., $\mathcal{S}_{\mathrm{diss}}$.
Sea-surface waves within a wind-covered area, still growing, are called a wind sea (Fig. 9 a). Mature waves leaving the wind-fetched area are called a swell (Fig. 9 b).

2.2.1 Definition of Sea-Surface Waves

Sea-surface waves (see Fig. 1) are deformations at the air–sea boundary and are characterized by their wavelength, λ (or reciprocally, their wavenumber, $k = 2\pi\lambda^{-1}$), their wave period, τ (or reciprocally, their angular frequency, $\omega = 2\pi\tau^{-1}$), their amplitude, ζ, and their direction of propagation, ϑ.
A sea-surface wave is a plane wave and therefore k and ϑ can be expressed in Cartesian coordinates as a two-component wavenumber vector, $\vec{k} = (k_x, k_y)$.
A linear sea-surface wave is of sinusoidal shape. Deviations from this shape are expressed as nonlinearities. A single sinusoidal plane wave has the form

$$\zeta(\Theta) = \hat{\mathcal{S}} e^{i(\vec{k}\cdot\vec{r}-\omega t)} + \hat{\mathcal{S}}^* e^{-i(\vec{k}\vec{r}-\omega t)}, \tag{2.2}$$

where ζ is the sea-surface elevation in the spatio-temporal domain $\Theta = (x, y, t)$, $\hat{\mathcal{S}} = \zeta_0 e^{i\phi_0}$ is the spectral Fourier coefficient (ϕ_0 is the initial phase), $\hat{\mathcal{S}}^*$ is the complex conjugated of $\hat{\mathcal{S}}$, $\vec{k}$ is the wavenumber vector and $\vec{r}$ is the spatial vector. The expression

$$\phi = \phi_0 + \vec{k} \cdot \vec{r} - \omega t \tag{2.3}$$

defines the phase, ϕ. A single deep-water wave is shown in Fig. 10.

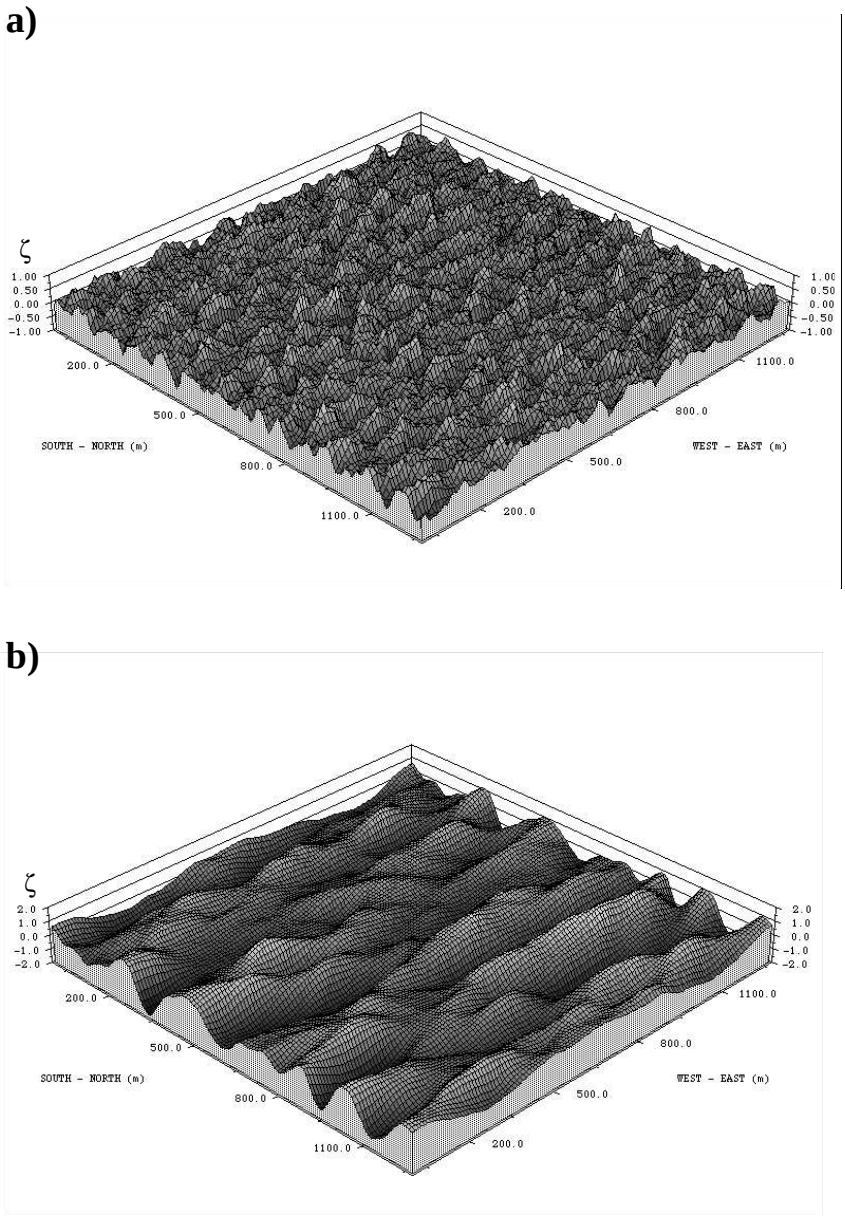

Figure 9: Wave fields simulated by a numerical model: **a)** a wind sea and **b)** a swell (source: [BdA94]).

2.2.2 Definition of Wave Fields

A linear wave field generally is assumed to be a superposition of single waves and its complicated shape is described by the sum

$$\zeta(\Theta) = \sum_{n=1}^{\infty} \hat{\mathcal{S}}_n e^{i(\vec{k}_n \vec{r} - \omega_n t)} + \sum_{n=1}^{\infty} \hat{\mathcal{S}}_n{}^{*} e^{i(\vec{k}_n \vec{r} - \omega_n t)} \tag{2.4}$$

where $\vec{k}_n$ is the n-th wavenumber vector, ω_n is the n-th frequency and $\hat{\mathcal{S}}_n = \zeta_n \cdot e^{i\,\phi_{0,n}}$ is the n-th Fourier coefficient of the n-th wave. The Fourier

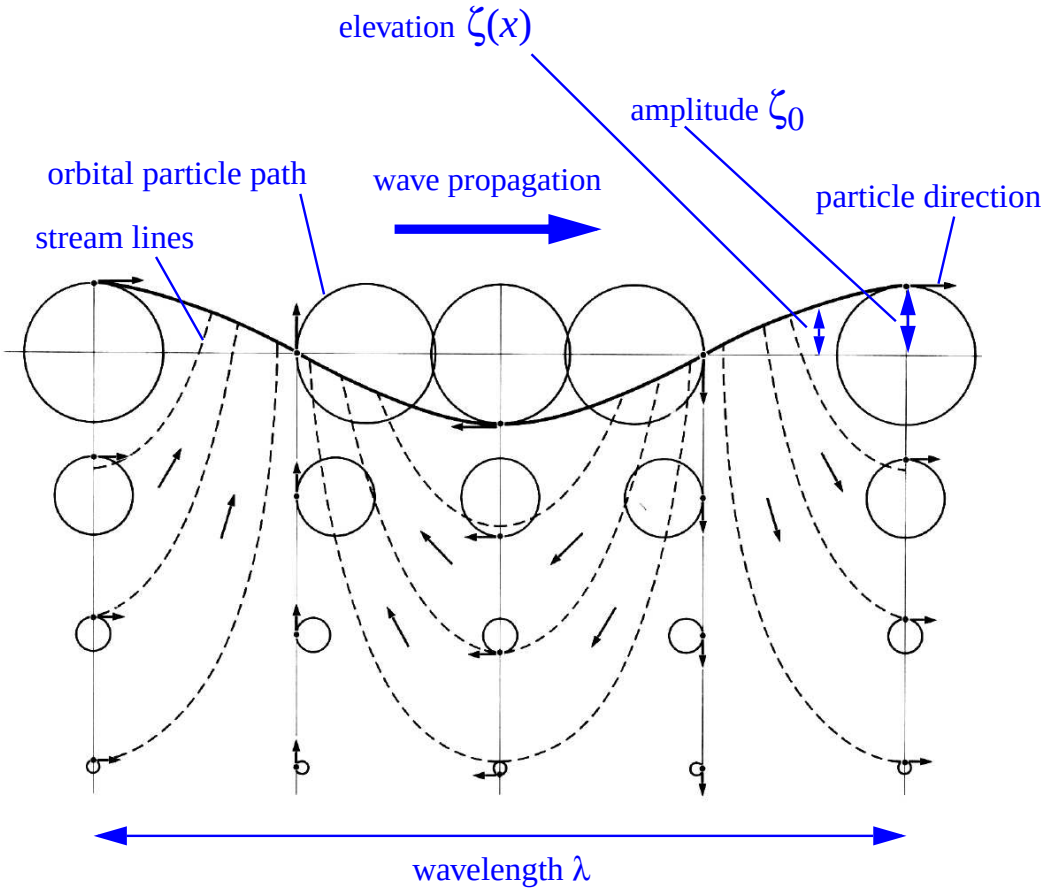

Figure 10: Orbital particle paths, stream lines, and propagation direction of particles of a deep-water wave (source: [DKKS75]).

decomposition of the wave field (2.4) assumes stationarity and homogeneity.

Because the elevation, ζ, is a real-valued quantity, the spectral Fourier coefficients are hermetic, i.e.

$$\hat{\mathcal{S}}_n(\vec{k}_n, \omega_n) = \hat{\mathcal{S}}_n^*(-\vec{k}_n, -\omega_n). \tag{2.5}$$

The spectral power of the waves is given by

$$\mathcal{S} = \hat{\mathcal{S}} \cdot \hat{\mathcal{S}}^*. \tag{2.6}$$

2.2.3 Dispersion Relation

Assuming a non-viscous, incompressible and homogenous liquid (i.e. water) the dispersion relation of sea-surface waves is derived from the Eulerian equations of motion, the continuity equation and the dynamic and kinematic boundary conditions at the sea surface and the sea floor. A detailed description of the derivation of the dispersion relation is given in [Win94].
The phase speed C_P and the group speed C_G are given by

$$C_P = \frac{\omega}{k} = \frac{\lambda}{\tau} \tag{2.7}$$

and

$$C_G = \frac{d\omega}{dk} = \frac{d\lambda}{d\tau}. \tag{2.8}$$

The phase speed C_P determines the speed of propagation of a single wave, and the group speed determines the speed of energy propagation of the wave field's beat wave. In extremely shallow water (wavelength $\lambda < 10/d$, where d is the water depth) $C_G = C_P$; in deep water ($\lambda > d/2$) the condition $C_G = C_P/2$ holds.
The dispersion relation describes the dynamic relation between wavenumber k and angular frequency ω (hereafter 'frequency') and determines the phase speed (speed of propagation) of a wave. The term 'normal' dispersion implies that longer waves have a higher phase speed than shorter waves. Normal dispersion holds for sea-surface gravity waves. 'Anormal' or 'inverse' dispersion indicates that shorter waves travel faster than longer waves. This performance holds for capillary waves. The linear dispersion relation for free capillary-gravity sea-surface waves is given by

$$\tilde{\omega}(\vec{k}) = \underbrace{\sqrt{gk\left(1 + \frac{\Gamma_{\mathrm{H_2O}} k^2}{\rho_{\mathrm{H_2O}} g}\right)\tanh(kd)}}_{\varsigma} + \underbrace{\vec{k}\cdot\vec{u}_c}_{\omega_D}, \tag{2.9}$$

where g is the gravitational accelaration, d is the water depth, $\vec{u}_c$ is the near-surface current, $\Gamma_{\mathrm{H_2O}}$ is the surface tension of clear water, $\rho_{\mathrm{H_2O}}$ is the density of clear water. Generally the density, ρ, is a function of temperature, pressure. Ocean water also is a function of salinity. The surface tension, Γ, is a function of temperature, salinity and additionally surfactants spread on the surface (a surfactant is a surface-active substance, e.g. washing detergent). In (2.9) the first term is called the intrinsic frequency, ς, and the second term is called the Doppler frequency, ω_D. The Doppler-frequency term, ω_D, indicates the effect of the near-surface current. Following (2.9), the accelerations which force an elevated particle to move back to the initial position, $\bar{\zeta}$, are g and $\Gamma_{\mathrm{H_2O}} k^2 \rho^{-1}_{\mathrm{H_2O}}$. The surface tension of water only has a significant effect on small waves ($\lambda < 0.1$ m). Those waves are called capillary-gravity waves. Waves longer than 0.1 m generally are called gravity waves. In (2.9) the surface tension, $\Gamma_{\mathrm{H_2O}}$, the water depth, d, and the near-surface current vector, $\vec{u}_c$, are free parameters influencing the shape of the dispersion shell in the wavenumber–frequency domain, Ω. Therefore the shape of the dispersion shell can be used to inversely determine these free parameters .
Gravity waves ($\lambda > 0.1$ m) are approximated by

$$\tilde{\omega}^{\pm}(\vec{k}) = \underbrace{\pm\sqrt{gk\tanh(kd)}}_{\varsigma^{\pm}} + \omega_D. \tag{2.10}$$

The dispersion relation generates a shell in the 3D Ω domain. The intrinsic dispersion shell is symmetric about the rotational axis (see Fig. 11). The intrinsic dispersion relation has two solutions, ς^+ and ς^-. These two solutions

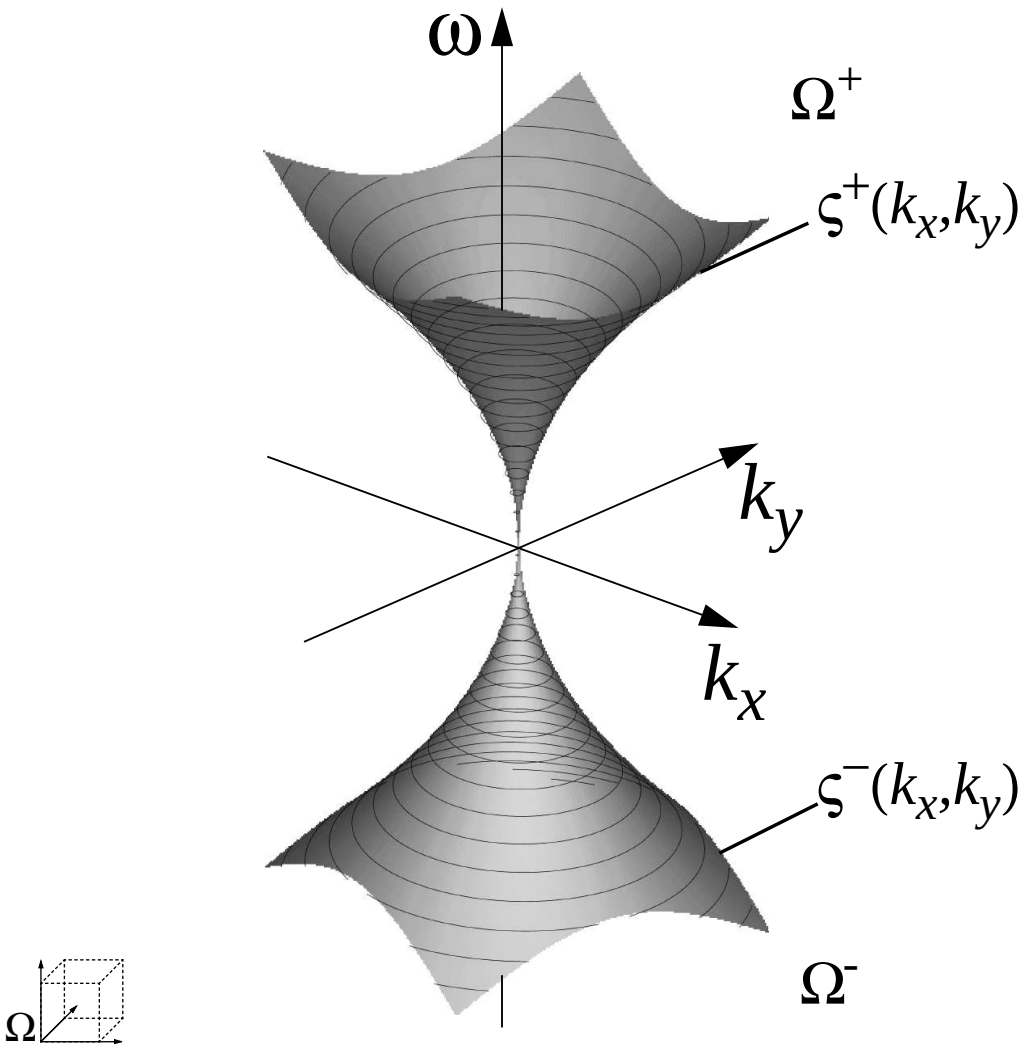

Figure 11: Positive and negative intrinsic dispersion relations, ς^+ and ς^-, of linear deep-water surface-gravity waves in the 3D Ω-domain (with positive and negative hemispheres, Ω_+ and Ω_-).

are redundant, a consequence of the symmetrical attribute $\varsigma^+ = -\varsigma^-$ of the Fourier transformation.
Because of the redundancy of the dispersion shells $\varsigma^+(\vec{k})$ and $\varsigma^-(\vec{k})$, due to (2.5), only one of the shells is needed to describe the energy of wave fields in the Ω domain. Using the positive solution, ς^+, of (2.10) the convention for the wave propagation direction is 'going to'. If ς^- is used, the 'coming from' convention is predefined. In this work the 'going to' convention is always used.

2.2.4 Near-Surface Current, Water Depth, Surface Tension

Near-surface current: If a near-surface current, $\vec{u}_c$, is present, waves are Doppler shifted. The Doppler shift, ω_D, leads to a frequency shift of $\tilde{\omega}$. If a current is directed in a direction opposite to that a wave, the wave's absolute

(in the inertial coordinate system of the observer) frequency is decreased (and vice versa). The deformation of the dispersion relation due to the Doppler effect is illustrated in Figs. 12 c) and 13 b).

Water depth: For deep-water waves, defined by the condition $d \gg \lambda$, the approximation $\tanh(kd) \approx 1$ holds and can be substituted into (2.9). By assuming $\vec{u}_c = 0$, the deep-water wave solution is as follows:

$$\varsigma^+(k) = \sqrt{gk}. \tag{2.11}$$

In shallow waters, where d is small compared to λ, the shallow-water dispersion relation

$$\varsigma^+(k) = k\sqrt{gd} \tag{2.12}$$

is obtained when the approximations $\tanh(kd) \approx kd$ and $\vec{u}_c = 0$ are substituted into (2.9). The deformation of the dispersion relation due to variation of waterdepth is illustrated in Figs. 12 b) and 13 a).

Surface tension: Water in contact with air has a surface tension that, when external forces are absent, leads to a minimum-area configuration of the surface. For short sea-surface waves ($\lambda \ll 0.1$ m) surface tension leads to a restoring force which lets a particle tend back to the initial position. For waves longer than 1.67 cm, the first term, driven by the gravitational acceleration, of the intrinsic term in (2.9) prevails; for shorter waves, the second term, driven by the surface tension, becomes dominant. This balance leads to an intermediate minimum of the phase speed at $C_P = 0.23$ ms^{-1}.

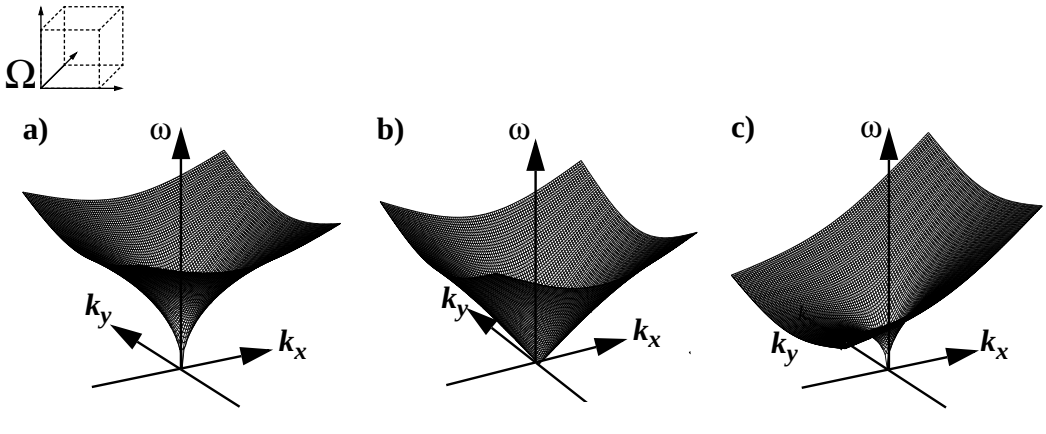

Figure 12: Dispersion relation of linear surface-gravity waves in the 3D Ω domain: **a)** intrinsic deep-water dispersion shell, **b)** intrinsic shallow-water dispersion shell and **c)** Doppler-shifted deep-water dispersion shell influenced by a near-surface current.

2.2.5 Stationary and Instationary Wave Fields

Stationary processes are invariant over time. For a wave field two conditions must hold to fulfill the criterion of stationarity: the local temporal phase

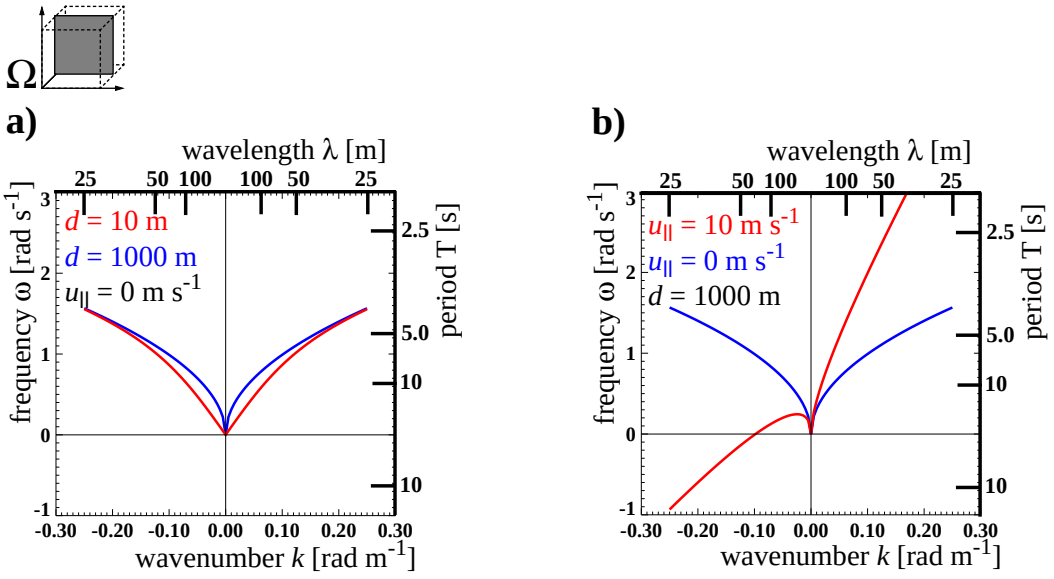

Figure 13: Dispersion relation of linear surface waves given in a 2D k–ω section of the 3D Ω domain: **a)** variation of the dispersion shell depending on the water depth (1000 m deep-water solution: blue line; 10 m shallow-water solution: red line) and **b)** variation of the dispersion shell depending on the parallel component $u_{\parallel}$ of the near-surface current ($u_{\parallel} = 0$ ms^{-1}: blue line; $u_{\parallel} = 10$ ms^{-1}: red line).

gradient, $\partial\phi_l/\partial t$, and the local amplitude, ζ_l, have to be invariant in time for a considered chunk:

$$\frac{\partial\phi_l}{\partial t} = \omega_l = \text{ const. and } \frac{\partial\zeta_{0,l}}{\partial t} = 0, \tag{2.13}$$

where ϕ_l is the temporally local phase, $\zeta_{0,l}$ is the temporally local amplitude, and ω_l is the temporally local frequency. If one of the above criteria does not hold for at least one wave of the wave field for a given chunk, the wave field is instationary.

2.2.6 Homogeneous and Inhomogeneous Wave Fields

Homogeneous processes are invariant in space. For a wave field in an oceanic box two conditions must hold to fulfill the criterion of homogeneity: the spatially local phase gradients, $\partial\phi_l/\partial x$, $\partial\phi_l/\partial y$, and the local amplitude, ζ_l, have to be invariant in space. Defined for the Cartesian coordinates x, y, the criterions of homogeneity are

$$\frac{\partial\phi_l}{\partial x} = k_{x,l} = \text{ const. and } \frac{\partial\zeta_{0,l}}{\partial x} = 0 \tag{2.14}$$

and

$$\frac{\partial\phi_l}{\partial y} = k_{y,l} = \text{ const. and } \frac{\partial\zeta_{0,l}}{\partial y} = 0, \tag{2.15}$$

where ϕ_l is the spatially local phase, $\zeta_{0,l}$ the spatially local amplitude, and $\vec{k}_l$ the spatially local wavenumber vector. If one of the above criteria does not hold in the considered ocean box for at least one wave of the wave field, the wave field is inhomogeneous.
The above-mentioned processes are inhomogeneous processes. The spectral effects due to inhomogeneous and instationary processes are illustrated in Fig. 14.

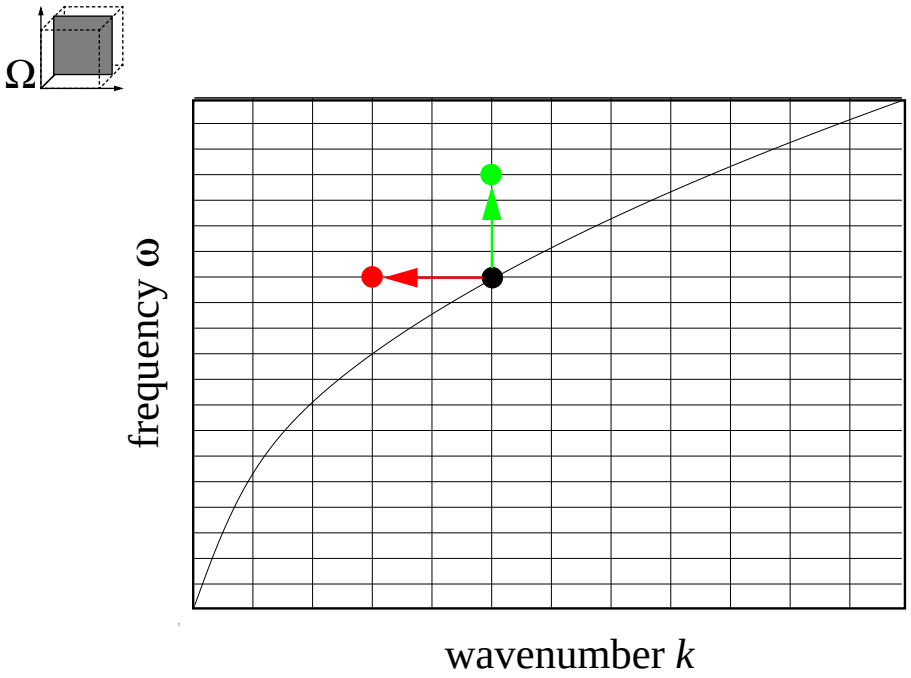

Figure 14: Spectral instationarity and inhomogeneity illustrated in a 2D k–ω section: if a wave field is instationary, the global spectral signal is smeared to other frequencies (green dot); if a wave field is inhomogeneous, the global spectral signal is smeared to other wavenumbers (red dot).

2.2.7 Refraction, Diffraction, and Reflection of Sea-Surface Waves

If sea-surface waves interact with obstacles, wave parameters change. Obstacles are the sea bottom in shallow waters, the coast, and coastal structures. Most of the concepts used to explain the interaction of sea-surface waves with obstacles have been adopted from the field of light optics.
Refraction: If a wave approaches an area with water depth $d < \lambda/2$, the wave 'feels' the sea bottom. The circular oscillation paths (see Fig. 10) of water particles change to elliptically shaped paths. For refraction the frequency, ω, is invariant and the wavenumber vector, $\vec{k}$, varies. Following (2.12), with decreasing water depth, the phase speed decreases. Wave crests in areas with ascending sea bottom come closer to each other, i.e. the wavelength decreases. Because waves in shallow waters are slower, the parts of a wave crest which are closer to the beach fall behind the deep-water parts more

distant to the coast. Considering a linearly sloping bathymetry perpendicular to the beach line, a wave, not travelling perpendicular to the beach line, turns its direction to the beach: waves are refracted towards the beach. The phase speed for a variable shallow bottom has a spatial dependency. Therefore refraction is an inhomogeneous process. The wave follows the path with the shortest possible propagation time. An example of refraction paths calculated by the shallow-water model HYPASUS (**Hy**brid **Pa**rametrical Wave Model **SU**per **S**hallow) [Win94] is shown in Fig. 15. Refraction as well can be induced by current shears ($\partial\vec{u}_c/\partial x \neq 0$ or ($\partial\vec{u}_c/\partial y \neq 0$) (in example tidal

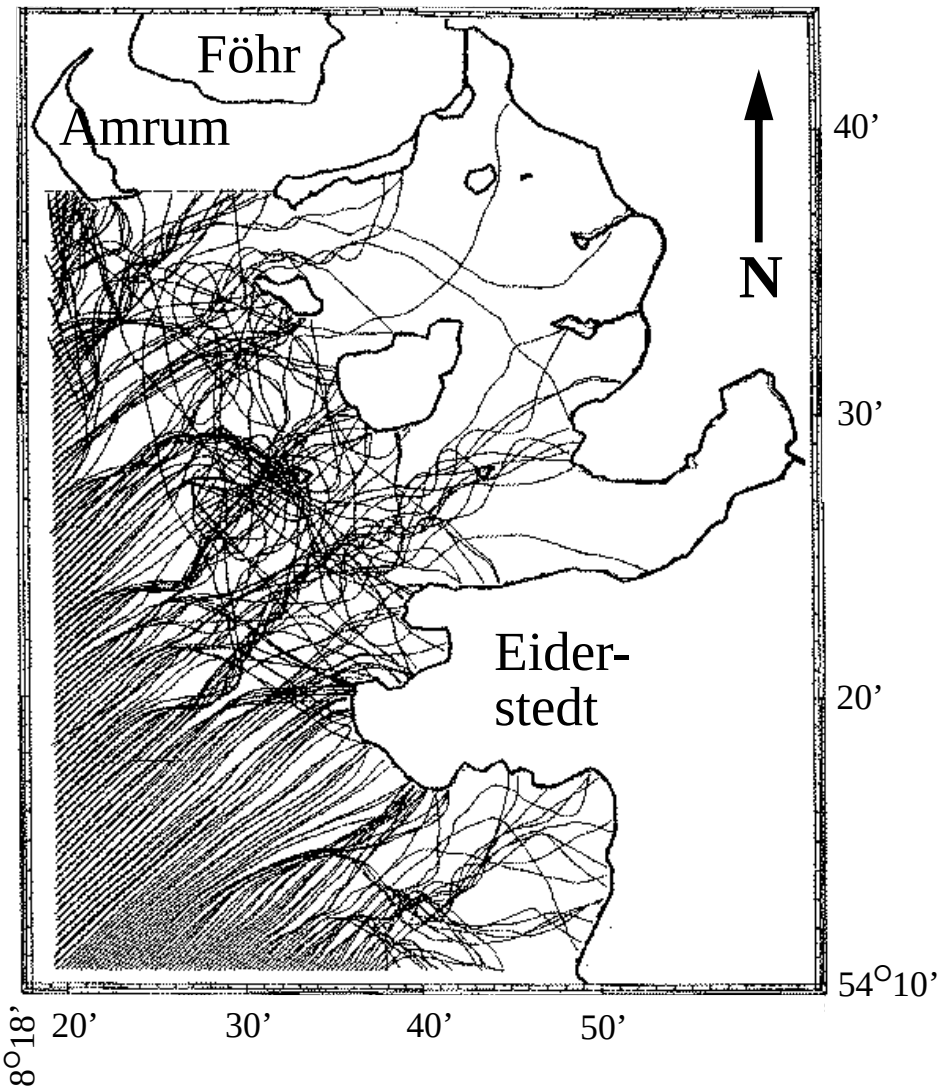

Figure 15: Refracted water waves in shallow water simulated by the numerical HYPASUS wave model (source: [Win94]): refraction paths at flood tide (+3.5 m NN) of a partial wave coming from southwest with a frequency of 0.07 Hz (wave period $\tau = 14.29$ s). The thin lines indicate the refraction paths, showing the local propagation directions (normal to the wave crest); the thick lines indicate the coastline.

currents). The effect of bathymetry and currents on waves is described in [Tol90].

Diffraction: This phenomenon occurs if a sea-surface wave impinges on obstacles (see Fig. 16) such as port constructions. Diffraction is restricted to an area within a few wavelengths of the obstacle. Diffraction can be explained by the principle of Huygens: the propagation of a wave can be constructed by the concept that each point on a wave crest is the source of a new elementary wave. Diffraction allows waves to propagate into geometrically shadowed zones. If a wave is diffracted, the wavenumber's magnitude k and the frequency ω are invariant. The unit-direction vector, $\vec{e}_k$, of the wavenumber vector, $\vec{k}$, and the local amplitude, $\zeta_l(R)$, change.

Reflection: At a vertical wall a wave is directly reflected by the geometrical-optics argument: the incidence angle of the propagating wave is equal to the reflection angle of the reflected wave.

For diffraction and reflection the solution of Sommerfeld [Som47], developed for light optics, has been transferred to sea-surface waves by [PP94]. Modern approaches are mainly based on numerical models or perturbation series. For a brief introduction see [Dan00].

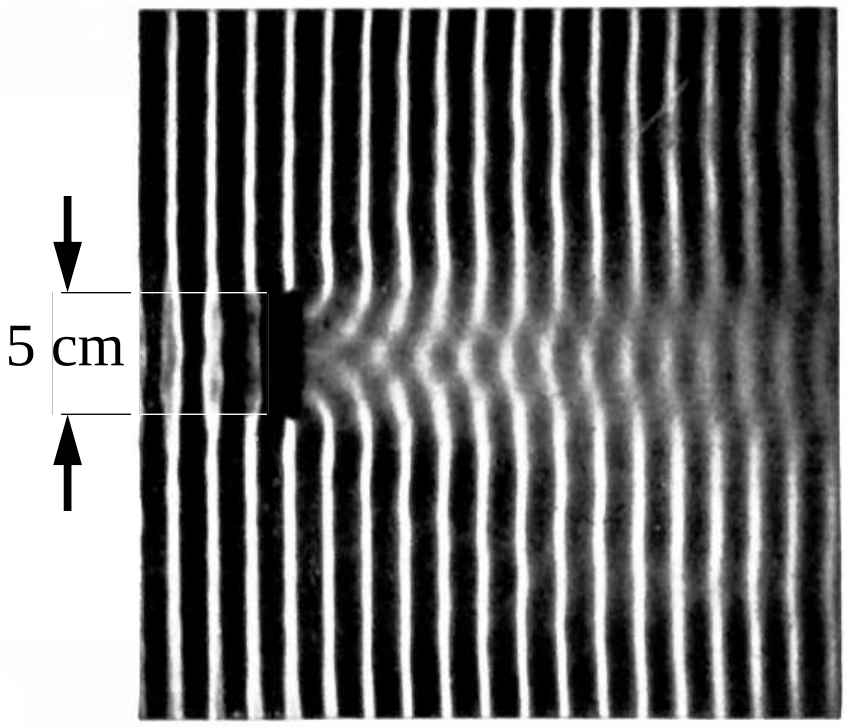

Figure 16: Diffracted water wave behind an obstacle (source: [Poh98]).

2.3 Statistical Description and Parametrization of Sea-Surface Waves

2.3.1 Statistical Description of Sea-Surface Waves

In nature a wave field is a stochastic process. In the homogeneous and stationary statistical theory, the wave components of a wave field are necessarily independent.
In Secs. 2.2.1 and 2.2.2 deterministic waves and wave fields were introduced. For a statistical description of a wave field, the Fourier coefficients, $\hat{\mathcal{S}}$, or amplitudes, ζ_n, or phases, ϕ_n (see (2.2) and (2.4)), are assumed to be random variables. These random variables follow probability functions. The term 'sea state' stands for the description of a wave field by the expected values of the random variables and derived quantities.
In the open ocean a fair approximation is given by the Gaussian wave field. For a Gaussian wave field the complex-valued Fourier coefficients, $\hat{\mathcal{S}}_n$, are Gaussian quantities. The real part, $\mathrm{Re}(\hat{\mathcal{S}}_n)$, and the imaginary part, $\mathrm{Im}(\hat{\mathcal{S}}_n)$, are not correlated (i.e. statistically independent). It follows that the phases, ϕ_n, are equally distributed.
If the stochastic characteristics of the wave field in an area do not change spatially, the wave field is homogeneous. If a wave field does not change its stochastic characteristics temporally, the wave field is stationary (see also Secs. 2.2.5 and 2.2.6).
In the statistical sense a measurement over a spatio-temporal area $X \otimes Y \otimes T \in \Theta$ is a realization. To obtain a stable statistical statement, the spatio-temporal extension of the measured spatio-temporal area should be sufficiently large. For example, a buoy measurement, yielding a time series, lasts approximately 20 min. A measurement with the operational system WaMoS, yielding a spatio-temporal measurement, lasts approximately 2 min. This time interval is sufficiently long because of the additional spatial information. Measurements are deterministic realizations of a random process.
In contrast to measurements, numerical wave models can be either statistical models driven by and delivering expectation values or deterministic models yielding numerical realizations.

2.3.2 Parametrizations in General

The parametrization of energy spectra allows, i.e. for prognostic purposes, the description of the sea state with regard to the free parameters. Most of the sea-state parametrizations are based on the separation ansatz for the energy spectrum,

$$\mathcal{S}(\omega, \vartheta) = \mathcal{S}(\omega)\mathcal{D}(\vartheta, \omega), \tag{2.16}$$

where $\mathcal{S}(\omega, \vartheta)$ is the directional-frequency spectrum, $\mathcal{S}(\omega)$ is the frequency spectrum and $\mathcal{D}(\vartheta, \omega)$ is the normed directional distribution dependent on the wave-travel direction, ϑ, and the frequency, ω.

2.3.3 Frequency Parametrizations

Examples of parametrizations for the factor $\mathcal{S}(\omega)$ in (2.16) are the Pierson–Moskowitz Spectrum for a fully developed wind sea [PM64] and the JONSWAP (**JO**int **N**orth **S**ea **WA**ve **P**rojekt 1968–1969) Spectrum [HBB+73] for a young developing wind sea. The JONSWAP parametrization, based on experimental observations, is given by

$$\mathcal{S}_J(\omega) = \alpha g^2 (2\pi)^{-4} \left(\frac{\omega}{2\pi}\right)^{-5} e^{\left[-\frac{5}{4}\left(\frac{\omega}{\omega_p}\right)^{-4}\right]} \gamma^{e^{\left[-\frac{(\omega-\omega_p)^2}{2\sigma_p^2\omega_p^2}\right]}}, \tag{2.17}$$

were ω is the frequency, ω_p is the peak frequency, α is the Phillips parameter, γ is the peak-expansion parameter and σ_p is the peak width, given by

$$\sigma_p = \begin{cases} \sigma_a & \text{if} \quad \omega \leq \omega_p \\ \sigma_b & \text{if} \quad \omega > \omega_p \end{cases} . \tag{2.18}$$

The empirically determined values are: $\sigma_a = 0.07$, $\sigma_b = 0.09$, and $\gamma = 3.3$. The use of the empirically determined functions

$$\frac{(2\pi)^{-1}\omega_p u_{10}}{g} = 3.5 \left(\frac{gX_W}{u_{10}^2}\right)^{-0.33} \quad \text{and} \quad \alpha = 0.076 \left(\frac{gX_W}{u_{10}^2}\right)^{-0.22} \tag{2.19}$$

yields the parameters ω_p and α. If for (2.19) the parameters wind fetch (the length scale of the wind-covered area), X_W, and wind speed at 10 m height, u_{10}, are known, the form of the frequency–energy spectrum can be determined with the parametrization (2.17). The JONSWAP spectrum merges into the Pierson–Moskowitz Spectrum, the saturated equilibrium case, by substituting the empirical relations $(2\pi)^{-1}\omega_p = 0.13\ g\ u_{10}^{-1}$, $\alpha = 0.0081$, and $\gamma = 1$ into (2.17). The high-frequency part of the ω spectrum is proportional to ω^{-5}.

2.3.4 Directional Parametrizations

A directional distribution of energy has been parametrized for example by [MTS+75]. This parametrization widely is used for example for the parametrization of buoy-mesurement data sets or for controlling wave paddels in multi-directional wave tanks. The approach of the Mitsuyasu-parametrization is

$$\mathcal{D}(\vartheta, \omega) = N(s_\omega) \cos^{2s_\omega}\left(\frac{\vartheta - \vartheta_p}{2}\right), \tag{2.20}$$

where ϑ_p is the peak wave-travel direction. The dimensionless expression N in (2.20) is given by

$$N(s_\omega) = \frac{s_\omega}{\pi} \frac{2^{(2s_\omega - 2)}\Gamma(s_\omega)\Gamma(s_\omega)}{\Gamma(2s_\omega)}, \tag{2.21}$$

where Γ is the Gamma function. The frequency-dependent parameter s_ω of the Mitsuyasu parametrization is given by

$$s_\omega = \begin{cases} 6.97 \left(\frac{\omega}{\omega_p}\right)^{4.06} & \text{if} \quad \omega \leq 1.05\ \omega_p, \\ 9.77 \left(\frac{\omega}{\omega_p}\right)^{-2.33} & \text{if} \quad \omega \geq 1.05\ \omega_p. \end{cases} \tag{2.22}$$

2.4 Nonlinear Sea-Surface Waves

In contrast to linear surface waves natural sea-surface waves are more of a trochoidal shape with sharp crests and flattened troughs (see Fig. 17 b) [Ger02]. An upper limit of the angle of a crest's peak is 120° for a Stokes wave (Fig. 17 a) [Sto47]. Above this angle waves start to break.
The linear wave theory is valid for waves with infinitesimally small amplitudes. Sea-surface waves in nature, having finite amplitudes, are generally nonlinear. In modern nonlinear wave theory, the equations of motion are typically solved by perturbation series.
The most simple case for nonlinear waves is created by the interaction of two waves, ζ_1 and ζ_2 [Phi60], yielding superharmonics at $(\vec{k}_1 + \vec{k}_2, \omega_1 + \omega_2)$, subharmonics at $(\vec{k}_1 - \vec{k}_2, \omega_1 - \omega_2)$, and first harmonics at $(2\,\vec{k}_1, 2\,\omega_1)$ and $(2\,\vec{k}_2, 2\,\omega_2)$. The second-order nonlinear waves are bound to the linear fundamental mode. For wave growth, the nonlinear interaction of at least three waves is needed [Has62].
The first harmonic and the consecutive p-th harmonics are the result of a scaling argument. To retrieve the p-th harmonic the linear dispersion shell is scaled by

$$(\vec{k}_p, \omega_p) = (p+1) \cdot (\vec{k}_0, \omega_0), \tag{2.23}$$

where $\vec{k}_p$ and ω_p are the spectral coordinates of the p-th harmonic and $\vec{k}_0$

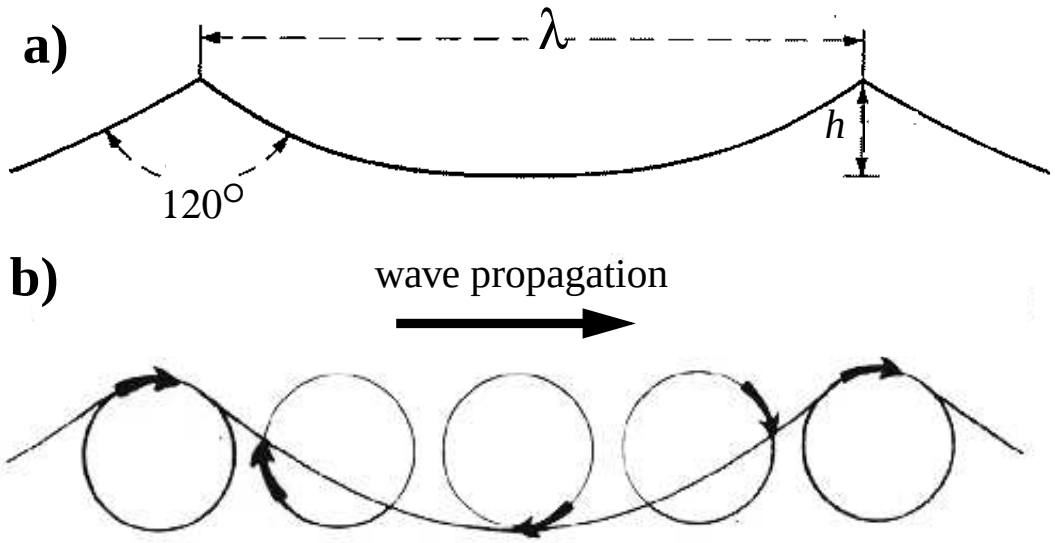

Figure 17: **a)** Schematic of a Stokes wave (source: [DKKS75]): with a maximum crest angle of 120°. The wave height $h = 2\zeta_0$ has a maximum value of $1/7\lambda$. **b)** Schematic of a trochoidal (Greek: 'trochos' = wheel) wave: the diameter of the 'wheel' is equal to the height of the wave. The period of the wave determines the time it takes for the wheel to turn one revolution. The approximate rate at which the water molecules rotate at their orbital (surface) velocity can be determined by dividing the circumference of the wheel by the wave period (source: [Sha98]).

and ω_0 are the spectral coordinates of the linear dispersion relation. Substituting (2.23) into the dispersion relation of sea-surface gravity waves (2.10) yields the p-th harmonic dispersion relation

$$\varsigma_p^+(k) = (p+1) \cdot \varsigma_0^+ \left(\frac{k}{p+1} \right) = \sqrt{(p+1) \cdot gk \cdot \tanh \left(\frac{kd}{p+1} \right)}. \qquad (2.24)$$

The Doppler term ω_D is linearily dependent on the wavenumber and therefore is not affected by the scaling argument.

3 Imaging of Sea-Surface Waves: Specular Reflection and Modulation Mechanisms

The length scales of the sea surface's roughness are orders of magnitude longer than the wavelengths of the electromagnetic waves in the optical band (i.e. visible light from 380 nm to 770 nm). This proposition holds also for the optical band of a CCD camera (see Fig. 18). The roughness of the water surface is smooth for optical frequencies but not for microwave-band (e.g. radar) frequencies. Water has a high absorption rate for IR (**I**nfra **R**ed) light.
To prevent light upwelling from the inner water body, in turbid water an IR filter is mounted on the lens of the CCD camera during the experiments. The characteristic curve of absorption and Rayleigh scattering (molecular scattering) is given in Fig. 19. In Sec. 3.1 the Fresnel coefficients, describing the reflection and refraction at a boundary, are discussed. In Sec. 3.2 the main mechanisms of modulation are discussed 1) tilt modulation and 2) the modulation caused by the geometrical projection of an elongated surface onto the image plane.

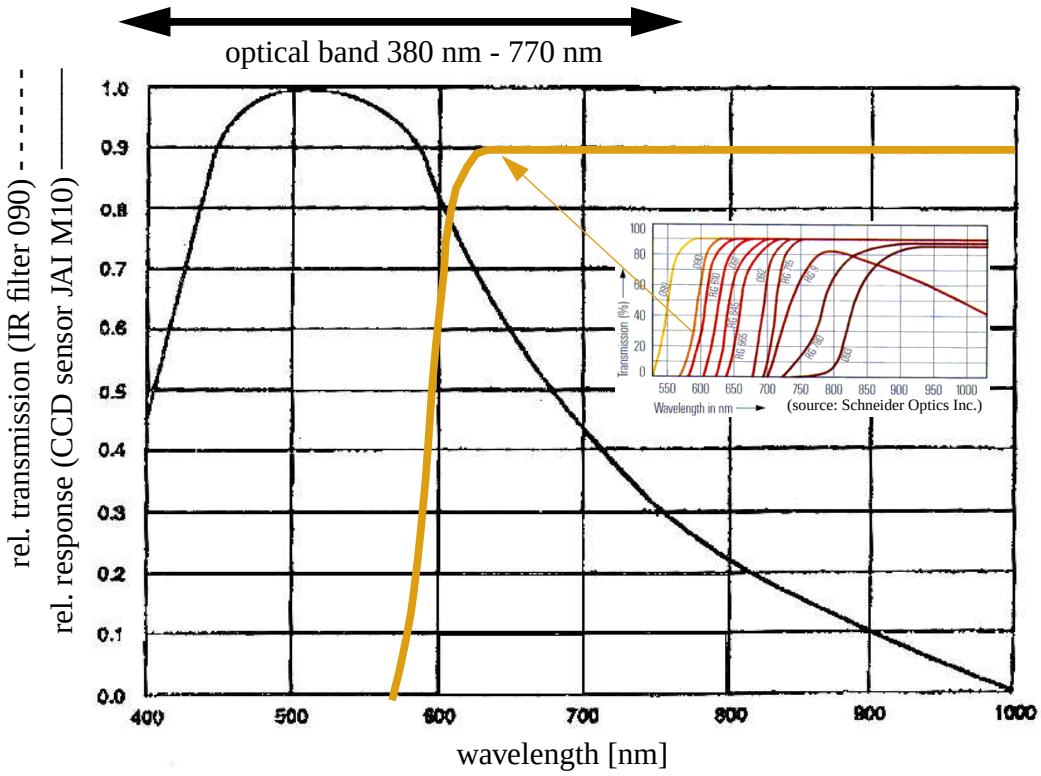

Figure 18: Diagram of the normalized response of the Sony CCD sensor for the JAI M10 CCD sensor (solid line) (source: [NN98c]) and the characteristic curve of the IR (or daylight band elimination) filter Schneider B+W ID 090, orange line (source: [NN98a]).

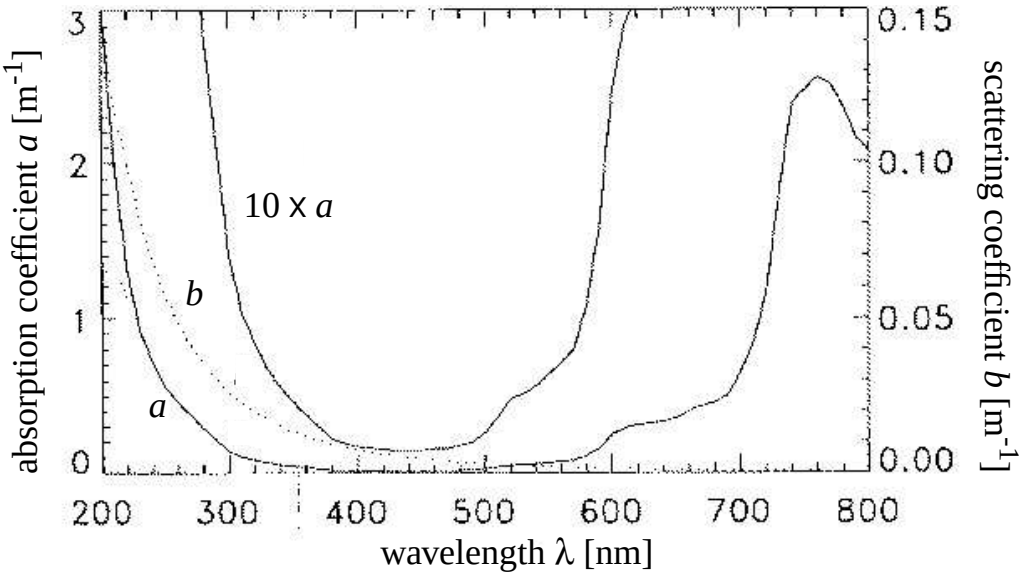

Figure 19: Absorption (solid line) and scattering (dotted line) coefficients of pure seawater, determined by [SB81] (source: [Mob94], p. 89.)

3.1 Specular Reflection

The mechanism of specular reflection at the water surface here is assumed to describe the imaging of the water surface depending on on the illuminating light source, $\mathcal{L}_0$; the local incidence angle; θ_l, and the polarization of the incident light field. In Fig. 20 the nomenclature used to describe reflection at a facet of the water surface is explained. The radiance of the light source radiance, $\mathcal{L}_0$, is defined [Jäh97] as

$$\mathcal{L}_0 = \frac{d^2\Phi}{\cos\theta_l d\Xi dA_0}, \tag{3.1}$$

where Φ is the power of radiant flux or energy per unit time, dQ/dt, A_0 is the unit area, θ_l is the local incidence angle and $d\Xi$ is the solid angle. The radiance is the radiant flux per solid angle and projected area.
The reflected radiance, $\mathcal{L}_R$, is given by

$$\mathcal{L}_R = \rho\mathcal{L}_0. \tag{3.2}$$

To determine the radiance reflected at the air–sea boundary, $\mathcal{L}_R$, the reflection coefficient (i.e. the reflectivity) is given by the Fresnel formulae (see Fig. 21:

$$\rho_{\parallel} = \frac{\tan^2(\theta_I - \theta_R)}{\tan^2(\theta_I + \theta_R)},\ \rho_{\perp} = \frac{\sin^2(\theta_I - \theta_R)}{\sin^2(\theta_I + \theta_R)},\ \rho_{\circledast} = \frac{\rho_{\parallel} + \rho_{\perp}}{2}, \tag{3.3}$$

with the angle of reflection, θ_R, the angle of refraction, θ_I, the parallely polarized Fresnel coefficient, $\rho_{\parallel}$, the perpendicularly polarized Fresnel coefficient,

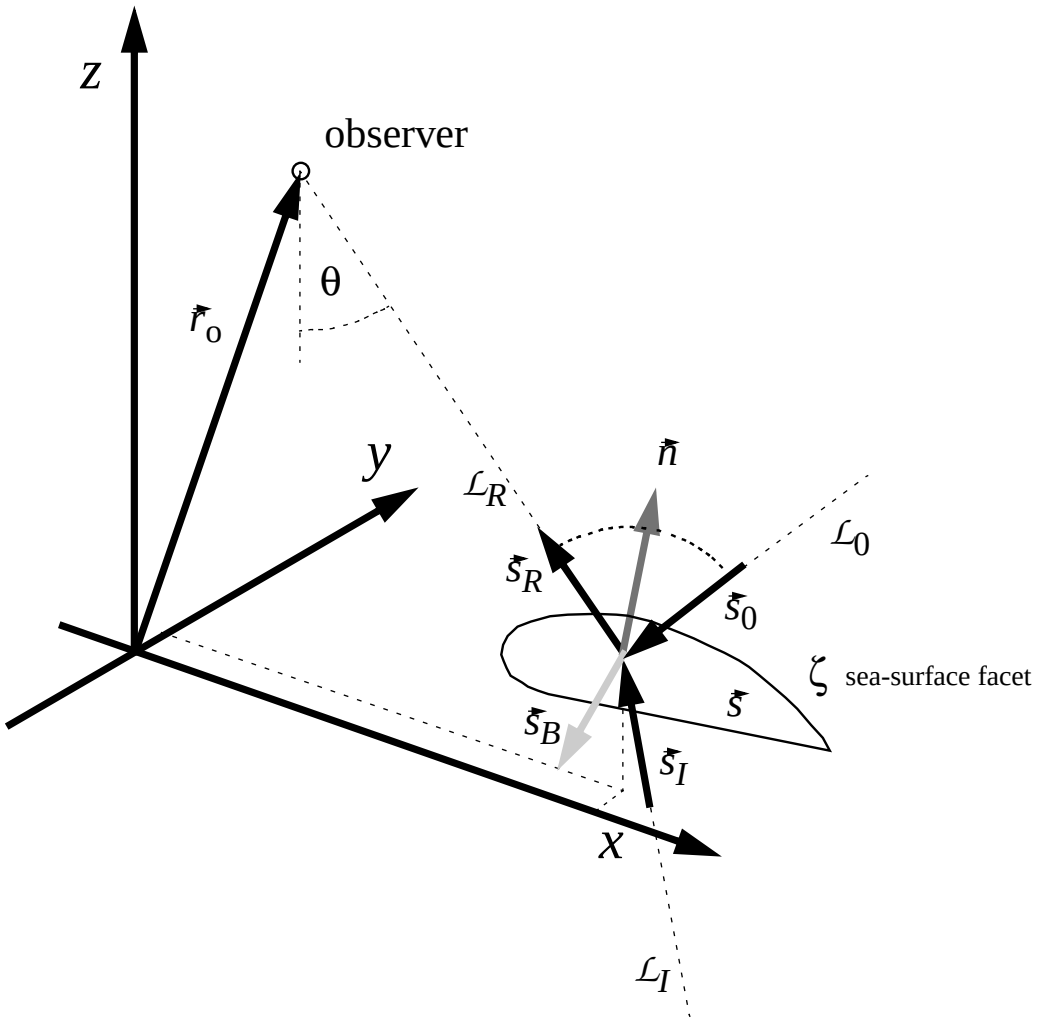

Figure 20: Reflection and refraction at a facet of the water surface: Consider one light ray from the illuminating light source, $\mathcal{L}_0$, with direction $\vec{s}_0$; this light ray is reflected and refracted at the facet. The facet is characterized by the local-slope vector, $\vec{s}$, or the normal vector $\vec{n}$ (dark gray arrow). The direction of the refracted light ray is given by $\vec{s}_B$ (light gray arrow). The refracted light is not visible to the observer. The incident light ray, $\mathcal{L}_0(\vec{s}_0)$, is reflected at the facet in the direction of the observer, $\vec{s}_R$. The reflected radiance, $\mathcal{L}_R$, viewed from the observers position, $\vec{r}_0$, with the incidence angle, θ, of the reflected beam is a function of the Fresnel formulae. Upwelling light from the water body, $\mathcal{L}_I(\vec{s}_I)$, refracted at the interface in the observers direction, $\vec{s}_R$, coincides with the reflected ray.

$\rho_\perp$, and the unpolarized Fresnel coefficient $\rho_\circledast$. The Snell's law describes the ratio of the angle of refraction, θ_I, and the angle of reflection, θ_R:

$$\frac{\sin\theta_I}{\sin\theta_R} = \frac{n_I}{n_R}, \tag{3.4}$$

with the refraction index of air, $n_I = 1$, and of water, $n_R = 1.33$.
The upwelling light field, $\mathcal{L}_I$, is added to the reflected light field, $\mathcal{L}_R$. In this

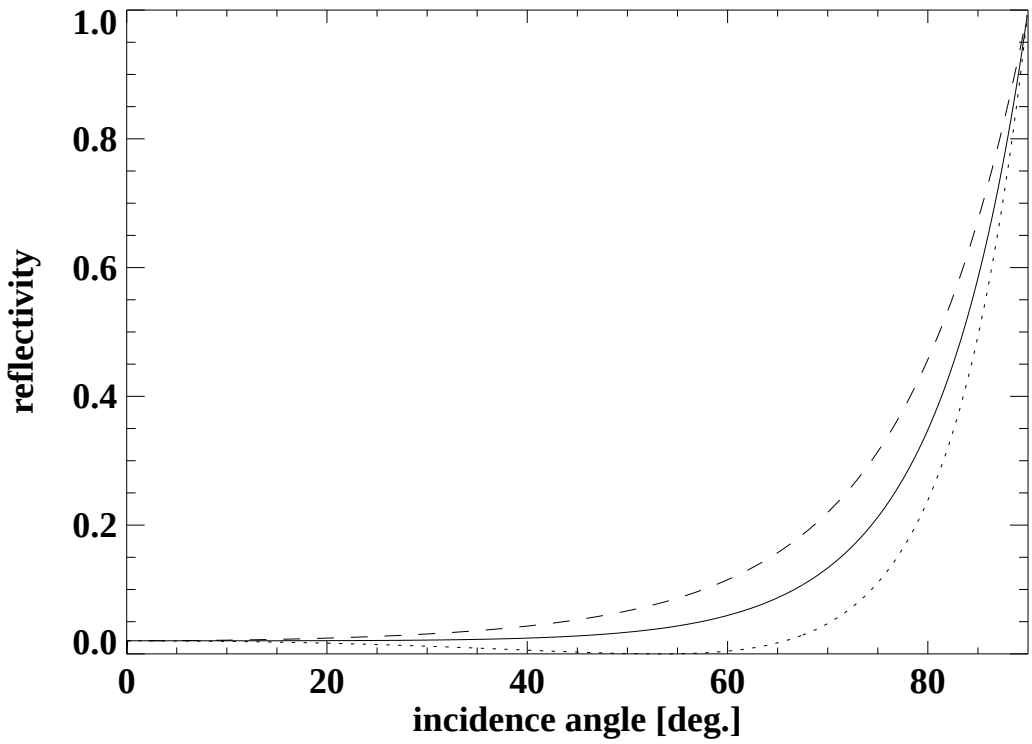

Figure 21: Diagram of the Fresnel formulae: Fresnel coefficients of unpolarized light, $\rho_{\circledast}$ (——), of vertically polarized light, $\rho_{\perp}$ $(\cdots)$, and of the horizontally polarized light $\rho_{\|}$ $(- - -)$, versus incidence angle, θ.

thesis the upwelled light field, $\mathcal{L}_I$, is neglected. The penetration depth of IR light into water is small in contrast to blue light (see Fig. 19). Therefore the use of an IR filter (or daylight band-elimination filter) supresses the imaging of the upwelling blue-band light field (see Fig. 18) and lets IR light pass.

3.2 Modulation-Transfer Function (MTF)

3.2.1 Definition of MTF and ITF

The complex-valued MTF describes the transformation between the complex-valued heave (or elevation) spectrum, $\hat{\mathcal{S}}(\Omega)$, and the complex-valued gray-value image spectrum, $\hat{\mathcal{G}}(\Omega)$. The MTF is defined as

$$\mathrm{MTF}(\Omega) = \frac{\hat{\mathcal{G}}(\Omega) \cdot \hat{\mathcal{S}}^*(\Omega)}{|\hat{\mathcal{S}}(\Omega)|^2}. \tag{3.5}$$

The phase of the MTF describes the phase shift between the surface waves and the image of the wave pattern.
The real-valued image-transfer function (ITF) is defined as the squared modulus of the MTF:

$$\mathrm{ITF} = |\mathrm{MTF}|^2. \tag{3.6}$$

The phase information is lost in (3.6). The ITF describes the relation between the linear part of the elevation and the image spectrum.

3.2.2 Parametrization of ITF

In order to validate an analytical expression for an ITF or if an analytical expression is not known, a parametrization of the ITF can establish an empirical relationship between a measured heave spectrum, $\mathcal{S}(\Omega)$, and the gray-level variance spectrum, $\mathcal{G}(\Omega)$.
Here for the parametrization of the ITF a power law of the form

$$ITF(\Omega) = \alpha(\tilde{\vartheta})k^{\beta}\delta(\omega - \tilde{\omega}) \tag{3.7}$$

is introduced, where α and β are the calibration coefficients, $\tilde{\vartheta}$ is the angle between wave-travel direction, ϑ, and observers horizontal viewing direction, φ, and the δ function using the dispersion relation, $\tilde{\omega}$, as a filter. Consider the fact, that the ITF reveals a relation between gray-level variance and heave variance, but the phase information is lost. Therefore – in contrast to shape-from-shading techniques [HB89] – the proposed parametrization approach is not introduced to undertake a shape reconstruction but to yield heave spectra calibrated with independent measurement devices. This technique has been implemented successfully for nautical radars into the operational system WaMoS II [Bor98].
The coefficients $\alpha(\tilde{\vartheta})$ and β are determined by least-squares methods using in situ data. The first coefficient, α, describes the depth of modulation depending on the spatial gradients of the illumination, the incidence angle of illumination and sensor, and polarization. The second coefficient, β, describes the wavenumber dependency of the imaging mechanism.
An image spectrum, $\hat{\mathcal{G}}(\Omega)$, of sea-surface waves can be filtered by the linear dispersion relation (2.9). The dispersion-filtered spectrum, $\hat{\mathcal{G}}_{\tilde{\omega}}(\Omega)$, therefore is a result of a linearization. Nonlinearities induced by the nonlinear wave field or by a nonlinear imaging process are skipped.

3.2.3 Tilt Modulation

The Fresnel coefficients $\rho_{||}$, $\rho_{\perp}$ and $\rho_{\circledast}$ in (3.3) depend on the position of the sensor, r_0; the incidence angle, θ; the light source, $\mathcal{L}_0$; and the local slopes, s_x and s_y, at the water surface $\zeta(\Theta_i)$ [BW91]. Except for the local slopes of the water surface, s_x and s_y, the foregoing parameters are all assumed to be invariant.
The local slopes, s_x and s_y, or the local-slope vector, $\vec{s} = (s_x, s_y)$, of a tilted facet of the water surface in the spatio-temporal domain, Θ, are defined as

$$s_x(\Theta) = \frac{\partial\zeta(\Theta)}{\partial x} \quad \text{and} \quad s_y(\Theta) = \frac{\partial\zeta(\Theta)}{\partial y}. \tag{3.8}$$

For a given incidence angle, θ_I, the local incidence and therefore the Fresnel coefficients, $\rho_{||}$, $\rho_{\perp}$ and $\rho_{\circledast}$, and the direction of incidence vector $\vec{s}_0$ vary with the local-slope vector, $\vec{s}$. There are two reasons for the variation of the reflected radiance:

- the variation of the local-slope vector has an effect on the local incidence angle, influencing the Fresnel coefficient according to the Fresnel formulae (3.3), and

- the direction in which the light ray, $\vec{s}_0$, is reflected to the camera depends on the variable local-slope vector of the water surface. Therefore the radiance of the source illumination, $\mathcal{L}_0$, changes due to a variation of the incident ray, $\vec{s}_0$, if the illumination is inhomogeneous.

The nonlinear radiance-to-slope relation, i.e. the dependency of the reflected radiance on the local slope vector, is depicted in Fig. 22 for the case of homogeneous illumination. To transform from the complex-valued spectral amplitudes of the spatio-temporal light-field pattern, $\mathcal{L}_R$, reflected at the water surface to the heave spectrum, the linear slope-to-radiance modulation, i.e. a tilt-modulation transfer function [Wal94], is used:

$$\hat{\mathcal{G}}(\Omega) = \frac{ik}{\mathcal{L}_0} \cdot \left[\left(\frac{\partial \mathcal{L}_R}{\partial s_x} \right)_{s_x=0} \cos\tilde{\vartheta} + \left(\frac{\partial \mathcal{L}_R}{\partial s_y} \right)_{s_y=0} \sin\tilde{\vartheta} \right] \cdot \hat{\mathcal{S}}(\Omega). \tag{3.9}$$

Resolving the product $\mathcal{L}_R = \mathcal{L}_0\rho$ following (3.2) results in two terms:

$$\frac{\partial \mathcal{L}_R}{\partial s_x} = \left(\frac{\partial \mathcal{L}_0}{s_x}\rho + \frac{\partial \rho}{s_x}\mathcal{L}_0 \right) \quad \text{and} \quad \frac{\partial \mathcal{L}_R}{\partial s_y} = \left(\frac{\partial \mathcal{L}_0}{s_y}\rho + \frac{\partial \rho}{s_y}\mathcal{L}_0 \right), \tag{3.10}$$

where in both equations the first term describes the dependency on the source illumination and the second term the dependency of modulation on the Fresnel formulae. The influence of the source illumination on the imaging of surface waves is illustrated in Fig. 23.
Substituting (3.9) into (3.7) results in

$$\alpha = \frac{1}{\mathcal{L}_0^2} \left[\left(\frac{\mathcal{L}_R}{s_x} \right)_{s_x=0} \cos(\tilde{\vartheta}) + \left(\frac{\mathcal{L}_R}{s_y} \right)_{s_y=0} \sin(\tilde{\vartheta}) \right]^2 \quad \text{and} \quad \beta = 2. \tag{3.11}$$

The calibration coefficients α and β can be used to calibrate gray-level variance spectra, $\mathcal{G}$. If the illuminating light field is known, a calibration procedure can be performed by implementing tilt modulation as a physical model to determine the ITF. If radiometric data sets are not available, instead of the explicit calculation, an empirical approach can be utilized: The sea-surface slopes or elevation can be measured by independent in situ wave measurements (i.e. wave wire gauges). With this empirical calibration approach, the ITF can be parametrized (see (3.7)).

3.2.4 Projective Bunching

The optical imaging of the elongated sea surface, $\zeta(R_i)$, to a 2D sensor plane results in a loss of height information; a loss of information may also occur the backside of waves are not imaged because of low camera incidence angles (occlusion). The mapping of the elongated surface to a 2D image plane leads to a repositioning of the imaged parts of the surface (see Fig. 24) and to occlusion of the sea surface (see Fig. 25).
The horizontal displacement, Δr (the horizontal component of the distance $\overline{P_1P_3}$ in Fig. 24), of the elevated surface, $\zeta(P_1)$, from the position P_1 to the

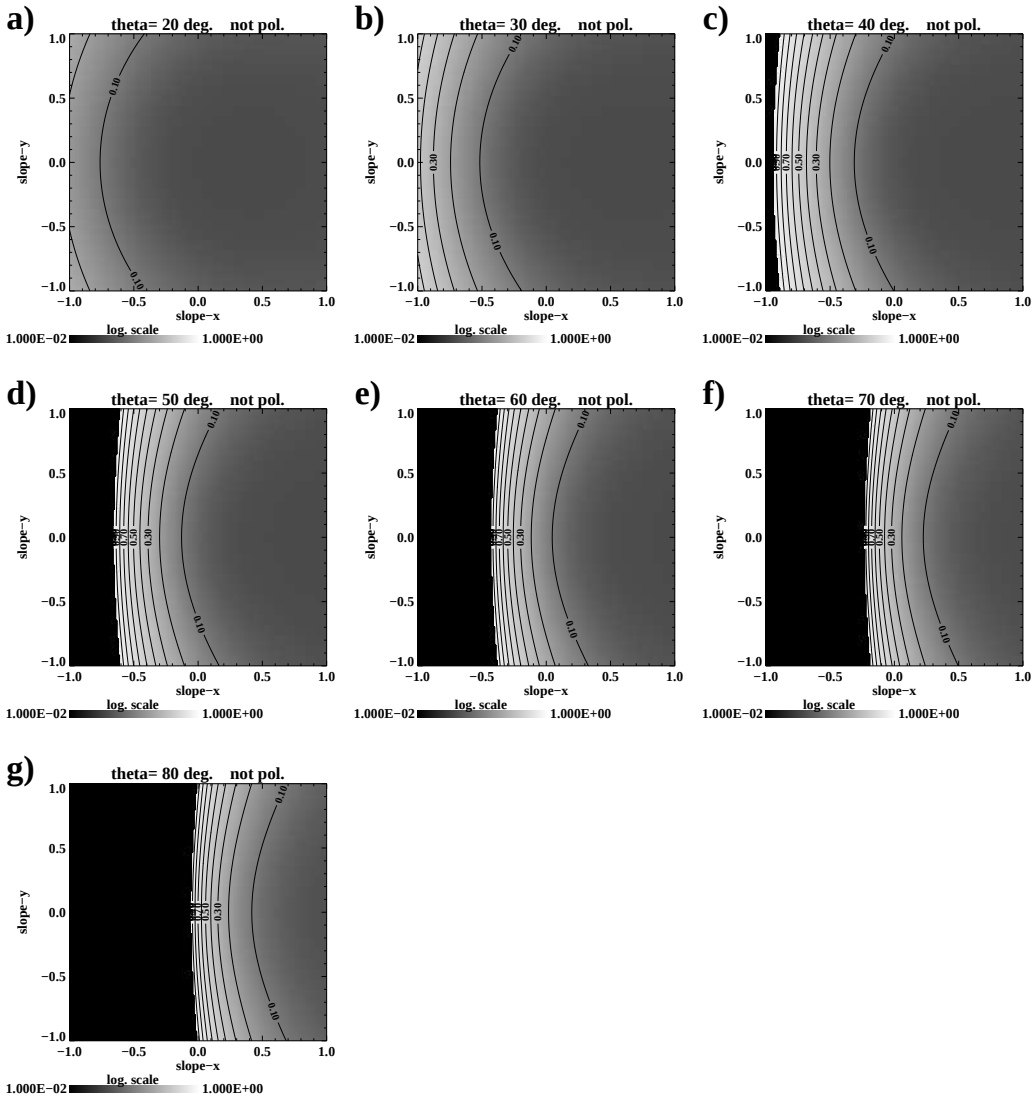

Figure 22: Unpolarized Fresnel coefficient in the 2D s_x–s_y gradient space for homogeneous illumination at the following incidence angles: **a)** $\theta = 20°$, **b)** $\theta = 30°$, **c)** $\theta = 40°$, **d)** $\theta = 50°$, **e)** $\theta = 60°$, **f)** $\theta = 70°$ and **g)** $\theta = 80°$. The unpolarized Fresnel coefficient ranges from 0.0 to 1.0. If the local incidence angle exceeds 90°, occlusion occurs; these areas are indicated in black. The closer the contour lines lie together, the higher the reflected illumination gradient and the higher the modulation. Modulation is mainly introduced by the s_x-component (directed toward the observer). The Fresnel coefficient is symmetric about the s_x axis; therefore the transformation is ambiguous.

displaced point, P_3, located on the projective plane of the mean water level $\zeta = 0$, is determined by

$$\Delta r = \tan\theta\, \zeta(P_1). \tag{3.12}$$

Following (3.12), the horizontal displacement, Δr, is only dependent on the camera's incidence angle, θ, and the elevation, $\zeta(P_1)$. In contrast to tilt modulation, the projective bunching modulation has no effect on the gray

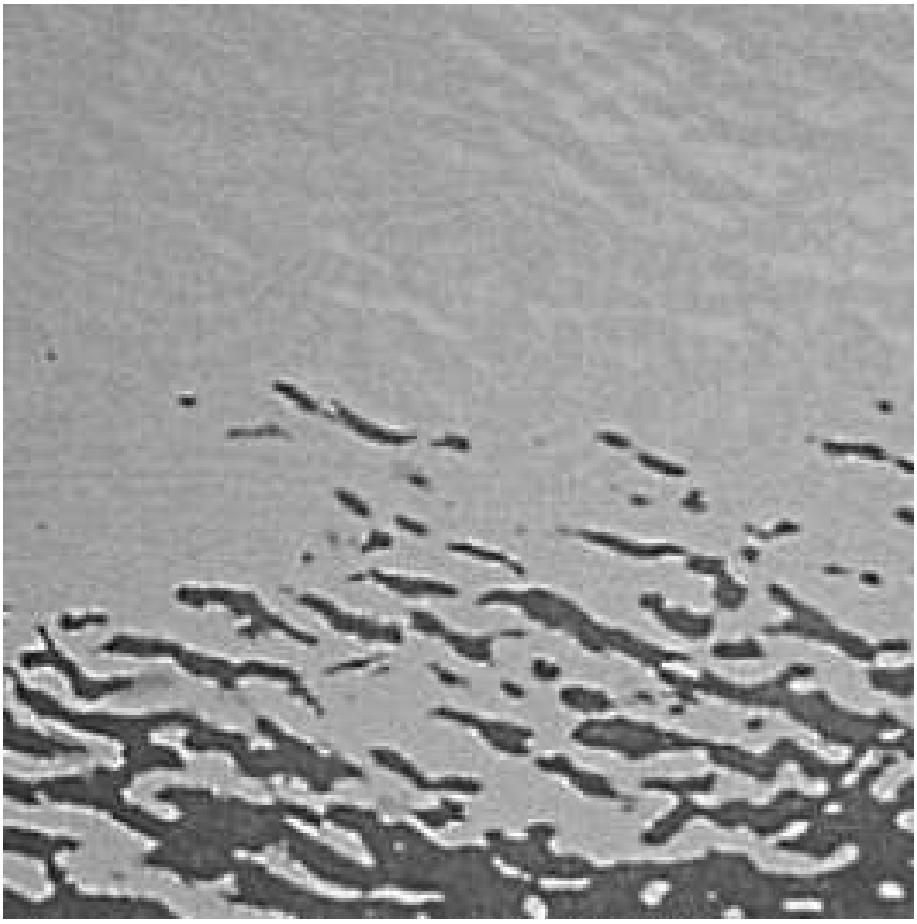

Figure 23: Illustration of surface-wave imaging: a wave field photographed perpendicular to a bridge. The parts of the wave field shadowed by the bridge are dark, the parts illuminated by the sky are bright. The highest modulation occurs at the imaged bridge–sky border, where neighbouring surface facets are illuminated differently, either by the sky or by the bridge (image source: author, 1998).

value of the displaced point and is not dependent on the surface slope but on the surface elevation. Parts of the surface are covered from the observer's point of view if interjacent parts of the surface break the line of sight. This surface self-covering results in occlusion and a loss of information.
The effects of tilt modulation and projective bunching on the imaging of the sea surface is examined numerically in Appendix E.

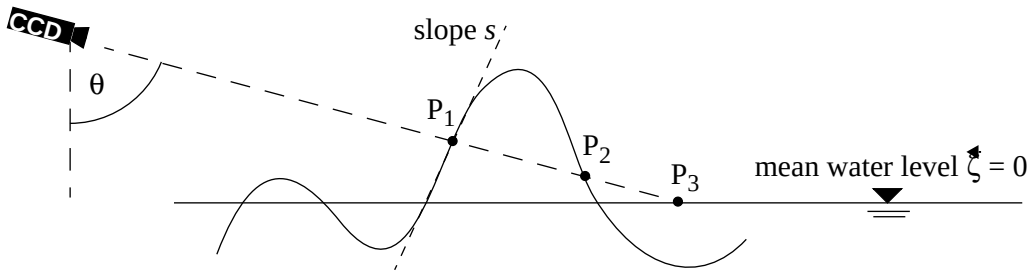

Figure 24: Scheme of projective bunching: point P_1 is geometrically projected to point P_3 located on the projection plane (here identical with the mean water level, $\bar{\zeta} = 0$). If the local slope, s, of the sea surface is higher than $1/\tan\theta$ the backside of the wave is not imaged, i.e. the information for point P_2 is lost in the image. This effect is called occlusion.

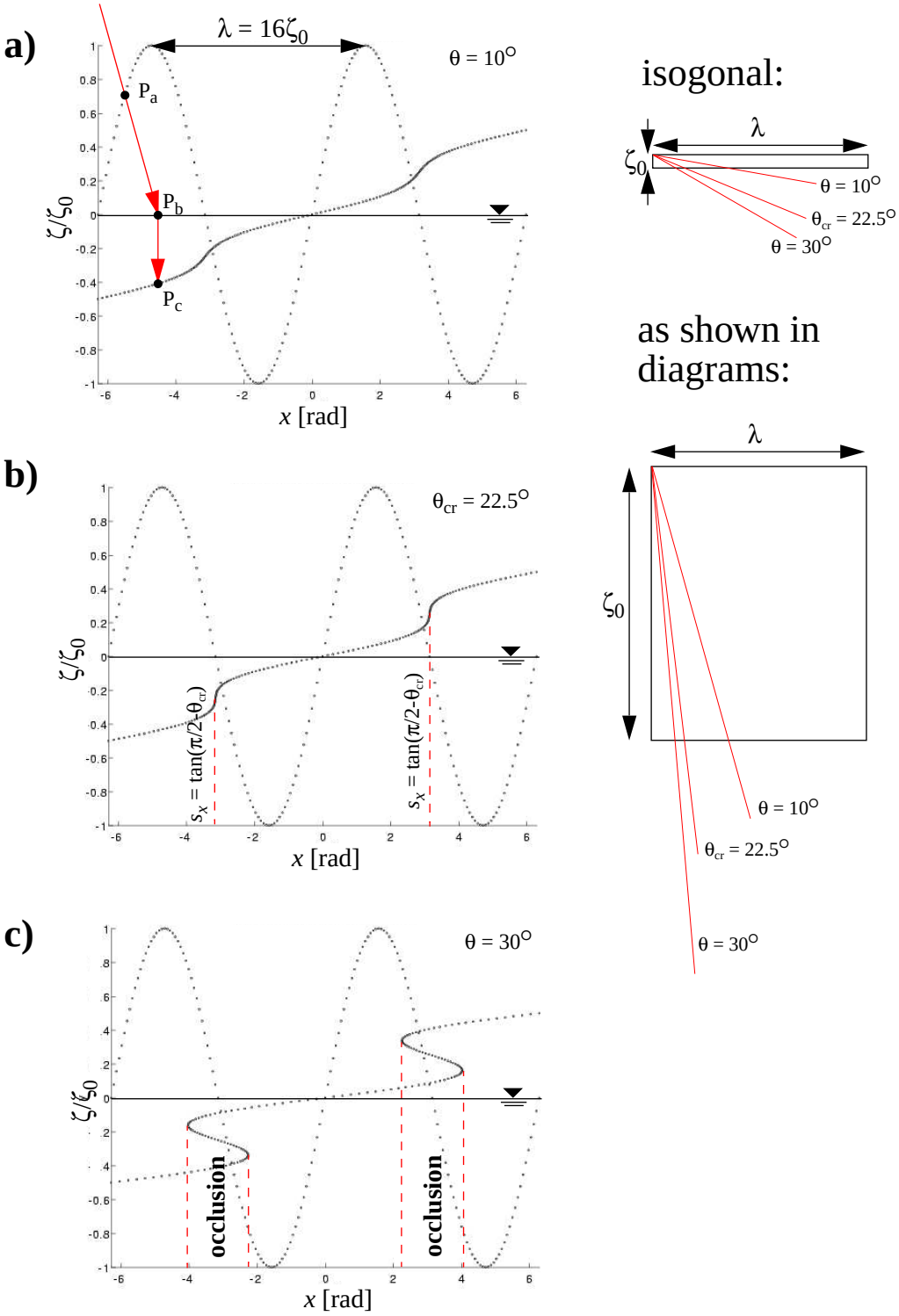

Figure 25: Projective bunching for a sinusoidal wave; the sinusoidal model wave has the arbitrary relation $16\zeta_0 = \lambda$. In **a)**, **b)** and **c)** the light rays have an incidence angle of $\pi/2 - \theta = 10°$, 22.5°, and 30°. The projection of point P_a located on the wave's surface to the mean surface $\zeta = 0$ is indicated by P_b. For a clear representation the point P_b is translated to P_c. The ordinal distance between P_b and P_c represents the phase of $\zeta(x)$. The diagram's coordinate systems are given in normed coordinates. Also for comprehensible representation the ordinate is magnified (see right side of diagrams).

4 Optical Image-Sequence Acquisition System

4.1 Instrument

The system for acquiring sequences of optical (video) images consists of video Charg-Coupled Device (CCD) cameras and a personal computer. The personal computer is equipped with a frame grabber to digitize the images and an adequately high amount of random access memory (RAM) to store the image sequence. A schematic of the acquisition of optical-image sequences is given in Fig. 26.
A CCD camera consists of a lens system which images a scene onto a CCD chip, which converts the imaged brightness into a standard-video signal. The camera is connected to a personal computer by a video cable, where the analog video signal is converted by a frame grabber into a digital format. The three-colour channel RGB frame grabber (RGB: conversion to red–green–blue colour space) can be equipped with one colour camera or up to three monochromatic cameras. To acquire a sufficient number of images in real time, the computer is equiped with 512 MB of RAM. After acquisition, the image sequence is stored from RAM to hard disc memory. All parts of the optical image-sequence acquisition system are industrial-standard components. In detail, the acquisition system used in this work consists of the following:

- Two JAI™ M10 RS cameras (for technical details see Tab. 1 and [NN98b]).
- a personal computer with a Pentium™ processor (200 MHz).
- 6 GB hard disc.

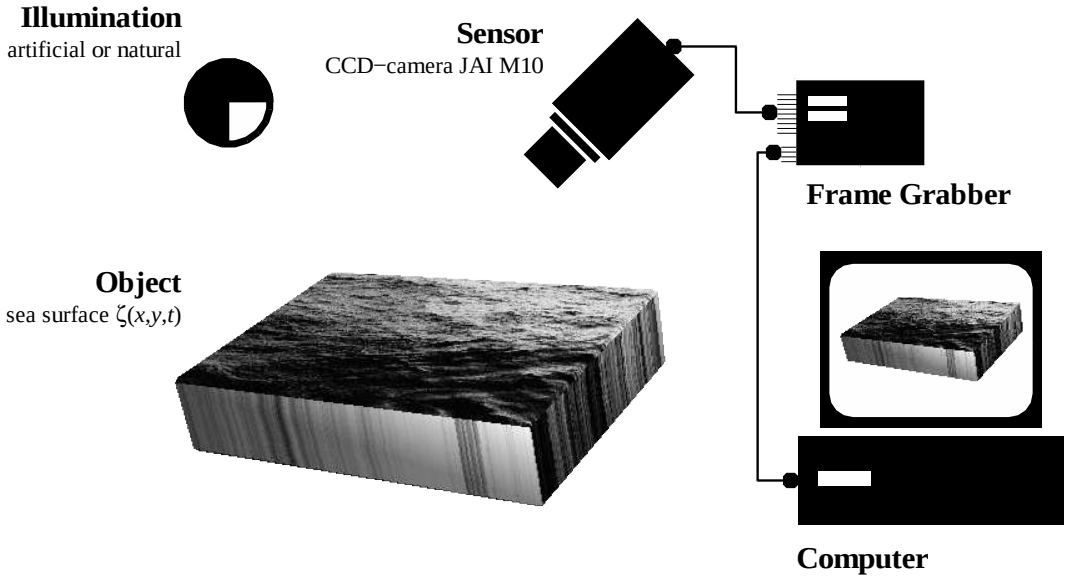

Figure 26: Schematic of the optical image-sequence aquisition system.

Table 1: Technical specification of a JAI M 10 RS camera.

Name	JAI CV-M10 RS
Type	CCIR progressive scan camera
CCD sensor	1/2" interline-transfer type
Number of sensor elements	782 (hor.) × 582 (vert.)
Pixel cell size	8.3 μm (hor.) × 8.3 μm (vert.)
Chip size	15.625 KHz (hor.) × 50 Hz (vert.)
Scanning mode 1	Full scan (non-interlaced) 625 lines in 1/25 s
Scanning mode 2	Half scan (interlaced) in 1/50 s
Resolution	550 lines (hor.) × 400 lines (vert.)
S/N ratio	55 dB or more
Synchronization	Internal, external, random
Electronic shutter	1/10000 s – 1/50 s
Lens mount	C-Mount

- 512 MB RAM.
- Frame grabber: IC-PCI™ image capture system with a high speed PCI bus interface; 4 MB video RAM for temporary image storage equipped with the exchangable analog AM–STD–RGB, acquisition module for colour and monochrome cameras (Imaging Technology Incorporated).
- Operating system: Windows™ NT Version 4.0.
- Frame grabber control software: ITEX-IC™ Version 3.2 for Win32, (Imaging Technology Incorporated).
- OPTIMATE™ 6.11: run-time version of OPTIMAS™ image-analysis software package (Optimas Corporation).
- Image-sequence acquisition software module of OPTIMATE™: OPTIMAS-MA™ Version E.6.2/3.3.1/1998 (Stemmer Imaging GmbH), a software module for triggered single and sequence acquisition of digital TIFF images.

4.2 Data Description

The above-described image-sequence acquisition system allows software remote control on the following acquisition parameters:

- number of images, N,
- acquisition frequency, f, (variable, with maximum frequencies of 50 Hz (interlaced) and 25 Hz (non-interlaced))

- starting time, t_0,
- electronic-shutter time, Δt_{sh},
- gain and
- gamma value.

A sequence recorded by the above-described acquisition system is stored as a quantity of 8-bit (256 gray values) TIFF images. Differing from the capabilities of the JAI M10 RS camera of 782 × 582 pixels, the frame grabber captures an active field of 765 × 569 pixels.

4.3 Experimental Setup

For the experimental setup of the optical image-sequence acquisition system see Figs. 20 and 27. The CCD camera is located at the position $\vec{r}_0$ and is directed onto the water surface with a predefined incidence angle, θ.

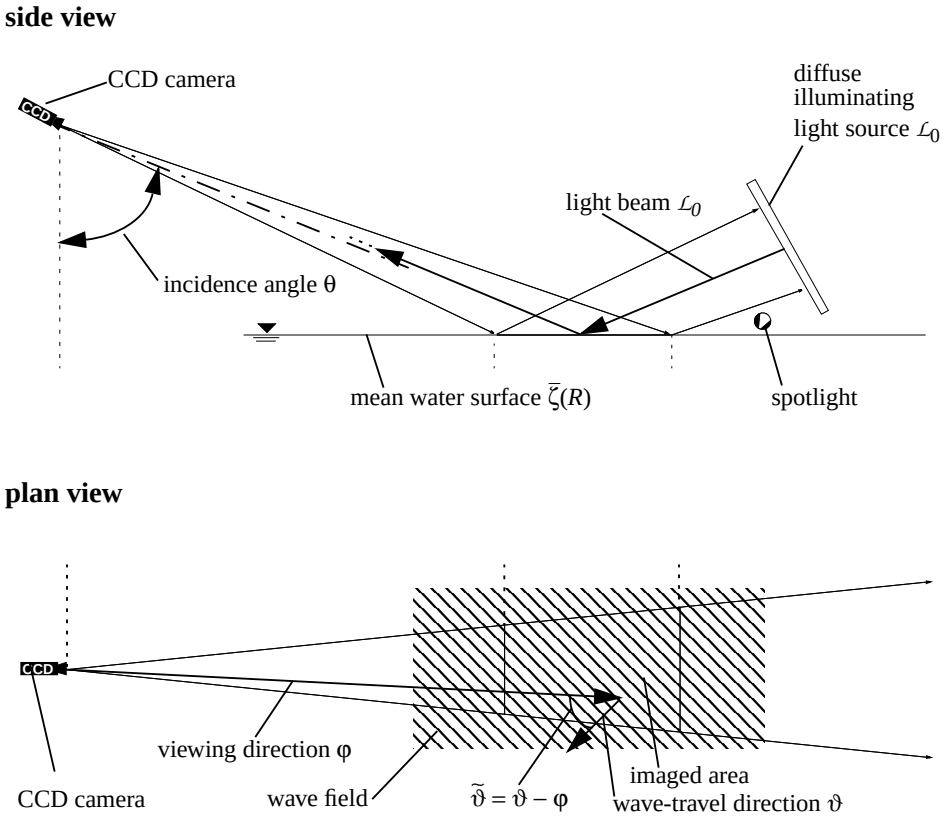

Figure 27: Schematic of the experimental setup of the optical image-sequence acquisition system: the CCD camera at position $\vec{r}_0$ is directed vertically by the incidence angle, θ, and horizontally by the azimuthal viewing angle, φ, which are both defined by the camera's optical axis referred to the defined coordinate system. The water surface is illuminated by a diffusor, preferably made of a matt reflecting white material. The diffusor is illuminated by a spotlight.

The parameters $\vec{r}_0$ and θ and the internal camera parameters determine the extension of the observed water-surface area.
In the observed area a number of reference points (ground control points: GCP's) are installed. The world coordinates x_{wc}, y_{wc} and z_{wc} of the GCPs are registered to enable a subsequent transformation of the acquired image sequences from image coodinates to world coordinates.
Independent measurement devices have to be installed for subsequent calibration of the image spectra.
As mentioned above (Sec. 3), the optical device records gray-values, which depend on the gradients of the reflected source illumination and the gradients of the reflectivity as a function of the slopes of the recorded surface facets, i.e. the reflected light modulated by the spatio-temporal wave field. For this purpose a predefined source illumination is installed. Preferably, the light source should be extended and diffuse. The extension of the diffusor ideally is chosen in the following way: for every generated water-surface slope all optical paths, acquired by the CCD camera, should come from the predefined diffusor. The illumination of the diffusor is performed by a spotlight. The illumination setup has been chosen time invariant to ensure uniform conditions during an experimental campaign. An example of a single image of a sequence acquired in a wave-tank facility is given in Fig. 28.

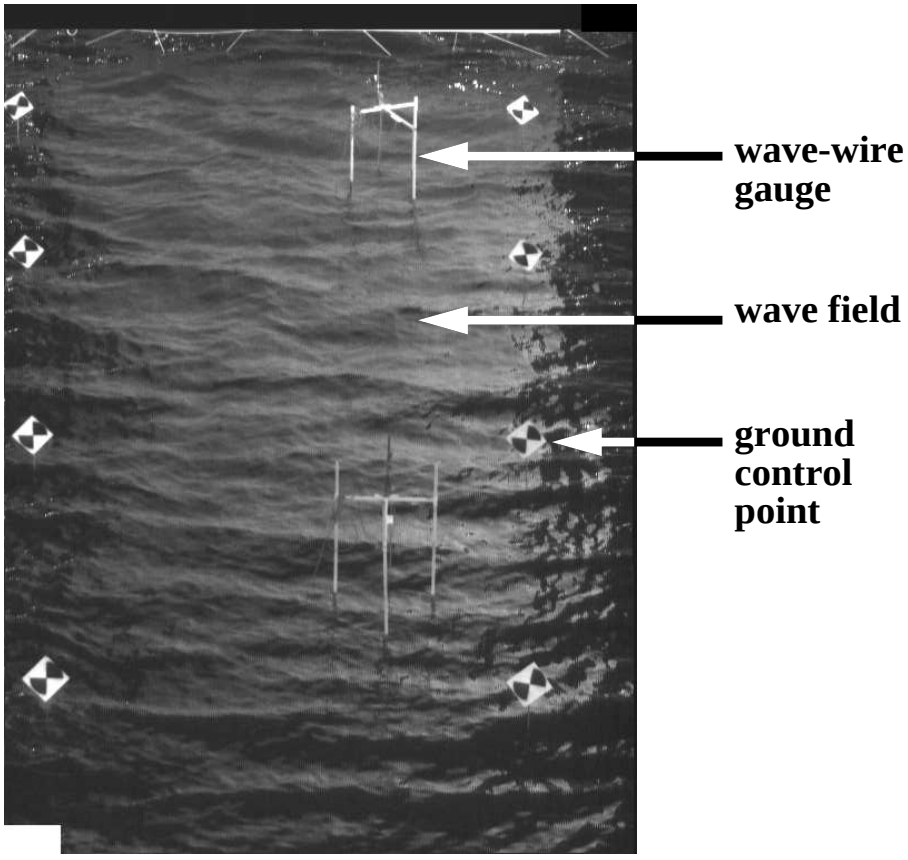

Figure 28: Example of a single image in a sequence taken at a hydraulic wave facility.

5 Methods to Analyze Optical Image Sequences

The algorithms presented here have been implemented in PV-Wave [May94], an interpreter programming language. PV-Wave is especially designed for image-analysis purposes and has a similiar structure to Matlab or IDL.
The aim of the analysis of image sequences is to determine physical parameters. The presented methods have been adapted for the analysis of image sequences of gravitational sea-surface waves (see Secs. 2.2 – 2.4). The physical model of the dispersion relation of gravitational sea surfaces is used to interpret the image sequences.
In Sec. 5.1 the pre-processing routines, mainly used to transform raw-image sequences recorded in image (or camera pixel) coordinates to world coordinates. In Sec. 5.2 the global analysis based on a 3D FFT is treated. This analysis method has been directly adopted from methods developed for nautical-radar image sequences [YRZ85] [Zie87] [See97] [Sen96] [Out98]. The global method determines the hydrographic parameters. Sec. (5.3) describes the newly developed method to determine spatial maps of hydrographic parameters. An overlook of the global and local analysis is given in Fig. 29.

5.1 Geometrical Transformation

The pixels of an image sequence, $G(\Theta_{i,\mathrm{ic}})$, acquired by a CCD camera, are given in discrete image coordinates, $\Theta_{i,\mathrm{ic}} = (R_{i,\mathrm{ic}}, t)$. The image coordinates are transformed to a rectangular world-coordinate plane $R_{i,\mathrm{wc}}$, here defined by the mean water level. For this transformation a least-squares method is used to 1) determine the internal and external camera parameter sets and 2) perform geometrical transformations [Tsa87]. A related application example of the Tsai algorithm is described in [Jan97], where image sequences of a shoreline of a beach were acquired to detect variations in the coastline.
The position and the extension of an observed object is quantified in a Cartesian world-coordinate system. World coordinates are denoted as 3D column vectors, $(x_{\mathrm{wc}}, y_{\mathrm{wc}}, z_{\mathrm{wc}})^T$. The coordinate system corresponding to the camera images is denoted as the image-coordinate system. The image coordinates, defined in the focal plane, are specified as 2D column vectors, $(x_{\mathrm{ic}}, y_{\mathrm{ic}})^T$.
The geometrical transformation from the world-coordinate system to the image-coordinate system and vice versa is performed by a four-step procedure (described in Appendix A). An overlook of the application of the Tsai algorithm is given in Fig. 30.
For the image sequence in world coordinates, $G(\Theta_{i,\mathrm{ic}})$, for the sake of simplification, waiving the index 'wc', $G(\Theta_i)$ is used consecutively.

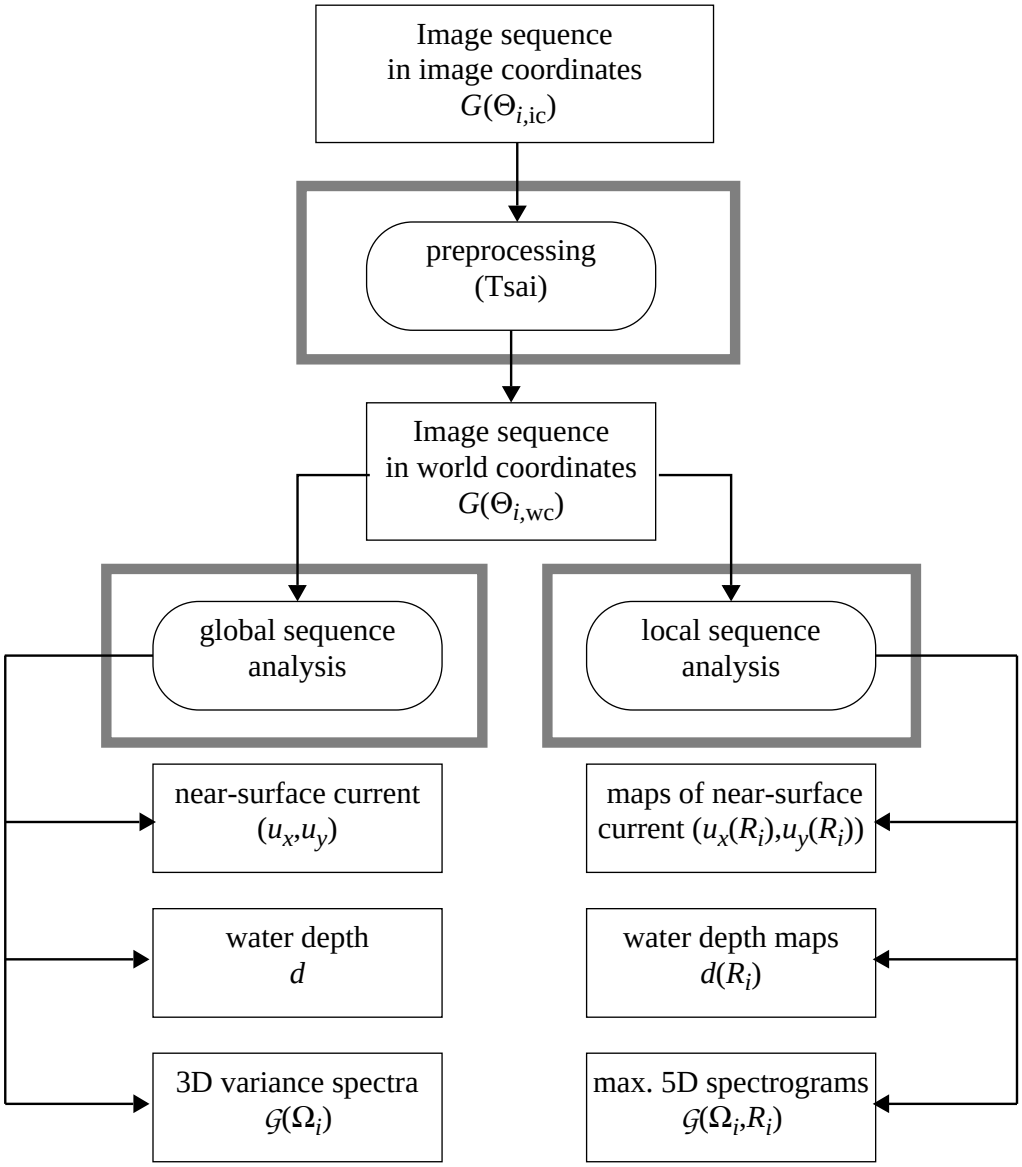

Figure 29: Schematic overview of the global and local analysis.

5.2 Global Analysis Method: 3D Fast-Fourier Transformation and Filtering

The global image-sequence analysis method (see Fig. 31) is based on a 3D Fast-Fourier Transformation (3D FFT). From the discrete complex-valued 3D image Ω_i spectrum, $\hat{\mathcal{G}}(\Omega_i)$, the discrete gray-level variance spectrum, $\mathcal{G}(\Omega_i)$, is calculated. The variance spectrum utilizes the information about the spectral power; the information about the spectral phase is neglected.

5.2.1 Assumptions of Global Analysis

The following requirements must be fulfilled to apply the global method on image sequences of the sea surface:

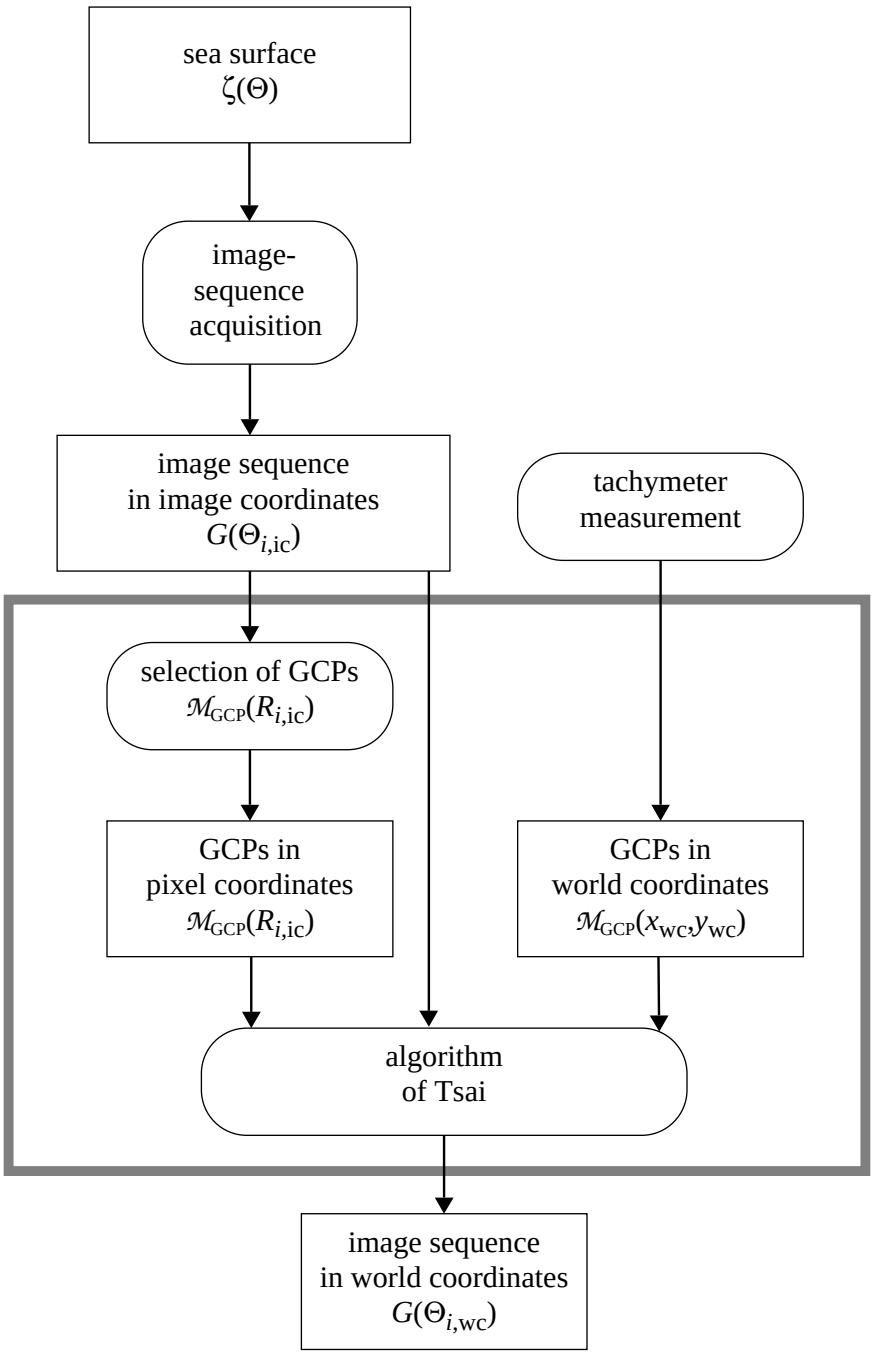

Figure 30: Schematic of the procedural and data flow of image-sequence pre-processing (GCPs: ground control points).

Stationarity: The image sequences have to be stationary. Here the same criteria as for a wave field hold (see Sec. 2.2.5). If the assumption of stationarity does not hold, the gray-level variance of the imaged sequence is spread over the dispersion shell in the frequency domain. The more instationary the observed wave field is, the higher the spreading (see Fig. 14).
Homogeneity: The criterion of homogeneity must hold for the image sequence, as for a wave field (see Sec. 2.2.6). If the assumption of homogeneity

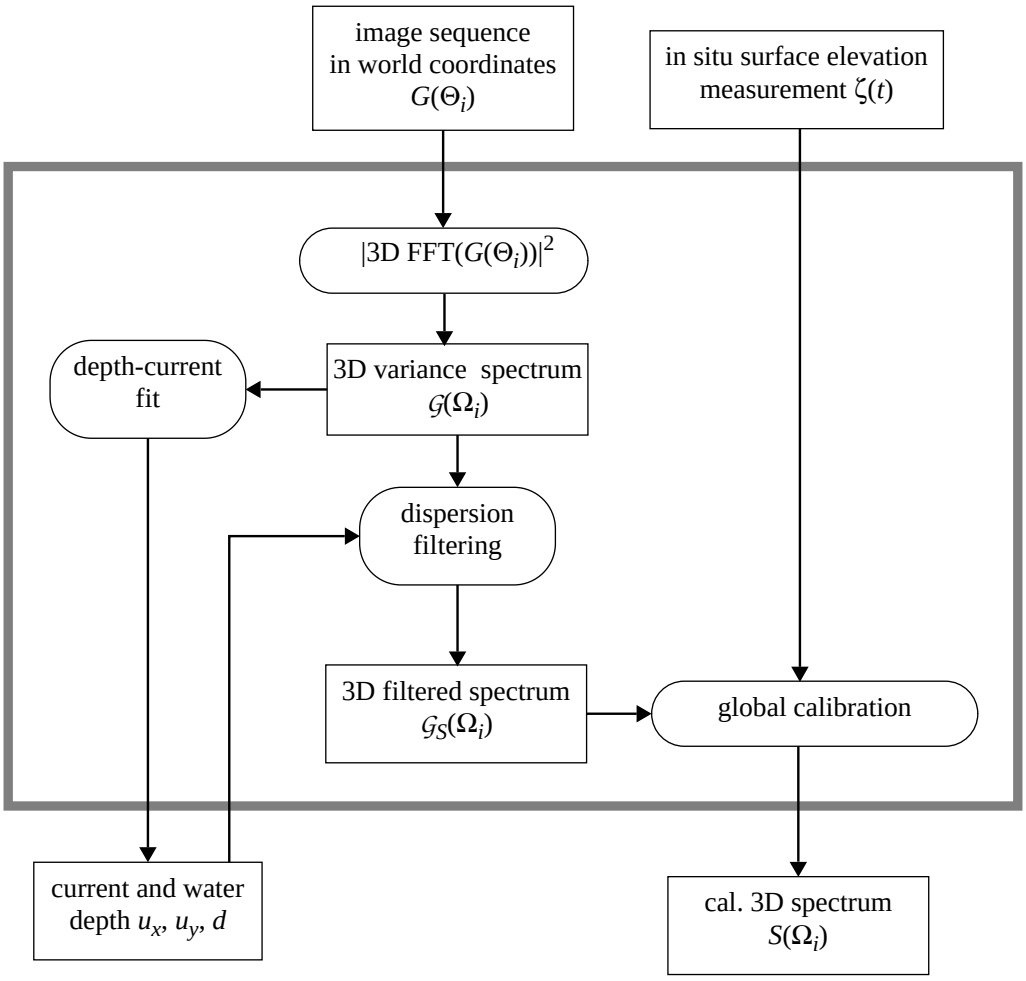

Figure 31: Schematic of the procedural and data flow of the global analysis.

does not hold, the gray-level variance of the imaged sequence is spread over the dispersion shell in the wavenumber domain. The more inhomogeneous the process is, the higher the spreading (see Fig. 14).

5.2.2 Input Parameters

The input parameter of the global analysis method is the image sequence $G(\Theta_i)$, which previously was transformed from image coordinates to world coordinates (see Sec. 5.1).
If a calibration procedure is performed on the image spectra, i.e. if an inverse ITF is applied, the synchronously acquired in situ data are input parameters.

5.2.3 3D Fast-Fourier Transformation

A discrete 3D Fourier Transformation (3D DFT) can be obtained by a decomposition into 1D DFTs. A 3D DFT can be decomposed into 1D DFTs because the kernel is separable. A 3D DFT using the world- and spectral

coordinates has the form

$$\hat{\mathcal{G}}(\Omega_i) = \frac{1}{MNW} \sum_{k=0}^{M} \left[\sum_{l=0}^{N} \left(\sum_{m=0}^{W} G_{m,n,w}(\Theta_i) V_W^{-wt} \right) V_N^{-ny} \right] V_M^{-mx}, \tag{5.1}$$

where M, N, and O are the numbers of the Ω_i coordinates $k_{x,m}$, $k_{y,n}$, ω_w and

$$V_{[M|N|W]} = \exp\left(\frac{2\pi i}{[M|N|W]}\right). \tag{5.2}$$

The result of (5.1) is a discrete complex-valued image spectrum $\hat{\mathcal{G}}(\Omega_i)$ of the 3D domain $\Omega_i = (k_{x,m}, k_{y,n}, \omega_w)$. The spatio-temporal extension $X \otimes Y \otimes T$ determines the discrete grid resolution of the 3D spectrum:

$$\Delta k_x = \frac{2\pi}{X} \text{ and } \Delta k_y = \frac{2\pi}{Y} \text{ and } \Delta\omega = \frac{2\pi}{T}. \tag{5.3}$$

The discrete grid resolution of the spatio-temporal image sequence determines the spectral extensions (i.e. the Nyquist criteria):

$$k_{x,\mathrm{Ny}} = \frac{\pi}{\Delta x} \text{ and } k_{y,\mathrm{Ny}} = \frac{\pi}{\Delta y} \text{ and } \omega_{\mathrm{Ny}} = \frac{\pi}{\Delta y}. \tag{5.4}$$

A detailed overview of continuous and discrete Fourier Transformations can be found in [JHG99a]. The 3D FFT used in this work is a PV-Wave function, implemented as a Cooley–Tukey FFT [CT65]. The implemented algorithm enables a calculation of multidimensional FFTs up to 8 dimensions.
Examples of the usage of a 3D FFT on image sequences of the sea surface with video or CCD cameras are given by [IGB86] [JKGH93]; for X-Band Doppler Radars an example is given in [FM95].
The real-valued 3D gray-level variance spectrum, $\mathcal{G}(\Omega_i)$, is retrieved by the squared modulus of the 3D complex-valued spectrum $\hat{\mathcal{G}}(\Omega_i)$:

$$\mathcal{G}(\Omega_i) = |\hat{\mathcal{G}}(\Omega_i)|^2. \tag{5.5}$$

The following analysis steps are based on the analysis of the 3D gray-level variance spectrum. The phase information is not used.

5.2.4 Spectral Corrections

The gray-level variance spectrum, $\mathcal{G}(\Omega)$, is low-pass filtered in the Υ domain because of the following effects:

- geometrical transformation of the images involves spatial interpolation and
- spatial averaging over a finite area (point-spread function);

furthermore the gray-level variance spectrum, $\mathcal{G}(\Omega)$, is low-pass filtered in frequency because

- of the accumulation over the shutter-integration time.

These effects are characterized by the optical-transfer function (OTF). In summary, the low-pass filtered image spectrum is given by

$$\mathcal{G}'(\Omega) = H(\Omega) \cdot \mathcal{G}(\Omega), \tag{5.6}$$

where

$$H(\Omega) = NN(\vec{k}) \cdot OTF(\vec{k}) \cdot OTF(\omega), \tag{5.7}$$

where $NN(\vec{k})$ is the spectral representation of the nearest-neighbour interpolation kernel, $OTF(\vec{k})$ is the wavenumber part and $OTF(\omega)$ is the frequency part of the OTF.
The low-pass-corrected image spectrum is reconstructed by the inversion of (5.6):

$$\mathcal{G}(\Omega) = H^{-1}(\Omega) \cdot \mathcal{G}'(\Omega) \tag{5.8}$$

if

$$|H(\Omega)| > \epsilon, \tag{5.9}$$

where ϵ is a critical level that depends on the signal-to-noise ratio. The detailed description of the correction factors of (5.7) is given in Appendix B.

5.2.5 Determination of Near-Surface Current-Velocity and Water Depth

In Sec. 2.2.4 the dependency of the dispersion relation, $\tilde{\omega}(\vec{k}, \vec{u}_c, d)$, on the near-surface current, $\vec{u_c}$, and the water depth, d, is described.
In the gray-level variance spectrum, $\mathcal{G}(\Omega_i)$, the linear portion of signal energy of the waves, $\mathcal{G}_0(\Omega_i)$, is localized on the dispersion shell of surface waves $\tilde{\omega}(\vec{k})$. The sum of the sensor's velocity, $\vec{u}_s$ (i.e. ship velocity), and the near-surface ocean's current, $\vec{u}_c$, deforms the dispersion shell due to the Doppler-frequency shift, ω_D.
A first approach to determine the near-surface current,

$$\vec{u}_c = \vec{u}_e - \vec{u}_s, \tag{5.10}$$

was presented in [YRZ85]. The authors introduced a least-squares fitting technique, which they applied to image sequences acquired by a nautical radar. The least-squares technique is based on the idea that the theoretical dispersion shell (2.9) is fitted to the linear portion (fundamental mode) of the spectral signal of the imaged waves, $\hat{G}_S(\Omega_i)$.
This least-squares fitting technique has been improved in accuracy 1) by considering the spectral signal found at higher harmonics (see Sec. 2.4) of the dispersion shell (see Sec. 2.2.3); 2) by taking into account aliasing effects generated due to temporal undersampling, because of the slow antenna rotation time of a nautical radar ($\mathcal{O}(2$ s)) [SZ95] [BZSS98] [SSH$^+$00]; and 3) by establishing a reliable error-estimation model.

The technique's accuracy, its limits, and its adaptability are described and discussed in [Sen96] [SSZ97] [SSZ01]. It is now possible to perform current and wave measurements from fast-moving vessels. The method is implemented in the operational product **WaMoS II** (**Wa**ve **Mo**nitoring **S**ystem based on nautical radars [RBD99] [RHBD99].
An integrated approach to determine the near-surface current and the water depth has been developed by [Out98]. The algorithms to determine the near-surface current and the water depth developed for a nautical radar have been adopted for use with optical image sequences [SBL+99a].
The method used in this work is based on a quasi-Newton method to find the global minimum of the cost function:

$$f(u_x, u_y, d) = \sum_{l=0}^{L-1} \left(\underbrace{\sqrt{g\vec{k}_l \tanh(\vec{k}_l d)} + k_{x,l}u_x + k_{y,l}u_y}_{\tilde{\omega}(\vec{k}_l, \vec{u}_c, d)} - \omega_l \right)^2 , \tag{5.11}$$

where u_x, u_y (components of the near-surface current) and d water depth) are the unknowns. The index, l, counts the elements of the set of spectral coordinates, k_l, $k_{x,l}$, $k_{y,l}$ and ω_l, which are selected in the 3D image spectrum. Consider that the dispersion relation $\varpi(\vec{k}; \vec{u}, d)$ is linearly dependent on u_x and u_y and nonlinearly dependent on d. The spectral coordinates are selected by a threshold criterion

$$\mathcal{M}_0 = \left\{ (k_{x,l}, k_{y,l}, \omega_l) \left| \frac{\mathcal{G}(k_{x,l}, k_{y,l}, \omega_l)}{\max(\mathcal{G})(k_{x,l}, k_{y,l}, \omega_l)} > \epsilon_S \right. \right\}, \tag{5.12}$$

where $\mathcal{M}_0$ is the subset of spectral-coordinate set selected by the normalized criterion ϵ_S, which discriminates the linear spectral signal from noise and other signal structures. In (5.12) k_l is the modulus of the wavenumber vector:

$$k_l = \sqrt{k_{x,l}^2 + k_{y,l}^2}. \tag{5.13}$$

The spectral-coordinate set, $\mathcal{M}_0$, defined in (5.12), is represented as a sorted vector with the indices $l = 0,\ldots,L-1$ where $L-1$ is the number of selected spectral coordinates.
An iterative algorithm is performed by the PV-Wave-Routine 'FMINV' using a quasi-Newton minimization method for nonlinear functions. For more details of the minimization, see [DS83]. After the first guess, where the linear spectral coordinates, $\mathcal{M}_0$, are selected, the locations of the fundamental mode dispersion shell, $\tilde{\omega}_0$, and of the p-th harmonics, $\tilde{\omega}_p$, are approximately known. The number of regression coordinates is then increased iteratively by taking the spectral coordinates of higher harmonics into account.

5.2.6 Spectral Filtering (Dispersion Filtering)

With the determination of the near-surface current, $\vec{u}_c$, and the water depth, d, the shape of the dispersion shell is determined. The localized dispersion

shell is used to filter the spectral signal of the imaged wave field from the background-noise component. The linear dispersion shell is used as a spectral filter (see (2.9)) to select the dispersive signal $\mathcal{G}_S(\Omega_i)$ from the 3D variance spectrum $\mathcal{G}(\Omega_i)$. By using the scaling argument (2.24) with the known linear dispersion shell, the p-th harmonic dispersions may also be determined. In Fig. 32 the linear dispersion shell and the quadratic terms are given. The nonlinear signal results 1) from nonlinearities of the sea state (see Sec. 2.4) and from the nonlinearities of the the imaging function (see Sec. 3.2).
The set of filtered signal coordinates,

$$\mathcal{G}(k_{x,m}, k_{y,n}, \omega_w) \subset \mathcal{M}_0, \tag{5.14}$$

is calculated as follows: for each 2D wavenumber vector, $(k_{x,m}, k_{y,n})$, with the

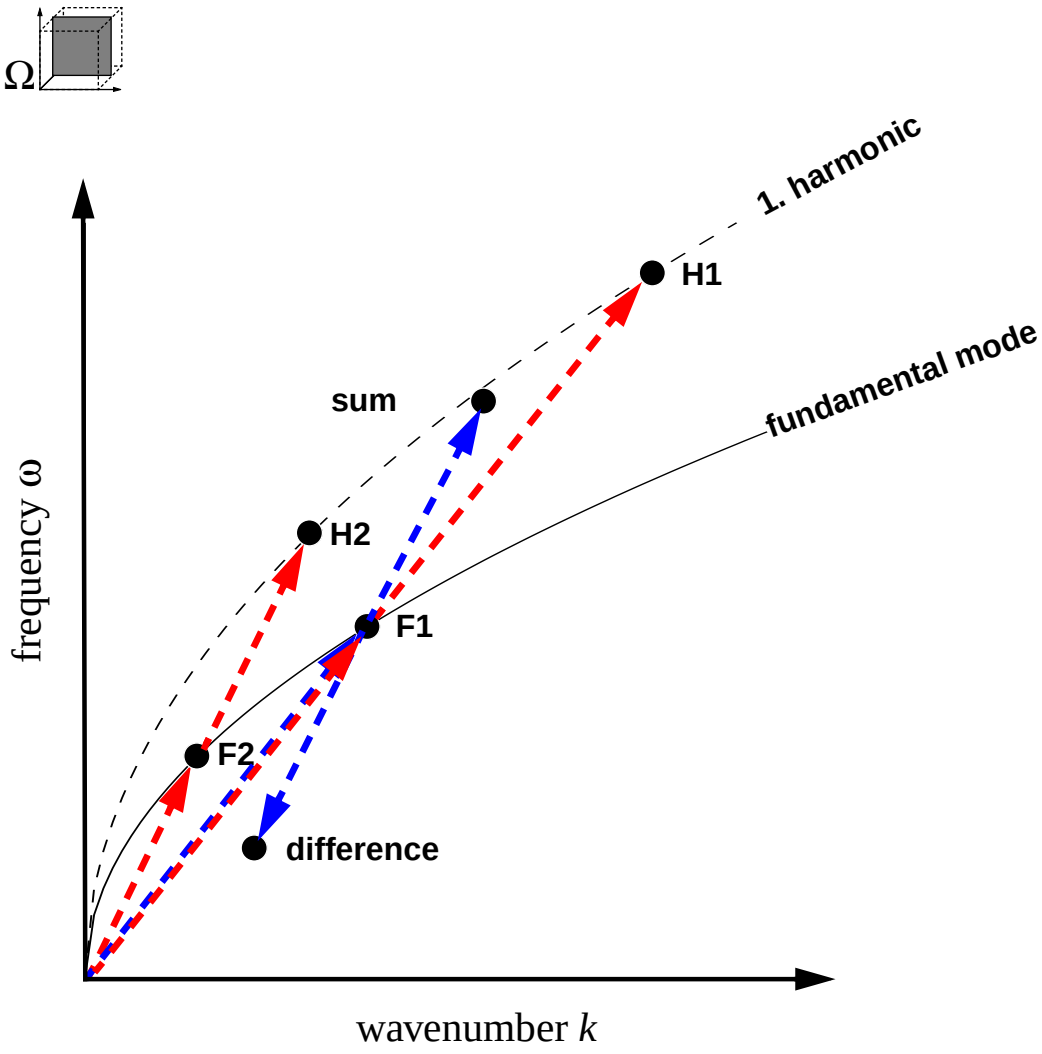

Figure 32: Spectral linear and quadratic structure of the imaged sea state: linear spectral parts, denoted as fundamental mode are localized on the curve given by the linear dispersion relation of sea state (solid line); the quadratic sum term is given by vector addition F1 + F1 = H1 or F2 + F2 = H2, the quadratic difference term is given by F1 − F2, and the first harmonic F1 + F2.

indices m and n, the direct and diagonal 2D wavenumber grid neighbours are selected (see Fig. 33 a)) and this results in a set of nine grid positions. For this grid set the frequency maximum and minimum of the continuous dispersion relation are calculated as follows

$$\begin{aligned}\omega_{\max}(m,n) := \max[\tilde{\omega}(\vec{k};u_x,u_y,d) \mid k_x &\in [m-1,m,m+1]\cdot\Delta k_x \\ \wedge\, k_y &\in [n-1,n,n+1]\cdot\Delta k_y]\end{aligned} \tag{5.15}$$

and

$$\begin{aligned}\omega_{\min}(m,n) := \min[\tilde{\omega}(\vec{k};u_x,u_y,d) \mid k_x &\in [m-1,m,m+1]\cdot\Delta k_x \\ \wedge\, k_y &\in [n-1,n,n+1]\cdot\Delta k_y].\end{aligned} \tag{5.16}$$

The set of filtered signal coordinates, $\mathcal{M}_F$, is given by

$$\mathcal{M}_F := \{(k_{x,m},k_{y,n},\omega_w)w \in [w_{\min}(m,n),w_{\max}(m,n)]\} \tag{5.17}$$

where

$$w_{\max}(m,n) = \mathrm{SC}\left(\frac{\omega_{\max}(m,n)}{\Delta\omega}\right)+1 \tag{5.18}$$

and

$$w_{\min}(m,n) = \mathrm{SC}\left(\frac{\omega_{\min}(m,n)}{\Delta\omega}\right), \tag{5.19}$$

where SC is the staircase function. A schematic of the discrete filter is given in Fig. 33 b).
The dispersion filtering of the 3D spectrum, described in Sec. 5.2.6 , enables the separation of the following parts of the spectral signal:

- linear signal, $\mathcal{G}_0(\Omega)$,
- higher harmonics, $\mathcal{G}_p(\Omega)$, and
- noise, $\mathcal{G}_{\mathrm{N}}(\Omega)$, superharmonics, $\mathcal{G}_+(\Omega)$, and subharmonics, $\mathcal{G}_-(\Omega)$.

Up to now the superharmonics, $\mathcal{G}_+(\Omega)$, and subharmonics, $\mathcal{G}_-(\Omega)$, have not been separated because $\mathcal{G}_+(\Omega)$ and $\mathcal{G}_-(\Omega)$ are widely spread in the Ω domain. This spreading does not allows a well-defined and easy-to-handle dispersion relation. For practical purposes these unlocated spectral signal parts are assigned to the spectral noise signal part, $\mathcal{G}_{\mathrm{N}}(\Omega)$.

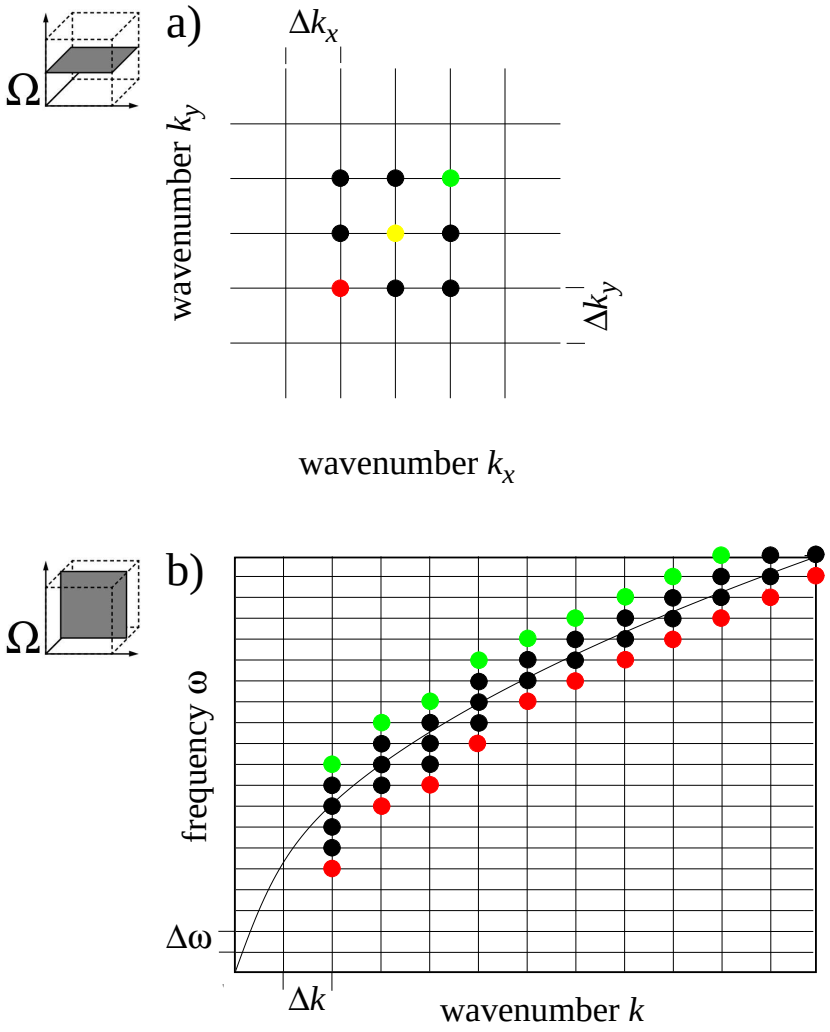

Figure 33: Discrete dispersion filter. **a)** All of the neighbours of a wavenumber vector, $(k_{x,m}, k_{y,n})$ (indicated by the yellow dot), are selected to determine the respective frequency maximum, $\omega_{\max}(m,n)$ (green dot), and frequency minimum, $\omega_{\min}(m,n)$ (red dot). **b)** 2D k–ω section with the dispersion curve is shown. At all positions on the wavenumber grid, $(k_{x,m}, k_{y,n})$, the frequency maxima (green dots) and the frequency minima (red dots) span the frequency interval of the discrete dispersion filter.

5.2.7 Integration

Intergration over the components of the wavenumber vector, k_x and k_y, or the frequency, ω, allows degradation of the three spectral dimensions. This degradation in turn allows image spectra to be compared with independent measurements, parametrizations, or numerical model results.
For the continuous dispersion relation (2.9) – a curved shell of infinitesimal thickness – degradations of dimensions are defined as integrals. The equations are given for the integration of variance spectra.

Here a 1D ω spectrum of the linear dispersion is given by

$$\mathcal{S}_0(\omega) = \int_{k_x}\int_{k_y} [\mathcal{G}_0(k_x, k_y, \tilde{\omega_0}(k_x, k_y, u_x, u_y, d))]\, dk_x dk_y. \tag{5.20}$$

To retrieve from (5.20) 1D ω spectra of higher harmonics, $\mathcal{G}_p(\omega)$, 3D spectra, $\mathcal{G}_p(\Omega)$, are substituted into (5.20). The spectral noise-signal part is given by

$$\Omega_{\mathrm{N}} := \{(k_x, k_y, \omega) | \, [\omega \neq \tilde{\omega}_0(k_x, k_y; u_x, u_y, d)] \vee [\omega \neq \tilde{\omega}_1(k_x, k_y; u_x, u_y, d)]\} \tag{5.21}$$

The integration over Ω_{N} yields the frequency noise spectrum:

$$\mathcal{G}_{\mathrm{N}}(\omega) = \int_{k_x,k_y} \left[\mathcal{G}_{\mathrm{N}}(\Omega_{\mathrm{N}})\right] dk_x dk_y. \tag{5.22}$$

The spectral-noise component, for example, is used for the WaMoS calibration procedure to determine the significant wave height Hs using the correlation between significant wave height and signal-to-noise ratio [AH82] [SZS97] [Bor98]. One definition of the significant wave height is given by

$$\mathrm{Hs} = 4\sqrt{m_0} \tag{5.23}$$

with the zero-th statistical moment of a time series.
Directional 2D k_x–k_y spectra are obtained by integrating over frequency:

$$\mathcal{G}_0(k_x, ky) = 2\int_{\omega>0} [\mathcal{G}_0(\mathcal{M}_0(k_x, k_y, \tilde{\omega}_0(k_x, k_y, u_x, u_y, d))]\, d\omega. \tag{5.24}$$

For discrete spectra the integrations are replaced by sums over the set of selected spectral coordinates. The discrete 1D ω spectrum of the linear dispersion is given by

$$\mathcal{G}_0(\omega_w) = \sum_m \sum_n [\mathcal{G}_0(\mathcal{M}_0(k_{x,m}, k_{x,n}, \omega_w))]\, \Delta k_x \Delta k_y. \tag{5.25}$$

The degradation to a directional 2D k_x–k_y spectrum is performed as follows:

$$\mathcal{G}_0(k_{x,m}, k_{x,n}) = \sum_w [\mathcal{G}_0(\mathcal{M}_0(k_{x,m}, k_{x,n}, \omega_w))]\, \Delta\omega. \tag{5.26}$$

5.3 Local Analysis: Dispersive Surface Classificator (DiSC)

The global analysis method is based on spectral filtering and the analysis of the real-valued 3D gray-variance spectra, $\mathcal{G}(\Omega_i)$. The spectral phase, which contains information on the local image structure [OL81], is not used. For the determination of physical parameters on a local spatial scale, the spatial structure of the image sequence here is recovered from the complex-valued 3D spectra, $\hat{\mathcal{G}}(\Omega_i)$. The core of the local-analysis method is a decomposition

of the complex-valued 3D image spectra, followed by a 2D FFT^{-1} (see Fig. 34) into the spatio-frequency R_i–ω domain.
The new method **DiSC** (**Di**spersive **S**urface **C**lassificator) analyzes image sequences, $G(\Theta i)$, of inhomogeneous surface-wave fields. Descriptions of uses of the method with optical image sequences may be found in [SSD+99b] [SBL+99a] [SBL+99b] [SSZ00d]. Applications on nautical-radar image sequences have been published in [SSD+99a] [SSWZ00] [SSZ00a]. Two patent applications have been submitted for DiSC to the German patent office [SSSZ00] [SSZ00b].
An examination of wave fields, diffracted at obstacles, was elaborated in a diploma thesis [Dan00]. The aim of this work was to show the potential of DiSC for coastal engineering purposes.
A DiSC overview is given in Fig. 35. The method includes the following steps:

1. 3D FFT: Transformation of the image sequence to the spectral Ω_i domain (see Sec. 5.3.3).

2. Decomposition of the complex-valued image spectrum. Two methods are used to retrieve spectral one-component filter bins: Dispersion Direction Frequency-Separation (DDF-S) (see Sec. 5.3.4) and Adaptive Gabor Filtering (AGF) (see Sec. 5.3.5).

3. Transformation of the filtered bins to the spatio-frequency R_i–ω domain using a 2D FFT^{-1} (see Sec. 5.3.6); in the R_i–ω domain each spectral filter bin corresponds to a complex-valued one-component image.

4. Determination of spatial maps of local-wavenumber vectors from the phase of the complex-valued one-component images. Initially an approximate version of the Multiple-Signal Classification algorithm (MUSIC) was used to estimate local wavenumber vectors blockwise (for a brief description see Appendix C). More efficient, with regard to computer run time, is a local-wavenumber estimation method developed by [HHB96] to characterize textures of single images (see Sec. 5.3.7). In addition to the complex-valued one-component images, the method utilizes the gradient one-component images. The method provides pixelwise (see Sec. 5.3.7) 1) local vectors of the wavenumber and 2) of the bandwidth. The method can also be performed blockwise, using a least-squares method (see Sec. 5.3.8). The blockwise formulation allows, in addition to the calculation of local wavenumber vectors and bandwidth vectors, the definition of a confidence coefficient. This confidence coefficient is a strong tool to increase the quality of DiSC by means of representing a criterion used to dispose of uncertain local wavenumbers.

5. Correction of local gray-level variance (see Sec. 5.3.9). The local gray-level variance of the one-component images is influenced by the ITF of

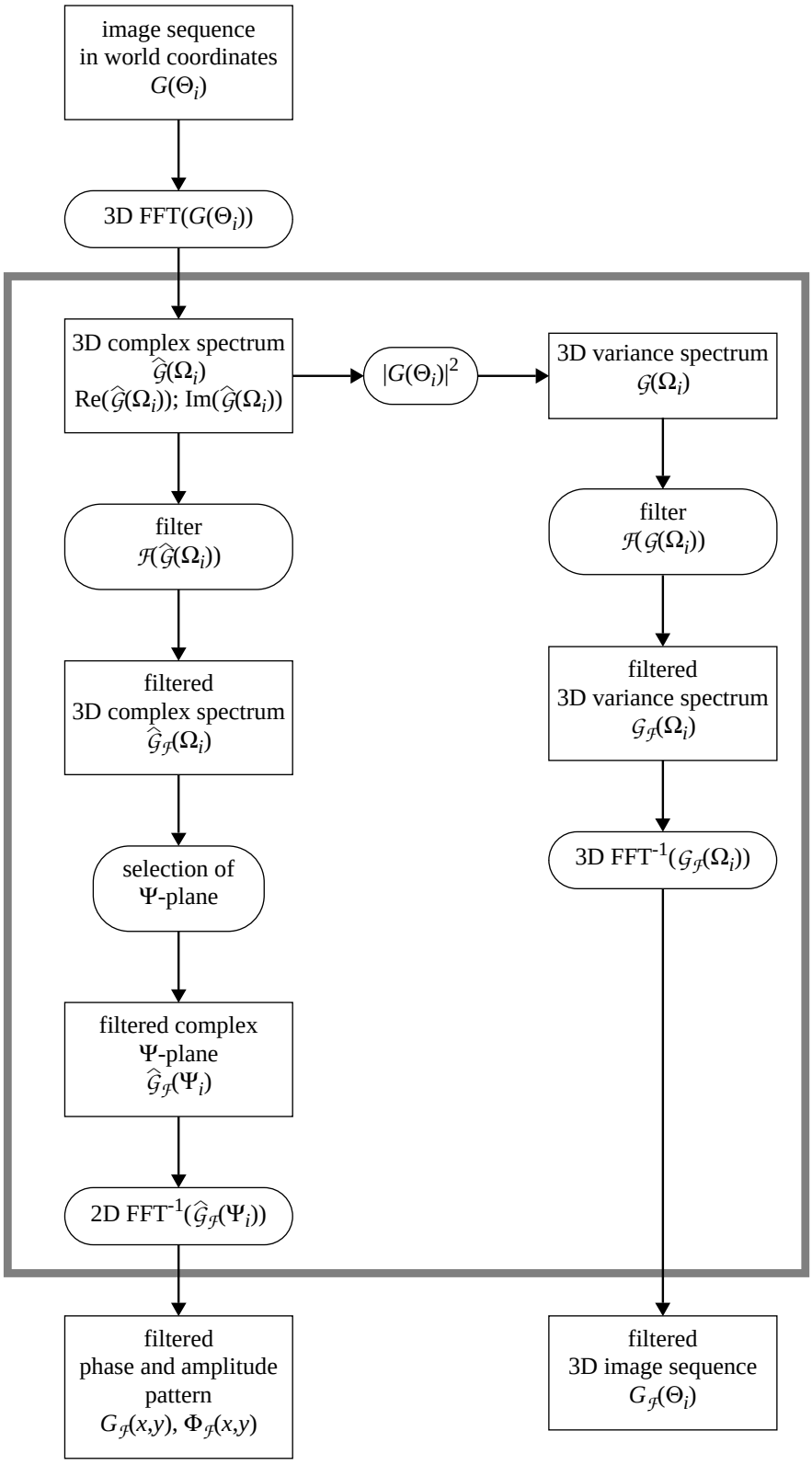

Figure 34: Overview of the inverse filter technique.

the filter used for spectral decomposition, and by the OTF of the image-acquisition system. To correct for these effects, the inverse transfer

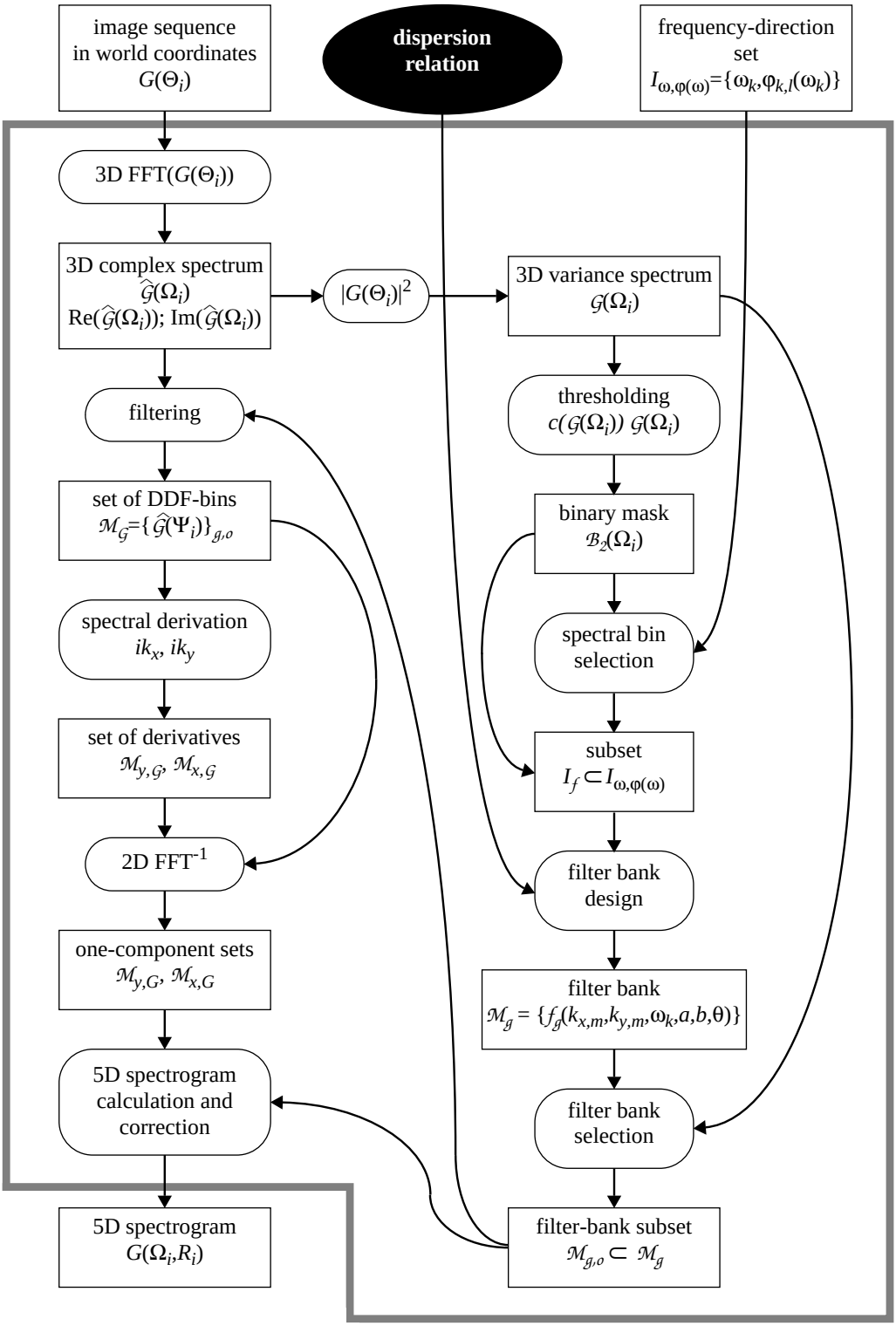

Figure 35: Scheme of the procedural and data flow of DiSC.

function has been implemented.

6. From spatial maps of local wavenumber vectors and power, hydrographic-parameter maps, i.e. maps of the near-surface current and water

depth (see Sec. 5.3.11), and local image spectra (see Sec. 5.3.10), are retrieved.

5.3.1 Input Parameters

A 3D image sequence, $G(\Theta_i)$, in world coordinates (see Sec. 5.1), that is to be analyzed, is the input data set of DiSC. Further, a set,

$$I_{\mathrm{FD}} = \{\omega_w, \phi_{w,l}(\omega_w)\}, \tag{5.27}$$

of user-defined frequency–direction sets to define anchor positions for the spectral filter bank in the 3D Ω-domain, which is used for spectral separation. In (5.27) ω_w locates a $\Upsilon_{i,w}$ domain at frequency ω_w, chosen for filtering. In each of these $\Upsilon_{i,w}$ domains, sets of directions $\phi_{w,l}$ are pre-defined. Indices are $w = 1,\ldots,W$ and $l = 1,\ldots,L$.

5.3.2 Assumptions of DiSC

Stationarity: The imaged process analyzed by DiSC has to be stationary. Stationarity implies the temporal invariance of a signal, G. Assuming stationarity, DiSC can treat the spatial Fourier decomposition of the distinct frequency components independently,

$$\hat{G}_w(R_i, \omega_w) = \sum_{n=1}^{N} \hat{\mathcal{G}}_w(\Upsilon_{i,\omega_w}) \cdot e^{i\vec{k}_n\vec{r}}, \tag{5.28}$$

with the complex-valued spatial image, $\hat{G}_w$, at constant frequency, ω_w, and the k_x-k_y-plane, $\Upsilon_{i,w}$.

Validity of the multi-component AM–FM image model: For inhomogeneous images the amplitudes or the spatial phase gradients (i.e. the local-wavenumber vectors) vary. This information is only implicitly included in the coefficients of the Fourier decomposition (5.28). To enable explicit analysis, the spatial Fourier decomposition is transformed to an image representation, composed of a superposition of 2D jointly amplitude–frequency-modulated, locally coherent, analytic signals (multi-component AM–FM image model [HHB96]):

$$\hat{G}_w(R_i) = \sum_{l=1}^{L} \Lambda_{w,l}(R_i)\, e^{i\Phi_{w,l}(R_i)}. \tag{5.29}$$

For each one-component analytic image the complex-valued local-wavenumber vector, $\vec{k}_{w,l}$, is unambiguously defined by the spatial gradient of the local phase:

$$\vec{k}_{w,l}(R_i) = \nabla_R \Phi_{w,l}(R_i). \tag{5.30}$$

The modulus of the normalized spatial gradient vector, $\vec{b}_{w,l}$, of the local amplitude, $\Lambda_{w,l}$, is given by

$$\vec{b}_{w,l}(R_i) = \frac{\nabla_R \Lambda_{w,l}(R_i)}{\Lambda_{w,l}(R_i)}. \tag{5.31}$$

The vector $\vec{b}_{w,l}(R_i)$ is the spatial local-bandwidth vector determining the degree of inhomogeneity [HHB73]. The components of the local-bandwidth vector are defined by the normalized gradient of the local amplitude in each coordinate direction.
For a real-valued single image an infinite set of pair-combinations of amplitude maps, $\Lambda(R_i)$, and phase maps, $\Phi(R_i)$, exists, resulting in the original image:

$$G(R_i) = \Lambda(R_i) \cdot \cos(\Phi(R_i)). \tag{5.32}$$

An unambiguous representation is obtained by adding the Hilbert transformation, $\mathcal{H}$, of the real-valued image:

$$\hat{G}(R_i) = G(R_i) + i \cdot \mathcal{H}(G(R_i)). \tag{5.33}$$

The Hilbert-transformed and now complex-valued image, $\hat{G}(R_i)$, is unambiguous by the fact that it defines an unambiguous direction and is called an analytic image. For single images the calculation of an analytic image is performed by zero-padding on one half-plane in the wavenumber domain. Zero-padding of one half-plane removes the redundant spectral information [HB95].
A decomposition of the multi-component image into one-component images, yielding an unambiguous analytic image, can be performed by a Gabor-filter bank covering one half-plane of the wavenumber domain (Fig. 36). For general texture analysis applications, the spectral locations of a signal a priori are not known. Therefore, full filter coverage of a half-plane is required.
Image sequences are already Hilbert-transformed by omiting one frequency hemisphere, Ω^- or Ω^+. Therefore a filter bank, defined in a $\Upsilon_{i,w}$ plane at constant frequency, ω_w, can span the whole $\Upsilon_{i,w}$ plane. Signals located at $\vec{k}_1(\Upsilon_{i,w})$ and $\vec{k}_2(\Upsilon_{i,w}) = -\vec{k}_1(\Upsilon_{i,w})$ on the same $\Upsilon_{i,w}$ plane are distinguishable. For image sequences of surface water waves, the spectral signal is located close to the dispersion shell. Because of inhomogeneities in the near-surface current and the water depth, the dispersion shell may spread in the global spectrum.
DiSC is based on a global spectral separation into complex-valued one-component images. In contrast to texture analysis of single images, the filter bank only covers a subspace close to the dispersion shell for the analysis of image sequences of the sea-surface waves.
If the dispersion relation is valid on a local spatial scale (quasi-homogeneity), after spectral decomposition, the local bandwidth of the complex-valued one-component images is small, even if the spectral signal in the global spectrum is spread due to inhomogeneities. If filtering is performed on spread spectral signals, the spectral filter size has to include the spreading. The global bandwidth of the filter is an upper limit to the spreading of the local wavenumber vectors of the one-component images.

5.3.3 3D FFT

By the 3D FFT algorithm (described in Sec. 5.2.3) an image sequence, $G(\Theta_i)$, is transformed to a complex-valued 3D spectrum, $\hat{\mathcal{G}}(\Omega_i)$. In contrast to the

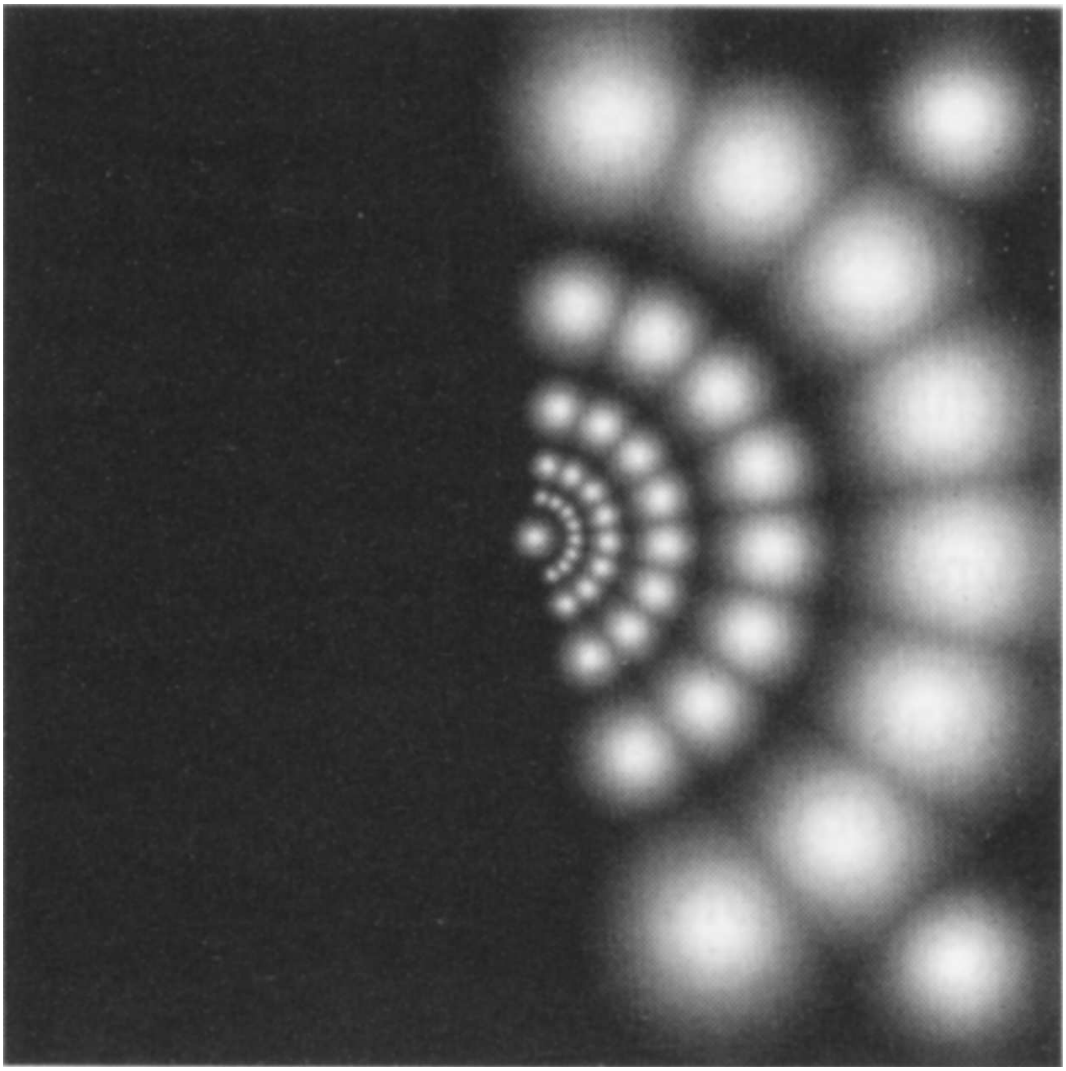

Figure 36: Spectral Gabor-filter bank used to decompose a multi-component image into a set of one-component images [HHB73].

global-analysis method, here the complex-valued image spectrum, $\hat{\mathcal{G}}(\Omega_i)$ (and not as for the global method the gray-level variance spectrum, $\mathcal{G}(\Omega_i)$) is utilized to obtain the local structure.

5.3.4 Spectral Decomposition: DDF-S

The spectral decomposition technique DDF-S (**D**irectional **D**ispersion **F**requency-**S**eparation) is based on the combination of

- a directional wedge filter,
- the dispersion-shell filter and
- a frequency separation,

yielding a spectral DDF bin. The principle of DDF-S is outlined in Fig. 37.

The applied directional wedge filter [SF96] (originally used as a convolution mask in the spatial domain) is the product of a radial and an azimuthal component:

$$F_W(k,\phi) = F_1(\phi) \cdot F_2(k). \tag{5.34}$$

The azimuthal function, $F_1(\phi)$, is defined as follows:

$$F_1(\phi) = F_c^2(\phi) + F_s^2(\phi), \tag{5.35}$$

where

$$F_c(\phi) = \sum_{n=1}^{N} w_n \cos[n(\phi - \phi_0)] \tag{5.36}$$

and

$$F_s(\phi) = \sum_{n=1}^{N} w_n \sin[n(\phi - \phi_0)]; \tag{5.37}$$

w_n are the weighting factors that determine the angular width of the filter. The weighting factors are determined by a least-squares approximation by

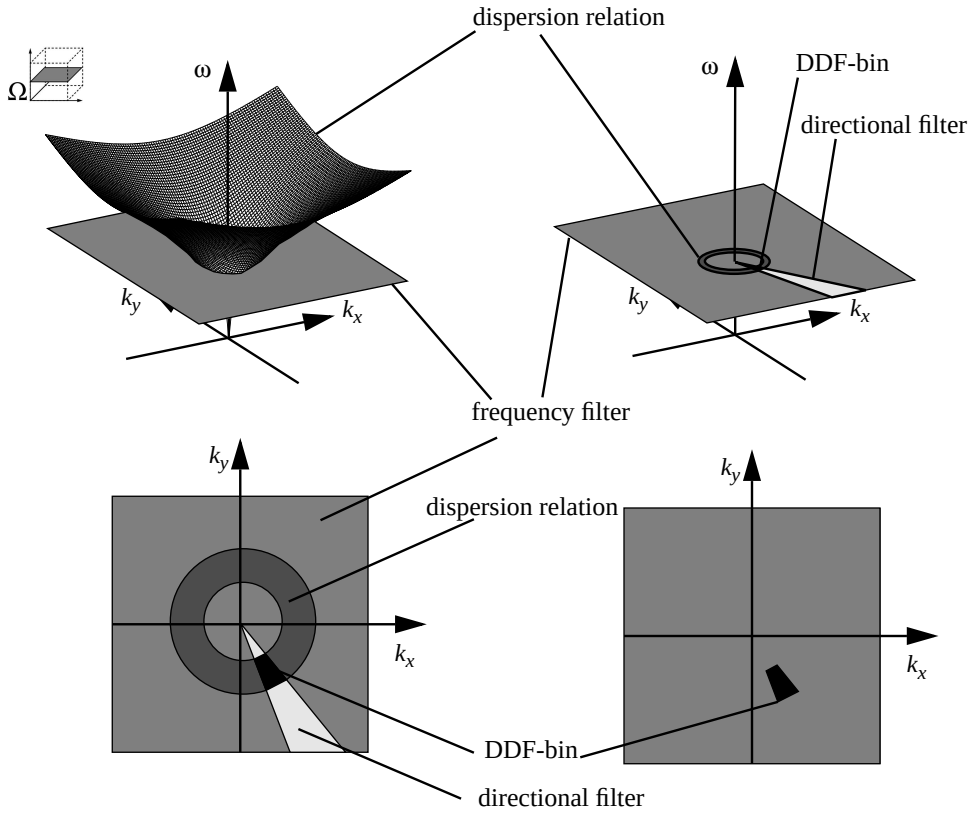

Figure 37: Schematic of Directional-Dispersion-Frequency Separation (DDF-S). The result of the DDF-S is a DDF bin.

minimizing

$$P(w_1, w_2, ..., w_n) = \int d\phi(\phi - \phi_0)^2 \cdot F_1(\phi). \tag{5.38}$$

The radial function (the spectral radial component is k) is defined as

$$F_2(k) = \begin{cases} 0 & \text{if} \quad k < K \\ \frac{1}{2}\left[1 - \cos\left(\frac{\pi(k-K)}{\delta k}\right)\right] & \text{if} \quad K \leq k \leq K + \delta k \\ 1 & \text{if} \quad k > K + \delta k \end{cases}, \tag{5.39}$$

where K is the lower-wavenumber cutoff and δk is the width of the staircase of the function $F_2(k)$ unless the function saturates to a value of 1. A spectral wedge filter is shown in Fig. 38.

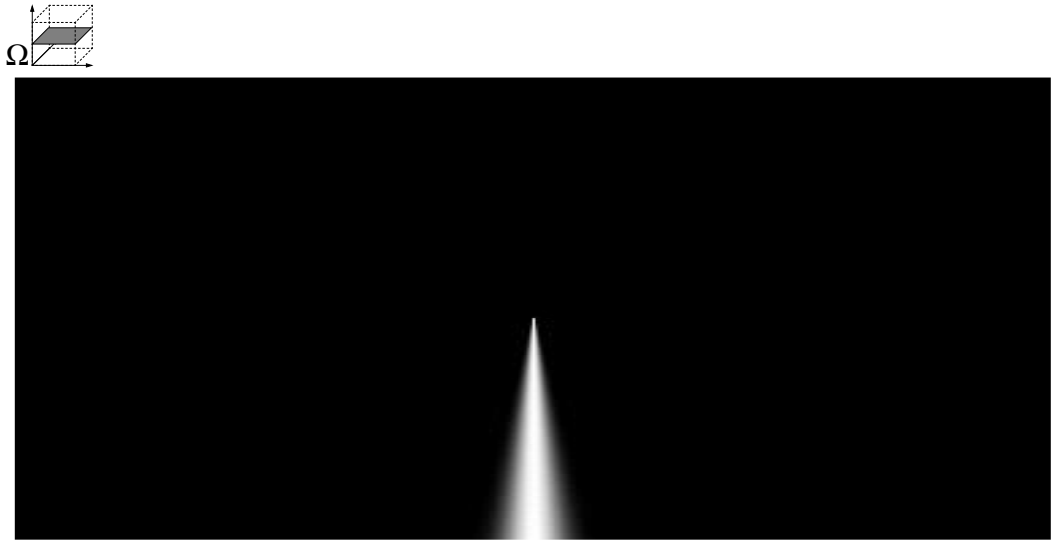

Figure 38: Example of a directional wedge filter in a 2D Υ plane.

5.3.5 Spectral Decomposition: AGF

As an alternative to the DDF-S concept, the spectral decomposition of the 2D $\Upsilon_{i,w}$ planes of the 3D image Ω_i spectrum may be performed by applying a bank of modified Gabor filters. The MTF of the Gabor filter [JHG99b] has the form

$$\mathrm{MTF}_G(\vec{k}) = \frac{1}{2\pi\sigma_{k_\phi}\sigma_{k_r}} \cdot e^{-\frac{1}{2}(\vec{k}-\vec{k}_m)^t \cdot \mathbf{A} \cdot (\vec{k}-\vec{k}_m)}, \tag{5.40}$$

where the matrix $\mathbf{A}$ is composed of a diagonal parameter matrix, $\mathbf{P}$, and a rotation matrix, $\mathbf{R}$:

$$\mathbf{A} = \mathbf{RPR}^{\mathrm{t}} = \begin{pmatrix} \cos(\phi) & -\sin(\phi) \\ \sin(\phi) & \cos(\phi) \end{pmatrix} \cdot \begin{pmatrix} \sigma_{k_\phi}^{-2} & 0 \\ 0 & \sigma_{k_r}^{-2} \end{pmatrix} \cdot \begin{pmatrix} \cos(\phi) & \sin(\phi) \\ -\sin(\phi) & \cos(\phi) \end{pmatrix}. \tag{5.41}$$

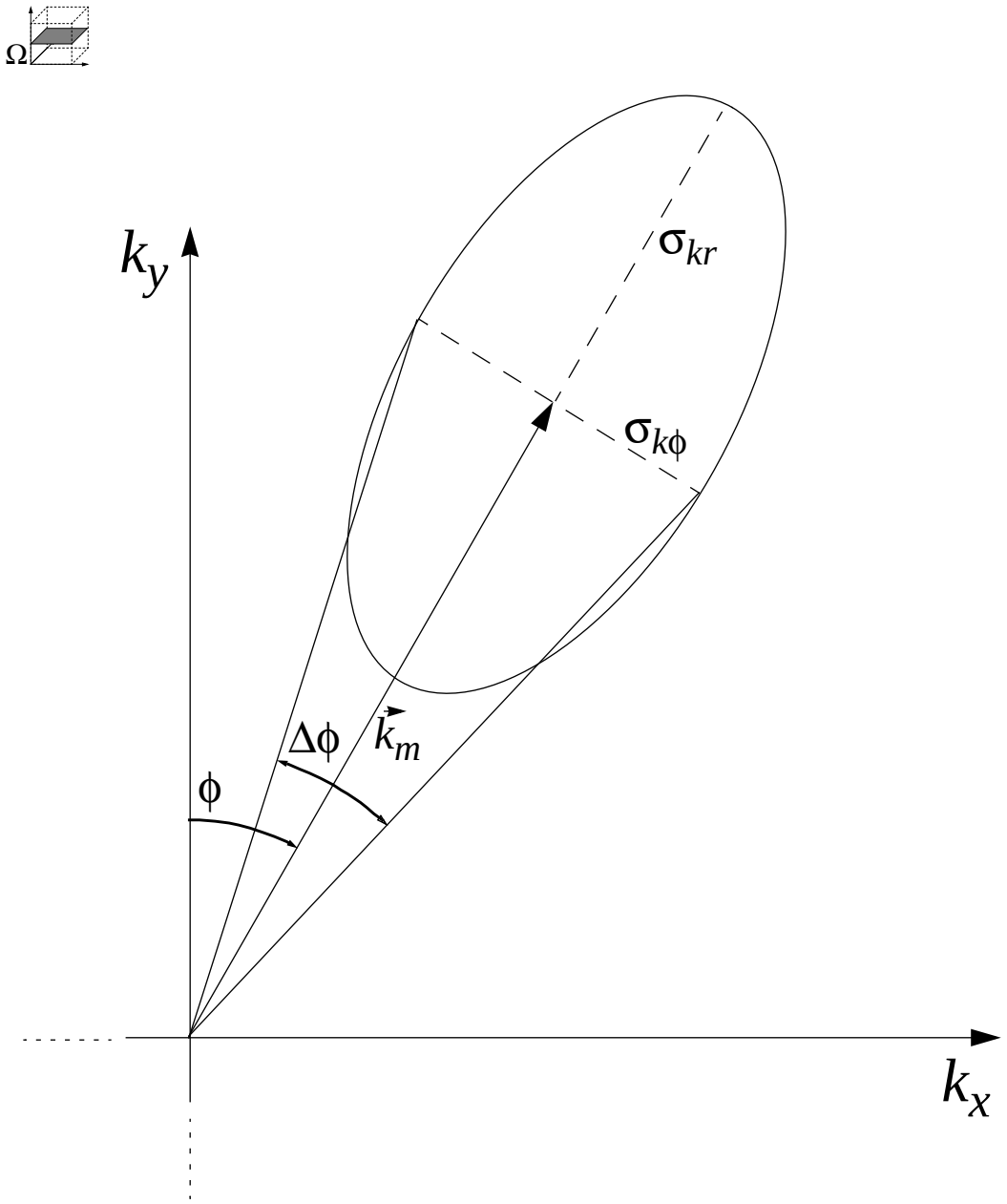

Figure 39: Parameters specifying the MTF (spectral representation) of a spectral Gabor filter: $\vec{k}_m$: centre wavenumber, ϕ: orientation angle, σ_{k_a}: azimuthal filter bandwidth and σ_{k_r}: radial filter bandwidth.

The parameters, specifying a Gabor-filter bin, MTF_G, are the centre wavenumber, $\vec{k}_m$, the orientation angle, ϕ, and the azimuthal and radial filter bandwiths, σ_{k_a} and σ_{k_r}. The parameters are illustrated in Fig. 39. The centre wavenumber is determined by

$$\vec{k}_m = k_m \cdot (\sin(\phi), \cos(\phi)). \tag{5.42}$$

The direction of the Gabor-filter centre coincides with the rotation angle, ϕ. Therefore the principal axis of the Gabor filter is always directed toward the

coordinate origin. The Gabor-filter parameters, k_m and σ_{k_r}, are determined adaptively. The subset of signal coordinates of the directional-frequency bins

$$\mathcal{M}_{0,w,l} = \{(k_x, k_y, \omega) \in \mathcal{M}_0 \mid \omega = \omega_w \ \wedge \ \angle(k_x, k_y) \in \ I_\phi\} \tag{5.43}$$

is collected. In (5.43) $\mathcal{M}_0$ is given by (5.12), $\angle(k_x, k_y)$ is the angle of the wavenumber vector (k_x, k_y), and the interval I_{ϕ_w} is given by

$$I_\phi = \left] \phi_{w,l} - \frac{\Delta\phi_w}{2}, \phi_{w,l} + \frac{\Delta\phi_w}{2} \right]. \tag{5.44}$$

The magnitude of the Gabor-filter centre is determined by the mean of all wavenumber magnitudes of the selected spectral coordinates:

$$k_m = \left\{ |\vec{k}| | \vec{k} \in \mathcal{M}_{0,w,l} \right\}. \tag{5.45}$$

The radial bandwidth σ_{k_r} of the Gabor filter is chosen to be equal to the standard deviation:

$$\sigma_{k_r} = \left\{ \sigma(|\vec{k}|) | \vec{k} \in \mathcal{M}_{0,w,l} \right\}, \tag{5.46}$$

and the azimuthal Gabor-filter width, σ_{k_ϕ}, is set to

$$\sigma_{k_\phi} = k_m \cdot \arctan\left(\frac{\Delta\phi_w}{2}\right), \tag{5.47}$$

where $\Delta\phi_w$ is adapted to the form of the dispersion shell. Therefore σ_{k_ϕ} is equal for each $\Upsilon_{i,w}$-plane of the 3D Ω_i spectrum. According to the dispersion relation (2.9) the following relations yield: $\Delta\phi_w \propto \omega^{-2}$ for deep-water waves and $\Delta\Phi_w \propto \omega^{-1}$ for shallow-water waves.
Due to temporal fluctuations of the mean intensity of the images, a spectral signature appears close to the frequency axis of the image spectrum (see, for example, the signal close to the ω axis in Fig. 50). For low wavenumbers, the Gabor filter may cover the coordinate origin of the $\Upsilon_{i,w}$ plane, collecting the disturbing signal. To avoid low-wavenumber signals, the concerned Gabor filters are modified. The modification restricts the extension of the modified Gabor filter to one wavenumber half plane. The magnitude of the modified Gabor filter approaches zero at the ω-axis. For 1D cases this modification method is given by [Bov00]. Extending Boviks approach to two dimensions yields

$$\mathrm{MTF}_{GM}(\vec{k}) = \begin{cases} \mathrm{MTF}_G(\vec{k}) - \mathrm{MTF}_G(-\vec{k}) & \text{if} \quad \vec{k} \cdot \vec{k}_m \geq 0 \\ 0 & \text{if} \quad \vec{k} \cdot \vec{k}_m < 0. \end{cases} \tag{5.48}$$

An example of an unmodified spectral Gabor filter, MTF_G, and a modified Gabor filter, MTF_{GM}, is shown in Fig. 40.

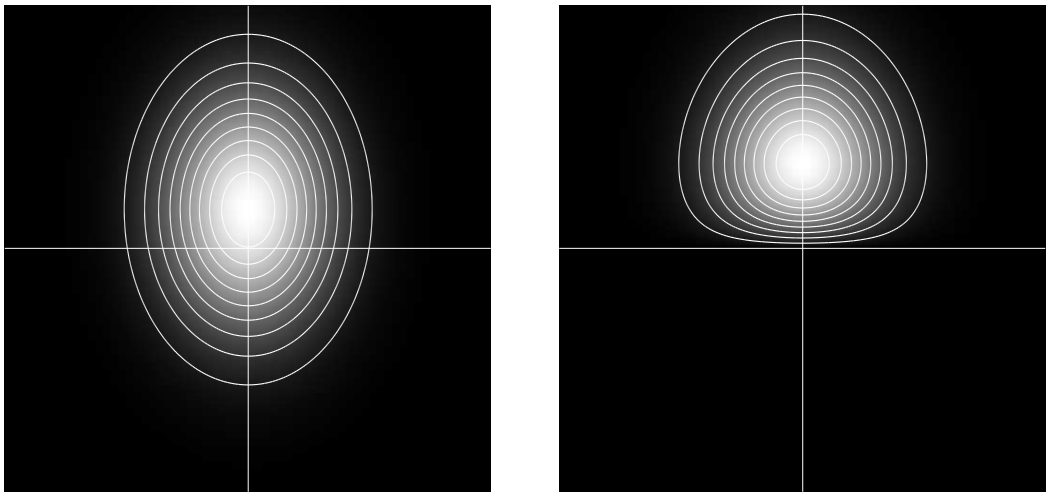

Figure 40: The MTF of a Gabor filter overlapping the coordinate origin (left) and the corresponding modified Gabor filter avoiding the overlap (right).

5.3.6 Inverse 2D FFT

Complex-valued one-component images are calculated by transforming the filtered $\Upsilon_{i,w}$-planes of the 3D image spectrum into the spatial domain, using a 2D FFT^{-1}:

$$\hat{G}_{w,l}(R_i) = \text{2D FFT}^{-1}(\text{MTF}_{w,l} \cdot \hat{\mathcal{G}}_w(\Upsilon_i)), \tag{5.49}$$

where $\text{MTF}_{w,l}$ indicates the MTF of a spectral filter. Complex-valued gradient images are calculated with (5.49) by multiplying $\hat{\mathcal{G}}_w(\Upsilon_i)$ with the MTF of the derivative operator, $i\vec{k}$:

$$\nabla_R \hat{G}_{w,l}(R_i) = \text{2D FFT}^{-1}(i\vec{k} \cdot M_{w,l} \cdot \hat{\mathcal{G}}_w(\Upsilon_i)). \tag{5.50}$$

5.3.7 Pixelwise Local-Wavenumber Calculation

For the complex-valued one-component images the following holds

$$\nabla_R \hat{G}_{w,l}(R_i) = i \cdot \vec{\hat{k}}_{w,l} \cdot \hat{G}_{w,l}(R_i). \tag{5.51}$$

The complex-valued local wavenumber vectors $\vec{\hat{k}}_{w,l}$ are calculated from (5.51) as follows:

$$\vec{\hat{k}}_{w,l}(R_i) = -i \cdot \frac{\hat{G}^*_{w,l}(R_i) \cdot \nabla_R \hat{G}_{w,l}(R_i)}{|\hat{G}_{w,l}(R_i)|^2}, \tag{5.52}$$

if the threshold criterion

$$|\hat{G}_{w,l}(R_i)|^2 > \epsilon \tag{5.53}$$

holds. The real and imaginary part of the complex-valued local-wavenumber vector is physically motivated as follows: the real part is equal to the spatial phase gradient and defines the real-valued local-wavenumber vector,

$$\vec{k}_{w,l}(R_i) = \text{Re}[\vec{\hat{k}}_{w,l}(R_i)] = \nabla_R \Phi_{w,l}(R_i); \tag{5.54}$$

the imaginary part is equal to the normalized gradient of the local amplitude defining the local-bandwidth vector,

$$\vec{b}_{w,l}(R_i) = \mathrm{Im}[\vec{\hat{k}}_{w,l}(R_i)] = \frac{\nabla_R \Lambda_{w,l}}{\Lambda_{w,l}}, \tag{5.55}$$

of the signal.

5.3.8 Blockwise Local-Wavenumber Fit

In the complex-valued one-component images, local singularities can occur due to the finite directional width of the spectral filters. Superposition of waves coming from slightly different directions covered by the azimuthal filter width can result in interferences.
To detect and exclude local singularities of a 2D phase pattern, a blockwise local-wavenumber fit is introduced. A positive side effect of the blockwise calculation is the resulting robustness with regard to spatially uncorrelated (white) noise. This robustness is particularly of interest for nautical-radar images, where speckle noise is a significant contribution to the signal. The complex-valued local-wavenumber vectors are calculated by minimizing the normalized error functions

$$\epsilon_{\hat{k}_x} = \frac{||\vec{v}_x - i\,\hat{k}_x \cdot \vec{v}||^2}{||\vec{v}||^2} \quad \text{and} \quad \epsilon_{\hat{k}_y} = \frac{||\vec{v}_y - i\,\hat{k}_y \cdot \vec{v}||^2}{||\vec{v}||^2}, \tag{5.56}$$

if

$$||\vec{v}||^2 > \epsilon, \tag{5.57}$$

with a very small numerical threshold, ϵ. The vectors $\vec{v}$, $\vec{v}_x$ and $\vec{v}_y$ are obtained by line-scanning a block [Pra75] of the one-component image. From the same block, the gradient images are calculated respectively. The norm is denoted by $||...||$ and the adjunct of a vector by the superscript + sign. The error functions (5.56) are minimized by the complex-valued wavenumber vectors

$$\vec{\hat{k}}_x = -i \cdot \frac{\vec{v}^+ \cdot \vec{v}_x}{||\vec{v}||^2} \quad \text{and} \quad \vec{\hat{k}}_y = -i \cdot \frac{\vec{v}^+ \cdot \vec{v}_y}{||\vec{v}||^2}. \tag{5.58}$$

The accuracy of the regression algorithm depends on the correlation of the images with their corresponding gradient images. The two components of the correlation coefficient are given by

$$\mathcal{C}_{\hat{k}_x} = 1 - \epsilon_{\hat{k}_x} = \frac{|\vec{v}^+ \cdot \vec{v}_x|^2}{||\vec{v}||^2 \cdot ||\vec{v}_x||^2} \quad \text{and} \quad \mathcal{C}_{\hat{k}_y} = 1 - \epsilon_{\hat{k}_y} = \frac{|\vec{v}^+ \cdot \vec{v}_y|^2}{||\vec{v}||^2 \cdot ||\vec{v}_y||^2}. \tag{5.59}$$

A harmonic-mean confidence coefficient here is defined as

$$\mathcal{C} = \frac{2 \cdot \mathcal{C}_{\hat{k}_x} \cdot \mathcal{C}_{\hat{k}_y}}{\mathcal{C}_{\hat{k}_x} + \mathcal{C}_{\hat{k}_y}}, \tag{5.60}$$

whose behaviour ensures that a low confidence is estimated if the correlation of the one-component images with one of the gradient images is low. The confidence coefficient, $\mathcal{C}$, is used as a threshold to discriminate uncertain local-wavenumber vectors.

5.3.9 Correction of Local-Variance Maps

The global decomposition procedures DDF-S and AGF result in a power loss of the gray-level variance of the filtered 3D spectrum and therefore of the local-variance pattern as well. For a given Gabor filter at the position of the centre wavenumber, the magnitude of gray-level variance is conserved. For other signals filtered by the Gabor filter, a power loss occurs.
This effect can expressed by the quasi-eigenfunction approximation [HHB00]:

$$(\Lambda'_{w,l})^2 = \mathrm{ITF}_{w,l}(\vec{k}_{w,l}(R_i)) \cdot (\Lambda_{w,l})^2. \tag{5.61}$$

The effect of the OTF (see Sec. 5.2.4) of the image-acquisition system is given by

$$(\Lambda'_{w,l})^2 = \mathrm{OTF}_{w}(\vec{k}_{w,l}(R_i)) \cdot (\Lambda_{w,l})^2. \tag{5.62}$$

In contrast to the global method, the inhomogeneity of the OTF can be taken into account. Both effects can be corrected by the inversion of (5.61) and (5.62):

$$(\Lambda_{w,l})^2 = \mathrm{OTF}_{w}^{-1}(\vec{k}_{w,l}(R_i)) \cdot \mathrm{ITF}_{w,l}^{-1}(\vec{k}_{w,l}(R_i)) \cdot (\Lambda'_{w,l})^2, \tag{5.63}$$

if

$$\left|\mathrm{OTF}_{w}(\vec{k}_{w,l}(R_i))\right| > \epsilon \qquad \text{and} \qquad \left|\mathrm{ITF}_{w,l}(\vec{k}_{w,l}(R_i))\right| > \epsilon. \tag{5.64}$$

5.3.10 Determination of Local Spectra

The modulation signal of the imaged waves is described by the AM–FM image model as a superposition of locally coherent wave patterns. These locally coherent wave patterns are characterized by their local gray-level variance, local-wavenumber vector, local-bandwidth vector, and frequency, ω_w,

$$\mathcal{G}(R_i, w, l) := \{\Lambda^2_{w,l}(R_i), \vec{k}_{w,l}(R_i).\vec{b}_{w,l}(R_i), \omega_w(R_i)\}, \tag{5.65}$$

This allocation is termed a local image spectrum. It differs from the global Fourier image spectrum in the following respects:

- Additional information about the spatial variation of the local amplitude is provided by the local-bandwidth vector; the local-bandwidth vector is a quantifier, determining the measure of local homogeneity. The more narrow the bandwidth, the more the postulated assumption of quasi-homogeneity is fulfilled. The bandwidth can be used as a qualifier, determining areas which do not fulfill the assumption of local homogeneity. These areas are excluded to prohibit unwanted data from further considerations.

- The wavenumber resolution is not restricted by the image size.

- The basis functions of the decomposition are not orthogonal.

2D local k_x–k_y spectra are obtained by skipping the frequency information. 1D local ω spectra are calculated by adding up the local gray-level variance of the directional bins:

$$\mathcal{G}(R_i, w) := \{\Lambda_w^2(R_i), \omega_w(R_i)\}, \tag{5.66}$$

where

$$\Lambda_w^2(R_i) = \sum_{l=1}^{L} \Lambda_{w,l}^2(R_i). \tag{5.67}$$

The local ω spectra only approximately represent the frequency dependency of the local variance, because of the non-orthogonality of the basis functions of the decomposition.

5.3.11 Determination of Hydrographic-Parameter Sets

The regression method, which is utilized to deduce global values of the near-surface current and the water depth from global 3D image spectra (see Sec. 5.2.5), is also used for the calculation of current and depth maps. From the set of local-wavenumber vector maps, calculated blockwise from the filtered one-component images, local signal-coordinate vectors are calculated by

$$\mathcal{M}_S(R_i) := \{(k_{x,w,l}, k_{y,w,l}, \omega_w)(R_i) | 1 - \mathcal{C}(R_i) < \epsilon\}. \tag{5.68}$$

Local-wavenumber vectors, selected by (5.68), qualify as reliable if the confidence (5.60) is close to 1, i.e. $1-\mathcal{C} < \epsilon$. For each location, R_i, the current and water depth are calculated by the minimization of the cost function (5.11).

6 Experiments

6.1 Experiment: Wind-Wave Tank Hamburg

In this section three experiments are presented, two optical experiments and one radar experiment.
The first preliminary test experiment at the Wind-Wave Tank (Hamburg, Germany), described in Sec. 6.1.1 had the following aims: 1) to test the functionality of the optical image-sequence acquisition system under laboratory conditions and to deliver first results showing the principal feasibility to determine physical parameters from optical image sequences of the sea surface 2) to test the system under diffuse and spot illumination conditions synchronously with two cameras.
The second optical experiment has been performed at the Multidirectional-Wave Tank (Madrid, Spain) (see Sec. 6.2). In contrast to the Wind-Wave Tank – where waves are created by an air blower – waves at Multidirectional-Wave Tank are created by electro-mechanical paddles. This type of surface-wave generation ensures the creation of gravity waves where, in contrast to wind-created waves, instationary waves processes (producing nonlinearities) are minimized. Therefore, it can be expected, that nonlinear signal structures found in the resulting image spectra, are a result primarily of the imaging mechanisms (see Sec. 3) and not of the nonlinear wave field (see Sec. 2.4).
Additional radar data sets retrieved in a long-term field experiment at the island of Sylt (see Sec. 6.3) are added to this work to 1) show the appropriateness of DiSC under natural conditions and for different types of sensors and 2) to verify the potential of DiSC to analyze inhomogeneous wave fields.

6.1.1 Wind-Wave Tank Hamburg

An experiment at the Wind-Wave Tank of the University of Hamburg was performed in March 1998. The Wind-Wave Tank is a long flume where waves can be created by wind and a wave flap. A scheme of the flume is depicted in Fig. 41. The wind flume's dimensions are 26 m long, 1 m wide, 1.5 m

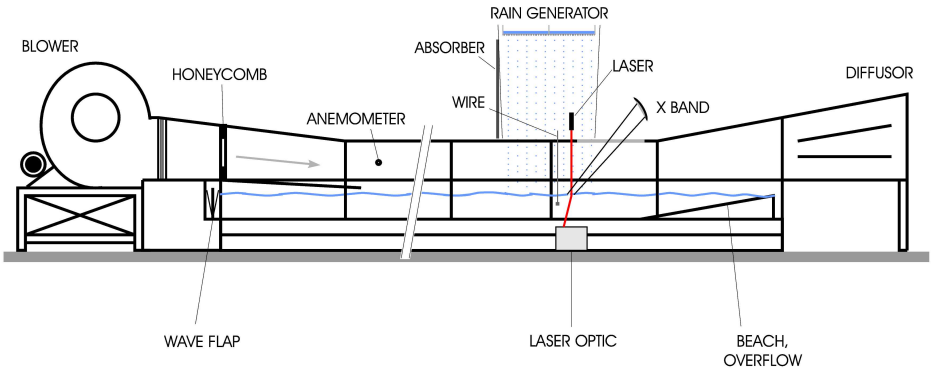

Figure 41: Side view of the Wind-Wave Tank of the University of Hamburg (source: [Bra98]).

high; the water depth is 0.5 m. The wind blower allows the generation of wind speeds from 1.5 ms^{-1} up to ca 25 ms^{-1}. The air flow is guided through a diffusing honeycomb construction to perform a homogeneous wind field. The wind begins to strike the water surface at the end of a guiding flat metal flap. Beneath the guiding flap, a mechanical wave generator flap is located. The total wind fetch is 17 m, and the wind fetch from the wind inflow to the wave gauge is 14.5 m. Detailed descriptions of the Wind-Wave Tank's abilities and applications can be found in [LH78] [GAE+98] [Bra98].

6.1.2 Experimental Setup

Two monochromatic CCD video cameras were installed – one in the downwind direction and one in the upwind direction. Fig. 42 outlines the experimental setup. Image sequences of a set of surface wave field realizations were taken under controlled illumination conditions. The water surface area observed by the camera $\mathbf{C}_1$ looking into upwind direction was illuminated by the spotlight $\mathcal{L}_1$. Thus the illumination is comparable to sun glitter illumination in nature. The area observed by CCD camera $\mathbf{C}_2$ was illuminated by a dull white coloured plate $\mathcal{L}_2^*$, which was illuminated by a spotlight, $\mathcal{L}_2$. The plate forms a diffusive light source.

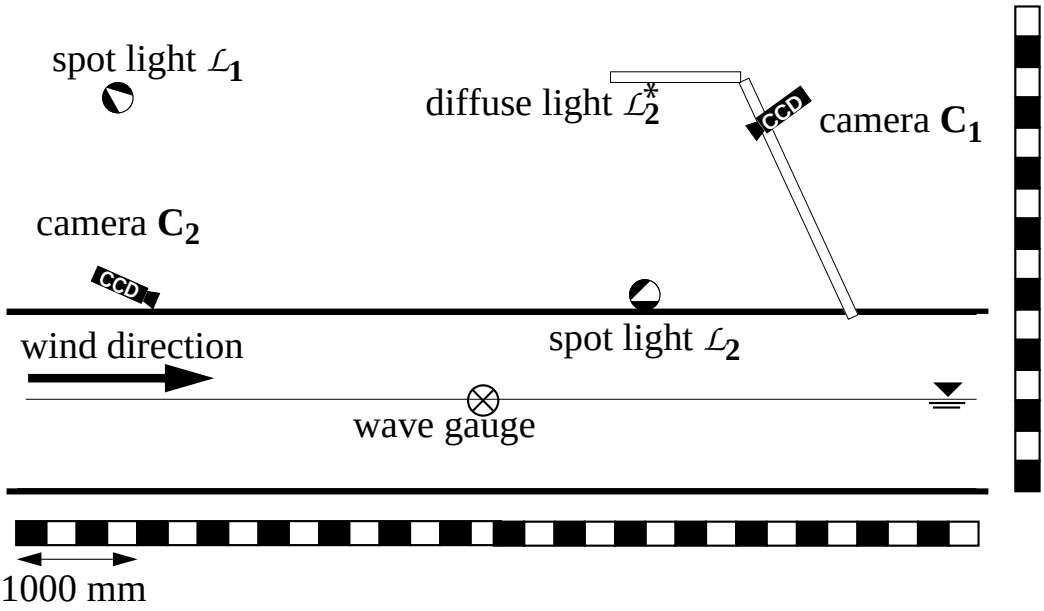

Figure 42: Experimental setup at the Wind-Wave Tank: two monochromatic JAI M10 CCD cameras are installed, one facing in the upwind direction (camera $\mathbf{C}_1$), and the other in the downwind direction (camera $\mathbf{C}_2$). The area observed by the cameras is illuminated for each of the cameras individually: camera $\mathbf{C}_1$ observes the water surface illuminated by a spotlight, $\mathcal{L}_1$; camera $\mathbf{C}_2$ observes the water surface illuminated by a diffuse light source, $\mathcal{L}_2^*$, which is irradiated by a spotlight, $\mathcal{L}_2$.

6.2 Experiment: Multidirectional-Wave Tank Madrid

An optical experiment took place at the Multidirectional-Wave Facility of the Spanish harbour authorities CEDEX (Centro de Estudios y Experimentacion de Obras Publicas) in Madrid. The wave tank is able to create multimodal and multidirectional sea states. Therefore, the proposed optical analysis (Sec. 5) can be tested for several hydrographic parameters.

6.2.1 Multidirectional-Wave Tank at CEDEX

The Multidirectional-Wave Tank (see Fig. 43) installed in the Centro de Estudios de Puertos y Costas (Cepyc) at CEDEX was build for the physical model testings of maritime engineering works, allowing the reproduction of irregular crossed, short-crested waves with an arbitrary directional spread of wave energy. The multidirectionality of the wave field is created by a wave

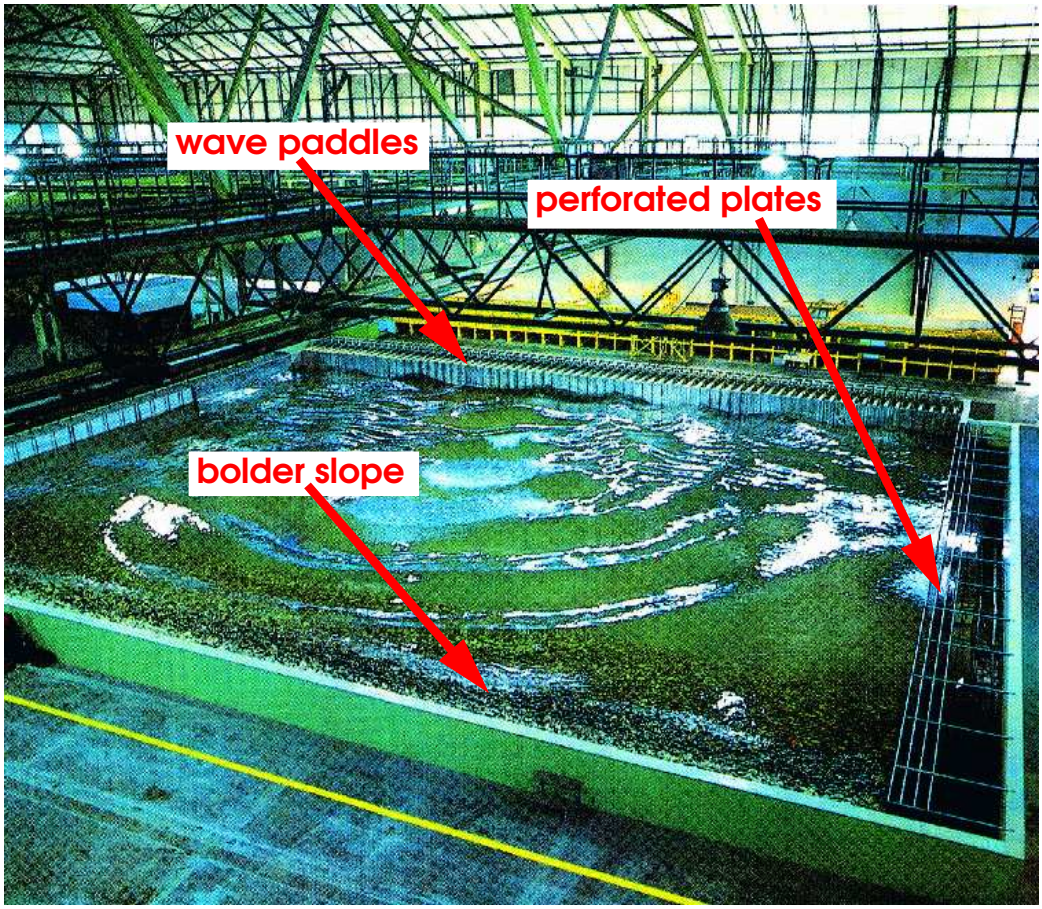

Figure 43: Multidirectional-Wave Facility at CEDEX: on the backside the wave generator, consisting of 72 single wave paddles, is indicated. The left and right sides of the wave tank are covered with perforated plates to damp waves at these boundaries. At the frontside a bolder slope prevents wave reflection. For this photograph a ring wave was created (source: CEDEX, Madrid).

generator consisting of multiple independent segments. The movements of these segments are controlled by network-linked servocomputers. An adequate combination of individual paddle movements produces any desired 2D sea state.
The technical characteristics of the tank are

- dimensions: 34 m long × 26 m wide × 1.6 m high,
- maximum water depth: 1.15 m,
- wave generator: 72 independent piston paddles (each 1.6 m high × 0.4 m wide) for a total wave front length of 28.8 m,
- actuators: electrically driven with 0.6 m stroke,
- maximum wave height: 0.58 m for frontal, regular waves,
- control system: main workstation connected by ETHERNET to digital servocomputers to control the actuators,
- lateral boundaries: perforated plate curtains for absorption or supression of reflected waves,
- longitudinal boundaries: wave generator (backside) and a boulder slope (frontside) to avoid direct wave reflection,
- current generation: variable flow up to 200 l/s, and
- wave synthesis and analysis software package.

Applications of the Multidirectional-Wave Tank at CEDEX are stability and performance tests of maritime structures, beach research (beach evolution and restoration design), and offshore structure tests.

6.2.2 Experimental Setup

The described experiment took place from 26 April to 24 May 1998. With a water depth of 0.7 m, a maximum wave height of 0.15 m was generated. The experimental setup in the wave facility is illustrated in Fig. 44. Area A is delimited by a wall construction (see Fig. 45). The wall creates a wave shadow zone where diffraction effects can be studied. In area B the wave patterns are homogeneous. Two monochromatic JAI M10 cameras were installed to simultaneously observe the wave field in the two areas of interest. The 25 mm camera lenses were mounted with near-infrared filters to suppress upwelling light from the inner water body. To control the reflected light field, two projection foils (lorry tarpaulins), with dimensions 5 m long x 8 m high, were positioned with ropes so that their reflection pattern is imaged at the water surface by the cameras. The reflectors were illuminated with spotlights; so the reflectors formed a diffusive light source. A schematic of the setup is given in Fig. 27. The light intensity of the diffusive light sources was measured using a radiometer. Close to the borders of the imaged areas

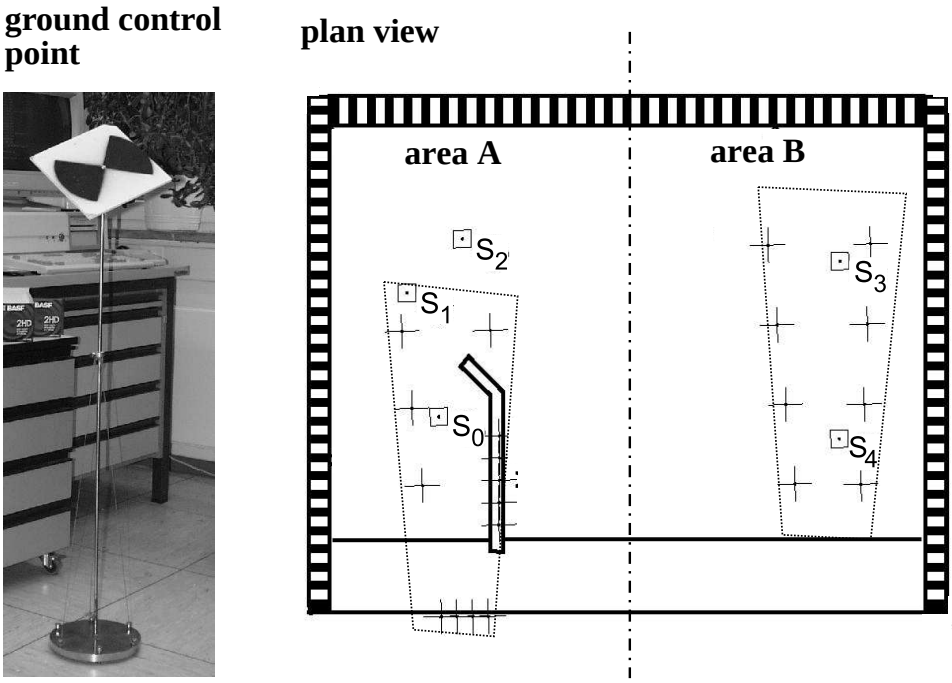

Figure 44: Photograph of a ground-control point (GCP) (left-hand side). Plan view of the experiment performed at the Multidirectional-Wave Tank at CEDEX (right-hand side. (+) GCP positions, (⊡) wave-wire gauges S_0, ..., S_4.

ground control points were placed for the geometric transformation routine described in Sec. 5.1. Five wave gauges – to retrieve in situ water elevation time series – were positioned in the observation areas. The spatial 3D world coordinates x, y and z of the ground control points and the wave gauges were measured using a tachymeter with an accuracy of a few millimeters.

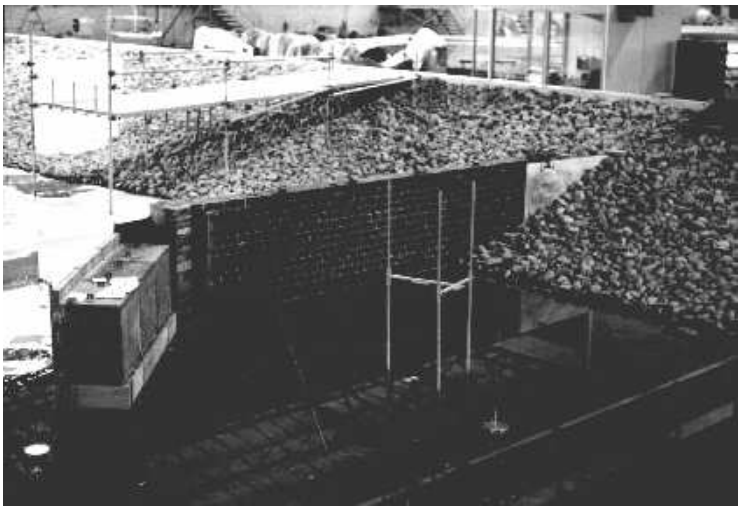

Figure 45: Wall construction: prevents waves coming from behind the wall, creating a wave shadow zone.

6.3 Experimental Setup: Sylt

A WaMoS using a nautical radar as the imaging sensor [Dit95] was mounted near the lighthouse List West on the island of Sylt in the German Bight (see Fig. 46). The area covered by the radar images show List West, the Lister Landtief, and parts of the Lister Tief. The reason for observing this coastal area is the high morphodynamical activity. A sand bar between the Lister Landtief and the Lister Tief is in the process of breaking. This event could change the flood stream situation dramatically.
The instrument used for the observation is a ground-based nautical X-band radar with horizontal polarization [Cro70]. The radar was mounted from February to June 1997 and from December 1998 to April 1999. Morphodynamic changes were detected by analyzing the static radar signatures [WSSZ99]. In addition, using DiSC the processes which cause the morphodynamic changes, e.g. the sea state and the current pattern, can be retrieved from of the dynamic radar signature caused by the surface waves.
During the storm surge from 4 to 5 February 1999, sequences which consisted of 256 single images were acquired with a time interval of approximately 1.8 s, which is equal to the antenna rotation time. Thus, the total sampling time was approximately 8 min. The polar images, which cover a radius of

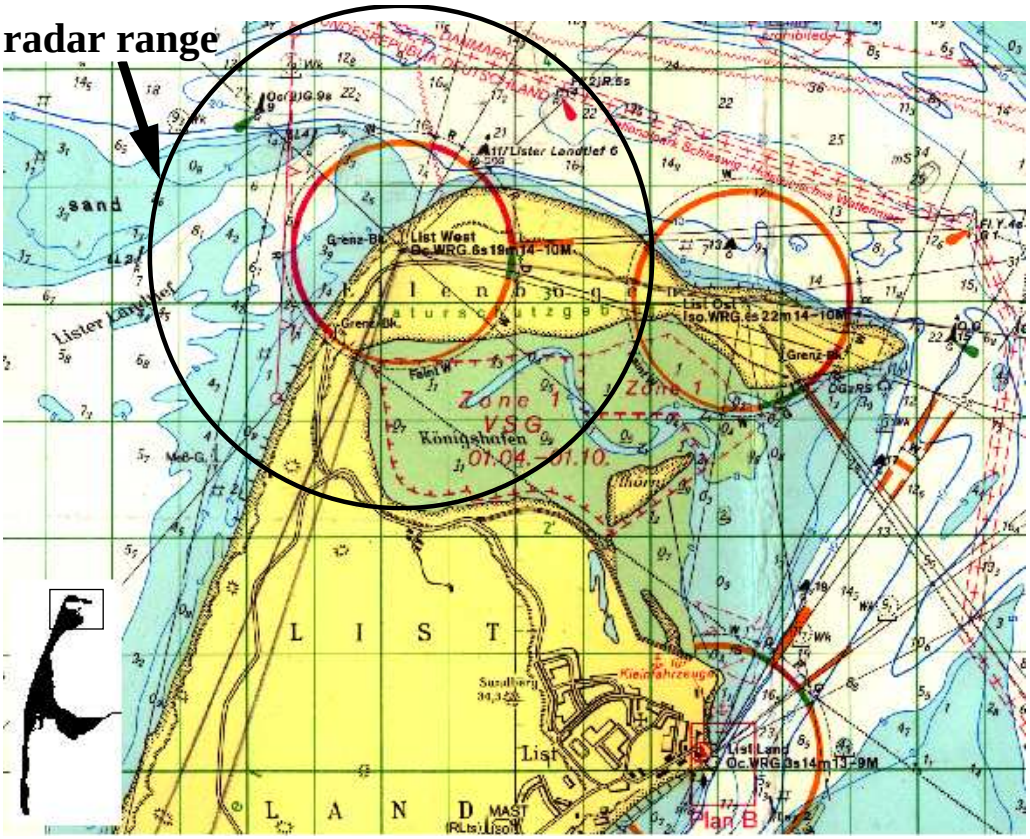

Figure 46: Experimental site Sylt (lighthouse List West): the radar range is indicated (sea-map source: Bundesamt für Seeschiffahrt und Hydrographie.).

approximately 2 km, were interpolated to a Cartesian grid with a cell size of 7 m $\times$ 7 m, corresponding to the spatial resolution of the radar. The number of pixels for one image is 576 $\times$ 576. For the observed time period, the tidal gauge, the wind direction and the wind speed at Westerland (Sylt) were recorded. A data set of the bathymetry of the observed area was taken using an echo sounder in summer 1997. The image sequence, presented here as an example, was acquired on 4 February 1999 at 20:00 h UTC at ebb tide (last slackwater high: 15:27 h UTC, next slackwater low: 21:41 h UTC).

7 Results

7.1 Results of the Global Method: Wind-Wave Tank Hamburg

7.1.1 Aims and Data Description

The global-analysis method (see Sec. 5.2) was tested on the basis of image sequences acquired during the optical experiment at the Wind-Wave Tank of the University of Hamburg (see Secs. 6.1.1 and 6.1.2). The aim was to test the global-analysis method for optical image sequences.
The image sequences were synchronously acquired by the two CCD cameras; therefore the image sequences are comparable in a deterministic sense. The number, N, of images is 256. The CCD image-sequence acquisition frequency was 25 Hz (157.08 rad s^{-1}) (25 images per second) and the electronic-shutter time was 60^{-1} s.
Only one of the two half frames of each CCD image is transformed because of the acquisition time gap of adjacent CCD image lines, belonging to separate image half frames. This sampling effect leads to an object-velocity dependent horizontal falling a part of objects in the later half frame, termed 'scanning distortion'. Therefore, the raw-image pixel resolution is decreased from 765 $\times$ 569 pixels to 765 $\times$ 284 pixels (all even lines) or to 765 $\times$ 285 pixels (all odd lines).
A raw-image example is shown in Fig. 47. The pixels of the images are

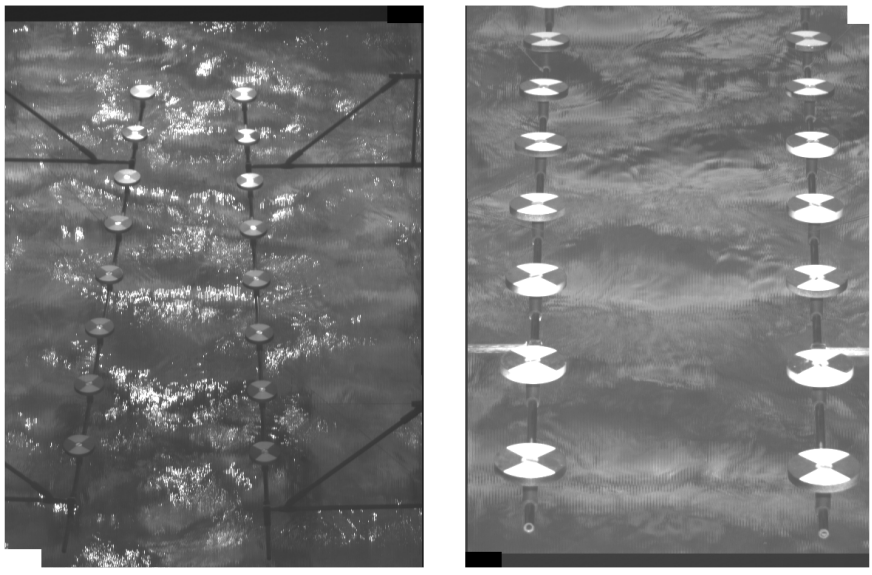

Figure 47: Raw images of a sequence acquired at the Wind-Wave Tank of the University of Hamburg: an image (left) acquired by camera $\mathbf{C}_1$ illuminated by a spotlight, $\mathcal{L}_1$, and an image (right) acquired by camera $\mathbf{C}_2$ illuminated by a diffuse reflector, $\mathcal{L}_2^*$. The framework holding the ground control points is situated above the water surface.

transformed to the rectangular world-coordinate plane (see Sec. 5.1) defined by the mean water level (see Fig. 48).
The parameters of the acquired image sequences, the parameters of the performed geometric transformation, and the parameters of the cut-out used for the 3D FFT are summarized in Tab. 2. Consider that the spatial resolutions of the cut-out used for the 3D FFT are reduced by averaging over the world coordinate maps: $\overline{\Delta x}_{\mathrm{cut}} = 6 \times \Delta x_{\mathrm{wc}}$ and $\overline{\Delta y}_{\mathrm{cut}} = 6 \times \Delta y_{\mathrm{wc}}$. The averaging is performed to preserve a sufficient box size, $X_{\mathrm{cut}} \otimes Y_{\mathrm{cut}}$, but to decrease the total amount of pixels of the image sequence to ensure the performance of the 3D FFT with a manageable amount of grid points.

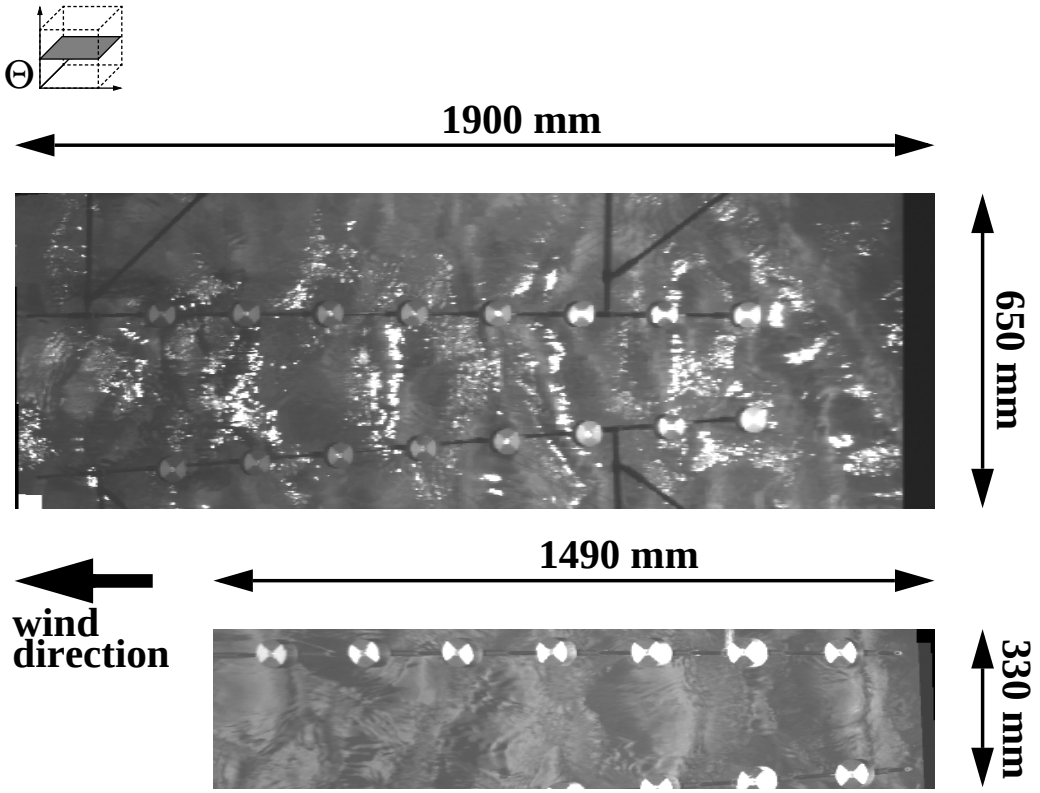

Figure 48: Images of a sequence in world coordinates: the top image was acquired by camera $\mathbf{C}_1$; the bottom image was acquired by camera $\mathbf{C}_2$.

7.1.2 Analysis and Results

For three wind speeds (3, 6 and 9 ms^{-1}), the global method with the current-fit algorithm is applied on the image sequences.
Using the 3D FFT, the set of three geometrically corrected image sequences were transformed to the Ω_i domain to test the current-fit algorithm.
Because the generated waves are deep-water waves, determination of the water depth, d, is not treated here. Therefore for the least-squares algorithm (see Sec. 5.2.5) the true water depth, $d = 0.5$ m, is substituted. The substitution reduces the number unknowns from three, u_x, u_y, and d, to two, u_x and u_y.

Table 2: Wind-Wave Tank: image-sequence parameters; $^{*6} \times \Delta x_{\mathrm{wc}}$ $^{**6} \times \Delta y_{\mathrm{wc}}$.

Parameter	camera $\mathbf{C}_1$ (spot)	camera $\mathbf{C}_2$ (diff.)
Number of images $N_{t,\mathrm{ic}}$	257	257
Shutter time	0.04 s	0.04 s
Chunk T_{ic}	10.28 s	10.28 s
no. of pixels $N_{x,\mathrm{ic}}$	765	765
No. of pixels $N_{y,\mathrm{ic}}$	569	569
No. of images $N_{t,\mathrm{wc}}$	256	256
Chunk T_{wc}	10.24 s	10.24 s
No. of pixels $N_{x,\mathrm{wc}}$	1000	1000
No. of pixels $N_{y,\mathrm{wc}}$	750	750
Resolution Δx_{wc}	2.01 mm	1.57 mm
Resolution Δy_{wc}	1.33 mm	0.80 mm
Length X_{wc}	2009.31 mm	1573.75 mm
Width Y_{wc}	1000.12 mm	602.13 mm
No. of images (analyzed) $N_{t,\mathrm{cut}}$	256	256
Chunk (analyzed) T_{cut}	10.24 s	10.24 s
No. of pixels (analyzed) $N_{x,\mathrm{cut}}$	128	128
No. of pixels (analyzed) $N_{y,\mathrm{cut}}$	64	64
Resolution (analyzed) $\overline{\Delta x}_{\mathrm{cut}}$	12.06 mm*	9.44 mm*
Resolution (analyzed) $\overline{\Delta y}_{\mathrm{cut}}$	8.00 mm**	4.82 mm**
Length (analyzed) X_{cut}	1543.68 mm	1208.32 mm
Width (analyzed) Y_{cut}	512 mm	308.48 mm

The results of the current-fit algorithm performed on the image sequences acquired with camera $\mathbf{C}_1$ (spot) are given in Tab. 3. The results show without further provement (no independent in situ current measurements were available during the experiment) the expected behaviour: For increasing wind speeds the component in wind direction u_x increases in a reasonable manner. The component normal to the wind direction exists for all wind speeds close to 0 ms^{-1}.
An additional indication that the result is reasonable is given in Fig. 49, where the k_x–ω sections for the wind speeds 3 ms^{-1} and 9 ms^{-1} are presented.

Table 3: Determination of the velocity of encounter: results using Wind-Wave Tank.

Wind speed $[\mathbf{ms}^{-1}]$	3	6	9
Camera $\mathbf{C}_1$ (spot): current u_x $[\mathrm{cms}^{-1}]$	2.855	5.002	9.305
Camera $\mathbf{C}_1$ (spot): current u_y $[\mathrm{cms}^{-1}]$	1.266	0.108	0.586
Camera $\mathbf{C}_1$ (spot): no. of regr. coordinates	5505	3087	1112

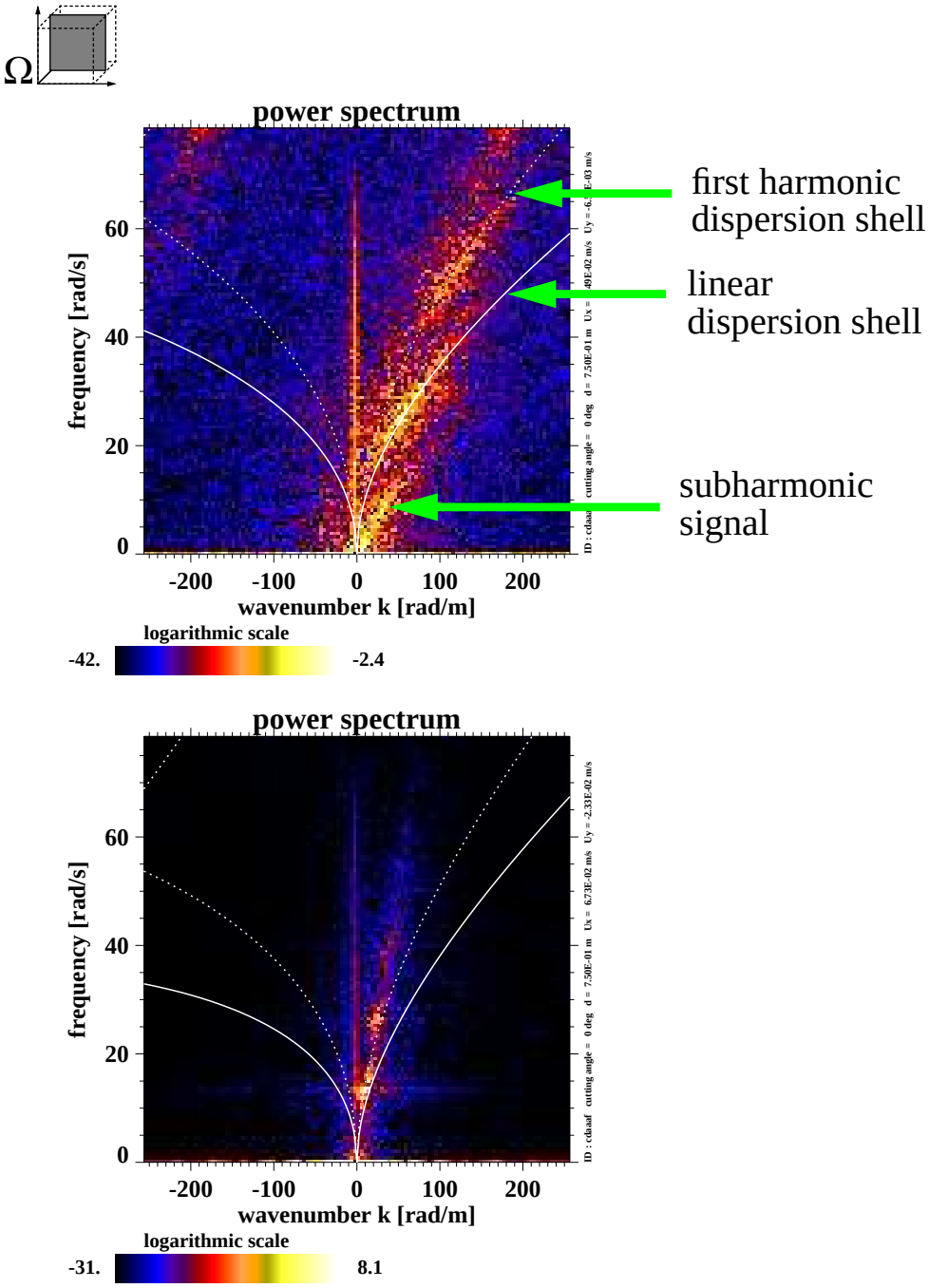

Figure 49: Wind-Wave-Tank: k_x–ω sections of the 3D gray-level variance spectra, acquired by camera $\mathbf{C}_1$ (spot illuminated) for wind speeds of 3 ms^{-1} (top) and 9 ms^{-1} (bottom) on a logarithmic scale. Over the signal, the fitted linear (solid line) and first harmonic (dashed line) dispersion shells are plotted. An increase in the Doppler shift ω_D is indicated by the larger deformation of the dispersion shells for the high-wind speed.

The locations of the fitted linear and first harmonic dispersion relations and the gray-level variance signal overlap consistently.

7.2 Results of the Global Method: CEDEX

7.2.1 Aims and Data Description

In Sec. 7.2.2 global image spectra are be presented and discussed, followed by the presentation of results of a calibration application which was performed by comparing optical-image frequency spectra and wave-gauge frequency spectra.

7.2.2 Image Spectra

An example of image sequences and the belonging optical image spectra is presented and discussed for area A and area B (see Fig. 44).
The parameter settings of the wave generator, associated to the image sequences, are a synthesized JONSWAP frequency spectrum (see Sec. 2.3.3) with a peak period of $T_p = 1$ s, a synthesized directional Mitsuyasu distribution (see Sec. 2.3.4) with a spread parameter of $s = 1$, mean wave travel direction $\vartheta = 30°$, and maximum wave height $\mathrm{H_{max}} = 0.15$ m. The accompanying in situ measurements of the wave gauges S0 – S4 are outlined in Tab. 4.

7.2.3 Analysis and Results: Spectra

The raw 3D Ω_i spectra of the image sequences have been calculated by a 3D FFT (see Sec. 5.2.3). In a 2D k–ω section, depicted in Fig. 50 for area A, of the 3D Ω_i spectrum, $\mathcal{G}_{\mathrm{A}}(\Omega_i)$, the theoretical intrinsic-dispersion relations of the fundamental mode, $\varsigma_0^+(k, \omega, u_x = 0\ \mathrm{ms}^1, u_x = 0\mathrm{ms}^1, d = 0.7\ \mathrm{m})$, and the first harmonic, $\varsigma_1^+(k, \omega, u_x = 0\ \mathrm{ms}^1, u_x = 0\ \mathrm{ms}^1, d = 0.7\mathrm{m})$, are charted. The k–ω section is directed into the mean wave-travel direction, ϑ. The intrinsic fundamental mode and the first-harmonic dispersion curves in the section of the image spectrum match the associated gray-level variance signal. As expected, this conformity indicates the absence of surface currents.
Beneath the fundamental-mode signal, another feature is visible. This signal structure, often called the 'group line' in the radar community [SPM96], may be associated with the group velocity or either the difference wave–wave interactions or the nonlinearities of the imaging process.
In Fig. 51 the filtered and integrated wavenumber spectra, $\mathcal{G}_{0,\mathrm{A}}(\Upsilon_i)$ and $\mathcal{G}_{0,\mathrm{B}}(\Upsilon_i)$, of area A (left) and area B (right) are presented. The filtering is performed over the linear-dispersion relation, $\varsigma_0^+(\Omega_i)$ and the integration is performed over positive frequencies.
The k_x–k_y spectrum, $\mathcal{G}_{0,\mathrm{B}}(\Upsilon_i)$, of the homogeneous case (area B) shows a symmetric directional behaviour consistent with the directional symmetry of the wave generator forcing. Additionally, a second more narrow wave system is visible coming from the direction of the wall construction of area A. This wave system overlays the wave field originally coming from the wave generator. It is obvious that this supplementary wave field is provoked by reflection of the original wave field at that wall construction. This example illustrates

Table 4: Wave heights and periods from wave gauges for the example case (area B, CEDEX Tank) with mean level (mean over all surace elevations H(t)), No. O. (number of observations), Hs (significant wave height), mean H (mean over all wave heights), max. H (maximum over all wave heights), min. H (minimum over all wave heights), RMS H (root-mean-square over all wave heights), σH (standard deviation of wave height), Ts (significant wave period), mean T (mean over all wave periods), max. T (maximum over all wave periods), min. T (minimum over all wave periods), RMS T (root-mean-square over all wave periods), and σ_T (standard deviation over all wave periods)

	S0	S1	S2	S3	S4
mean level	0.001	-0.002	-0.005	-0.004	-0.005
No. O.	677	686	695	703	728
Hs	0.06	0.07	0.08	0.07	0.06
mean H	0.04	0.05	0.05	0.05	0.04
max. H	0.11	0.12	0.13	0.12	0.10
min. H	0.00	0.00	0.00	0.00	0.00
RMS H	0.05	0.05	0.06	0.05	0.04
σ_{H}	0.02	0.02	0.03	0.02	0.02
Ts	0.95	0.95	0.94	0.94	0.93
mean T	0.89	0.87	0.86	0.85	0.82
max. T	1.63	1.60	1.51	1.50	1.43
min. T	0.14	0.13	0.20	0.11	0.19
RMS T	0.91	0.90	0.89	0.88	0.86
σ_T	0.23	0.22	0.22	0.22	0.24

that, in contrast to point-measuring devices, fully directional information can be obtained from image sequences of the water surface.
In contrast to the k_x–k_y spectrum, $\mathcal{G}_{0,\mathrm{B}}(\Upsilon_i)$, the k_x–k_y spectrum, $\mathcal{G}_{0,\mathrm{A}}(\Upsilon_i)$ displays an asymmetric directional distribution of the main wave field coming from the wave generator. Especially for higher wavenumbers the directional distribution tends to asymmetric behaviour. If only geometrical shadowing of the incoming waves due to the wall construction would be taken into account, the asymmetrical behaviour would not show a wavenumber dependency. The loss of gray-level variance – especially for short waves – therefore is a hint that diffraction plays a significant role. Long waves are diffracted into the geometrical-shadow zone and short diffracted wave lose their energy on short spatial scales close to the tip of the wall.

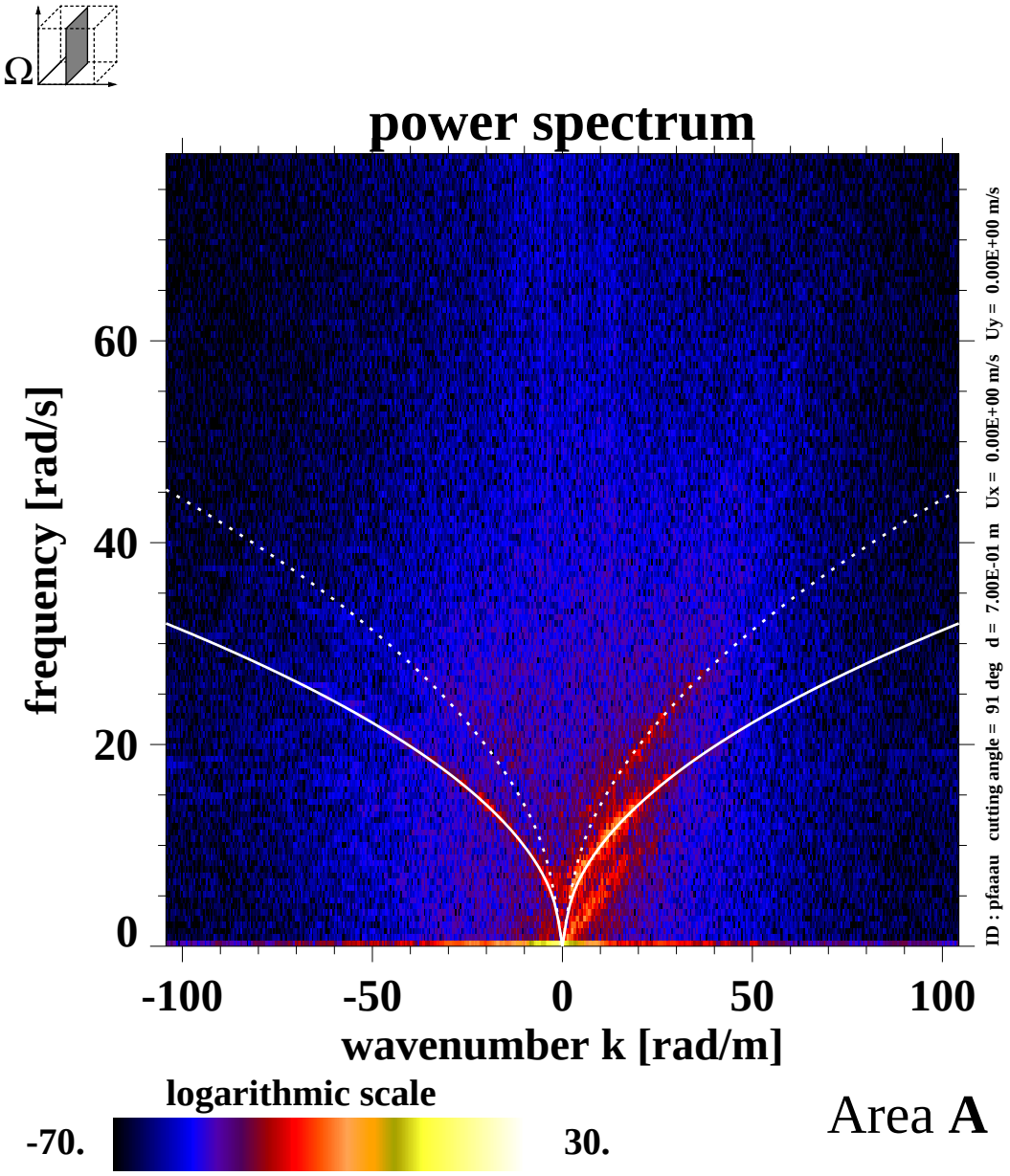

Figure 50: 2D k–ω section of a global gray-level variance spectrum, $\mathcal{G}_{\mathrm{A}}(\Omega_i)$, for CEDEX area A. The solid curve indicates the linear intrinsic dispersion relation, $\varsigma_0^+(k, \omega, u_x = 0\ \mathrm{ms}^1, u_x = 0\ \mathrm{ms}^1, d = 0.7\ \mathrm{m})$, the dashed line indicates the intrinsic first-harmonic dispersion relation, $\varsigma_1^+(k, \omega, u_x = 0\ \mathrm{ms}^1, u_x = 0\ \mathrm{ms}^1, d = 0.7\ \mathrm{m})$.

7.3 Results of the Local Method DiSC: CEDEX

7.3.1 Aims and Data Description

The image sequence used to demonstrate DiSC was acquired in the homogeneous area B. Here the spatial distribution of the hydrographic parameters, to be calculated by the method DiSC, are a priori known and are spatially constant with a given water depth, $d = 0.7$ m, and current, $u_x = 0\ \mathrm{ms}^{-1}$,

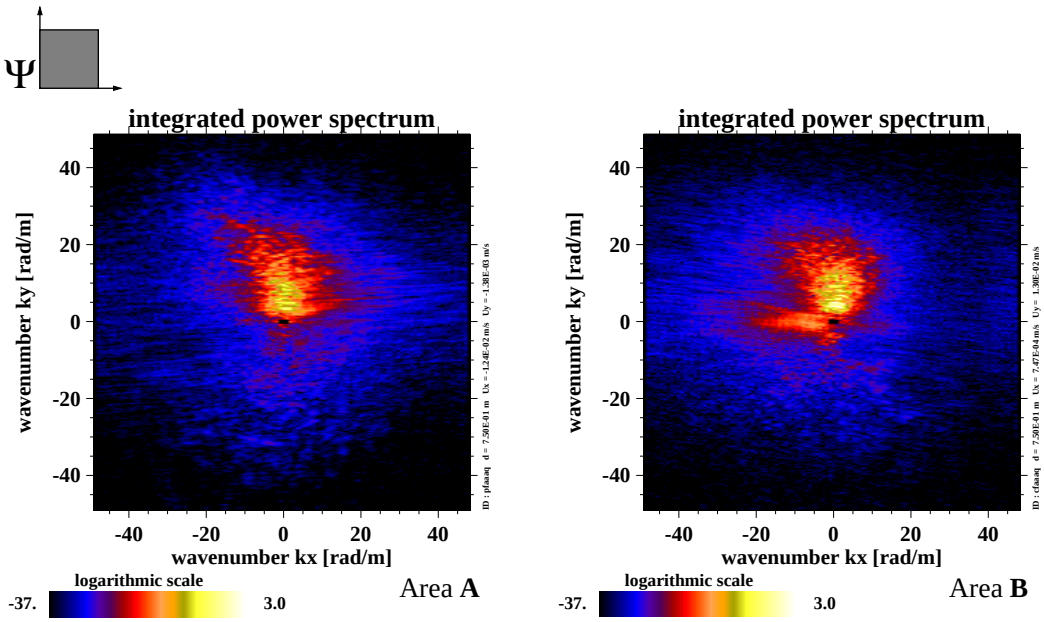

Figure 51: Filtered and integrated directional k_x–k_y spectra, $\mathcal{G}_{0,\mathrm{A}}(\Upsilon_i)$ and $\mathcal{G}_{0,\mathrm{B}}(\Upsilon_i)$, of CEDEX area A (left) and CEDEX area B (right). The 3D spectra, $\mathcal{G}_{\mathrm{A}}(\Omega_i)$ and $\mathcal{G}_{\mathrm{B}}(\Omega_i)$, were filtered by the intrinsic linear dispersion relation, $\varsigma_1^+(k, \omega, u_x = 0\ \mathrm{ms}^1, u_x = 0\ \mathrm{ms}^1, d = 0.7\ \mathrm{m})$. The integration of the filtered spectra, $\mathcal{G}_{0,\mathrm{A}}(\Omega_i)$ and $\mathcal{G}_{0,\mathrm{B}}(\Omega_i)$, is performed over frequency using the linear dispersion relation as a filter.

$u_y = 0\ \mathrm{ms}^{-1}$. Any deviation of the spatial hydrographic-paramter maps, calculated with the method DiSC, from these constant values of water depth and current may give a hint to the limitations and accuracy of DiSC.
For the data set, presented here, the images were transformed from image to world coordinates with the same parameters as given in Sec. 7.2 have been used: number of pixels, $N_x = 512$, $N_y = 512$; spatial grid resolution, $\Delta x = 0.01$ m, $\Delta y = 0.03$ m; and spatial image size $X = 5.12$ m, $Y = 15.36$ m. The 256 images of the sequence were acquired with an acquisition frequency of 6.25 Hz (nominal value) and a measurement duration of 40.96 s (nominal value).
The parameters of the wave generator are as follows: peak period of the wave field, $T_p = 2$; directional spread parameter, $s = 1$; and maximum wave height, $\mathrm{H_{max}} = 0.15$ m.
The first image of the image sequence is presented in Fig. 52 (left-hand side). At the right edge of the analyzed the waves are only partially illuminated by the illumination source (i.e. the reflector), resulting in strong modulation. The temporally averaged image (see Fig. 52, right-hand side) depicts the illumination pattern. An illumination gradient is established perpendicular to the camera pointing direction (from right to left). The lower-left corner of the area is only weakly illuminated. The areas of the images covered by the groung control points and the wave gauges are excluded from the local analysis by a binary mask. For the blockwise DiSC calculation (see

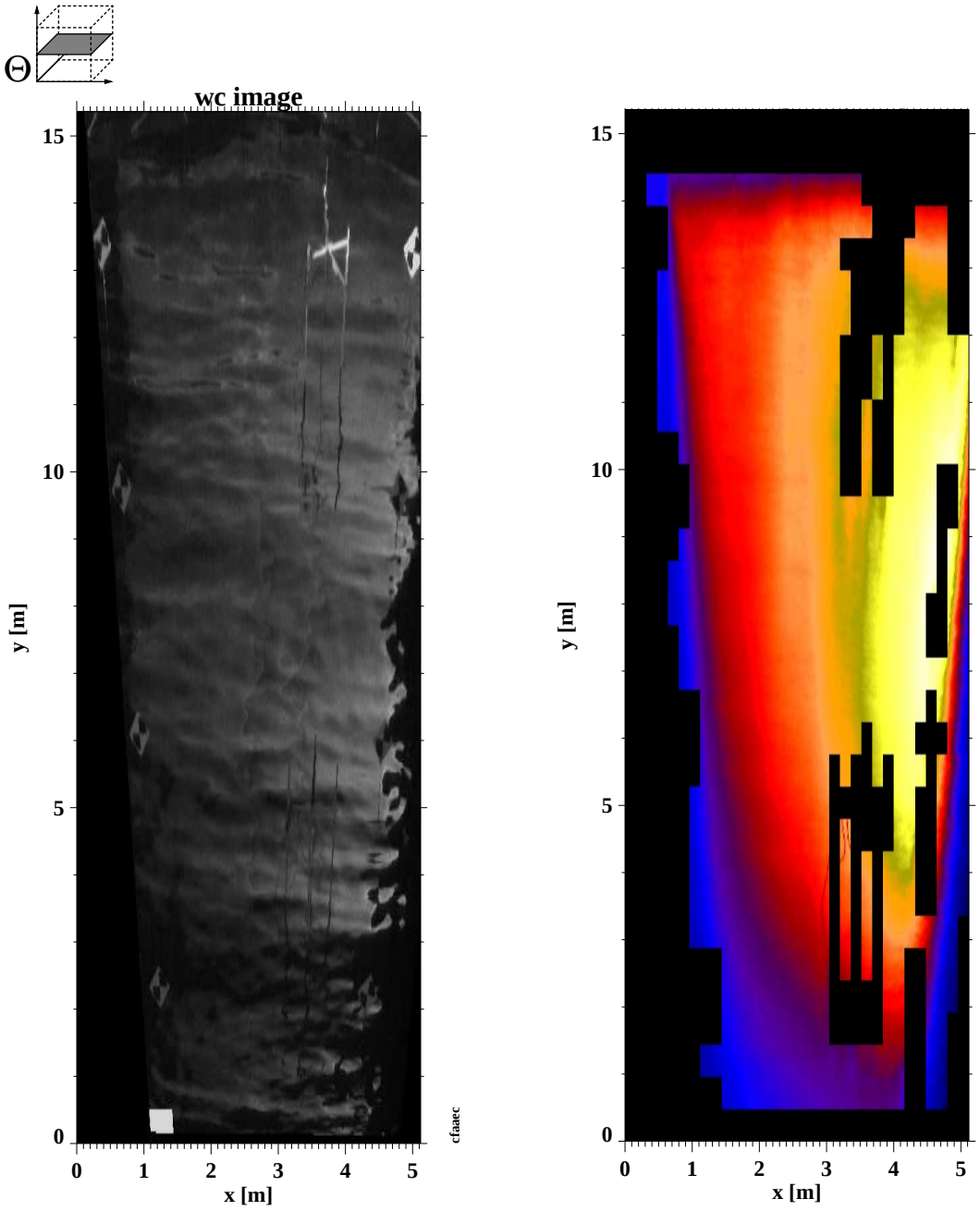

Figure 52: CEDEX Tank: first image and averaged image of a sequence acquired in area B (left), temporally averaged image sequence (right). The wave gauges and the ground-control points are excluded from the analysis by a binary mask.

Sec. 5.3.8) blocks of 16 (N_{xe}) × 16 (N_{ye}) pixels are chosen with a spatial dimension of 0.16 m (X_e) × 0.48 m (Y_e).

7.3.2 Results: Global Spectra

A 2D k–ω section of the 3D global gray-level variance Ω_i spectrum is presented in Fig. 53. The intrinsic dispersion relations of the fundamental

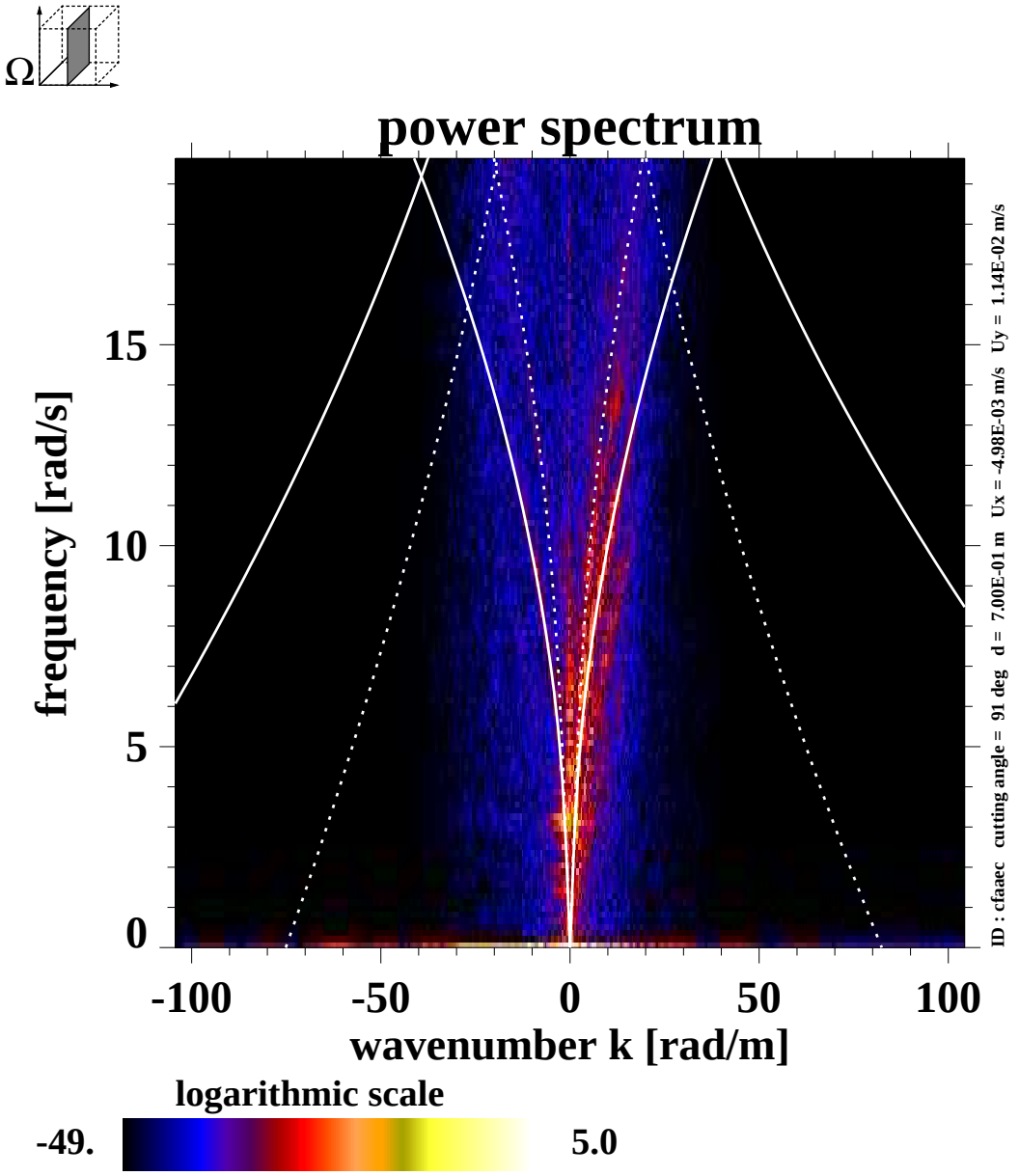

Figure 53: CEDEX Tank: 2D k–ω section of the 3D global Ω_i spectrum. The linear dispersion shell (——), $\varsigma_0^+(\vec{k}, d)$, and the first-harmonic dispersion shell (- - - - -) are indicated.

mode, $\varsigma_0^+(\vec{k}, d)$, and of the first harmonic, $\varsigma_1^+(\vec{k}, d)$, are indicated, so are their temporally aliased dispersion shells. The spectral gray-level variance of the wave-field is located close to the ω axis. The reason for this fact is the limited size of the CEDEX Tank, and therefore the cameras viewing area covers only a few of the wavelengths, especially of the long waves. The signal's closeness to the ω axis implies that the Gabor-filter bins will cover only a few spectral pixels with a coarse resolution. A 2D Υ_i plane of the 3D global Ω_i spectrum is presented in Fig. 54. The 2D Υ_i plane is dissected at a frequency of 7.21 rad s^{-1}, where the peak of the fundamental mode signal is located. The signal peak is located on the intrinsic dispersion relation, $\varsigma_0^+(\vec{k}, d)$. To the

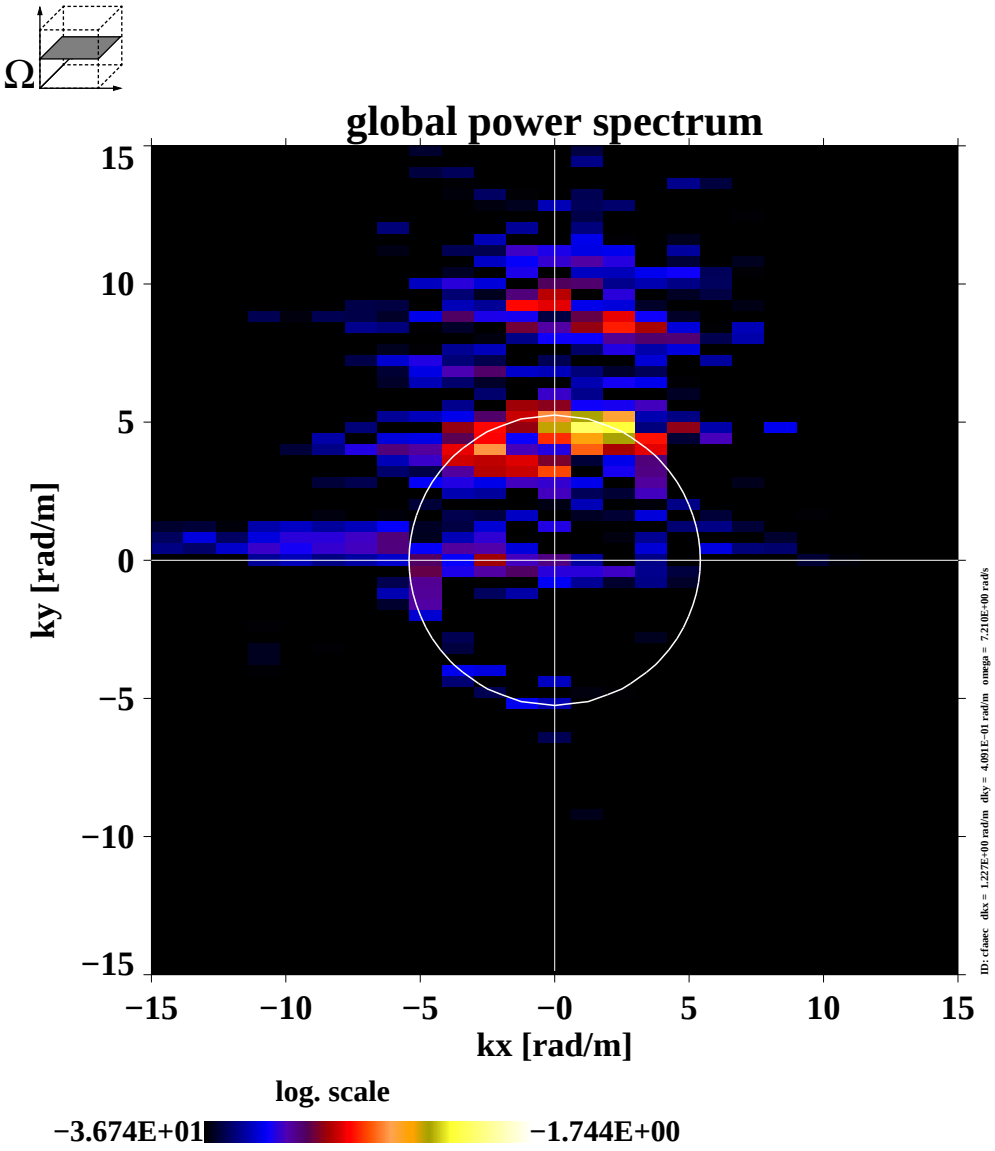

Figure 54: CEDEX Tank: 2D Υ_i plane of the 3D global Ω_i spectrum at a constant frequency of $\omega = 7.21$ rad s^{-1}.

2D Υ_i plane at constant frequency, $\omega = 7.21$ rad s^{-1}, in Fig. 54, the Gabor-filter design (see Sec. 5.3.5) is applied. The Gabor-filter bank is presented in Fig. 55. Spectral Gabor filtering is demonstrated in Fig. 56 for a single Gabor-filter bin; the Υ_i plane, the single Gabor filter with filter direction $\phi = 11.25°$, and the filtered signal are shown.

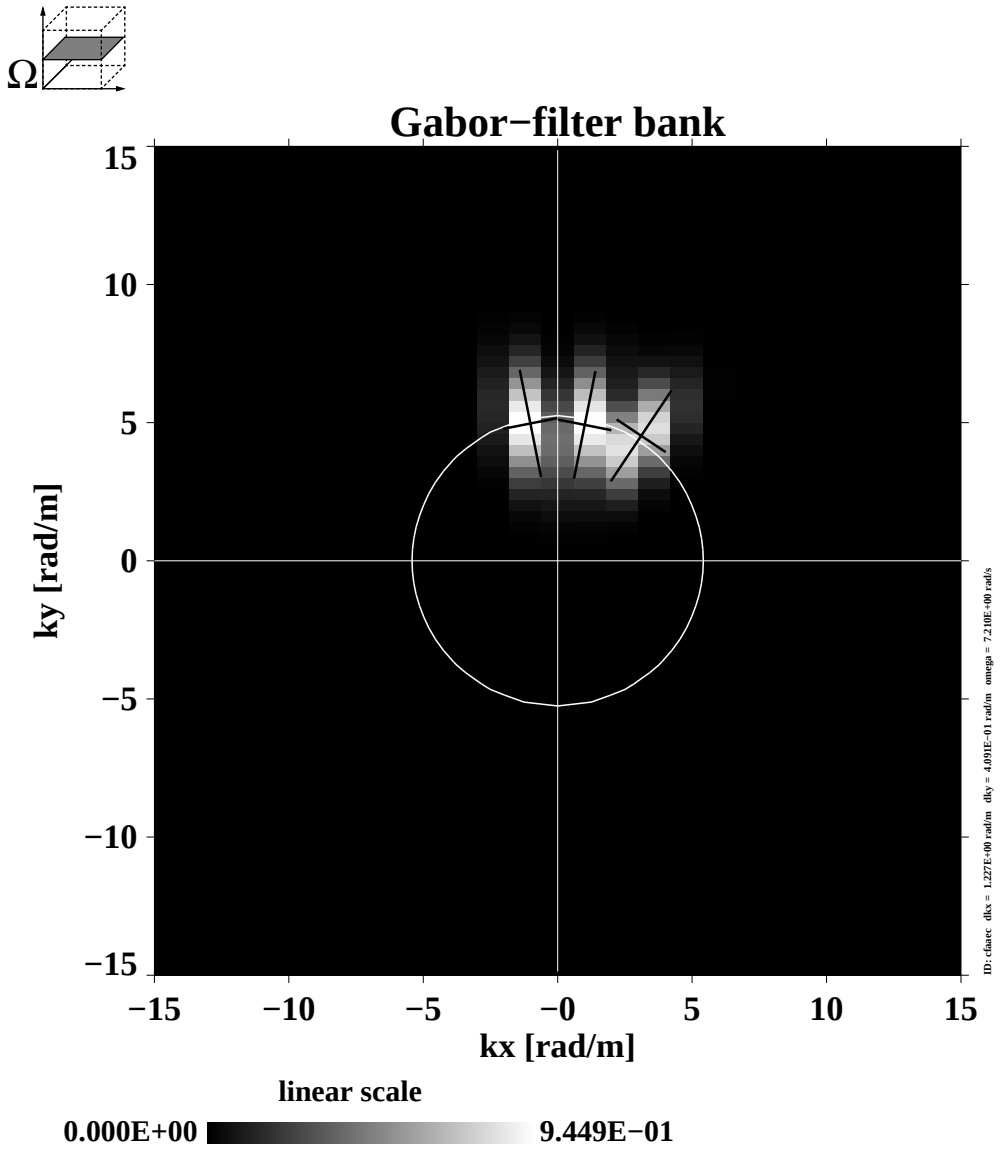

Figure 55: CEDEX Tank: example of a Gabor-filter bank in a Υ_i plane at constant frequency of $\omega = 7.21$ rad s^{-1}. The locations of the Gabor filters are indicated by their main axes, the gray-level indicates the Gabor MTF. The intersection line of the Υ_i plane with the dispersion shell is outlined (white circle).

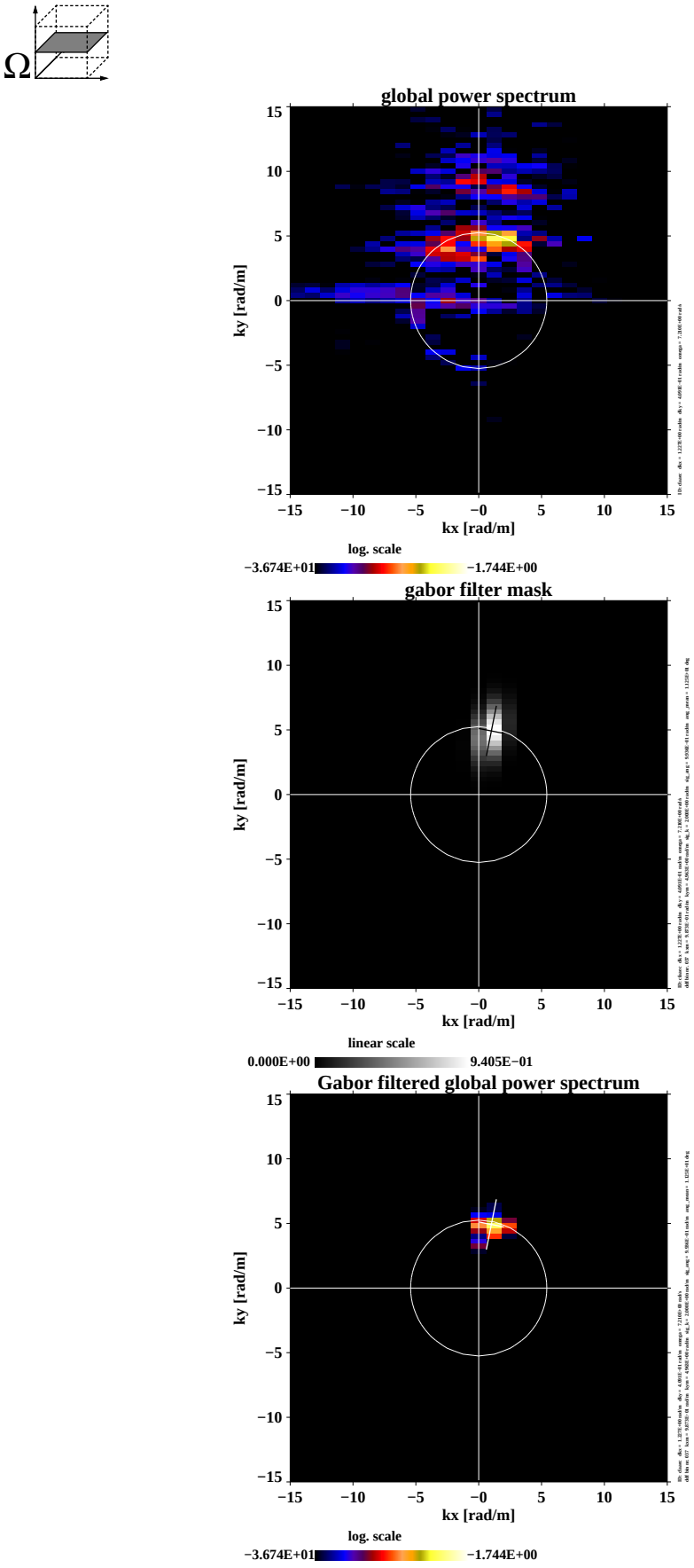

Figure 56: CEDEX Tank: spectral Gabor filtering. Top: unfiltered Υ_i plane of the global 3D Ω_i spectrum; centre: spectral Gabor-filter mask; bottom: a selected spectral bin.

7.3.3 Results: Spatial Maps

The spectral Gabor-filtered bin is transformed to the spatial domain by a 2D FFT^{-1} (see 5.3.6) yielding a complex-valued one-component image of constant frequency. In Fig. 57 local-phase maps and gray-level variance maps of the Gabor-filtered signal, and the gradients are presented. The local-phase maps indicate, as expected, a phase shift between the complex-valued images and the gradient images. The variance images indicate that the modulation signal is high at the bottom part of the images. This pattern is representative for all one-component images. This result indicates that the ITF, in particular the coefficient α, is inhomogeneously distributed, still considering that the condition of a homogeneous wave field holds. The upper part of the analyzed images is weakly illuminated. In weakly illiminated areas (this holds especially for nautical-radar results) the background noise seems to lead to phase singularities (i.e. forks in the phase pattern). These singularities also seem to appear more often close to the boundaries of the analyzed areas. The black cross in the center of the maps indicates the spatial resolution of the Gabor filter, utilized for spectral selection. The spatial resolution is deduced from the radial and azimuthal bandwidth of the Gabor filter by the uncertainty relation.
In Fig. 58 histograms which are calculated from complex-valued spatial maps and gradient maps of the Gabor separated wave field ($\omega = 7.21$ rad s^{-1}, $\phi = 11.25°$) are presented. The real and imaginary parts of the complex-valued gray-level amplitude show a sharp peak at the mean value of 0. The histograms are not Gaussian distributed as expected for natural waves. For a natural sea state, the real and imaginary parts of the local amplitude should be Gaussian distributed. Here, only a few bins of the global spectrum are selected by the Gabor filter. Therefore the reconstructed complex-valued gray-level amplitudes of the one-component images are expected to be non-Gaussian distributed. For a single sine wave, as well as for a Gaussian wave field, the local phase should be equally distributed. In contrast a small, but significant deviation from the expected equal distribution is observed. This behaviour do not occur in nautical-radar cases (not presented in this work) where the phases are equally distributed. Up to now the nonequal distribution is an open question. In Fig. 59 spatial maps of the local-wavenumber components, $k_{x,l}$, $k_{y,l}$ and the local-wavenumber modulus are presented, indicating a first impression of the inhomogeneous spatial distribution of the local wavenumbers. The maps are calculated pixelwise (see Sec. 5.3.7) and blockwise (see Sec. 5.3.8) showing the same spatial behaviour. In Fig. 60 spatial maps of the local-bandwidth components, given by the normalized gradient of the local amplitude (see Sec. 5.3.7), and the modulus are presented. The bandwidth maps quantify the degree of spatial inhomogeneity.
In Fig. 61 maps of the blockwise calculated confidence $1 - \mathcal{C}$ and local wavelength (arrows, mapped on the phase pattern) are presented. The confidence is close to 1. Therefore, the confidence $1 - \mathcal{C}$ is presented on a logarithmic scale: a small value [dB] represents high confidence. The wave-travel direction is resolved without 180° ambiguity; the convention is 'coming from'.

Fig. 62 demonstrates the correction of the local power by applying the inverse Gabor-filter ITF on the spatial gray-level variance map. The Gabor-filter correction contributes to the gray-variance conservation to a certain degree. Up to now the overlap of several Gabor-filter bins has not been considered.
In Fig. 63 histograms of the local-wavenumber and bandwith components are presented. The histograms indicate the scatter of the wavenumbers and wavenumber components determined, and of the bandwidths and bandwidth components for pixelwise and blockwise calculation. The means and the standard deviations, retrieved from pixelwise calculation, do not differ from those retrieved by the blockwise calculation. The standard deviation of the wavenumbers and wavenumber components are on the order of ca 0.2 to 0.25 rad m^{-1}. The bandwidth, indicating the local inhomogeneity, is on the order of 0.35 rad m^{-1} to 5.5 rad m^{-1}.
In Fig. 64 a histogram of the confidence is outlined. The mean of $1 - \mathcal{C}$ on a logarithmic scale is -33 dB, corresponding to a confidence level of $\mathcal{C} = 0.9995$. In Fig. 65 the distributions of local-wavenumber vectors and local-bandwidth vectors of one-component image with a frequency of $\omega = 7.21$ rad s^{-1} and a mean-filter direction of $\phi = 11.25°$ are presented in the 2D Υ_i domain, both for the pixelwise calculation and for the blockwise calculation. For the pixelwise calculation the distibution of the local-wavenumber and bandwidth vectors in the 2D Υ_i domain is represented as a colour-coded density function. For the blockwise calculation the vectors are represented as single points in the 2D Υ_i domain. The plots indicate that the scatter of the calculated wavenumbers is smaller than the Gabor-filter width. This is a convincing indicator of the consistency of the method. Another feature observed in the scatter plots is the non-Gaussian distribution. There seems to exist an at-present unexplained systematic distribution maybe of the data set or of numerical origin.
In Fig. 66 the accuracy of the local-wavenumber vector fit as a function of confidence, represented logarithmically as $1 - \mathcal{C}$ [dB], is outlined. The error for the estimation of the local wavenumber k is calculated as follows: The frequency, corresponding to the one-component image, is used to calculate the local wavenumber, using the intrinsic dispersion relation with a water depth of $d = 0.7$ m. Assuming the dispersion relation to be valid on a local spatial scale, this value is exact, and can be used as a reference for the error calculation. The normalized and absolute confidences are charted. The plot is used to obtain an overview of the scatter in order to discriminate badly determined wavenumber vectors from reliable vectors. The relative error amounts to ca 0.1, i.e. 10%, and the absolute error has the magnitude 0.5 rad/m. The distribution of the error is scattered inside of this limit; only a few outliers occur. The lower the confidence, the larger the error of the outliers. Therefore, for further calculation of the current and water depth maps, the exclusion condidence is set to a value of 0.998. Although the density of the outliers is low, the inclusion of these outliers results in a failure of the current-depth fit. Therefore, they are excluded by a high confidence threshold close to 1.
In Tab. 5 the wavenumber resolution of the global- and the local-analysis

Table 5: Wavenumber resolution of the global- and local analysis methods.

Method	Area	Resolution	Magnitude [rad/m]
Global	Image	Δ_{kx}	1.23
Global	Image	Δ_{ky}	0.41
Global	Block	Δ_{kx}	39.27
Global	Block	Δ_{ky}	13.09
Local	block	σ_k	0.5

methods are compared. Although the local-analysis area (the whole analysis area) is a factor of 32×32 smaller than the global-analysis area, the wavenumber resolution is comparable. If hypothetically the global-analysis method were performed on an area of the block size, the wavenumber resolution would be much coarser compared to the local-analysis method.
In addition to the validation of the local wavenumbers, the CEDEX data set was used to validate current and water depth. During the experimental setup no current was apparent (apart from a possible wave-induced current) and the water depth was $d = 0.7$ m. Maps of the water depth and the near-surface current were calculated using the method described in Sec. 5.3.11. Firstly, the threshold of confidence was chosen to be $\mathcal{C} = 0.95$ ($1 - \mathcal{C} = -13\,dB$). For this case a failure at 80% of the analyzed blocks occurs: the water depth is calculated with a value of $d > 2$ m, i.e. the deep-water solution was found. The reason is the occurrence of outliers of the local wavenumber, if the phase pattern contain singularities (forks in the phase pattern). In Fig. 66 it is shown that the outliers can be suppressed using a high threshold of confidence. In Fig. 67 maps and histograms of the water depth and the near-surface current retrieved by using a threshold value of $\mathcal{C} = 0.9988$ ($1 - \mathcal{C} = -29.2$ dB) are shown. No systematic error occurs for the calculated values of the hydrographic parameters, except for the water depth in the bottom-left part of the image ($x_e = 2.5$ m, $y_e = 1.5$ m). This area is only weakly illuminated. Therefore a clear wave pattern, bearing the information about the hydrographic parameters, is absent. The spatial variabilities of the estimated parameters are $u_x = 0.029$ ms^{-1} $\pm$ 0.030 ms^{-1}, $u_y = 0.014$ ms^{-1} $\pm$ 0.016 ms^{-1}, and $d = 0.757$ m $\pm$ 0.181 m, i.e., the estimated values fall inside the error bounds of the a priori known values of the current and water depth.
Information about the local gray-level variance, the wavenumber vector, the bandwidth vector, and the frequency is summarized in a local Ω_i spectrum. A 2D Υ_i plane ($\omega = 7.210$ rad s^{-1}) from the center of the analyzed area (x_m = 2.64 m, $y_m = 7.92$ m) is shown in Fig. 68. The intersection line (white) with the dispersion shell is depicted. The wavenumber vectors, clustered close to the dispersion shell, are represented as circles in the 2D Υ_i plane. The gray-level variance is colour -coded, and the diameter is a measure of confidence (the outer green ring corresponds to $1 - \mathcal{C} = -40$ dB and the

diameter 0 corresponds to $1 - \mathcal{C} = -10$ dB). Underlayed as a gray-level plot is the Gabor-filter bank, used for the decomposition of the 3D global Ω_i spectrum. As expected, the estimated local-wavenumber vectors fit into the bandwidth of the Gabor filters. The local bandwidth vectors, equal to the normalized gradient of the local amplitude, are depicted by green arrows. The same representation is chosen to display the local 2D integrated k_x–k_y spectrum (see Fig. 69) from the center of the analyzed area. Because the wavenumber vectors are estimated by a regression algorithm, the spectral power is representated irregulary in the Υ plane. In contrast to the 2D global k_x–k_y spectrum, additional information is available about the local bandwidths of the components.

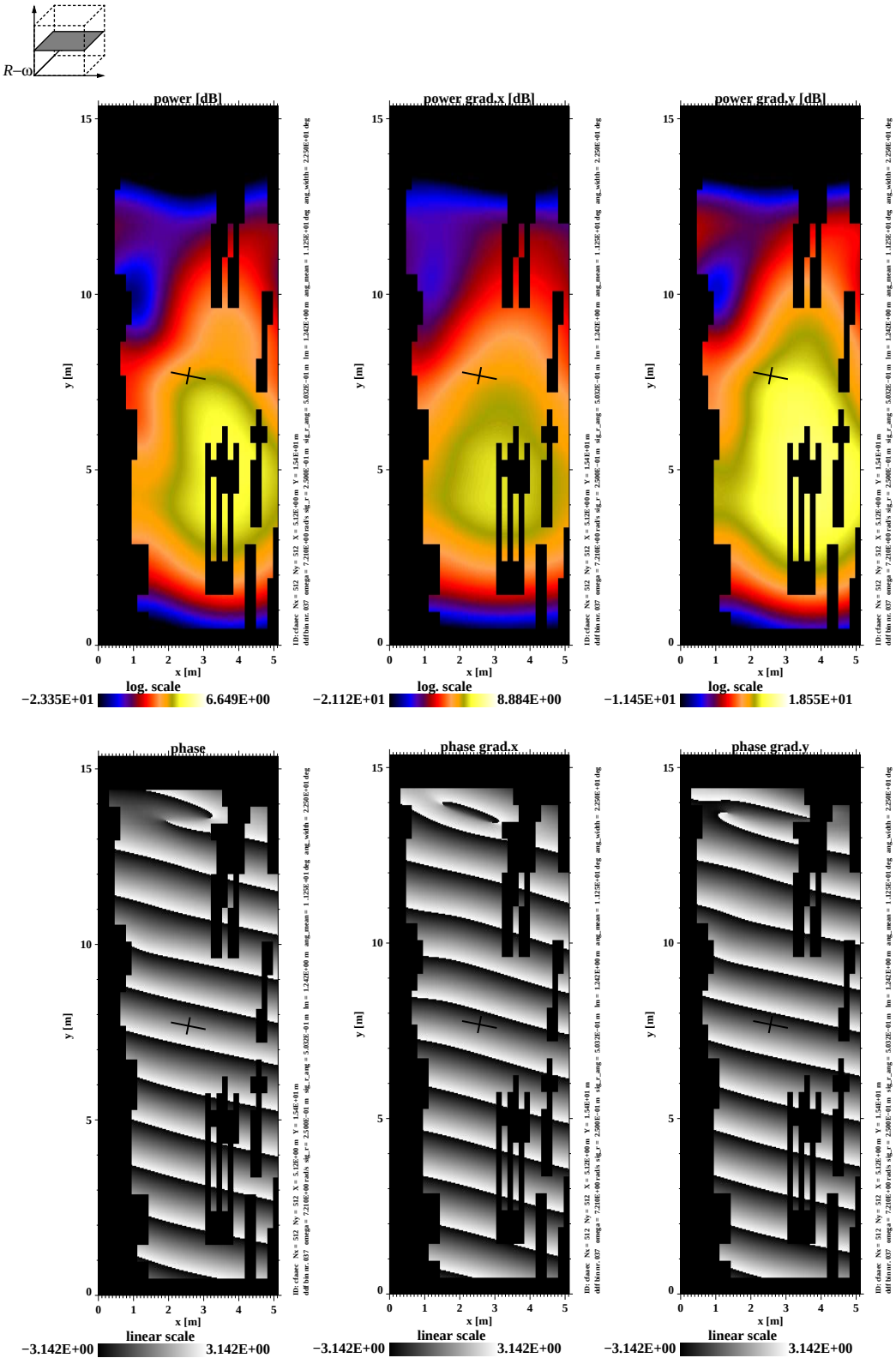

Figure 57: CEDEX Tank (area B): Complex-valued spatial maps and gradient maps of the Gabor-separated wave field ($\omega = 7.21$ rad s^{-1}, $\phi = 11.25°$): complex-valued map, $\hat{G}$ (left), gradient map, $\hat{G}_x$ (center), and gradient map, $\hat{G}_y$ (right). For $\hat{G}$, $\hat{G}_x$, and $\hat{G}_y$, the gray-level variance maps are presented in the top row and the phase maps are depicted in the bottom row. The black cross in the center of the presented maps indicates the spatial representations of the utilized spectral Gabor-filter bin $\Delta r_a = (2\sigma_a)^{-1} = 0.54$ m and $\Delta r_r = (2\sigma_r)^{-1} = 0.25$ m.

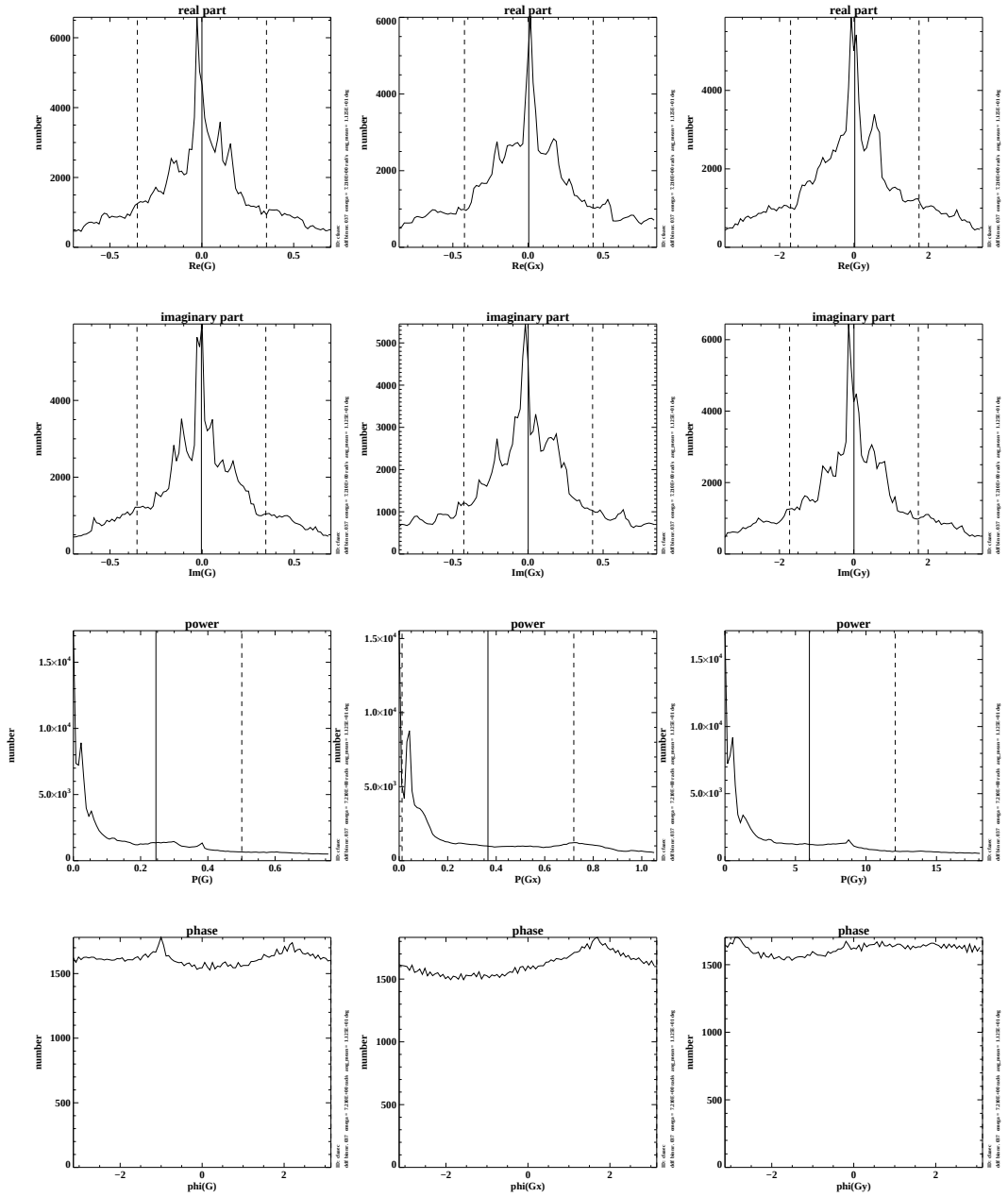

Figure 58: CEDEX Tank, area B: histograms of complex-valued spatial maps and gradient maps of the Gabor-separated wave field (ω = 7.21 rad s^{-1}, ϕ = 11.25°) for the complex-valued map, $\hat{G}$, gradient map, $\hat{G}_x$, and gradient map, $\hat{G}_y$ (from left to right); calculated from the real part, the imaginary part, the power, and the phase (from top to bottom).

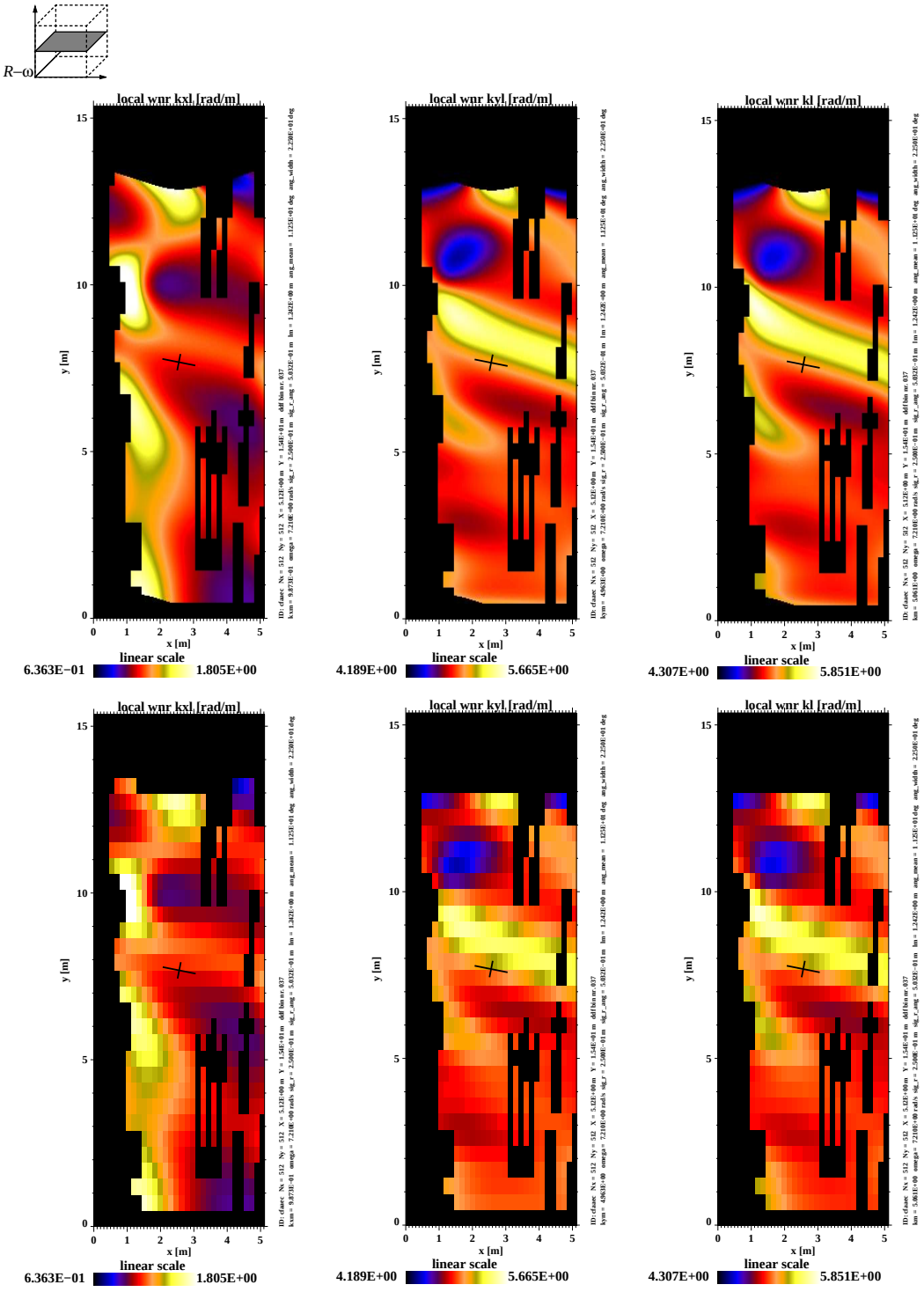

Figure 59: CEDEX Tank, area B: spatial maps of local wavenumber; x-component (left), y-component (center), and modulus (right) of the local wavenumber vector; pixelwise calculation (top) and blockwise calculation (bottom).

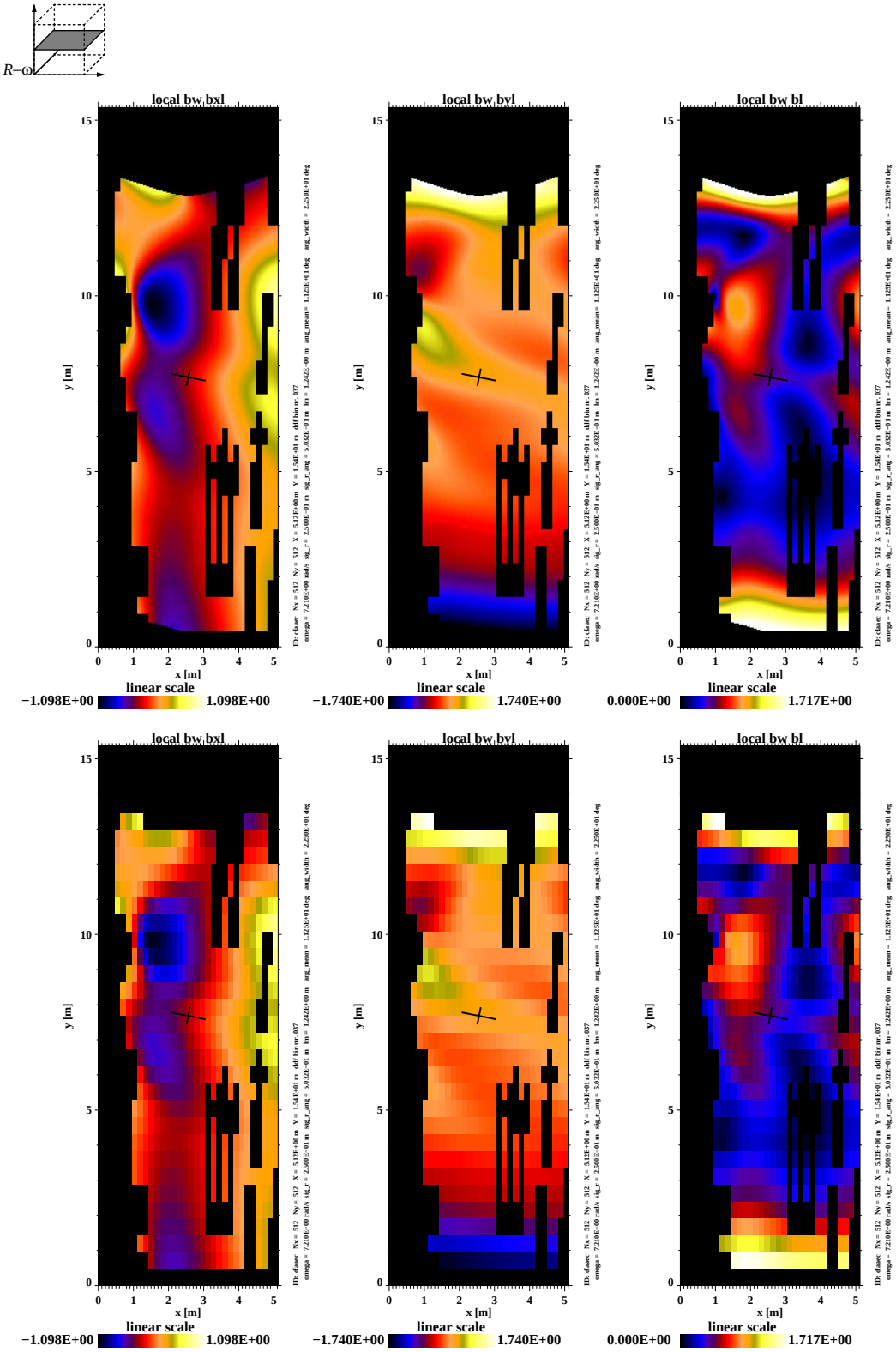

Figure 60: CEDEX Tank, area B: spatial maps of the local bandwidth; x-component (left), y-component (center), and modulus (right) of the local bandwidth vector; pixelwise calculation (top) and blockwise calculation (bottom).

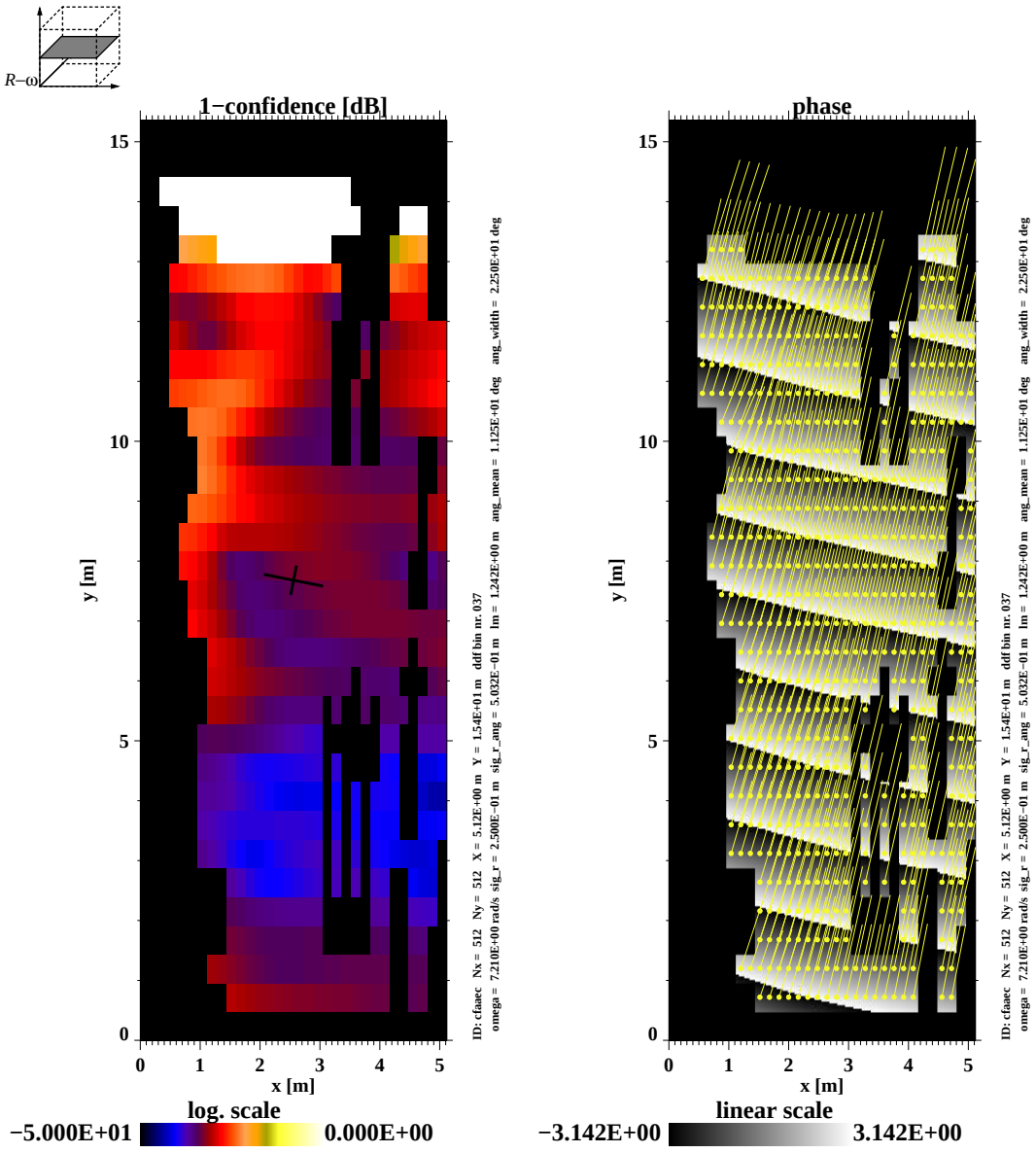

Figure 61: CEDEX Tank, area B: spatial maps of confidence parameter, $1-\mathcal{C}$, on a logarithmic scale and local wavelength arrows mapped on the respective phase pattern. The wave-travel direction has the convention 'coming from'.

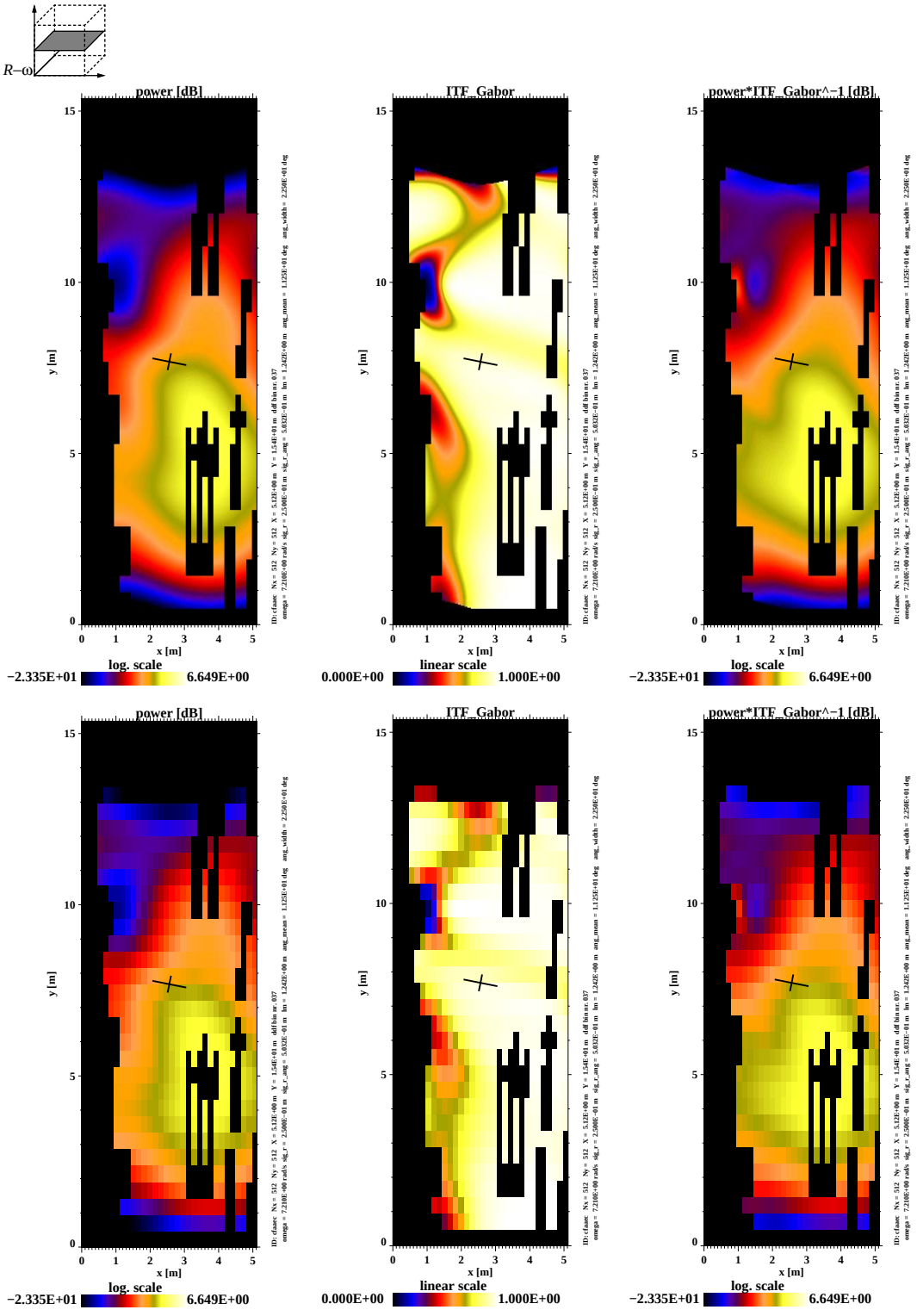

Figure 62: CEDEX Tank, area B: correction of local power by applying the inverse Gabor-filter ITF; uncorrected gray-level variance map (left), local gray-level variance of the Gabor filter's ITF (center), and corrected power map (right); pixelwise calculation (top) and blockwise calculation (bottom).

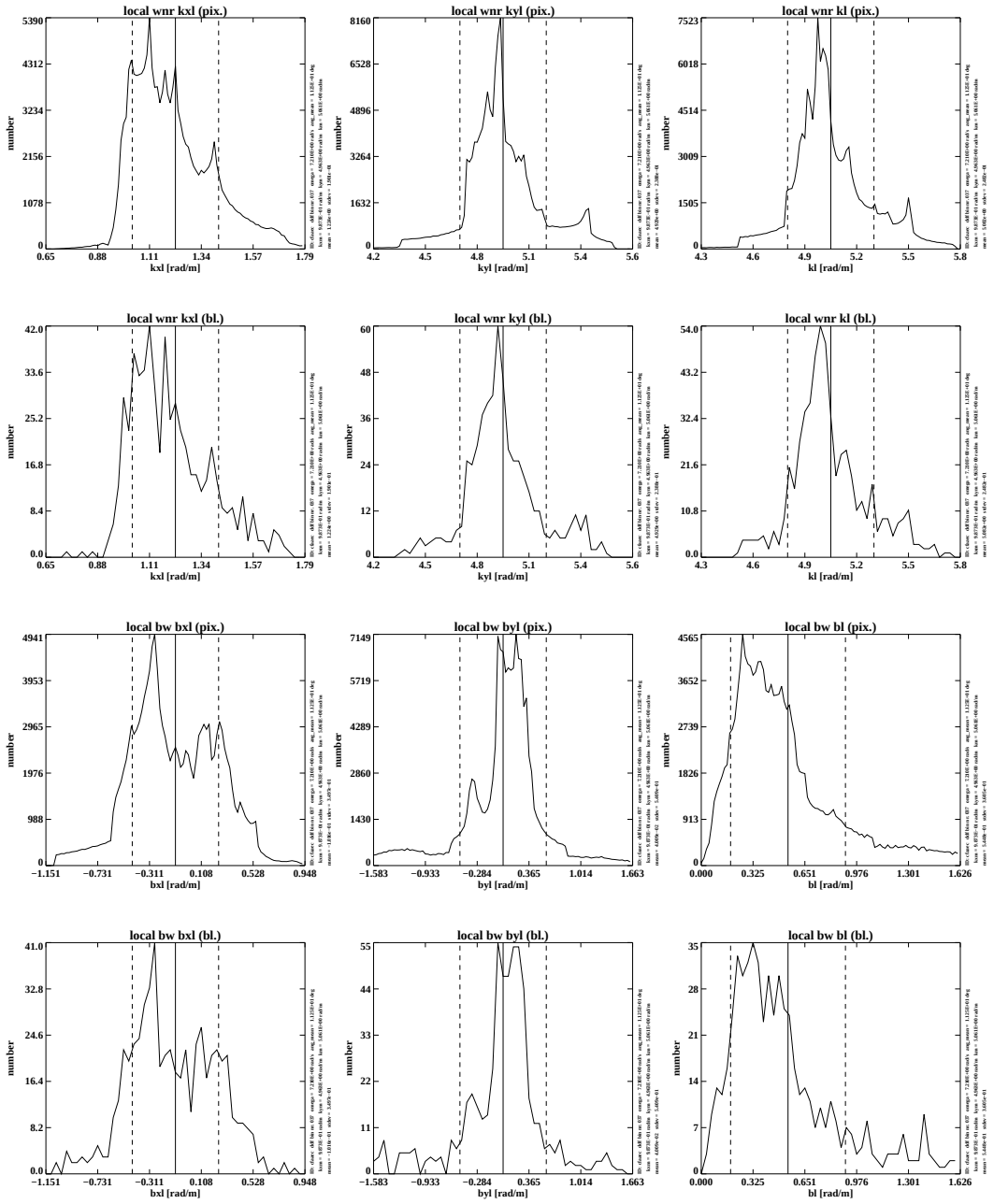

Figure 63: CEDEX Tank, area B: Histograms of local-wavenumber and bandwidth components; local wavenumber calculated pixelwise (first row), local wavenumber calculated blockwise (second row), local bandwidth calculated pixelwise (third row), and local bandwidth caclulated blockwise (fourth row); x-component (left), y-component (center), and modulus (right).

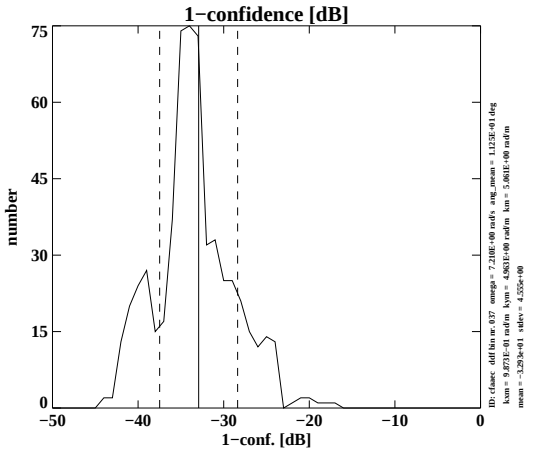

Figure 64: CEDEX Tank, area B: histogram of $1 - \mathcal{C}$ [dB].

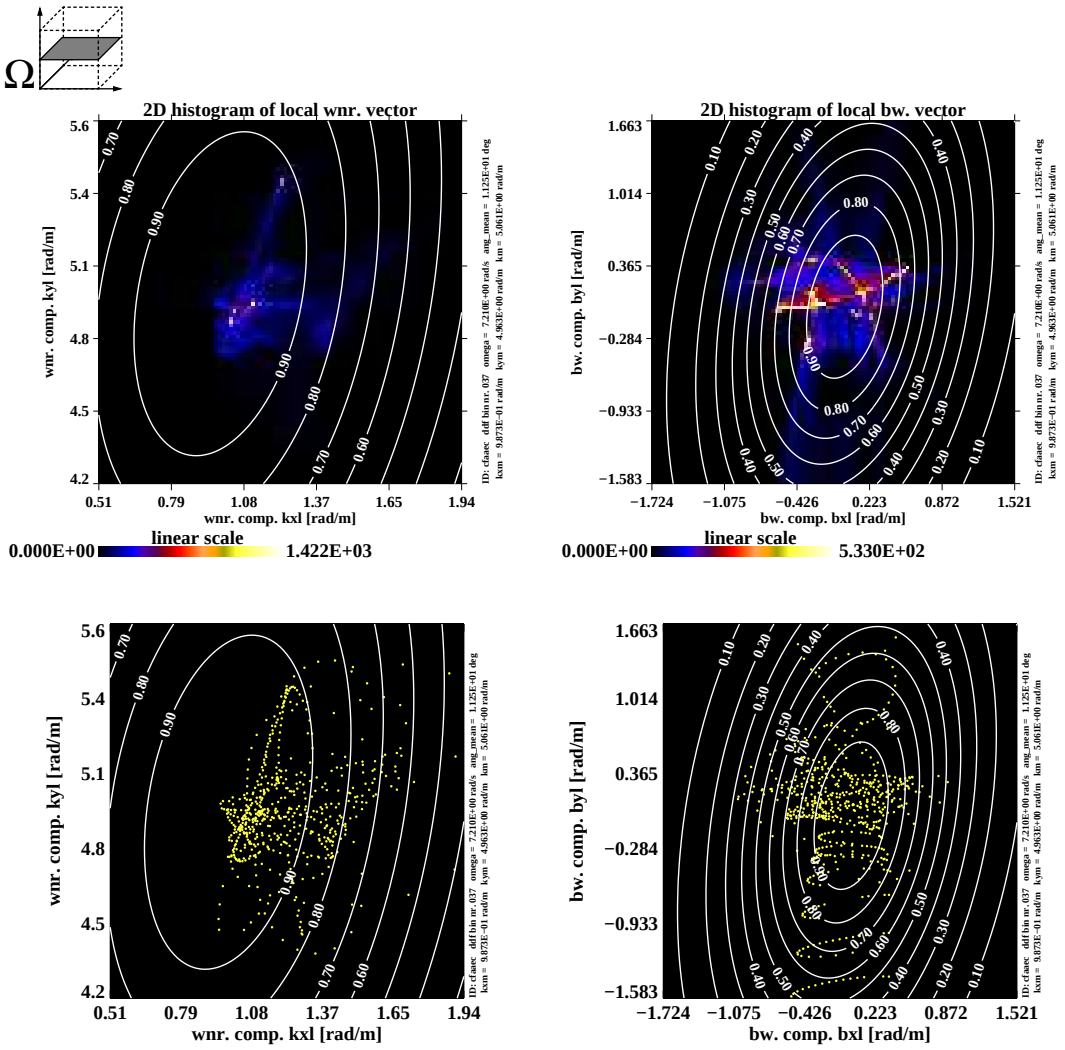

Figure 65: CEDEX Tank, area B: distributions of local wavenumber vector (left) and bandwidth vector (right); pixelwise calculated (top; represented as colour-coded density) and blockwise calculated (bottom; represented as individual dots). Overlayed are the contour lines of the Gabor-filter bin, performed to select the corresponding signals. The Gabor filter is centered at $\vec{k}_m$ for the wavenumber vector distibution, and at the wavenumber coordinate origin for the bandwidth vector distribution.

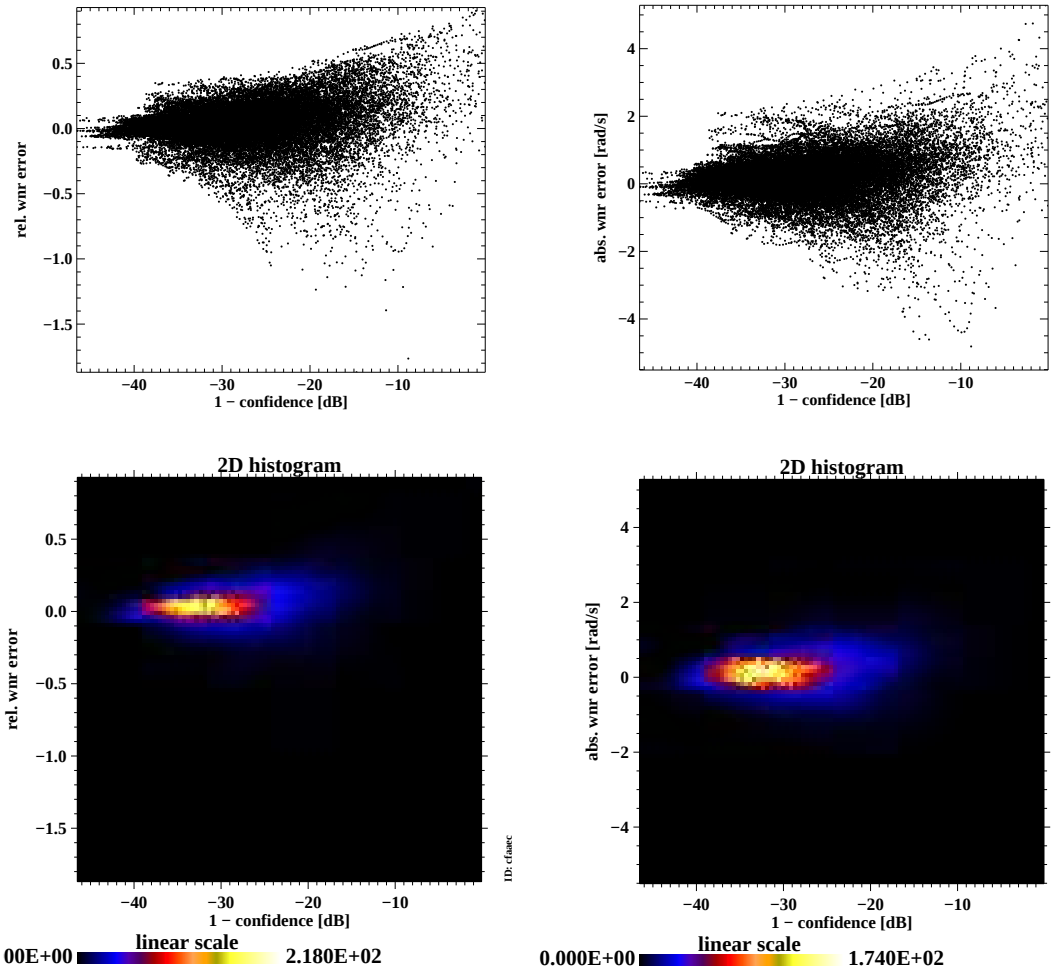

Figure 66: CEDEX Tank, area B: accuracy of the local-wavenumber fit as a function of confidence: scatter plot (top) and 2D dot density (bottom); normalized (left) and absolute (right) wavenumber error. The value $1 - \mathcal{C}$ is depicted on a logarithmic scale. On this scale, the threshold of confidence set for the current-depth fit is -29.1 dB.

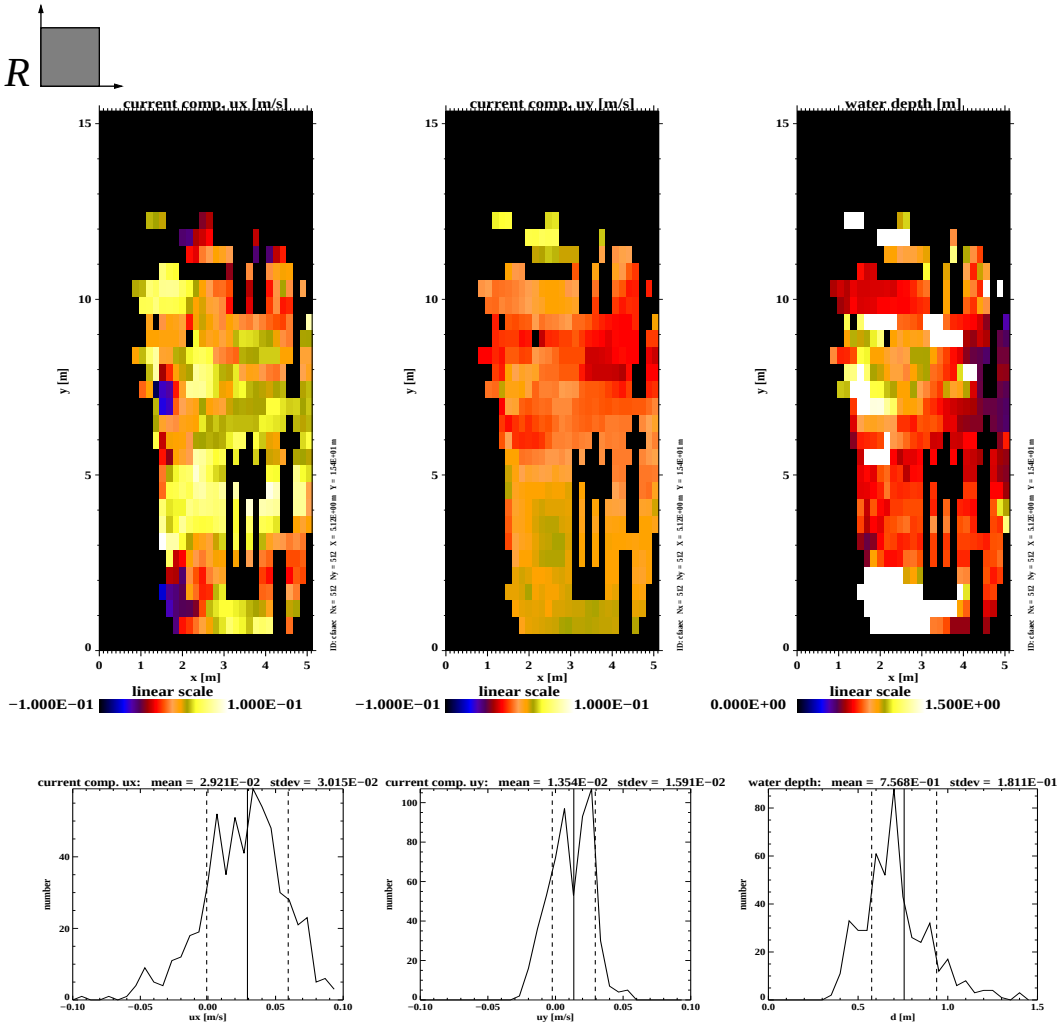

Figure 67: CEDEX Tank, area B: Results of current-depth regression. Maps (top) and histograms (bottom) of the near-surface current and the water depth. The threshold of the utilized confidence is $\mathcal{C} = 0.9988$.

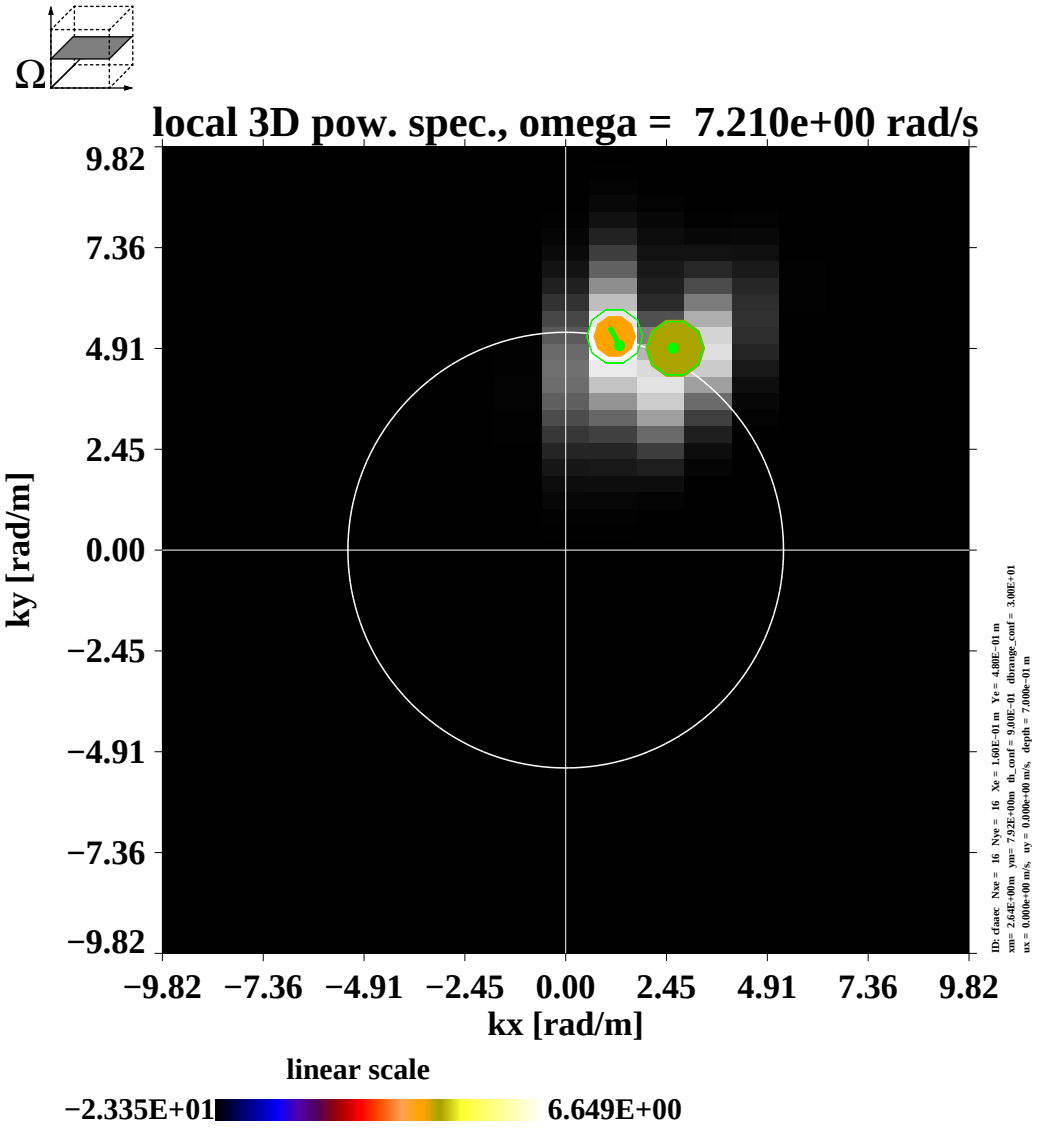

Figure 68: 2D Υ plane of a local 3D image Ω_i spectrum.

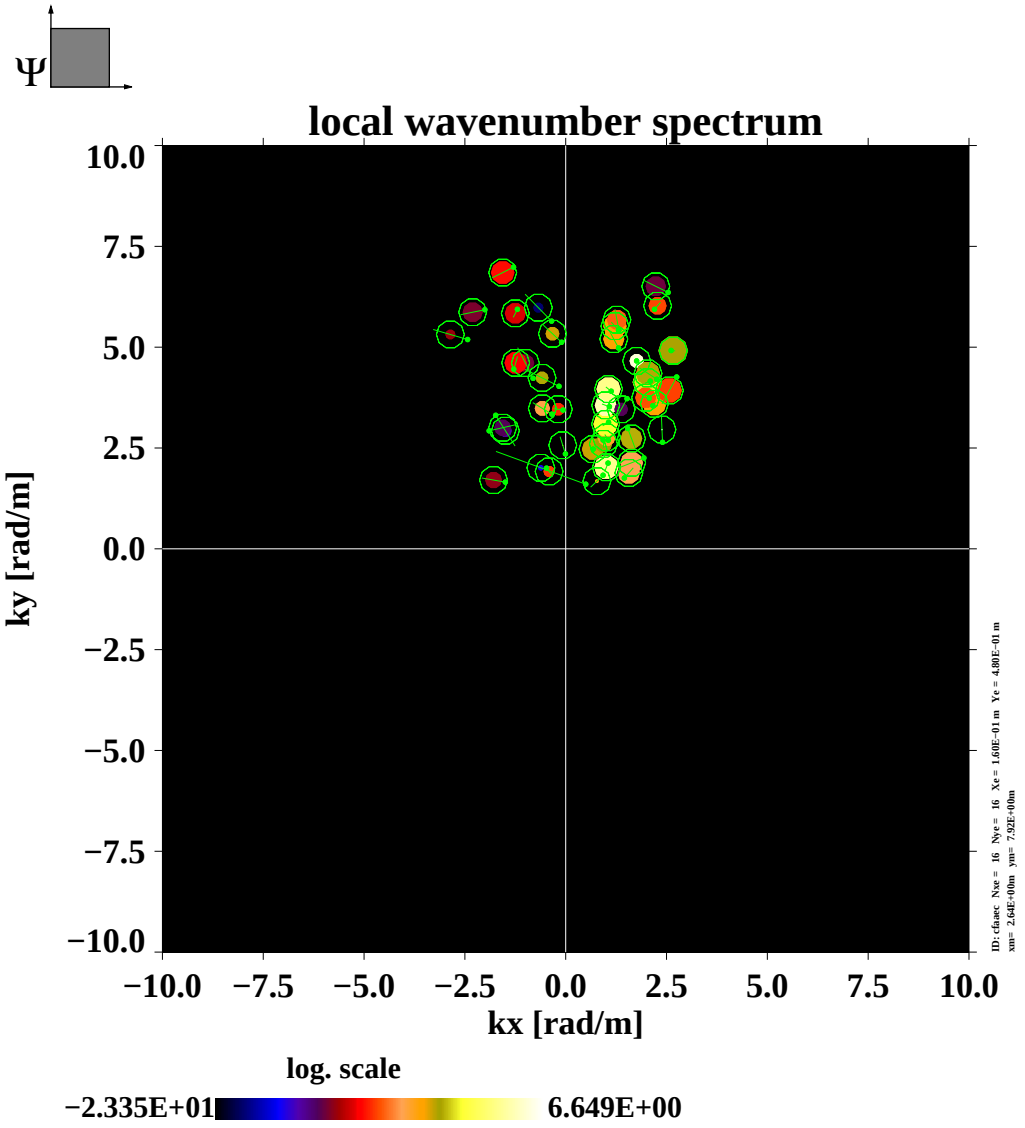

Figure 69: CEDEX Tank, area B: local 2D integrated k_x–k_y spectrum.

7.4 Results: Sylt Radar Image Sequences

The potential of the image-sequence analysis method DiSC for coastal monitoring purposes is shown by a nautical-radar based wave measurement. The image sequence was taken during the storm surge from 4 to 5 February 1999 at the experimental site Sylt List/West. The polar radar images cover a radius of $\approx$ 2 km, and the duration of the measurement was $\approx$ 8 min. For the analysis the image sequence was interpolated on a Cartesian grid (see Tab. 6). The first image of the sequence, which is presented in Fig. 70, indicates that the sea state is characterized by a wide directional spread, and the different interfering waves change their wavelengths and travel directions due to inhomogeneity of the current and water depth (refraction). A global 3D image Ω_i spectrum of this measurement is presented in Fig. 71. A k–ω section in west–east direction and a Υ_i plane at a frequency $\omega = 0.624$ rad s^{-1} is presented. At this frequency the waves are coming from the west, with a directional spread of 90°. The intersection line of the dispersion shell is depicted. Using the global method a mean current of $u_x = 0.16$ ms^{-1}, $u_y = 1.19$ ms^{-1} was calculated, assuming a water depth of $d = 12$ m. The dispersion shell is formed like a cone, i.e., the dispersion relation is strongly affected by the water depth (shallow-water waves). In contrast to the optical CEDEX experiment, the wave signal is spreaded in the wavenumber domain due to wave refraction induced by inhomogeneities of the water depth and the tidal current. The background noise level is much higher than in the optical image spectra, a consequence of the occurrence of speckle noise, a feature apparent with radar imaging (or in general with coherent illumination). Because of the background-noise pedestal, AGF decomposition is especially important for radar image-sequence processing in order to obtain undistorted phase pattern in the spatio-frequency domain. Using the DDF-S decomposition, the distortion of the speckle noise collected by the DDF filter bins is too large to retrieve reliable local-wavenumber vectors from the one-component images. Here, as an example, the analysis of a one-component image with the frequency $\omega = 0.624$ rad s^{-1} and the filter direction $\Phi = -33.8°$ is shown. Fig.

Table 6: Specification of the Cartesian grid of the images and local-analysis blocks.

N_x	576	N_{xe}	16
Δx	6.82 m	Δx	6.82 m
X	3928 m	X_e	109 m
N_y	576	N_{ye}	16
Δy	6.82 m	Δy	6.82 m
Y	3928 m	Y_e	109 m
N_t	256	N_t	256
Δt	1.77 s	Δt	1.77 s
T	453 s	T	453 s

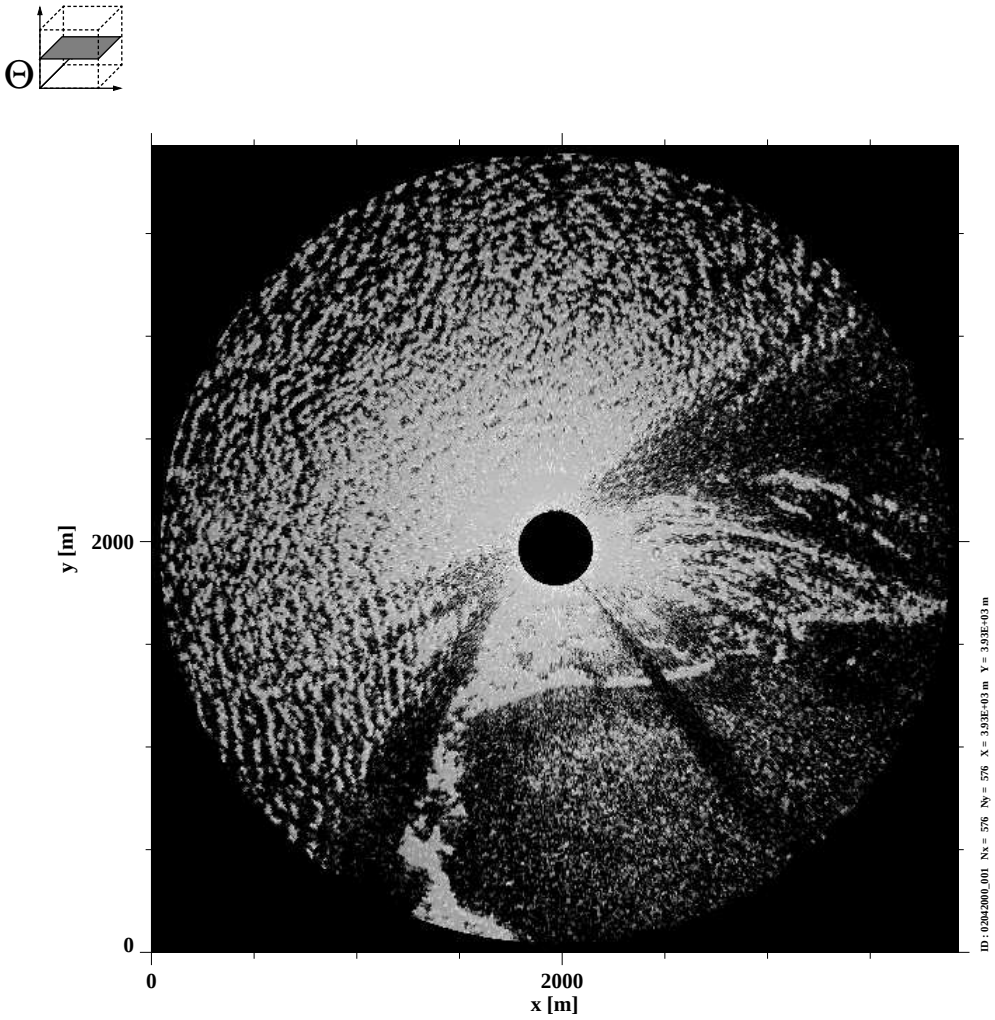

Figure 70: First image of a radar image sequence acquired at the lighthouse List West on the island of Sylt during the storm surge on 4 February 1999.

72 presents a spatial map of local wavelengths, mapped onto the respective phase pattern. In the northern area the waves are longer than in the eastern area.
The changing of local wavelength is caused by the different local water depths (15 m and 7 m). The local values of the water depth and the tidal current are retrieved using the regression method for each block. The resulting map is presented in Fig. 73.
The depth map was compared with echo soundings taken in summer 1997 by the Amt für ländliche Räume (ALR) showing the same qualitative behaviour. The analyzed image sequence was acquired at 20:00 UTC, 100 min before slackwater low. The retrieved current pattern is consistent with an ebb stream situation, and the magnitude of the obtained current values is credible.

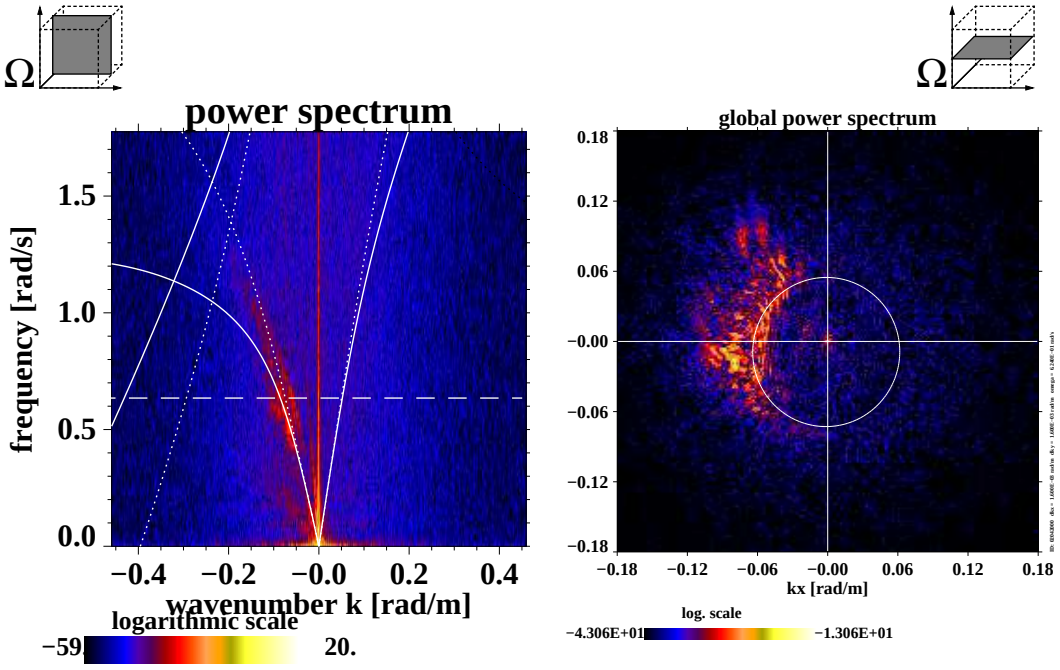

Figure 71: 2D k–ω section (left) and 2D Υ_i plane (right) of the 3D global Ω_i spectrum.

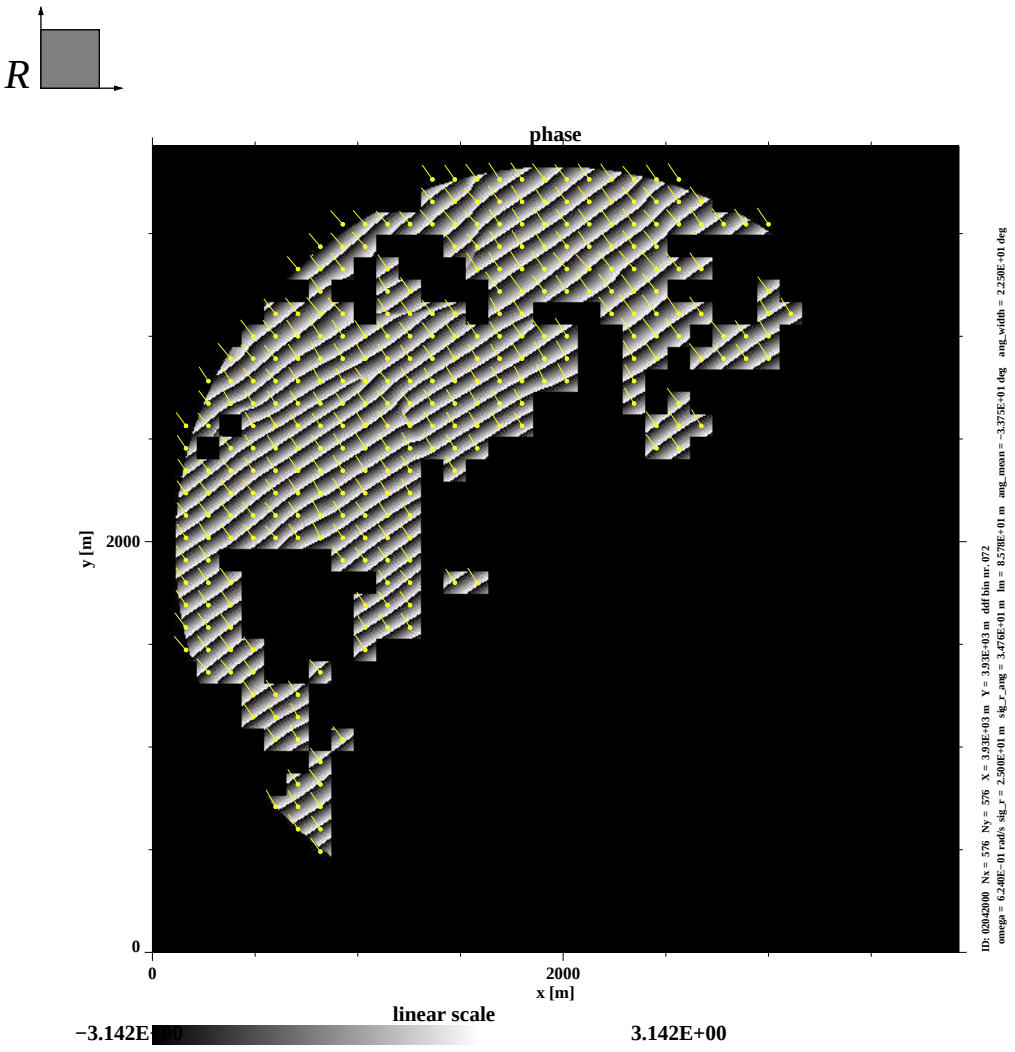

Figure 72: Spatial map of local wavelengths, mapped on the phase pattern for the frequency $\omega = 0.624$ rad s^{-1} and the direction $\Phi = -38.8°$.

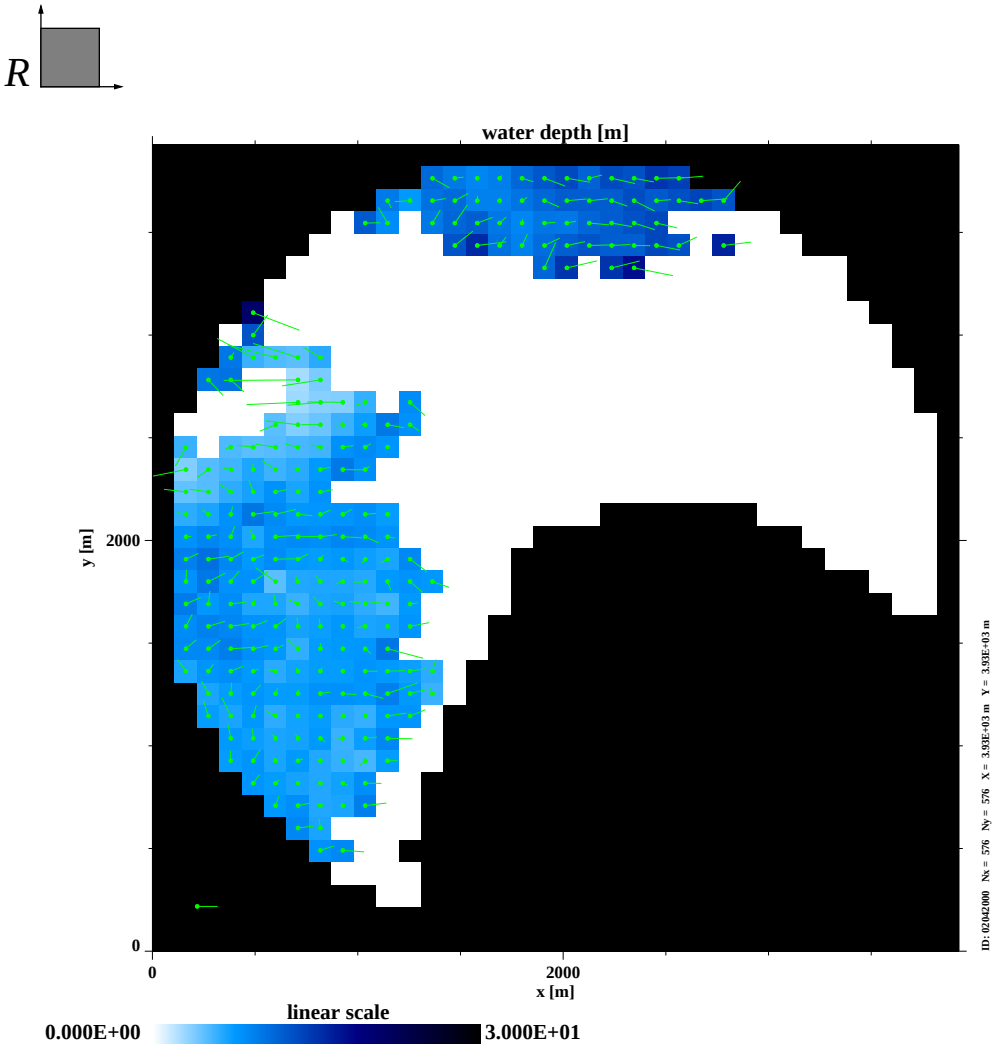

Figure 73: Current-depth map retrieved from the radar image sequence. The local water depth is represented by the blue colour table, and the local current vectors by the green arrows. The arrow in the lower/left corner indicates 1 ms^{-1}.

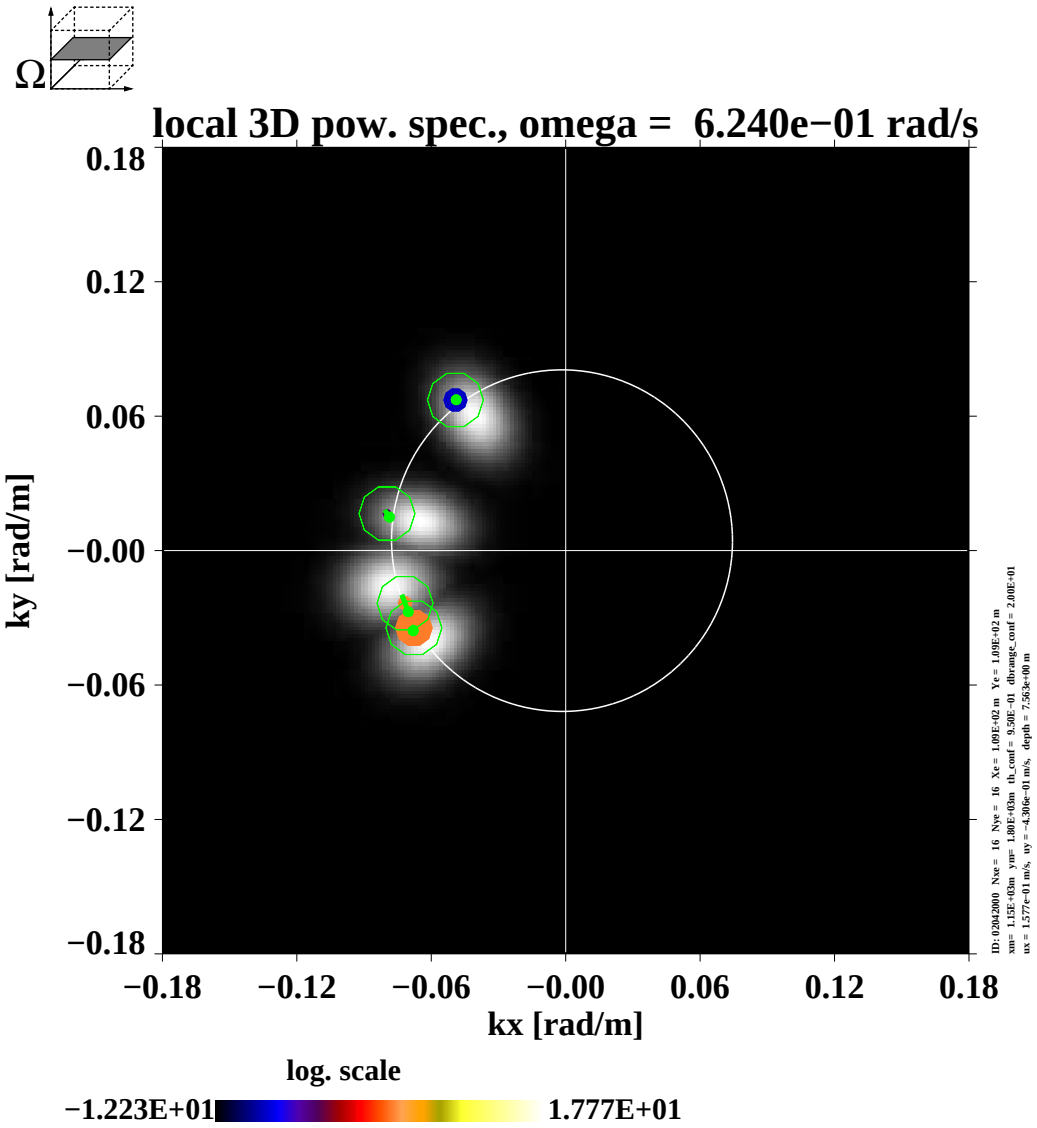

Figure 74: 2D Υ plane of a local 3D image spectrum. The Gabor filters are underlayed indicated by grayscale plots. The dispersion shell is depicted as a white line.

A 2D Υ plane of a local 3D image Ω_i spectrum is presented in Fig. 74. The spectrum was acquired from the position $x_m = 1150$ m, $y_m = 1800$ m. The intersection line with the dispersion shell is depicted; the estimated value of the local current is $u_x = 0.16$ ms^{-1}, $u_y = 0.43$ ms^{-1}, and the local water depth $d = 7.56$ m. The estimated wavenumber vectors are located very close to the dispersion shell, i.e. the local spectrum is very narrow band compared with the global spectrum (Fig. 71). This fact is a strong indicator of the validity of the assumption of local homogeneity.

8 Discussion

Wind-Wave Tank

The Wind-Wave Tank results of the global-analysis method show the ability of the method to determine the wind-induced surface drift for the first time with the analysis of optical image sequences. Consider, that for the given results from the Wind-Wave Tank Hamburg no inhomogeneities and no instationarities have been taken into account. Therefore this first approach of the global-analysis method on this type of data set is insufficient. Anyhow, it can be asserted with precaution, that a trend – as expected the calculated surface current increases with increasing wind speed – can be detected.

CEDEX: Global method

The CEDEX results of the global-analysis method show the ability of image-sequence analysis to determine measurements of the multidirectionality of a wave field, consisting of a set of waves coming from different directions.

CEDEX: Local method

It has been shown that the method DiSC on the local scale has an accuracy on the same order of magnitude as the results of the global analysis method, although the spatial factor between the local-area extension and the global-area extension is 32. The advantages of the DDF-S are the direct filter definition, if the near-surface current and the water depth are known. A disadavantage of the presented DDF-S is the staircase function defined for the dispersion filter. The spatial resolution of the local method, limited by the uncertainty relation, $\sigma_r \cdot \sigma_k \geq c_f$, is lower for spectral filtering when using a rectangular function (the radial component of the dispersion filter) rather than a Gaussian (Gabor filter), which minimizes the uncertainty product. Therefore, larger areas in the vicinity of obstacles, i.e. the wall construction in area A of the CEDEX experiment, are influenced by filtering side effects, using DDF-S. The pre-definition of the DDF-S parameters implies that the filter design is not adaptive. Therefore the filter bank cannot be optimally designed for a given spectral spreading due to inhomogeneities of the wave field. If the DDF-S might be performed for problems other than the examination of wave fields, the dispersion relation utilized as the effective physical model has to be replaced by another physical model.

Gabor-filter bank design

Regarding the adaptive Gabor-filter bank design, the missing a priori information about the physical behaviour is a disadvantage. Up to now the only method used for the separation of the signal from the noise and other disturbing signals is the separation using a threshold. If an examination for nonlinearities where performed, the algorithm might run into problems. On the other hand, an agreeable advantage of the adaptive Gabor-filter bank design is the fact that a physical model is not needed to perform a separation. The transfer to other dynamic-surface applications needs no algorithm adaption (except the adaption of the threshold value). Furthermore the performance of Gabor filters may be made optimal by means of a minimization of the uncertainty relation, implying a minimum value of $\frac{1}{2}$ [Coh95].

Especially for radar data sets, where speckle noise is a significant contribution to the spectral energy, the performance of the adaptive Gabor-filter bank design yields an excellent decrease in the spectral noise. A precise determination of wavenumbers from the complex-valued, one-component maps is now possible. This has been shown for the Sylt case, where refraction leads

to very wide spectral spreading. Here, by applying the adaptive Gabor-filter bank, reliable results are obtained, whereas by using the concept of DDF-S, obvious wavenumber misfits are observed in some areas. The consistency of the adaptive Gabor-filter design has been proved by checking the locations of spectral energy in regard to the location of the fitted dispersion relation in the local Ω-spectra.
Modification of the adaptive Gabor-filter bank design allows supression of the unwanted disturbance signal close to the ω axis, with the accompanying disadvantage that the uncertainty relation increases.
A near-future step, to improve the filter-bank design, is a combination of both concepts. In a first step the filtering of the dispersion relation yields the location of the linear and nonlinear dispersion shells. The locations of the dispersion shells can be used as first guess information to anchor the centers of the Gabor filters. Only the radial extension of a Gabor filter is determined adaptively. The advantage of this combination of the dispersion relation and the Gabor-filter concept is a more safekeeping discrimination of the different spectral signal parts.

DiSC ... yielding spatial hydrographic parameter maps

With DiSC for the first time an analysis technique performed on inhomogeneous multidirectional wave fields has been introduced, enabling the determination of reliable results for hydrographic-parameter maps of the near-surface current vector and the water depth. The method has been proved, and first tests have shown the accuracy range and the reliability in regard to these parameters for optical image sequences.
The blockwise determination of local wavenumbers allows the definition of a confidence measure. This confidence has been used as a selection criterion to sort out badly determined local wavenumbers. For the presented current and water-depth maps, the confidence has been set from a value of 0.95 to 0.9988. For the low confidence case ca. 80% failed. The increase in confidence to 0.9988 has led to a decrease in incorrect calculations of the water depth of ca. 90% to ca. 10%. A least-squares regression method is used to estimate the current and depth values. Therefore, if on a location only a few outliers of the wavenumber fit occur, a misfit of the local current and water depth results. The reason for the outliers in the determination of the local wavenumber are interferences occurring in the one-component images because the filter has a finite azimuthal extension. The angle aperture is higher for low wavenumbers. Therefore the probability of the occurrence of interference ascends, because the filter includes waves from higher angle aperture for low wavenumbers than it would for high wavenumbers. The confidence decreases if a block includes the occurrence of bifurcations due to interferences.
For the presented nautical-radar measurements no accompanying in situ data sets either for water depth or for current measurements were available from the experimental test site. The presented spatial maps of the water depth are determined from measurements acquired in 1999. The last available echo-sounding campaign determining the bathymetry of the observed area was performed by the Amt für ländliche Räume (Husum) in 1997. Qualitatively both independent measurements show the same behaviour. Because of the high morphodynamical activity, strong variations in the bathymetry between

1997 and 1999 have to be expected. Therefore this first comparison has a qualitative value. The utilization of the Gabor-filter bank to separate the spectrum of the nautical-radar images has decreased the signal-to-noise ratio significantly compared to the DDF-S. Since the implementation of the Gabor-filter bank, DiSC has become more robust to noise.

9 Summary and Outlook

9.1 DiSC: State of the Art

The Dispersive Surface Classificator DiSC is a tool which allows, for the first time, the determination of spatial maps of the hydrographic parameters near-surface current and water depth from image sequences of water waves. This image-sequence analysis technique quantifies hydrographic-parameter maps by the involvement of the dispersion relation as a physical model. DiSC has been applied to optical image sequences measured in reflection and to nautical-radar data sets. For both cases DiSC delivers reasonable results.
For the retrieval of the parameter maps of the near-surface current and the water depth, no further calibration implementations are necessary because the determination of these parameters is based on the analysis of the spatial phase patterns. The variance in this context is only used as a threshold determining the magnitude of modulation. The magnitude is used as a qualifier if the calculation of a wavenumber vector is reasonable at a certain location. A comprehensive validation comparing independent in situ current and bathymetry measurements and the results of DiSC performed on nautical-radar image sequences has been performed during 2001 - 2002 in the project ValDiSC.

9.2 Validation and Operationalisation of DiSC

Sea state and tides are inhomogeneous in areas close to the coast due to the spatial variations in the sea-bottom's bathymetry. The dynamical processes result in long-term sand transport. This transport can endanger coastal structures and shorelines. This phenomenon occurs around the island of Sylt where tremendous sand transport occurs due to the sea state and strong tidal currents .
The German public authorities are responsible for observing these changes in order to minimize potential harme. The project ValDiSC ('Validierung des Verfahrens DiSC zur Berechnung lokaler hydrographischer Parameter (Strömung und Wassertiefe) aus Radar-Bildsequenzen'), has been finished recently. Radar-image sequences acquired during a tidal cycle during a storm event and a side-scan sonar data set have been utilised to validate the water depth. In the frame of the project it has been shown, that DiSC can reach an accuracy up to an order of ca. 0.3 – 0.4 m for the determination of water depth for radar-image sequences, acquired under the same conditions as described in Sec. 6.3. This accuracy approaches the order of accuracy of classical instrumentations, i.e. side-scan sonar (accuracy in the order of ca. 0.2 m).
In coorperation with the Amt für ländliche Räume (Husum) the specifications and the end-user demands for DiSC is under evaluation [SS02a] [SS02b]. The phase of the optimization and operationalization (EC project OROMA[1]) of the method DiSC is in progress.

[1] http://www.gkss.de/pages.php?page=k_kor_projects_OROMA-V2.html&language=d&version=g

9.3 DiSC: Calibration Strategy

A calibration strategy enabling the determination of maps of the significant wave height Hs (see (5.23)) is proposed in Appendix G and initial results have been obtained. These results show the ability of DiSC to apply a correction of the MTF or ITF on a local scale. Here, in a first step, the combination of an empirical approach prospectively with an azimuthal-dependency extension of the the ITF is attempted.
The introduction of the Gabor-filter bank to separate the image spectrum has improved the spatial resolution and decreased the magnitude and spatial extension of side effects significantly, and therefore DiSC can also be utilized on wave fields disturbed by obstacles.
The presented concept to perform DiSC on optical image sequences on wave-fields in hydraulic wave tanks has the potential to reach an operational stage, because (1) the light conditions are controllable and (2) independent in situ measurements are generally in operation in those facilities and therefore DiSC can be combined with additional sensors using data-fusion methods to retrieve calibrated local wave spectra.
The concept will eventually be transferred to field measurements, but currently the system is expected to stay on an experimental level for optical image sequences because of the following reasons: (1) The optical system is passive; therefore measurements at night are not possible without artificially illuminating the observed wave field and (2) The natural sky illumination is variable in space and time; this results in a variation of the illumination gradients and therefore in a change of the modulation strength of the reflected light field. Sun glitter may appears as an additional illumination effect, resulting in strong modulation.
Reason (1) leads to difficult experimental setups for deployment at night, complicating operationalization for natural wave fields. Reason (2) implies an additional setup of a radiometric device acquiring the sky-light illumination. This potential device could be an additional CCD camera directed towards the sky, acquiring image sequences of the sky light synchronously to the acquisition of image sequences of the wave field.
For nautical-radar image sequences, which are acquired with an active system (a nautical radar antenna sends and receives microwave pulses) a calibration yielding spatial maps of the significant wave height is a straight-forward task. A local empirical approach analogous to the global calibration procedure is an encouringing future task.

9.4 DiSC: Methodic and Application Perspectives

9.4.1 Transfer to Related Applications

It is proposed to transfer DiSC from the hydrographic application of analyzing water waves to other disciplines. A brief strategy is outlined enabling the potential transfer of DiSC to solid-matter physics by the replacement of the physically motivated dispersion relation.

With the DDF-S concept, DiSC uses the dispersion relation as a physical model to interpret image sequences of fluid-surface waves. The modular concept of DiSC allows the exchange of the physical model without technical difficulties. Other dispersion relations can be implemented to examine other dispersive surfaces.
In solid-matter physics elastic-surface waves are known to be dispersive, depending on parameters specific to the microstructure of matter. Examples of these parameters are elasticity and plasticity. The elasticity parameter often is used to quantify the bonding strength of crystals.
For example, film layers coated onto a substrate have a strong influence on elastic-surface wave propagation [SS97] (see Fig. 75). Elastic constants of the thin film may deviate from values of the substrate. Elastic-surface waves can be stimulated by applying vibrations or acoustic waves. Normally for homogeneous isotropic materials the dispersion is not dependent on the wave's frequency. The phase velocity of the surface wave is related to Young's modulus, E, Poisson's ratio, ν, and the density, ρ. If a substrate is coated, the stiffness and the density in the near-surface region changes, resulting in a change of phase speed of the waves. The film can load or stiffen the surface. A higher Young's modulus or a higher density of the film compared to the substrate has a stiffening effect and vice versa.
The elastic-surface waves can be visualized by choosing a suitable imaging sensor and a defined experimental setup. Applying DiSC with an elasitic-surface wave module instead of the water-wave dispersion relation could enable the determination of spatial maps of the influenced parameters mentioned above. This might be of interest for quality control of film thickness or other material characteristics.

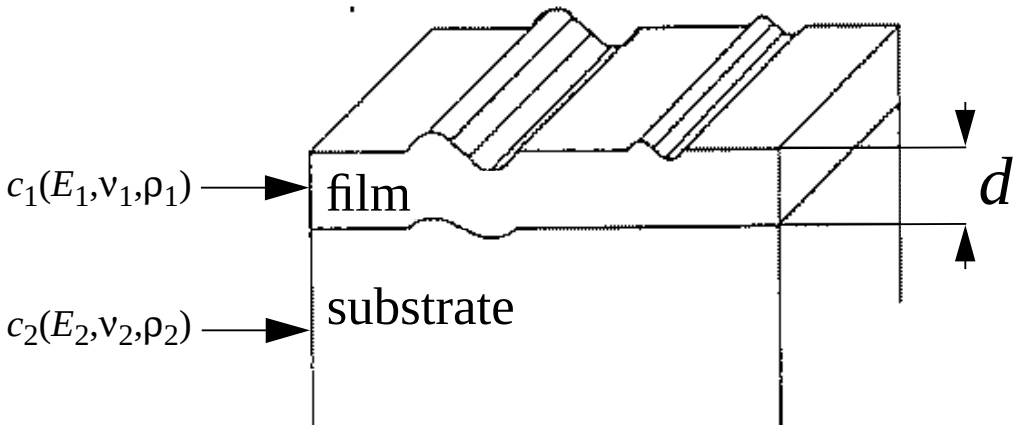

Figure 75: Elastic waves propagating on a thin film. Two waves are apparent: one at the air–film boundary and one at the film–substrate boundary (source: [SS97]).

9.4.2 Reconstruction of Refraction Patterns

Havlicek et al. termed the computation of multi-component AM–FM image models (see Sec. 5.3.2) by the estimation of local amplitudes and wavenumbers from each channel of a filter bank the Channelized-Component Approach. This is analogous to the representation of the inhomogeneous wave field with a map of local image spectra.
An alternative representation is obtained by a tracked multi-component analysis, i.e. combination of the result of the local filters with new recombined one-component images. The latter each arise locally from different filter channels. After combining different one-component images, the new recombined one-component images are composed of a spatially smooth variation of the local amplitude and wavenumber vector (see Fig. 76). If a priori knowledge of the images is not available, i.e. for general texture analysis purposes, a Kalman filter has been used for tracking [HBC99].
Here, it is proposed to use, instead of this statistical approach, the refraction laws to estimate the refraction patterns from the different local 3D spectra to examine the wave field approaching shallow-water areas. The refraction laws describe the refraction paths as a function of the estimated current and bathymetric patterns (see Sec. 2.2.7 and Fig. 15).

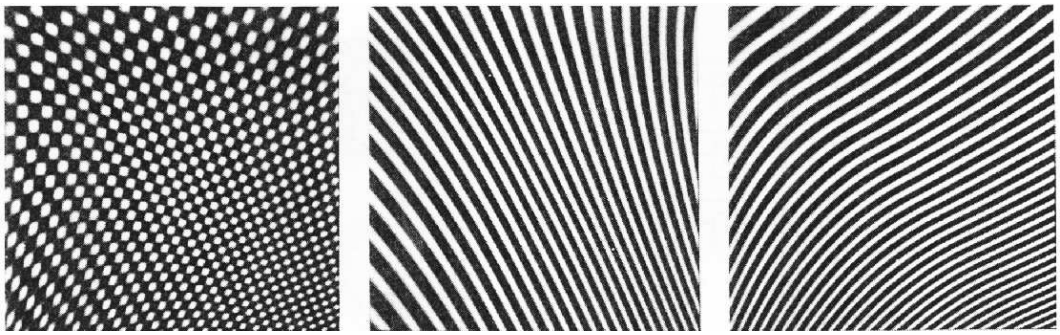

Figure 76: Inhomogeneous multi-component decomposition into highly coherent images. Composite image (left), component one (center), component two (right) (source: [HHB96]).

9.4.3 Extension to Instationary Processes

Up to now DiSC has been limited to inhomogeneous processes. Instationary processes are not in the scope of DiSC. Extending the adaptive Gabor-filter bank from a 2D definition to an adaptive 3D definition, would yield 3D spectral bins analogous to Fig. 6 **a)**. These 3D spectral bins are 3D subspaces of the the 3D Ω_i domain. Where the 2D Gabor-filter implementation contains the spectral signal, which is spread in the Υ_i domain, including the inhomogeneous signal, the 3D definition could yield instationary spreading in the frequency direction too. The inverse FFT has to be extended from the 2D FFT^{-1} to a 3D FFT^{-1} over the two wavenumber components, k_x and k_y, and over the frequency interval spanned by the actual Gabor-filter frequency width. The result would be a one-component image sequence containing the

inhomogeneous and instationary wave from a defined direction. The method of Havlicek et al. has been defined n-dimensionally [HHB73]. Therefore the implementation is a straight-forward problem. This separation approach is similiar to wavelet-separation approaches [SKL94]. The advantage of the proposed DiSC 3D filter bank extension, as for the available DiSC 2D filter bank extension, is the adaption to the widely spreaded spectral signal; it is superior to the concept of a data-independent fixed filter bank, because it saves computation time by decreasing the number of necessary filters and the necessary succeeding number of highly time-consuming back-transformations.
The proposed extension may lead to a strategy for an algorithm to determine the spatio-temporal distribution of the surface tension Γ (see (2.9)).

9.4.4 Extension to Stereo-Image Sequences

The method used to determine maps of local wavenumbers has been used to determine elevation models from pairs of stereo images by determining the disparity between the two stereo images [JJ88]. One precondition for the method of Jenkins and Jepson is the demand for a narrow bandwidth of the signal on a local spatial scale. For simple patterns the method of Jenkins and Jepson enables the determination of elevation models.
A similar approach is that of Chen et al., who have developed a stereo-disparity estimation method, which uses the AM–FM image model after decomposition by a Gabor-filter bank (see Sec. 5.3.2) [CBC95].
Wave fields with a widespread directional distribution are generally not narrowbanded on a local spatial scale. If the validity of the dispersion relation on a local spatial scale is assumed, a separation into one-component images allows the wave field to be divided into simple (i.e. narrow bandwidth) structured, one-component images. It is proposed to combine the stereo concept with DiSC to determine maps of spatial disparities between two stereo one-component images. A stereo approach combined with the abilities of DiSC may be promising in determining elevation models from sea surfaces, avoiding correspondence problems.

References

[AH82] W. Alpers and K. Hasselmann. Spectral signal to clutter and thermal noise properties of ocean wave imaging synthetic aperure radars. *International Journal of Remote Sensing*, 3:pages 423–446, 1982.

[BdA94] J.C. Nieto Borge and M. de Alfonso. Methods of sea state simulation. Report 56, Ente Publico Puertos del Estado, 1994.

[BHR99] J.C. Nieto Borge, K. Hessner, and K. Reichert. Estimation of the significant wave height with X-band nautical radars. In *Proceedings of the OMAE99/OSU-3063 Conference*, pages published on CD–ROM, 1999.

[Bor98] J.C. Nieto Borge. Significant wave height estimation from nautical radar data sets. External Report GKSS/98/E/28, GKSS Research Center, 1998.

[Bov00] Al Bovik, editor. *Handbook of Image and Video Processing*, chapter 4.8: Multiband Techniques for Texture Classification and Segmentation, pages 367–381. Academic Press, 2000.

[Bra98] N. Braun. Laboruntersuchungen zum Einfluß von künstlichem Regen auf eine Wasseroberfläche mit Hilfe von Wellendraht-, Laser und Radarsonden. Master's thesis, University of Hamburg, Institute of Oceanography, Hamburg, Germany, 1998.

[BW91] M. Born and E. Wolf. *Principles of Optics*. Pergamon Press, 6th edition, 1991.

[BZSS98] J.C. Nieto Borge, F. Ziemer, J. Seemann, and C.M Senet. Overcome of the Nyquist in frequency in nautical radar measurement of wave fields. In *Proceedings of the 17th OMAE Conference*, pages published on CD–ROM, 1998.

[CBC95] T.Y. Chen, A.C. Bovik, and L.K. Cormack. Stereo disparity from local image phase. Technical Report UT-CVIS-TR-95-003, University of Texas at Austin, 1995.

[CM54a] C. Cox and W. Munck. Measurements of the roughness of the sea surface from photographs of the sun's glitter. *Journal of the Optical Society of America*, 44:838–850, 1954.

[CM54b] C. Cox and W. Munck. Statistics of the sea surface derived from sun glitter. *Journal of the Optical Society of America*, 44:838–850, 1954.

[Coh95] L. Cohen. *Time-Frequency Analysis*. Prentice-Hall, Englewood Cliffs, N.J., 1995.

[Cro70] J. Croney. *Radar Handbook*, chapter Civil Marine Radar, pages 31–1–31–37. McGraw Hill, 1970.

[CT65] J.W. Cooley and J.W. Tuckey. An algorithm for the machine calculation of complex Fourier series. *Mathematics of Computation*, 19:pages 297–301, 1965.

[Dan00] H. Dankert. Räumliche Analyse der Diffraktion von Wellenfeldern anhand von Bildsequenzen und Simulationen. External report, University of Rostock, Institute for Coastal Engineering, GKSS Research Center, Geesthacht, Wismar, Germany, 2000.

[DDSW01] M.A. Donelan, W.M. Drennan, E.S. Saltzmann, and R. Wanninkhof, editors. *Gas Transfer at Water Surfaces*, volume 127. American Geophysical Union, Geophysical Monograph Series, 2001.

[Dit95] J. Dittmer. Use of marine radars for real time wave field survey and speeding up the transmission / processing. In *Proceedings of the WMO/IOC Workshop on Operational Ocean Monitoring using Surface Based Radars*, pages 133–137, 1995.

[Dit99] J. Dittmer. WaMoS II – An operational Wave Monitoring System. Technical data sheet, source: http://www.oceanwaves.de/, OceanWaveS GmbH, Lüneburg, Germany, 1999.

[DKKS75] G. Dietrich, K. Kalle, W. Krauss, and G. Siedler. *Allgemeine Meereskunde – Eine Einführung in die Ozeanographie*. Gebrüder Borntraeger, Berlin, 1975.

[DS83] J.E.Jr. Dennis and R.B. Schnabel. *Numerical Methods for Unconstrained Optimization and Nonlinear Equations*. Prentice Hall, Englewood Cliffs, N.J., 1983.

[DSFF96] J.P. Dugan, H.H. Suzukawa, C.P. Forsyth, and M.S. Farber. Ocean wave dispersion surface measured with airborne IR imaging system. *IEEE Transactions on Geoscience and Remote Sensing*, 34(5):pages 1282–1284, 1996.

[FM95] S. Frasier and R. McIntosh. Three dimensional spectra of X-band doppler radar backscatter from the ocean surface. In *Proceedings of the IEEE International Geoscience and Remote Sensing Symposium*, pages 1370–1374, 1995.

[GAE+98] M. Gade, W. Alpers, S.A. Ermakov, H. Hühnerfuß, and P.A. Lange. Wind-wave tank measurements of bound and freely propgating short gravity-capillary waves. *Journal of Geophysical Research*, 1(3):pages 3167–3178, 1998.

[Ger02] F. Gerstner. Theorie der Wellen usw. Technical report, Abhandlungen der Königlichen Böhmischen Gesellschaft der Wissenschaften, Prague, 1802.

[GI80] B.L. Gotwols and G.B. Irani. Optical determination of the phase velocity of short gravity waves. *Journal of Geophysical Research*, 85:3964–3970, 1980.

[GI82] B.L. Gotwols and G.B. Irani. Charge-coupled device camera system for remotely measuring the dynamics of ocean waves. *Applied Optics*, 21:851–860, 1982.

[GK95] G.H. Granlund and H. Knutsson, editors. *Signal Processing for Computer Vision*. Kluwer Academic Publishers, 1995.

[Has62] K. Hasselmann. On the non-linear energy transfer in a gravity-wave spectrum; Part 1: General theory. *Journal of Fluid Mechanics*, 12:pages 481–500, 1962.

[HB89] B.K.P. Horn and M.J. Brooks, editors. *Shape from Shading*. The MIT Press, 1989.

[HB95] J.P. Havlicek and A.C. Bovik. AM-FM models, the analytic image, and nonlinear demodulation techniques, TR-95-001. Technical report, Laboratory for Vision Systems, University of Texas, Austin, TX 78712-1084, 1995.

[HBB+73] K. Hasselmann, T.P. Barnett, E. Bouws, H. Carlson, D.E. Cartwright, K. Enke, J.A. Ewing H. Gienapp, D.E. Hasselmann, P. Krusemann, A. Meerburg, P. Müller, D.J. Olbers, K. Richter, W. Sell, and H. Walden. Measurements of wind-wave growth and swell decay during the joint north sea wave project (JONSWAP). *Deutsche Hydrographische Zeitschrift; Deutsches Hydrographisches Institut*, Reihe A(12), 1973.

[HBC99] J.P. Havlicek, A.C. Bovik, and D. Chen. *Visual Information Representation, Communication, and Image Processing (Optical Engineering, 64)*, chapter 12: AM-FM Image Modeling and Gabor Analysis, pages 343–385. Marcel Dekker, Inc., 1999.

[HHB73] J.P. Havlicek, D.S. Harding, and A.C. Bovik. Multicomponent multidimensional signals. *Multidimensional Systems and Signal Processing*, 9:pages 391–398, 1973.

[HHB96] J.P. Havlicek, D.S. Harding, and A.C. Bovik. The multicomponent AM–FM image representation. *IEEE Transactions on Image Processing*, 5(6):pages 1094–1100, 1996.

[HHB00] J.P. Havlicek, D.S. Harding, and A.C. Bovik. Multidimensional quasi-eigenfunction approximations and multicomponent AM-FM models. *IEEE Transactions on Image Processing*, 9(2):pages 227–242, 2000.

[HMM94] I. Hennings, J. Matthews, and M. Metzner. Sunglitter radiance and radar cross-section modulations of the sea bed. *Journal of Geophysical Research*, 99(C8):16303–16326, 1994.

[IGB86] G.B. Irani, B.L. Gotwols, and A.W. Bjerkaas. *Wave Dynamics and Radio Probing of the Ocean Surface*, chapter The 1978 Ocean Wave Dynamics Experiment, Optical and In Situ Measurement of the Phase Velocity of Wind Waves, pages 165–179. Plenum Press, 1986.

[Jäh97] B. Jähne. *Image Processing for Scientific Applications*, chapter 4.3.b – 4.3.5e; 3.3.4f, pages 148–151. CRC Press, 1997.

[Jan97] P.C. Janssen. Intertidal beach level estimations from video images. Master's thesis, University of Technology, Faculty of Civil Engineering, Hydraulic and Geotechnical Engineering Division, Delft, The Netherlands, 1997.

[Jef24] H. Jeffreys. On the formation of water waves by wind. *Proc. Soc.*, A:pages 189–206, 1924.

[JHG99a] B. Jähne, H. Haußecker, and P. Geißler, editors. *Handbook of Computer Vision and Applications – Signal Processing and Pattern Recognition*, volume 2, chapter Spatial and Fourier Domain, pages 35–66. Academic Press, 1999.

[JHG99b] B. Jähne, H. Haußecker, and P. Geißler, editors. *Handbook of Computer Vision and Applications - Signal Processing and Pattern Recognition*, volume 3, chapter The Neural Active Vision System Navis, pages 543–568. Academic Press, 1999.

[JJ88] M.R.M. Jenkin and A.D. Jepson. *Computational Processes in Human Vision: An Interdisciplinary Perspective*, chapter The Measurements of Binocular Disparity, pages 69–98. The Canadian Institute for Advanced Research Series in Artificial Intelligence, 1988.

[JKGH93] B. Jähne, J. Klinke, P. Geißler, and F. Hering. *Imaging in Transport Processes*, chapter Image Sequence Analysis of Ocean Wind Waves, pages 257–268. Begell House, Inc., 1993.

[JW89] B. Jähne and S. Waas. Optical measuring technique for small scale water surface waves. *SPIE, Advanced Optical Instrumentation for Remote Sensing of the Earth's Surface from Space*, 1129:pages 122–128, 1989.

[JWK92] B. Jähne, S. Waas, and J. Klinke. Critical theoretical review of optical techniques for short-ocean-wave measurements. In Estep and Leland, editors, *Proceedings of SPIE 'Optics of the Air-Sea Interface: Theory and Measurements'*, volume 1749, pages 204–215, 1992.

[Kli96] J. Klinke. Optical measurements of small-scale wind-generated water surface waves in the laboratory and the field. Master's thesis, University of Heidelberg, Interdisciplinary Center for Scientific Computing, Heidelberg, Germany, 1996.

[LH78] P.A. Lange and H. Hühnerfuß. Drift response of monomolecular slicks to wave and wind action. *Journal of Physical Oceanography*, 8:pages 142–150, 1978.

[Mar87] S.L.Jr. Marple. *Digital Spectral Analysis with Applications.* Prentice-Hall, Englewood Cliffs N.J., 1987.

[May94] M. Mayer. PV-Wave quick reference guide. PV-Wave techn. notes, Visual Numerics, Inc., 1994.

[Mil75] J.W. Miles. On the generation of surface waves by shear flow; part 1. *Journal of Fluid Mechanics*, 3:pages 185–204, 1975.

[MK81] F.M. Monaldo and R.S. Kasevich. Daylight imagery of ocean surface waves for wave spectra. *Journal of Physical Oceanography*, 11:272–283, 1981.

[Mob94] C.D. Mobley. *Light and Water - Radiative Transfer in Natural Waters.* Academic Press, Inc, San Diego, USA, 1994.

[MTS+75] H. Mitsuyasu, F. Tasai, T. Suhara, S. Mizuno, M. Ohkusu, T. Honda, and K. Rikiishi. Observations of the directional spectrum of ocean waves using a cloverleaf buoy. *Journal of Physical Oceanography*, 5:pages 750–760, 1975.

[NN98a] NN. Filters: General information. Technical report, Schneider Optics Inc., Hauppauge, USA, available at http://www.schneideroptics.com/filters/list/7/info.htm, 1998.

[NN98b] NN. Progressive scan CCD camera – CV-M10 series – operation manual. Technical report, JAI AS, Glostrup, Denmark, 1998.

[NN98c] NN. Sony CCD data sheet, ID: ICX075AL. Technical report, personal communication, E. Weiss (Fa. Stemmer), 1998.

[OL81] A.V. Oppenheim and J.S. Lim. The importance of phase in signals. *Proceedings of the IEEE*, 69:pages 529–541, 1981.

[Out98] O. Outzen. Bestimmung der Wassertiefe und der oberflächennahen Strömung mit einem nautischen Radar. Master's thesis, University of Hamburg, Institute of Oceanography; GKSS Research Center, Geesthacht, Hamburg, Germany, 1998.

[Phi57] O.M. Phillips. On the generation of waves by turbulent wind. *Journal of Fluid Mechanics*, 2:pages 417–445, 1957.

[Phi60] O.M. Phillips. On the dynamics of unsteady gravity waves of finite amplitude. *Journal of Fluid Mechanics*, 9:pages 193–217, 1960.

[PM64] W.J. Pierson and L. Moskowitz. A proposed spectral form for fully developed wind seas based on the similarity theory of S.A. Kitaigorodskii. *Journal of Geophysical Research*, C1(69):pages 5181–5190, 1964.

[PO78] N.A. Peppers and J.S. Ostrem. Determination of wave slopes from photographs of the ocean surface. *Applied Optics*, 17(21):3450–3458, 1978.

[Poh98] R.W. Pohl. *Einführung in die Physik; Band I; Mechanik, Akustik und Wärmelehre*. Springer Verlag, 17th edition, 1998.

[PP94] W.G. Penney and A.T. Price. Diffraction of sea waves by breakwaters. External report, Directorate of Miscellaneous Weapons Development History, 1994.

[Pra75] W.K. Pratt. Vector space formulation of two-dimensional signal processing operations. *Computer Graphics and Image Processing*, 4:pages 1–24, 1975.

[RBD99] K. Reichert, J.C. Nieto Borge, and J. Dittmer. Wamos II: An operational wave monitoring system. In *Proceedings of the Oceanology International'99*, pages published on CD–ROM, 1999.

[RHBD99] K. Reichert, K. Hessner, J.C. Nieto Borge, and J. Dittmer. Wamos II: A radar based wave and current monitoring system. In *Proceedings of the ISOPE'99*, volume 3, pages 139–143, 1999.

[SB81] R.C. Smith and K. Baker. Optical properties of the clearest natural waters. *Applied Optics*, 20(2):pages 177–184, 1981.

[SBL+99a] C.M. Senet, N. Braun, P.A. Lange, J. Seemann, H. Dankert, and F. Ziemer. Image sequence analysis of water surface waves in a hydraulic wind wave tank. In *Proceedings of the SPIE'99 Conference – Applications of Digital Image Processing XXII*, pages 148–158, 1999.

[SBL+99b] C.M. Senet, N. Braun, P.A. Lange, J. Seemann, G. Schymura, and F. Ziemer. Optical image sequence analysis and interpretation of stationary and instationary wave fields. In *Proceedings of the IEEE International Geoscience and Remote Sensing Symposium '99*, pages 387–389, 1999.

[SC66] R.L. Snyder and C.S. Cox. A field study of the wind generation of ocean waves. *Journal of Marine Research*, 24:pages 141–178, 1966.

[See97] J. Seemann. *Interpretation der Struktur des Wellenzahl-Frequenzspektrums von Radar-Bildsequenzen des Seegangs.* PhD thesis, University of Hamburg, Institute of Oceanography, GKSS Research Center, Geesthacht, Hamburg, Germany, 1997.

[Sen96] C.M. Senet. Untersuchungen zur Bestimmung der oberflächennahen Strömungsgeschwindigkeit mit einem nautischen Radar. Master's thesis, University of Hamburg, Institute of Oceanography, GKSS Research Center, Geesthacht, Hamburg, Germany, 1996.

[SF96] E.P. Simoncelli and H. Farid. Steerable wedge filters for local orientation analysis. *IEEE Transactions on Image Processing*, 5:pages 1377–1382, 1996.

[Sha98] V. Shane. *Drag Device Data Base: Using Parachutes, Sea Anchors and Drogues to Cope with Heavy Weather.* Para-Anchor International, 4th edition, 1998.

[SKL94] G.R. Spedding, J. Klinke, and S.R. Long. *The Air-Sea Interface: Radio and Acousting Sensing, Turbulence and Wave Dynamics*, chapter Estimating $\vec{\omega}(\vec{k})$ in an Unsteady, Wind-Generated Surface Wave Field from 2D Complex Wavelet Transform of the Surface Slope, page 373. Rosenstiehl School of Marine and Atmospheric Science, University of Miami, 1994.

[SN89] R. Stoica and A. Nehorai. MUSIC, maximum likelihood, and Cramer-Rao bound. *IEEE Transactions on Acoustics, Speech, and Signal Processing*, 37:pages 720–741, 1989.

[Som47] A. Sommerfeld. *Vorlesungen über Theoretische Physik*, volume VI. Dieterichsche Verlagsbuchhandlung, 1947.

[SPM96] M.J. Smith, E.M. Poulter, and J.A. McGregor. Doppler radar measurements of wave groups and breaking waves. *Journal of Geophysical Research*, C6(101):pages 14269–14282, 1996.

[SS97] D. Schneider and T. Schwarz. A photoacoustic method for characterising thin films. *Surface and Coating Technology*, 91:pages 136–146, 1997.

[SS02a] C.M. Senet and J. Seemann. Studie I: 'State of the Art'. Technical report, GKSS Research Center, Geesthacht, Germany and V2T VISION TO TECHNOLOGY GmbH, Geesthacht, Germany. In German, in preparation, 2002.

[SS02b] C.M. Senet and J. Seemann. Studie II: 'Validation'. Technical report, GKSS Research Center, Geesthacht, Germany and V2T VISION TO TECHNOLOGY GmbH, Geesthacht, Germany. In German, in preparation, 2002.

[SSD+99a] J. Seemann, C.M. Senet, H. Dankert, H. Hatten, and F. Ziemer. Radar image sequence analysis of inhomogeneous water surfaces. In *Proceedings of the SPIE'99 Conference – Applications of Digital Image Processing XXII*, volume 3808, pages 536–546, 1999.

[SSD+99b] C.M. Senet, J. Seemann, H. Dankert, J.R. Amoros Serret, J.C. Nieto Borge, and F. Ziemer. Optical image sequence analysis and interpretation of the water surface in a multidirectional wave tank and its application in coastal engineering. In *Proceedings of the 2nd International Symposium on Operationalization of Remote Sensing*, pages published on CD–ROM, 1999.

[SSH+00] J. Seemann, M. Senet, H. Hatten, J.C. Nieto Borge, and F. Ziemer. Three-dimensional frequency-wavenumber radar spectra from image sequences of the water surface. *Transactions on Geoscience and Remote Sensing*, submitted 2000.

[SSSZ00] C.M. Senet, J. Seemann, G. Schymura, and F. Ziemer. Verfahren und Vorrichtung zur Ermittlung von ein Seegangsfeld in einem Wellentank beschreibenden hydrographischen Parametern. *German patent office, Munich, Germany, in German, German and international patent application, Ref. No. 100 35 931.0 (German patent application), Ref. No. PCT/DE 00/02413 (international patent application)*, 2000.

[SSW+00] J. Seemann, C.M. Senet, U. Wolff, H. Hatten, and F. Ziemer. Hydrographic parameter maps retrieved from nautical radar image sequences of inhomogeneous water surfaces. In *Proceedings of the IEEE International Geoscience and Remote Sensing Symposium '2000*, volume V, pages 1898–1900, 2000.

[SSWZ00] J. Seemann, C.M. Senet, U. Wolff, and F. Ziemer. Nautical X-band radar image processing: Monitoring of morphodynamic processes in coastal waters. In *Proceedings of the Oceans'2000 MTS/IEEE Conference*, pages published on CD–ROM, 2000.

[SSZ97] C.M. Senet, J. Seemann, and F. Ziemer. An iterative technique to determine the near surface current velocity from time series of sea surface images. In *Proceedings of the Oceans '97 MTS/IEEE Conference, 500 Years of Ocean Exploration*, volume 1, pages 66–72, 1997.

[SSZ00a] J. Seemann, C.M. Senet, and F. Ziemer. *Mustererkennung 2000*, chapter Local Analysis of Inhomogeneous Sea Surfaces in Coastal Waters Using Nautical Radar Image Sequences, pages 179–186. Springer, Berlin, 2000.

[SSZ00b] J. Seemann, C.M. Senet, and F. Ziemer. Verfahren zur Ermittlung von ein in situ Seegangsfeld beschreibenden hydrographischen Parametern mittels einer Radareinrichtung. *German patent*

office, Munich, Germany, in German, German and international patent application, Ref. No. 100 35 921.3 (German patent application), Ref. No. PCT/DE 00/02413 (international patent application), 2000.

[SSZ00c] C.M. Senet, J. Seemann, and F. Ziemer. Dispersive surface classification: Local analysis of optical image sequences of the water surface to determine hydrographics parameter maps. In *Proceedings of the Oceans'2000 MTS/IEEE Conference*, pages published on CD–ROM, 2000.

[SSZ00d] C.M. Senet, J. Seemann, and F. Ziemer. Hydrographic parameter maps deduced from CCD image sequences of the water surface supplemented by in-situ wave gauges. In *Proceedings of the IEEE International Geoscience and Remote Sensing Symposium '2000*, volume II, pages 843–846, 2000.

[SSZ01] C.M. Senet, J. Seemann, and F. Ziemer. The near-surface current velocity determined from image sequences of the sea surface. *IEEE Transactions on Geoscience and Remote Sensing*, 39(3):492–505, 2001.

[Sti69] D.Jr. Stilwell. Directional spectra of the sea surface from photographs. *Journal of Geophysical Research*, 74:1974–1986, 1969.

[Sto47] G.G. Stokes. On the theory of oscillatory waves. *Transactions of the Cambridge Philosophical Society*, 8:pages 441–455, 1847.

[SZ95] J. Seemann and F. Ziemer. Computer simulation of imaging ocean wave fields with a marine radar. In *Proceedings of the Oceans'95 MTS/IEEE Conference – Challenges of our changing Global Environment*, pages 1128–1133, 1995.

[SZS97] J. Seemann, F. Ziemer, and C.M. Senet. A method for computing calibrated ocean wave spectra from measurements with a nautical X-band radar. In *Proceedings of the Oceans '97 MTS/IEEE Conference, 500 Years of Ocean Exploration*, volume 2, pages 1148–1154, 1997.

[TCM96] E. Trouve, M. Caramma, and H. Maitre. Fringe detection in noisy complex interferograms. *Applied Optics*, 35:pages 3799–3806, 1996.

[Tho71] W. Thomson. (1st Baron Kelvin of Largs), influence of wind at capillarity on waves in water supposed frictionless. *Mathematical Physical Papers*, 4:pages 76–85, 1871.

[Tol90] H.L. Tolman. The influence of unsteady depths and currents of tides on wind-wave propagation in shelf seas. *Journal of Physical Oceanography*, 20:pages 1166–1174, 1990.

[Tsa87] R.Y. Tsai. A versatile camera calibration technique for high accuracy 3D machine vision metrology using off-the-shelf TV cameras and lenses. *IEEE Journal of Robotics and Automation*, RA-3(4):pages 323–344, 1987.

[Wal94] R.E. Walker. *Marine Light Field Statistics*. Wiley-Interscience publications, 1994.

[Win94] N. Winkel. *Modellierung von Seegang in extremen Flachwasser*. PhD thesis, University of Hamburg, Faculty of Geosciences, GKSS Research Center, Geesthacht, Hamburg, Germany, 1994.

[Wit57] G. Witt. Noctilucent cloud observations. *Tellus*, 9(3):pages 365–371, 1957.

[Wol92] G. Wolberg. *Digital Image Warping*. IEEE Computer Society Press, 1992.

[WSSZ99] U. Wolff, J. Seemann, C.M. Senet, and F. Ziemer. *Mustererkennung '99*, chapter Analysis of Morphodynamical Processes with a Nautical X-Band Radar, pages 372–380. Springer, Berlin, 1999.

[YRZ85] I.R. Young, W. Rosenthal, and F. Ziemer. A three-dimensional analysis of marine radar images for the determination of ocean wave directionality and surface currents. *Journal of Geophysical Research*, 90(C1):pages 1049–1059, 1985.

[Zie87] F. Ziemer. *Untersuchung zur quantitativen Bestimmung zweidimensionaler Seegangsspektren aus Messungen mit nautischem Radar*. PhD thesis, University of Hamburg, Faculty of Geosciences, GKSS Research Center, Geesthacht, Hamburg, Germany, 1987.

List of Figures

List of Tables

Symbols

∂	partial derivation operator
$\angle(\dots)$	angle of ...
∇	Nabla operator
$\underline{\Delta}$	Laplace operator
$*$	convolution
$\langle\dots\rangle$	ensemble average of ...
$\overline{\dots}$	mean value of ...
$\forall$	for all
$\exists$	exists
$\neq$	not equal
$\tilde{..}$	variance of ...
$\hat{..}$	complex number
$(\dots)^*$	complex conjugate of ...
$\lvert\dots\rvert$	modulus of ...
$\lVert\dots\rVert$	norm of ...
$[\dots\lvert\dots\lvert\dots]$	optional
$\mathrm{Im}(\dots)$	imaginary part of a complex number
$\mathrm{Re}(\dots)$	real part of a complex number

$\mathcal{C}$	confidence
$\mathcal{D}$	directional distribution of sea state [rad^{-1}]
$\mathcal{G}(\Omega_i)$	3D discrete gray-level variance (or image) spectrum
$\hat{\mathcal{G}}(\Omega_i)$	3D discrete complex-valued image spectrum
$\mathcal{G}_\mathrm{N}(\Omega_i)$	3D background noise part of image spectrum
$\mathcal{G}_\mathrm{S}(\Omega_i)$	3D signal part of image spectrum
$\mathcal{G}_p(\Omega_i)$	3D p-th harmonic signal part of image spectrum
$\mathcal{G}_\mathrm{max}$	maximum of image spectrum
$\mathcal{H}$	Hilbert transformation
$\mathcal{L}$	light field
$\mathcal{L}_0$	illuminating light field
$\mathcal{L}_R$	light field reflected from the sea surface
$\mathcal{L}_I$	light field refracted at the sea surface into the water body
$\mathcal{M}_{\dots}$	set or entity of ...
$\mathcal{O}(\dots)$	in the order of
$\mathcal{S}(\Omega)$	3D variance spectrum of sea state [$\mathrm{m}^4\mathrm{s\ rad}^{-3}$]
$\mathcal{S}_\mathrm{max}$	maximum of sea-state spectrum [$\mathrm{m}^4\mathrm{s\ rad}^{-3}$]
$\hat{\mathcal{S}}(\Omega)$	3D complex-valued spectrum of sea state [$\mathrm{m}^4\mathrm{s\ rad}^{-3}$]
$\mathcal{S}_\mathrm{atm}$	atmospheric source term
$\mathcal{S}_\mathrm{diss}$	dissipation source term
$\mathcal{S}_\mathrm{nl}$	nonlinear source term

$\vec{E}$	3D electric field strength [(Vm^{-1},Vm^{-1},Vm^{-1})]
$\vec{H}$	3D magnetic field strength [(Am^{-1},Am^{-1},Am^{-1})]
$\vec{b}$	local bandwidth vector
$\vec{k}$	2D wavenumber vector of sea-surface waves [(rad m^{-1},rad m^{-1})]
$\vec{k}_{\mathrm{em}}$	3D electro-magnetic wavenumber vector [(rad m^{-1},rad m^{-1},rad m^{-1})]
$\vec{n}$	unit vector normal to surface
$\vec{r}$	spatial vector [(m,m,m)]
$\vec{r}_0$	spatial vector: orign of coordinate system toward observer [(m,m,m)]
$\vec{s}$	2D surface-slope vector
$\vec{s}_0$	direction of incident light ray vector
$\vec{s}_B$	direction of refracted light ray vector
$\vec{s}_I$	direction of upwelling light ray vector
$\vec{s}_R$	direction of reflected light ray vector
$\vec{u}_c$	2D near-surface current vector [(ms^{-1},ms^{-1})]
$\vec{u}_e$	2D vector of the velocity of encounter [(ms^{-1},ms^{-1})]
$\vec{u}_s$	2D vector of sensor velocity [(ms^{-1},ms^{-1})]

A_0	unit area
C_G	group velocity of a group of sea-surface waves [(ms^{-1},ms^{-1})]
C_P	phase velocity of a sea-surface wave [(ms^{-1},ms^{-1})]
$E(\dots)$	expectation value
$G \in \mathbb{B}_n$	gray value
Hs	significant wave height [m]
M	modulation-transfer function [m^{-1}]
M_0	linear part of the MTF [m^{-1}]
M_q	quadratic part of the MTF [m^{-1}]
M_n	n-th harmonic part of the MTF [m^{-1}]
R	2D spatial domain [(m,m)]
R_i	discrete 2D spatial domain [(m,m)]
T	measurement duration [s]
W	wind velocity [ms^{-1}]
X, Y	spatial measurement lengths [m]
$X \otimes Y \otimes T$	3D spatio-temporal measurement box [(m,m,s)]
X_W	wind fetch [km]

c	speed of light [ms^{-1}]
d	water depth [m]
d_λ	penetration depth of a sea surface wave [m]
$d\eta$	spectral amplitude of a sea surface wave [m]
f	frequency [s^{-1}]
g	gravitational acceleration [ms^{-2}]
i	imaginary unit
k	wavenumber [rad m^{-1}], magnitude
k_{EH}	electromagnetic wavenumber [rad m^{-1}], magnitude
k_x, k_y, k_z	Cartesian wavenumber components [rad m^{-1}]
$k_{x,Ny}, k_{y,Ny}$	Nyquist wavenumber components [rad m^{-1}]
$p(\dots)$	probability density of ...
$s_x,\ s_y$	components of the surface-slope vector $\vec{s}$
t	time [s]
x, y, z	spatial (Cartesian) coordinates [m]

$\Gamma(\dots)$	Gamma function of ...
Γ	surface tension of the air–water surface [Nm^{-1}]
$\Gamma_{\mathrm{H_2O}}$	surface tension of the air–water (clear water) surface [Nm^{-1}]
Δ	difference
Θ	3D spatio-temporal domain [(m,m,s)]
Θ_i	discrete 3D spatio-temporal domain [(m,m,s)]
Λ	local gray-level amplitude
$d\Xi$	solid angle
Υ	wavenumber domain [(rad m^{-1},rad m^{-1})]
Υ_i	discrete wavenumber domain [(rad m^{-1},rad m^{-1})]
Φ	radiant flux [N s^{-1}]
$\Phi(\cdots)$	phase map
Ω	3D wavenumber-frequency domain [(rad m^{-1},rad m^{-1},rad s^{-1})]
Ω_i	discrete 3D wavenumber-frequency domain [(rad m^{-1},rad m^{-1},rad s^{-1})]

ζ	sea-surface elevation [m]
ζ_0	amplitude of a sea-surface wave [m]
θ	incidence angle
ϑ	wave-travel direction
$\tilde{\vartheta}$	angle between wave-travel and observers direction
λ	wavelength [m]
λ_{em}	electromagnetic wavelength [m]
ρ	density [kg m^{-3}]
$\rho_{\mathrm{H_2O}}$	density of clear water [kg m^{-3}]

$\rho_{\parallel}$	parallely polarized Fresnel coefficient
$\rho_{\perp}$	perpendicularly polarized Fresnel coefficient
$\rho_{\circledast}$	unpolarized Fresnel coefficient
ς	intrinsic dispersion of sea-surface waves [rad s^{-1}]
ς^+, ς^-	positive and negative solution of dispersion [rad s^{-1}]
τ	wave period [s]
ϕ	wave phase
ϕ_0	initial wave phase
φ	observers horizontal viewing direction
ω	circular frequency [rad s^{-1}]
ω_D	Doppler frequency [rad s^{-1}]
$\tilde{\omega}$	dispersion [rad s^{-1}]
$\tilde{\omega}^+$	positive dispersion [rad s^{-1}]
$\tilde{\omega}^-$	negative dispersion [rad s^{-1}]

Abbreviations

1D	one-dimensional
2D	two-dimensional
3D	three-dimensional
AGF	**A**daptive **G**abor **F**ilter
ALR	**A**mt für **L**ändliche **R**äume
AM-FM	**A**mplitude **M**odulation **F**requency **M**odulation
CCD	**C**harged **C**oupled **D**evice
CEDEX	**CE**ntro **D**e **E**studio y E**X**perimentacion
CEPYC	**CE**ntro de **P**uertos **Y** **C**ostas
DDF-S	**D**ispersive-**D**irectional-**F**requency **S**eparation
DiSC	**Di**spersive **S**urface **C**lassificator
FFT	**F**ast **F**ourier **T**ransformation
FFT^{-1}	inverse **F**ast **F**ourier **T**ransformation
GCP	**G**round **C**ontrol **P**oint
HYPASUS	**Hy**brid **Pa**rametrical Wave Model **Su**per **S**hallow
IR	**I**nfra **R**ed
ISG	**Image** **S**lope **G**auge
ITF	**I**mage-**T**ransfer **F**unction
JONSWAP	**JO**int **N**orth **S**ea **WA**ve Ex**P**eriment
MTF	**M**odulation-**T**ransfer **F**unction
MTF_G	Gabor filter
MTF_{GM}	modified Gabor filter
MUSIC	**MU**ltiple **SI**gnal **C**lassification
OTF	**O**ptical-**T**ransfer **F**unction
RAM	**R**andom **A**ccess **M**emory
RGB	**R**ed **G**reen **B**lue
SAR	**S**ynthetic **A**perture **R**adar
TMA	**T**exel **M**arsen **A**rsloe
WaMoS	**Wa**ve **Mo**nitoring **S**ystem

Icons

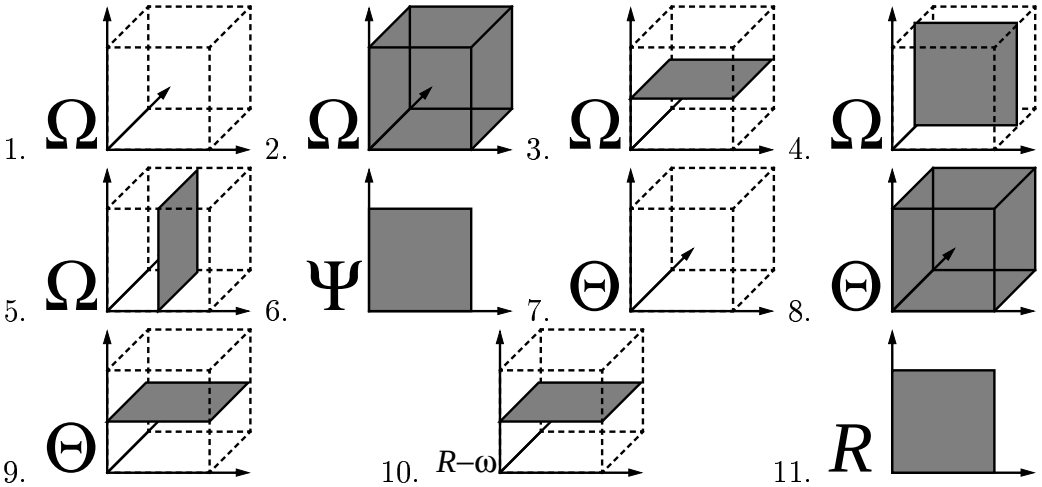

Figure 77: Illustrative icons for the following: **1.** 3D domain Ω, **2.** 3D spectrum $\mathcal{S}(\Omega) \in \Omega$, **3.** 2D Υ plane $\in \Omega$, **4.** 2D k_x–ω section $\in \Omega$, **5.** 2D k_y–ω section $\in \Omega$, **6.** 2D integrated Υ-spectrum $\in \Upsilon$, **7.** 3D spatio-temporal domain Θ, **8.** 3D spatio-temporal measurement box $X \otimes Y \otimes T \in \Theta$, **9.** 2D spatial image $X \otimes Y \in \Theta$, **10.** 2D spatial image $X \otimes Y$ at frequency ω, and **11** 2D spatial map.

A Mapping from World-Coordinate to Image-Coordinate System Using the Tsai Algorithm

A.1 Mapping from World-Coordinate to Camera-Coordinate System

The origin of the camera-coordinate system is the optical centerpoint, the intersection of the optical axis and the image plane. The z axis coincides with the optical axis, and the x axis and the y axis are aligned with the horizontal and vertical pixel lines, respectively. The camera coordinates are denoted by column vectors $(x_{\mathrm{cc}}, y_{\mathrm{cc}}, z_{\mathrm{cc}})^T$. Transition from world to camera coordinates requires a translation and a rotation:

$$\begin{pmatrix} x_{\mathrm{cc}} \\ y_{\mathrm{cc}} \\ z_{\mathrm{cc}} \end{pmatrix} = \mathbf{R} \cdot \begin{pmatrix} x_{\mathrm{wc}} \\ y_{\mathrm{wc}} \\ z_{\mathrm{wc}} \end{pmatrix} + \vec{t}, \tag{A.1}$$

where

$$\mathbf{R} = \begin{pmatrix} r_1 & r_2 & r_3 \\ r_4 & r_5 & r_6 \\ r_7 & r_8 & r_9 \end{pmatrix} \tag{A.2}$$

denotes a rotation matrix and $\vec{t}$ denotes a translation vector. The elements of the matrix $\mathbf{R}$ and $\vec{t}$ represent the extrinsic parameters of the camera-calibration model which convey the information about the camera position and orientation with respect to the world-coordinate system.

A.2 Perspective Projection

Next, the camera coordinates are projected to the image plane according to a pinhole-camera model. The projected coordinates are assigned to the undistorted image-coordinate system, denoted by 2D column vectors, $(x_{\mathrm{uc}}, x_{\mathrm{uc}})^T$. The relationship between the camera and the undistorted image coordinate system is given by

$$\begin{pmatrix} x_{\mathrm{uc}} \\ y_{\mathrm{uc}} \end{pmatrix} = \frac{f}{z_{\mathrm{cc}}} \cdot \begin{pmatrix} x_{\mathrm{cc}} \\ y_{\mathrm{cc}} \end{pmatrix}. \tag{A.3}$$

The effective focal length, f, of the pinhole-camera model belongs to the intrinsic parameters conveying the internal information about the camera components and about the interface of the camera with the viewing system.

A.3 Lens Distortion

As a result of lens distortion the pinhole-camera model does not hold and has to be replaced by models that take positional errors on the image plane due

to lens distortion into account. Because of the radial symmetry of optical lens systems, to the first order not the angle but only the radius is distorted. The radial distortion is approximated by

$$R_{\mathrm{uc}} = R_{\mathrm{dc}} \cdot (1 + \kappa_1 \cdot R_{\mathrm{dc}}^2), \tag{A.4}$$

where

$$R_{\mathrm{uc}} = \sqrt{x_{\mathrm{uc}}^2 + y_{\mathrm{uc}}^2} \text{ and } R_{\mathrm{dc}} = \sqrt{x_{\mathrm{dc}}^2 + y_{\mathrm{dc}}^2} \tag{A.5}$$

are the undistorted radius and distorted radii respectively. The intrinsic parameter, κ_1, in (A.4) is termed the first-order radial distortion coefficient. The distorted image coordinates are given by

$$\begin{pmatrix} x_{\mathrm{dc}} \\ y_{\mathrm{dc}} \end{pmatrix} = \frac{R_{\mathrm{dc}}}{R_{\mathrm{uc}}} \cdot \begin{pmatrix} x_{\mathrm{uc}} \\ y_{\mathrm{uc}} \end{pmatrix}. \tag{A.6}$$

A.4 Transformation to Pixel Coordinates

Finally the distorted image coordinates are transformed to pixel coordinates by scaling, and translation:

$$\begin{pmatrix} x_{\mathrm{ic}} \\ y_{\mathrm{ic}} \end{pmatrix} = \begin{pmatrix} \frac{S_x}{dp_x} & 0 \\ 0 & \frac{1}{dp_y} \end{pmatrix} \cdot \begin{pmatrix} x_{\mathrm{dc}} \\ y_{\mathrm{dc}} \end{pmatrix} + \begin{pmatrix} C_x \\ C_y \end{pmatrix}. \tag{A.7}$$

The following intrinsic parameters specify the transformation: the translation vector, $(C_x, C_y)^T$, specifies the z axis intercept of the camera-coordinate system. The parameters dp_x and dp_y denote the effective x and y dimensions of the pixels in the frame grabber. A scale factor, S_x, accounts for any uncertainty in the frame grabber's resampling of the horizontal scanline.

B Description of Spectral Corrections

The facors of (5.7) are described in the Secs. B.1 to B.4.

B.1 Geometrical Transformations in the Wavenumber Domain

The transformation of the transfer functions $NN(\vec{k})$ and $OTF(\vec{k})$ from pixel-wavenumber to world-wavenumber coordinates requires the transfer of the geometrical transformation steps from the spatial to the wavenumber domain. Affine coordinate transformations are transferred as follows: Let

$$g(\vec{x}) = f(y(\vec{x})) = f(\mathbf{A}[\vec{x} + \vec{b}]). \tag{B.1}$$

Their corresponding Fourier transformations are related by

$$\hat{g}(\vec{k}_{\mathrm{WC}}) = \frac{1}{|\mathrm{det}\mathbf{A}|} \cdot \exp(i\, \vec{k}_{\mathrm{WC}}^T \cdot \vec{b}) \cdot \hat{f}([\mathbf{A}^T]^{-1}\, \vec{r}_{\mathrm{WC}}), \tag{B.2}$$

where the wavenumber vector, $\vec{k}_{\mathrm{WC}}$, corresponds to the spatial world-coordinate vector $\vec{r}_{\mathrm{WC}}$ [GK95].
Because a spatial translation results only in a phase shift in the wavenumber domain, this translation is neglected. Additionally, the factor $1/|\mathrm{det}\mathbf{A}|$ is neglected, because $NN(\vec{k}_{\mathrm{WC}})$ and $OTF(\vec{k}_{\mathrm{WC}})$ are normalized after transferring the wavenumber coordinates according to

$$\vec{k}_{\mathrm{CC}} = [\mathbf{A}^T]^{-1} \cdot \vec{k}_{\mathrm{WC}}, \tag{B.3}$$

where the wavenumber vector, $\vec{k}_{\mathrm{CC}}$, corresponds to the spatial camera-coordinate vector, $\vec{r}_{\mathrm{CC}}$. The geometrical transformation steps are transferred into the wavenumber domain as follows:

1. **Mapping of the world-coordinate to the camera-coordinate system**
   World coordinates are transformed to camera coordinates by the following equation

$$\begin{pmatrix} k_{x,\mathrm{CC}} \\ k_{y,\mathrm{CC}} \end{pmatrix} = \frac{1}{r_1 \cdot r_5 - r_2 \cdot r_4} \cdot \begin{pmatrix} r_5 & -r_4 \\ -r_2 & r_1 \end{pmatrix} \cdot \begin{pmatrix} k_{x,\mathrm{WC}} \\ k_{y,\mathrm{WC}} \end{pmatrix}. \tag{B.4}$$

2. **Perspective projection**
   The camera coordinates are transformed to the undistorted camera coordinates by

$$\begin{pmatrix} k_{X,\mathrm{UC}} \\ k_{Y,\mathrm{UC}} \end{pmatrix} = \frac{z_{\mathrm{CC}}}{f} \cdot \begin{pmatrix} k_{x,\mathrm{CC}} \\ k_{y,\mathrm{CC}} \end{pmatrix}, \tag{B.5}$$

   where

$$z_{\mathrm{CC}} = r_7 \cdot x_{\mathrm{WC}} + r_8 \cdot y_{\mathrm{WC}} + t_z. \tag{B.6}$$

   The perspective projection is inhomogeneous because it is dependent on the pixel location $(x_{\mathrm{WC}}, y_{\mathrm{WC}})^T$.

3. **Lens distortion**
   This step is not an affine transformation. But the effect is small and can be neglected:

$$\begin{pmatrix} k_{X,\mathrm{dc}} \\ k_{Y,\mathrm{dc}} \end{pmatrix} \approx \begin{pmatrix} k_{X\mathrm{uc}} \\ k_{Y\mathrm{uc}} \end{pmatrix}. \tag{B.7}$$

4. **Transformation to pixel coordinates**
   The distorted camera coordinates are transformed to pixel coordinates by

$$\begin{pmatrix} k_{X_f} \\ k_{Y_f} \end{pmatrix} = \begin{pmatrix} \frac{dp_x}{s_x} & 0 \\ 0 & dp_y \end{pmatrix} \cdot \begin{pmatrix} k_{X,\mathrm{dc}} \\ k_{Y,\mathrm{dc}} \end{pmatrix}. \tag{B.8}$$

B.2 Nearest-Neighbour Interpolation

The rectangular grid of the selected region of interest (ROI), specified in world coordinates, is mapped to pixel coordinates following the geometrical transformation steps 1–4 backward to pixel coordinates. The ROI grid is filled with gray levels of the nearest pixel of one of the half images. The nearest-neighbour interpolation imposes a low-pass filter in the wavenumber domain. In the spatial domain the interpolation kernel is a 2D box function, whose spectral representation is a 2D sinc function [Wol92]. The sinc function is transformed from pixel-wavenumber to world-wavenumber coordinates (see Fig. 78).

B.3 Wavenumber-Optical-Transfer Function

The OTF in pixel-wavenumber coordinates is determined with a method outlined by [Jäh97]. The diffraction-limited optical system is parametrized by a cone. The cone is transformed from pixel-wavenumber to world-wavenumber coordinates. The wavenumber-optical-transfer function was similiar to Fig. 6.13 in [Jäh97] (see also Fig. 78).

B.4 Frequency-Optical-Transfer Function

It is assumed that the shutter acts like a box function, and therefore the frequency part of the OTF is parametrized by a sinc function. For the shutter time of 1/60 s used during the experiments here the spectral sinc function is given in Fig. 79.

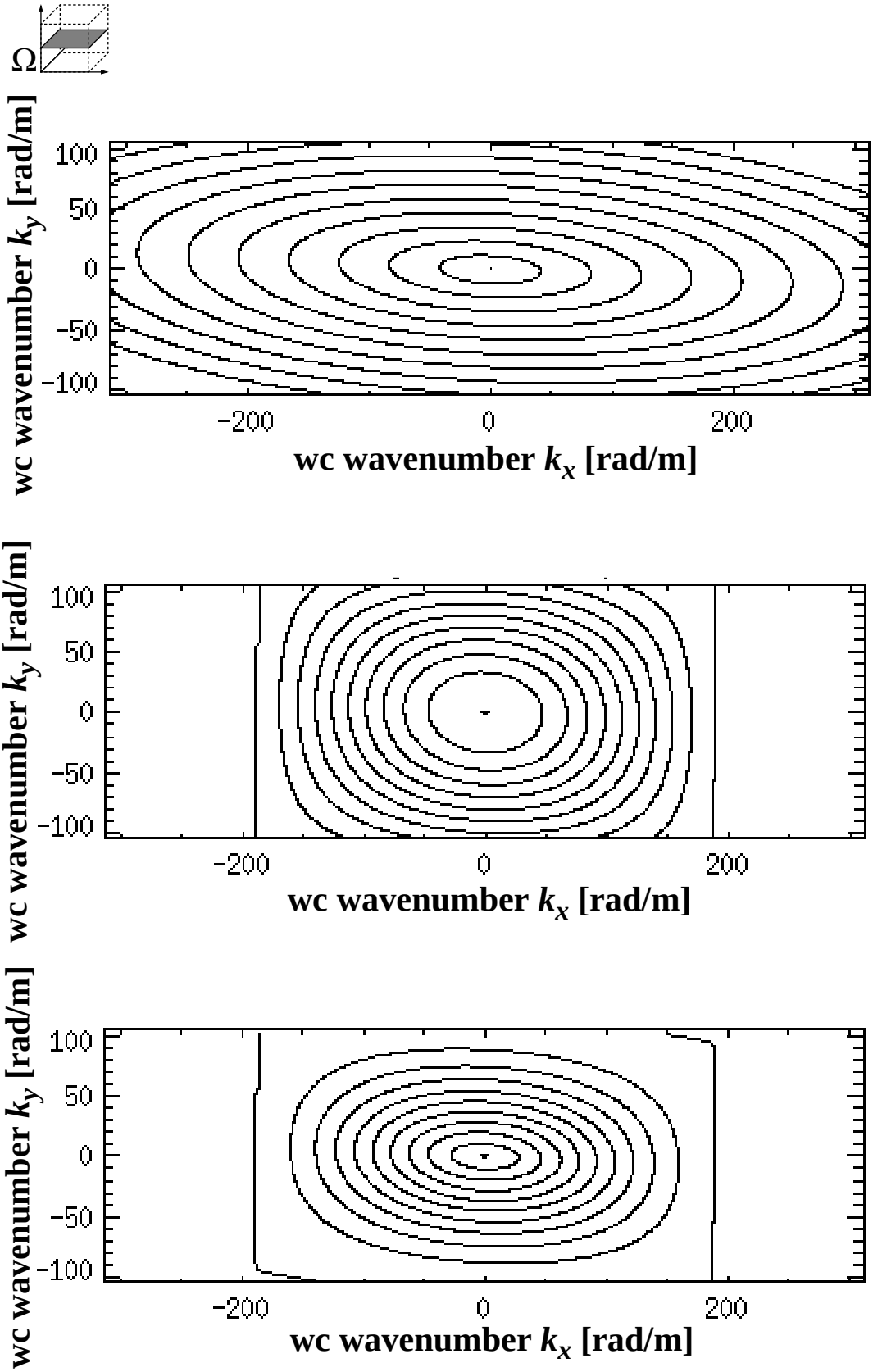

Figure 78: Optical Transfer Function, OTF. Top: $\mathrm{OTF}(\vec{k})$, center: $\mathrm{NN}(\vec{k})$, bottom: $\mathrm{OTF}(\vec{k}) \cdot \mathrm{NN}(\vec{k})$.

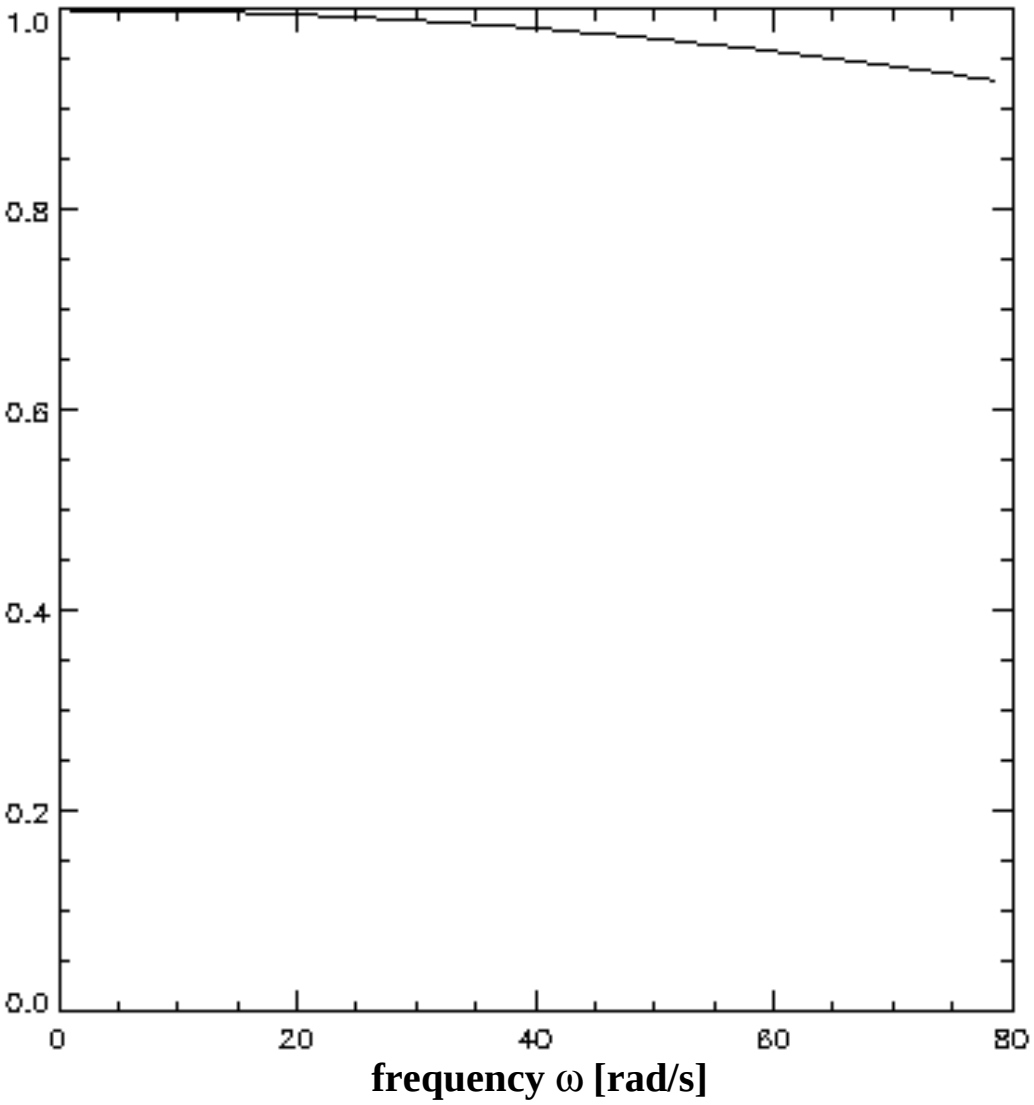

Figure 79: Frequency part of the spectral OTF(ω), given for a shutter time of 1/60 s.

C MUSIC Algorithm

After decomposition of a multi-component image sequence in a set of one-component images, the parametric spectral model

$$\begin{aligned} \hat{G}(x,y) &= \hat{S}(x,y) + \hat{N}(x,y) \\ &= \hat{A} \cdot \exp\{i(k_x x + k_y y)\} + \hat{N}(x,y) \end{aligned}$$

$$\begin{aligned} x &= \{0, 1, ..., n_{xs} - 1\} \\ y &= \{0, 1, ..., n_{ys} - 1\}, \end{aligned}$$

assumed by the MUSIC algorithm [Mar87] [SN89], can be applied. The complex values $\hat{G}$ in a local signal window of $n_x \times n_y$ pixels, are composed additively of a complex sine wave, $\hat{S}$, and a white-noise component, $\hat{N}$. For the analysis of radar images, the noise component results from speckle. According to this model, the autocorrelation matrix of the signal window is given by

$$\begin{aligned} \Gamma_{\hat{G}} &= \Gamma_{\hat{S}} + \Gamma_{\hat{N}} \\ &= \sigma_S^2 \, \vec{E} \cdot \vec{E}^{+} + \sigma_N^2 \, I, \end{aligned}$$

with the identity matrix, I, the variances of the signal and noise component σ_S^2 and σ_N^2 respectively, and the line-scanning vector $\vec{E}$ of the 2D complex sine wave

$$\vec{E} = \begin{pmatrix} 1 \\ \exp\{ik_x\} \\ ... \\ \exp\{i\,(n_{xs}-1)\,k_x\} \\ - - - \\ \exp\{ik_y\} \\ \exp\{i\,(k_x + k_y)\} \\ ... \\ \exp\{i\,((n_{xs}-1)\,k_x + k_y)\} \\ - - - \\ ... \\ - - - \\ \exp\{i\,(n_{ys}-1)\,k_y\} \\ ... \\ \exp\{i\,(n_{xs}-1)\,k_x + (n_{ys}-1)\,k_y\} \end{pmatrix}. \qquad \text{(C.1)}$$

Estimation values of $\Gamma_{\hat{G}}$ are obtained by shifting the signal window over a larger window.

The original MUSIC algorithm is based on an eigenvalue analysis of the autocorrelation matrix. The computational load of the algorithm is not practicable for the size of image data handled here. Therefore, an approximate algorithm, limiting computation time, is used [TCM96]. The direct estimation method exploits the block structure of the noise-free autocorrelation matrix $\vec{E} \cdot \vec{E}^{+}$.

- Inside a line block, each line is equal to the previous one multiplied by $a_x = \exp(i\,k_x)$. The coefficient a_x can be computed by minimizing the normalized error function

$$\epsilon_{a_x} = \frac{||\vec{v}_2 - a_x \cdot \vec{v}_1||^2}{||\vec{v}_2||^2}, \tag{C.2}$$

with the vectors formed by the lines $\vec{v}_1$ and $\vec{v}_2$ related by the factor a_x. The error function (C.2) is minimized by

$$a_x = \exp(ik_x) = \frac{\vec{v}_1^{+} \cdot \vec{v}_2}{||\vec{v}_1||^2}. \tag{C.3}$$

- The lines of each block are equal to the lines of the previous block multiplied by $a_y = \exp(i\,k_y)$. The coefficient a_y is computed by minimizing the normalized error function

$$\epsilon_{a_y} = \frac{||\vec{w}_2 - a_y \cdot \vec{w}_1||^2}{||\vec{w}_2||^2}, \tag{C.4}$$

with the vectors formed by the lines $\vec{w}_1$ and $\vec{w}_2$ related by the factor a_y. The error function (C.4) is minimized by

$$a_y = \exp(ik_y) = \frac{\vec{w}_1^{+} \cdot \vec{w}_2}{||\vec{w}_1||^2}. \tag{C.5}$$

D Local 3D Variance Spectra

The 2D Υ planes of a 3D local gray-level variance spectrum, calculated from the homegeneous area B of the optical CEDEX experiment is presented in Figs. 80 to 83. The local image spectrum was retrieved from one block located at $X_e \times Y_e = 0.16$ m $\times$ 0.48 m from the center of the analyzed area ($x_m = 2.64$ m, $y_m = 7.92$ m). The dispersion shell, intersecting the Υ plane is depicted by a white line. The wavenumber vectors, clustered close to the dispersion shell, are represented as circles in the wavenumber plane. The gray-level variance level is colour-coded, and the diameter is a measure of confidence (the outer green ring corresponds to $1 - \mathcal{C} = -40$ dB and the diameter 0 to $1 - \mathcal{C} = -10$ dB). Underlayed as a gray-level plot are the masks of the Gabor filters used for the decomposition in the global spectrum. The local bandwidth vectors, which are equal to the normalized gradients of local amplitude, are depicted by green arrows.

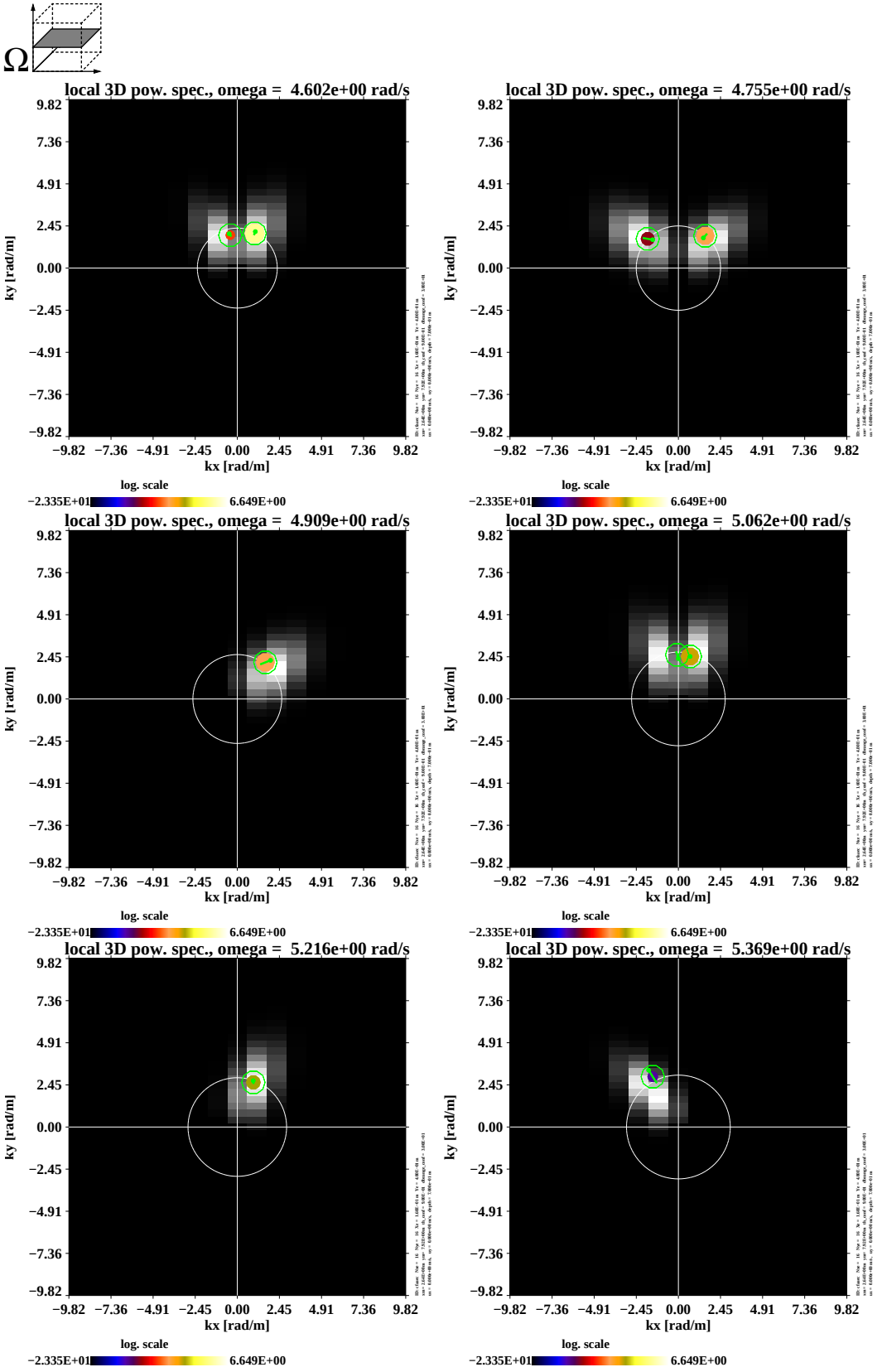

Figure 80: 2D Υ planes of a local 3D gray-level variance spectrum (from $\omega = 4.602$ rad/s to $\omega = 5.369$ rad/s).

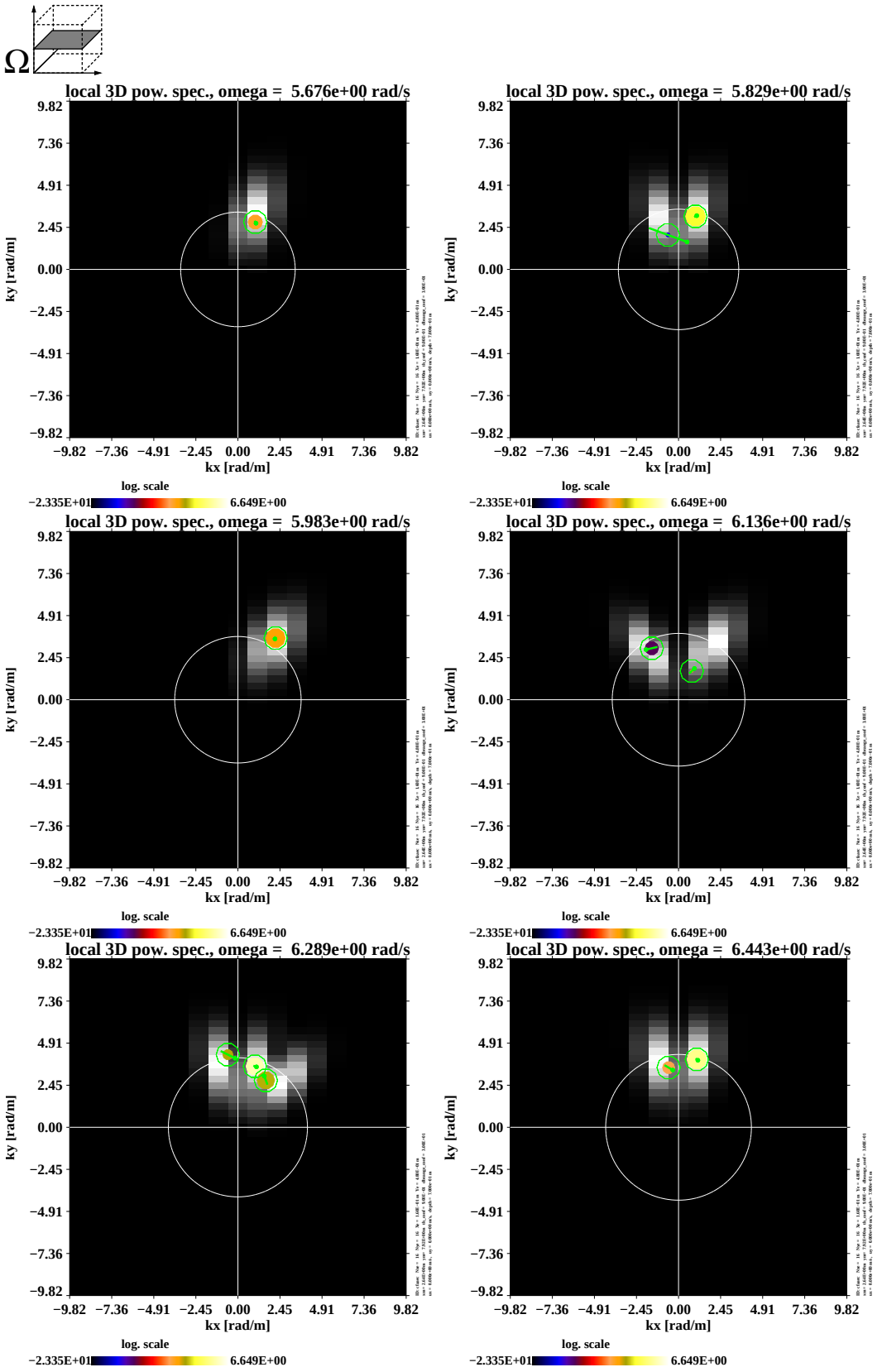

Figure 81: 2D Υ planes of a local 3D gray-level variance spectrum (from $\omega = 5.676$ rad/s to $\omega = 6.443$ rad/s).

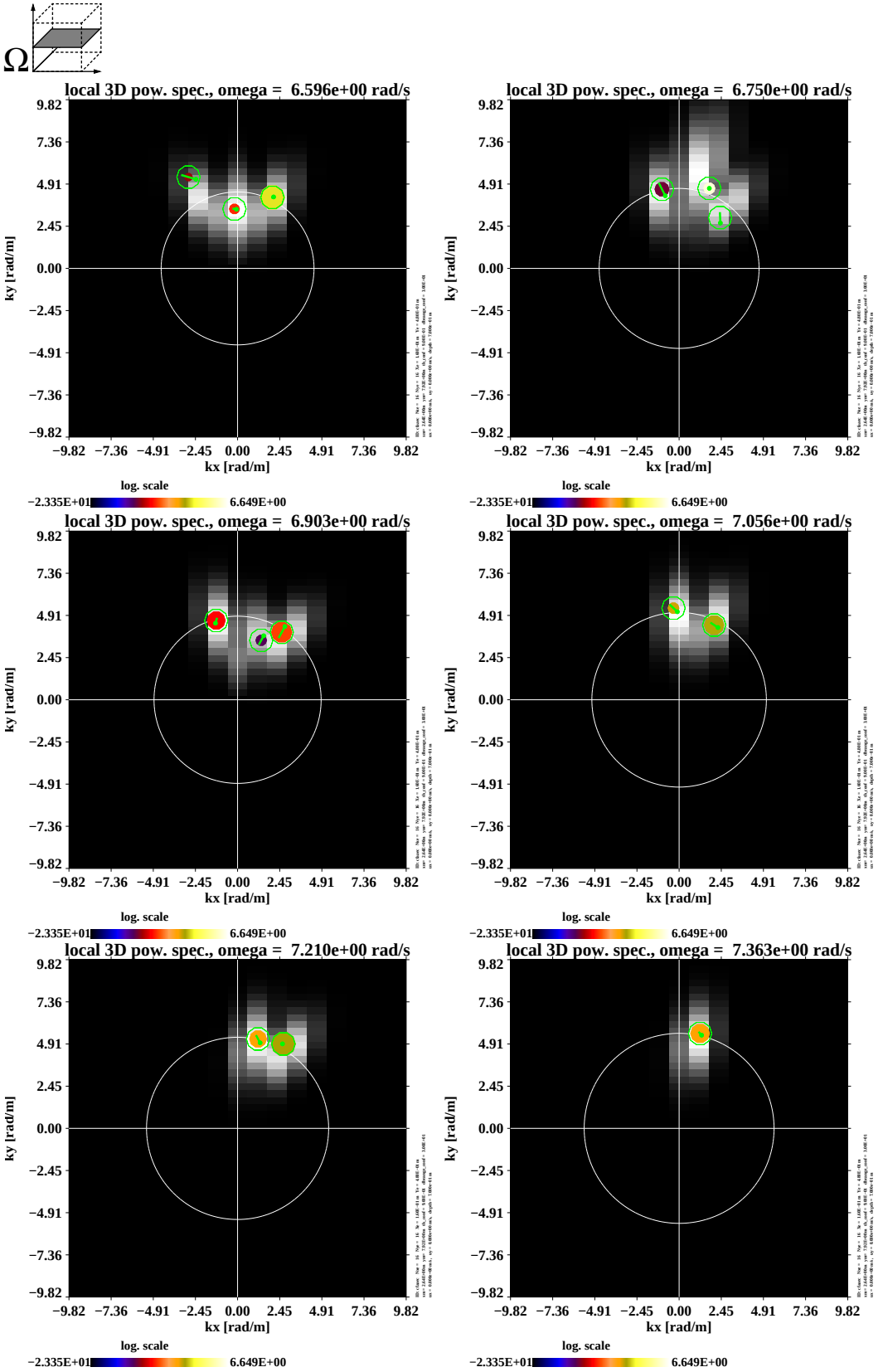

Figure 82: 2D Υ planes of a local 3D gray-level variance spectrum ($\omega = 6.596$ rad/s to $\omega = 7.363$ rad/s).

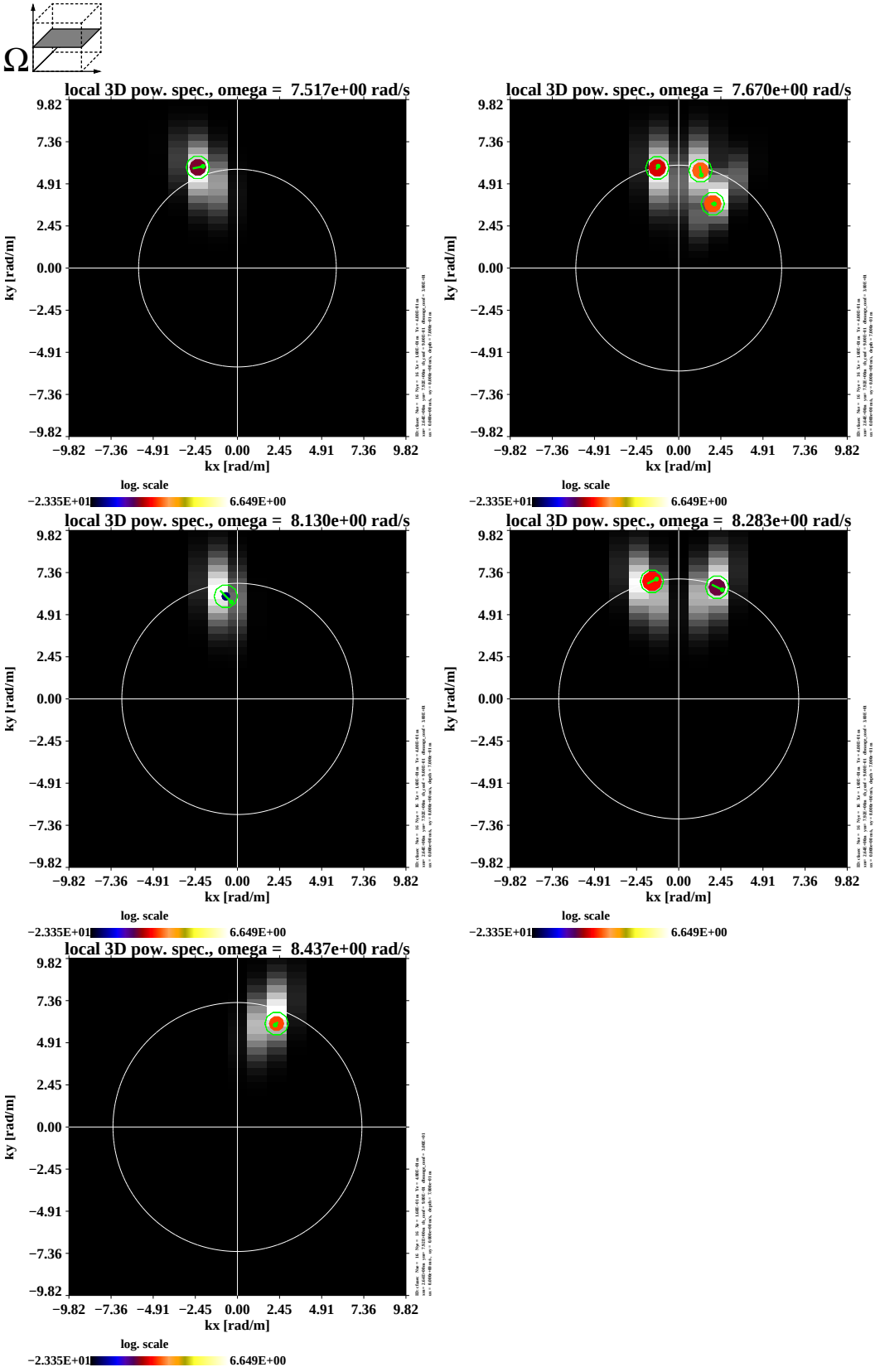

Figure 83: 2D Υ planes of a local 3D gray-level variance spectrum (from $\omega = 7.517$ rad/s to $\omega = 8.437$ rad/s).

E 1D Imaging Model

A numerical 1D model, based on ray tracing has been implemented to examine the transfer functions of tilt modulation and projective bunching (see Figs. 24 and 25) for the imaging of a sinusoidal wave. The assumptions of the 1D model are

- the surface model is a 2D complex-valued sine wave, $\zeta(x, y) = \zeta e^{i(k_x x + k_y y)}$, and
- parallel projection (this assumption holds if the distance from wave surface to camera is large compared to k and ζ_0).

The projection is calculated by ray tracing. In Fig. 84 the diagrams show the sinusoidal wave, the same wave imaged by tilt modulation, by projective bunching, and imaged by both imaging mechanisms. The following parameters are variables of the 1D model:

- camera incidence angle, θ,
- azimuthal angle, $\phi = \text{atan}(k_x, k_y)$,
- amplitude, ζ_0,
- wavenumber, k, and
- illumination (homogeneous, vertical and horizontal gradients, parallel polarized or perpendicular polarized) or unpolarized Fresnel coefficient).

The case of homogeneous unpolarized illumination will be presented here; only the principal results are shown.

1. **Azimuthal dependency**
   The azimuthal dependencies of the linear ITF and the energy ratio of the first-harmonic dispersion relation and the fundamental-mode dispersion relation are depicted in Fig. 85. In the upper row the thin lines indicate the linear tilt modulation. If only tilt modulation is performed by the 1D model (indicated by the thick line) weak nonlinear effects are observed. The modulation due to projective bunching significantly differs from the linear tilt modulation and therefore has a strong effect on the modulation. This can be seen in the right upper diagram, where tilt modulation and projective bunching are performed on the 1D model. Here two peaks are observed. This result is a strong indication that the effects due to projective bunching cannot be neglected. The lower row of Fig. 85 also indicates a strong contribution of projective bunching to nonlinear modes.

2. **Camera incidence-angle dependency**
   In Fig. 86 the linear ITF and the energy ratio of the first-harmonic dispersion relation and the fundamental-mode dispersion relation are

depicted. If only tilt modulation is performed, an increase in the ITF is given for high camera incidence angles (e.g. grazing incidence). The linear ITF is equal to 1 if only projective bunching is performed; this holds until the camera-incidence angle $90° - \theta$ is lower then the local-slope angle. The loss of information at the backside of a wave leads to a decrease in the ITF. The energy ratio of the tilt-modulation case indicates a weak nonlinear effect for low camera-incidence angles and high camera-incidence angles for projective bunching.

3. **Wavenumber dependency**
   The wavenumber dependencies on the linear ITF and on the energy ratio of the first harmonic and the fundamental mode dispersion relation are given in Fig. 87. A log–log plot type is chosen to prove whether if the wavenumber dependency can be described by a power law similiar to the ITF in (3.7). For the tilt-modulation case an increase in the ITF and the energy ratio is observed. For the projective-bunching case the linear ITF has a value of 1 for a wide range of wavenumbers. At high wavenumbers a decrease in the linear ITF indicates a loss of information on the shape of the wave due to occlusion. The coefficient β, having a theoretical value of 2 for linear tilt modulation, is also close to this value for a wide range of wavenumbers, also if projective bunching is included in the 1D model. Deviations are due to coverage of steep waves. The energy ratio for all three cases shows an increase in the nonlinear energy with increasing wavenumber. The energy ratio can also be described by a power law with the value $\beta = 2$.

4. **Harmonic dependency**
   The fundamental-mode signal and the first-harmonic signal are compared with reference to the wave amplitude (and therefore implicitely to the wave slope). In Fig. 88 the ratio of the first-harmonic signal and the fundamental-mode signal is given for tilt modulation, projective buncing, and the combination of both imaging mechanisms. The results indicates that tilt modulation alone introduces first-harmonic signal. The projective-bunching diagrams only shows numerical noise. By Selecting the fundamental mode and the first harmonic with corresponding dispersion filters, the power ratio may be used to calibrate experimental image spectra.

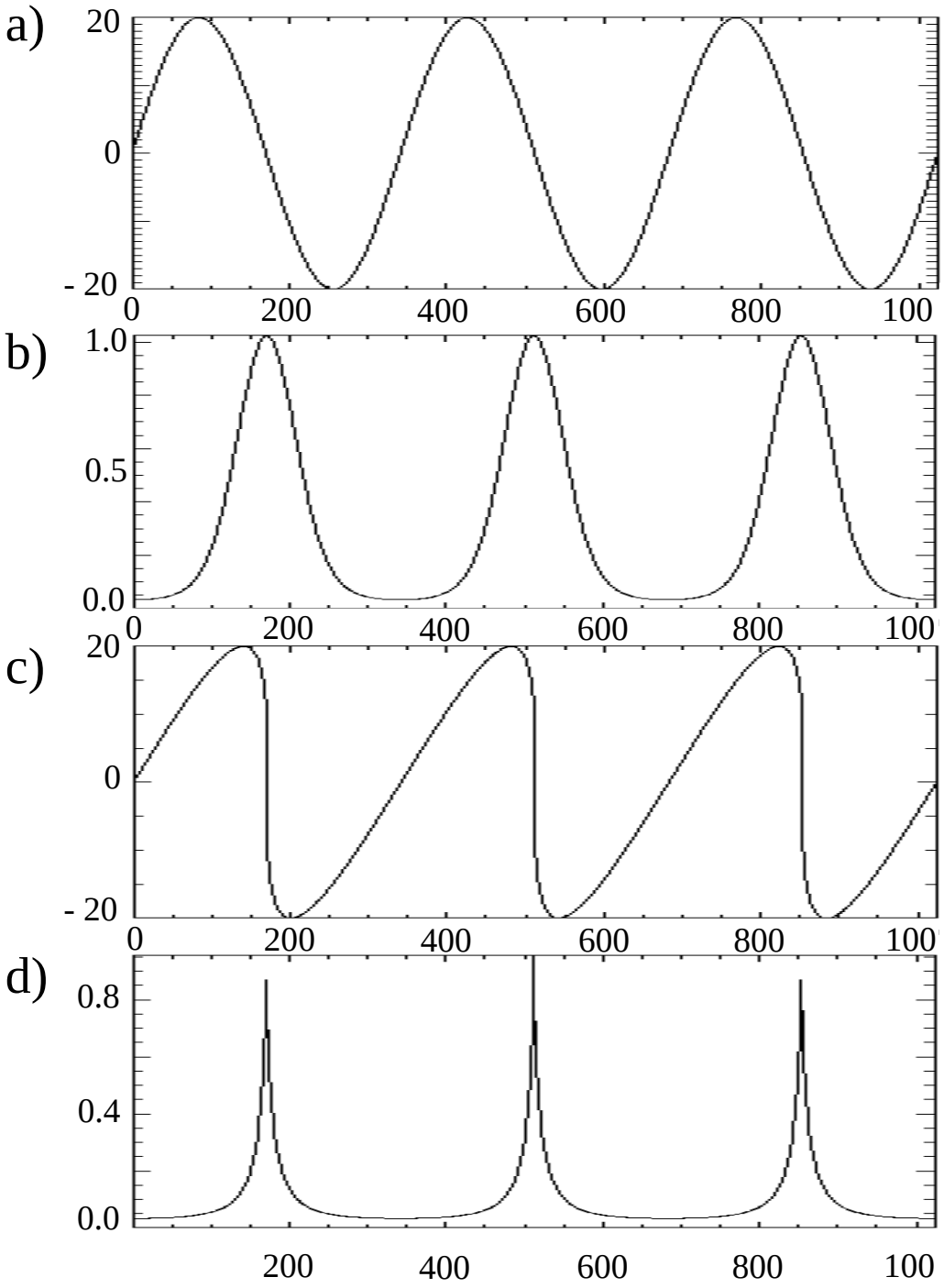

Figure 84: 1D imaging of a complex-valued sinusoidal plane wave: **a)** real part of the sinusoidal wave, **b)** wave imaged by tilt modulation, **c)** wave imaged by projective bunching, and **d)** wave imaged by both imaging mechanisms.

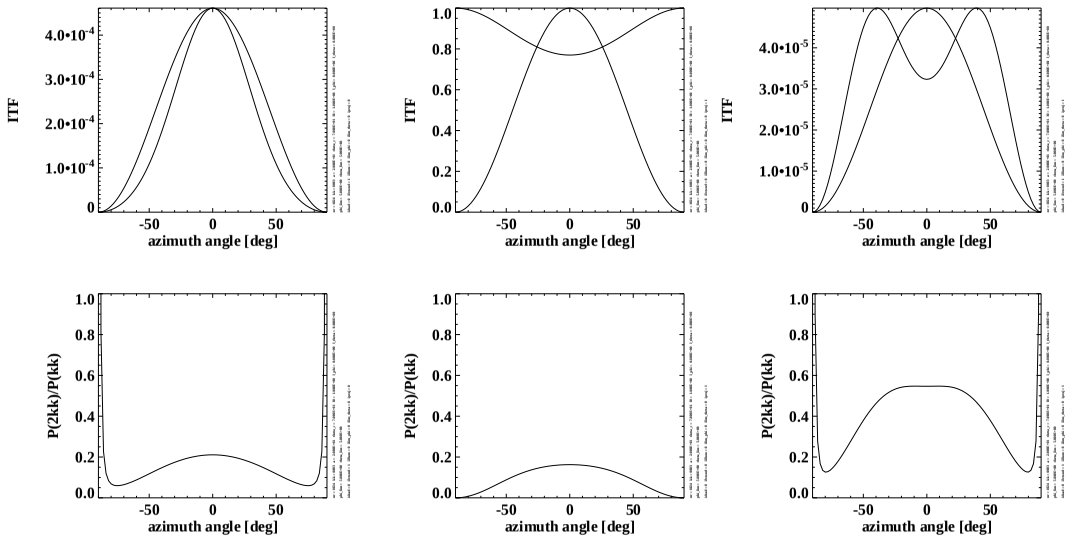

Figure 85: In the upper row the dependence of the ITF on the azimuthal angle is given. Bold lines indicate the results of the 1D optical model, and thin lines indicate the theoretical azimuthal dependency of the theoretical linear tilt modulation. In the lower row the ratio of the energies of the first-harmonic dispersion relation and the fundamental-mode dispersion relation are presented. In the left column tilt modulation is presented, in the middle column projective bunching is shown, and in the left column both imaging mechanisms are taken into account. The wave amplitude and the wavenumber have the magnitudes $k = 0.0184$ rad/pixel and $\zeta = 20$ pixel, i.e. the steepness is equal to $\zeta\lambda = 0.0584$.

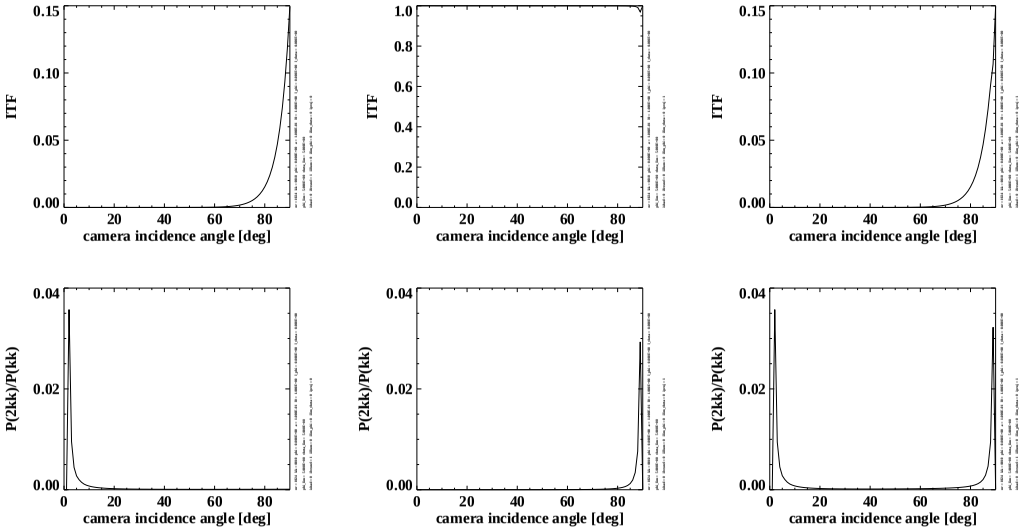

Figure 86: In the upper row the ITF of the camera's incidence-angle dependency is depicted. In the lower row the ratio of the energies of the first-harmonic dispersion relation and the fundamental-mode dispersion relation is presented. The left column depicts tilt modulation, the middle column projective bunching, and the right column both imaging mechanisms. The wave amplitude and the wavenumber have the magnitudes $k = 0.0613$ rad/pixel and $\zeta = 0.1$ pixel, i.e. the steepness is equal to $\zeta\lambda = 0.000976$.

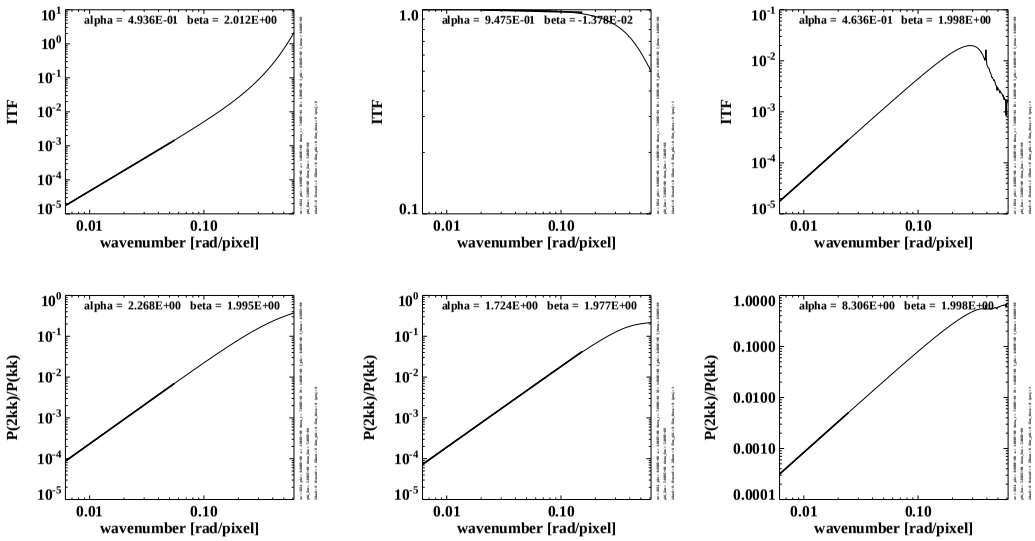

Figure 87: In the upper row the wavenumber dependency of the ITF is depicted on a log–log scale. The thin lines indicate the numerical results of the 1D model. The bold lines are the result of a least-squares fit of a straight line. The coefficients α and β indicate the intercept and the gradient of the line. In the lower row the ratio of the energies of the first-harmonic dispersion relation and the fundamental-mode dispersion relation is depicted on a log–log scale. In the left column tilt modulation is given, in the middle column projective bunching, and in the left column both imaging mechanisms. The wave amplitude has the magnitude $\zeta = 1$ pixel.

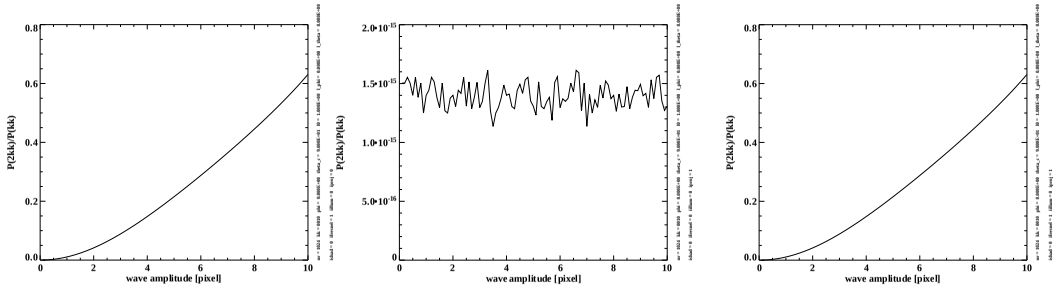

Figure 88: Ratio of the first-harmonic signal to the fundamental-mode signal versus wave amplitude for tilt modulation (left), projective bunching (middle), and both imaging mechanisms (right). The wavenumber has the magnitude $k = 0.0613$ rad/pixel.

F Test Images

Inhomogeneous test images with a maximum of two components and additive spectral noise are generated to examine the use of Gabor filtering for noise suppression and the separation into different components. The accuracies of the pixelwise- and blockwise local wavenumber are compared.

F.1 Definition

The test images are modeled with regard to the superposition of two wave components. Each of the components is an amplitude- and phase-modulated complex-valued function of the form

$$\hat{g}(x,y) = \sum_{i=1}^{2} g_i(x,y)\, e^{j\Phi_i(x,y)}. \tag{F.1}$$

$$g_i = g_{0,i} + g_{x,i} \cdot x + g_{y,i} \cdot y, \tag{F.2}$$

and the phase of a wave component is given by

$$\Phi_i = \Phi_{0,i} + k_{x,i} \cdot x + k_{y,i} \cdot y + \frac{1}{2} \cdot k_{xx,i} \cdot x^2 + k_{xy,i} \cdot xy + \frac{1}{2} \cdot k_{yy,i} \cdot y^2. \tag{F.3}$$

The local-wavenumber vector of a one-component image is created by the spatial gradient of the phases Φ_i:

$$\vec{k}_{l,i} = \nabla_r \Phi_i = \vec{k}_i + \mathbf{K}_i \cdot \vec{r}. \tag{F.4}$$

The matrix

$$\mathbf{K}_i = \begin{pmatrix} k_{xx,i} & k_{xy,i} \\ k_{xy,i} & k_{yy,i} \end{pmatrix} \tag{F.5}$$

describes a linear spatial variation of the local-wavenumber vector.
In the spectral domain, additive uncorrelated white Gaussian noise is applied to the wave components:

$$\hat{\mathcal{G}}(\Upsilon) = \hat{\mathcal{G}}_s(\Upsilon) + \hat{\mathcal{G}}_n(\Upsilon), \tag{F.6}$$

where $\hat{\mathcal{G}}_s$ is the signal, defined by (F.1), (F.2), (F.3) and (F.5), and $\hat{\mathcal{G}}_n$ is the spectral noise. $\hat{\mathcal{G}}_n$ is a complex-valued random variable. The real and imaginary parts are Gaussian distributed with mean 0 and standard deviation σ_n.

F.2 Parameter Settings

The parameters of the Cartesian grid of the test images are specified in Tab. 7. In Tab. 8 the two components are specified. The parameters of the Gabor filters used for the selection of the two components are given in Tab. 9. The noise level is set to $\sigma_n = 0.01$.

Table 7: Specification of the Cartesian grid of the test images.

N_x	256
Δx	1
X	256
N_y	256
Δy	1
Y	256

Table 8: Specification of the two components of the test images.

Parameter	C1	C2
g	1	0.5
g_x	0	0
g_y	0	0
Φ_0	0	0
k_x	0	0
k_y	$\pi/8$	$-\pi/8$
k_{xx}	$\pi/1600$	$\pi/1600$
k_{xy}	0	0
k_{yy}	$\pi/3200$	$\pi/3200$

Table 9: Specification of the two Gabor filters.

Parameter	G1	G2
k_{xm}	0	0
k_{ym}	$\pi/8$	$-\pi/8$
σ_{k_ϕ}	0.354	0.354
σ_{k_r}	0.141	0.141
ϕ	0°	0°

F.3 Noise Suppression

A one-component test image ($g_2 = 0$) is used to demonstrate the necessity for noise suppression for local-wavenumber estimation (see Fig. 89). The local wavenumber is blockwise estimated using a window of $n_{x,e} = 16$ pixels and $n_{y,e} = 16$ pixels. For the noiseless test image, a map of local wavenumbers is estimated, and the local wavelengths are overlayed on the phase image. To the test image a noise pedestal with a standard deviation of $\sigma_n = 0.01$ was added; this corresponds to a signal-to-noise ratio of 1.073 (total signal-to-noise ratio) or 64 (maximum signal-to-noise ratio). At this power ratio the local-wavenumber estimation fails. The applied Gabor filter is adapted to

the bandwidth of the global image spectrum. When Gabor filters are used, the noise level is decreased significantly. The noise reduction allows the local wavenumbers to be estimated.

F.4 Selection of One-Component Images

To obtain estimates of the local-wavenumber vector the multi-component image has to separated into one-component images. In Fig. 90 the synthesis of a complex-valued two-component image from two one-component images with an amplitude ratio of 2/1 is demonstrated. Both components are selected using Gabor filters which are adapted to the bandwiths of the global image spectrum (see Fig. 91).

F.5 Accuracy of Local-Wavenumber Estimation

The noisy one-component test images ($g_2 = 0$), after noise suppression by Gabor filtering, are used to compare the accuracy of the pixelwise and the blockwise local-wavenumber estimation method (with block sizes of 4 pixels $\times$ 4 pixels and 16 pixels $\times$ 16 pixels). In Fig. 92 scatter diagrams of the estimated versus the exact wavenumbers are given, and in Fig. 93 absolute errors of the estimated wavenumbers are presented. Using a block size of 4 pixels $\times$ 4 pixels, the accuracy is not improved in regard to the pixelwise calculation. Using a block size of 16 pixels $\times$ 16 pixels, the wavenumber resolution is enhanced by a factor between 3 and 4, at the expense of the spatial resolution. In the scatter diagrams (see Fig. 92) it can be seen that at the edges of the test image systematic errors occur due to edge effects of the Gabor filtering.

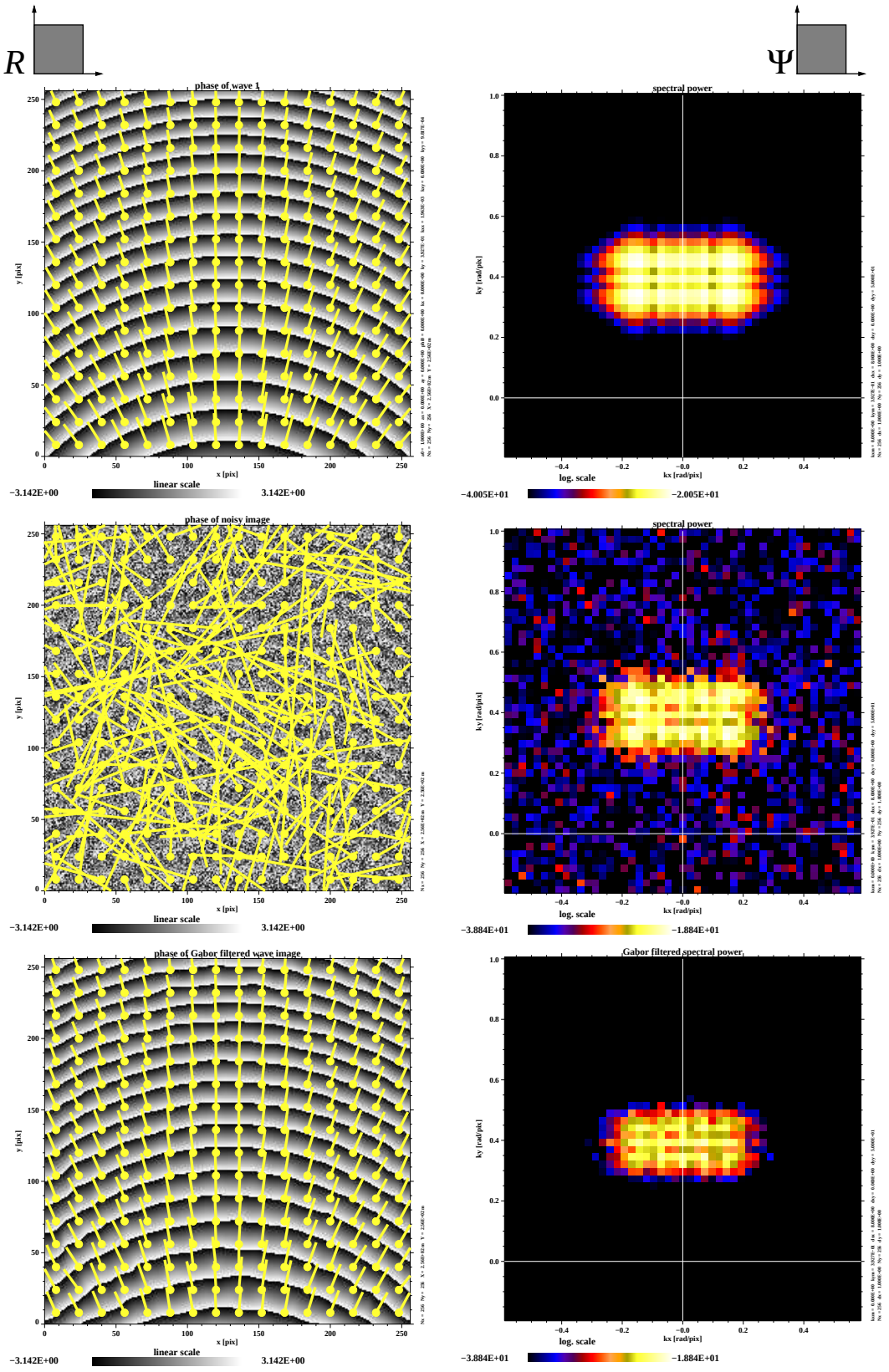

Figure 89: Noise reduction using a Gabor filter. Left: phase of the complex-valued images, with local wavelengths overlayed; right: global image spectra. Top: noiseless test image; center: noisy test image; bottom: test image with the noise removed.

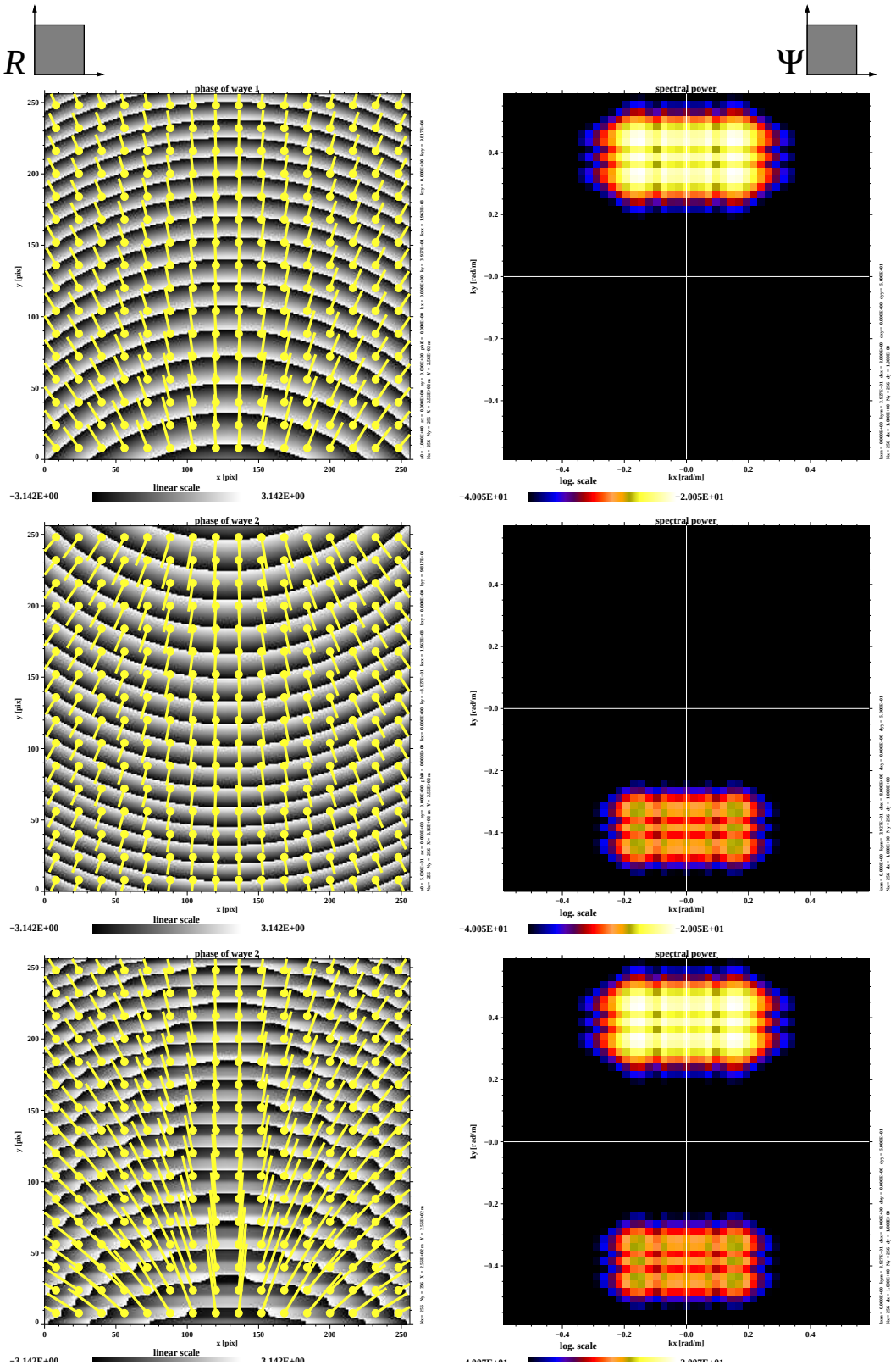

Figure 90: Synthesis of a two-component image. Left: phase of the complex-valued images, with overlayed local wavelengths; right: global image spectra. Top: first component; center: second component; bottom: the synthesized two-component image.

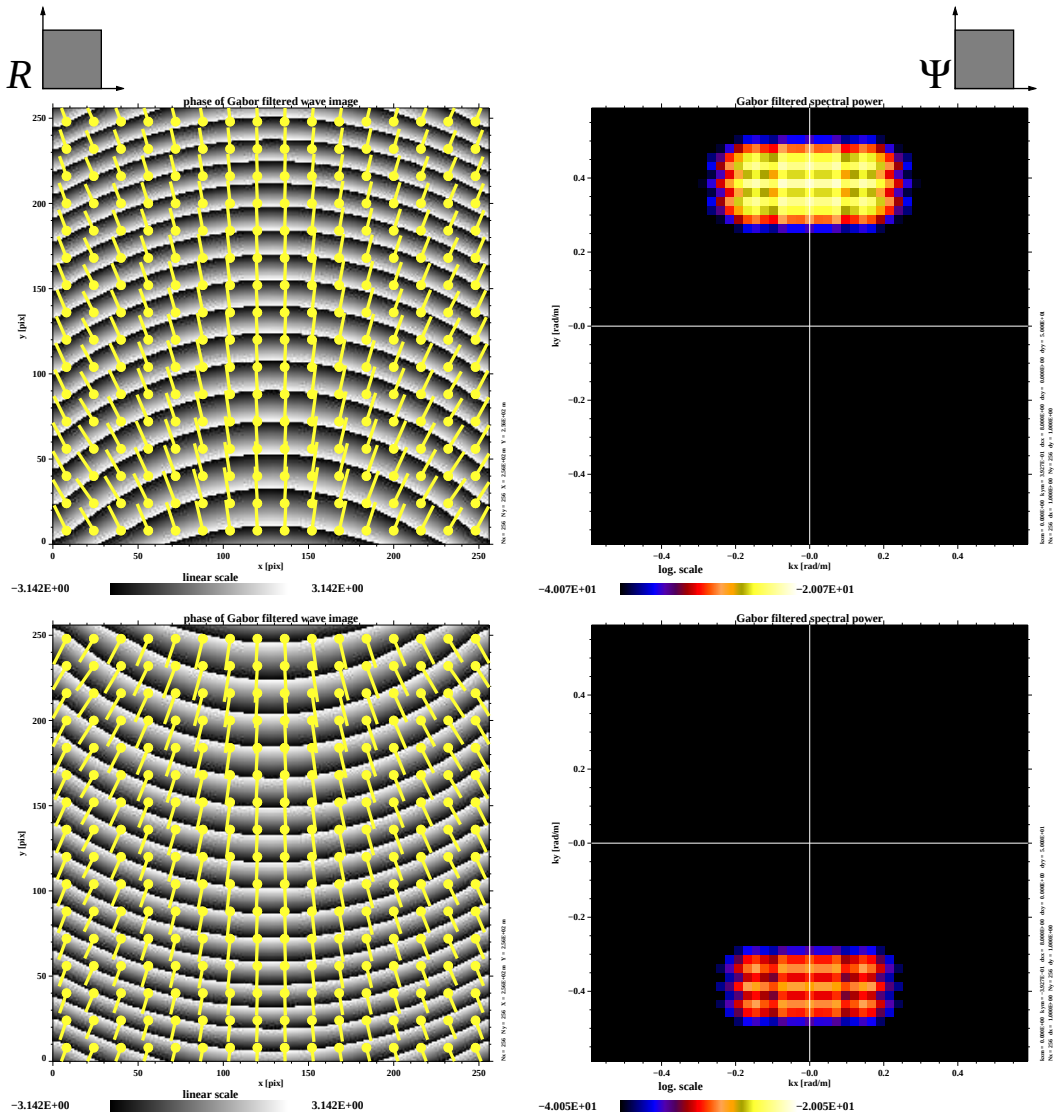

Figure 91: Selection of single components. Left: phases of the selected components, with overlayed local wavelengths; right: Gabor filtered global image spectra. Top: selected first component; bottom: second component.

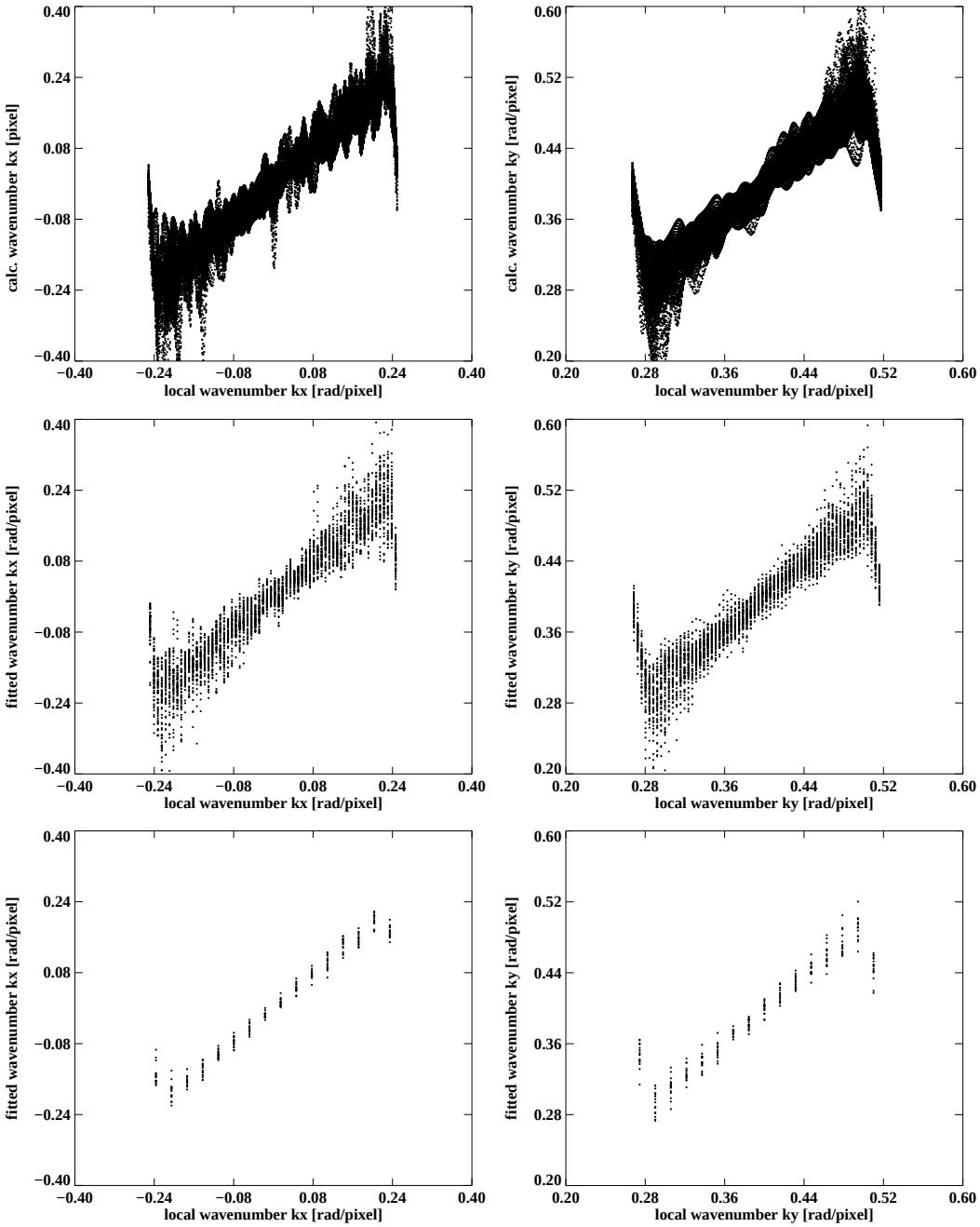

Figure 92: Scatter diagrams of the accuracy of local-wavenumber estimation: calculated wavenumber as a function of exact wavenumber. Left: wavenumber-vector component k_x; right: wavenumber-vector component k_y. Top: pixelwise estimation; center: blockwise estimation with block sizes 4 pixels × 4 pixels (center); bottom: 16 pixels × 16 pixels.

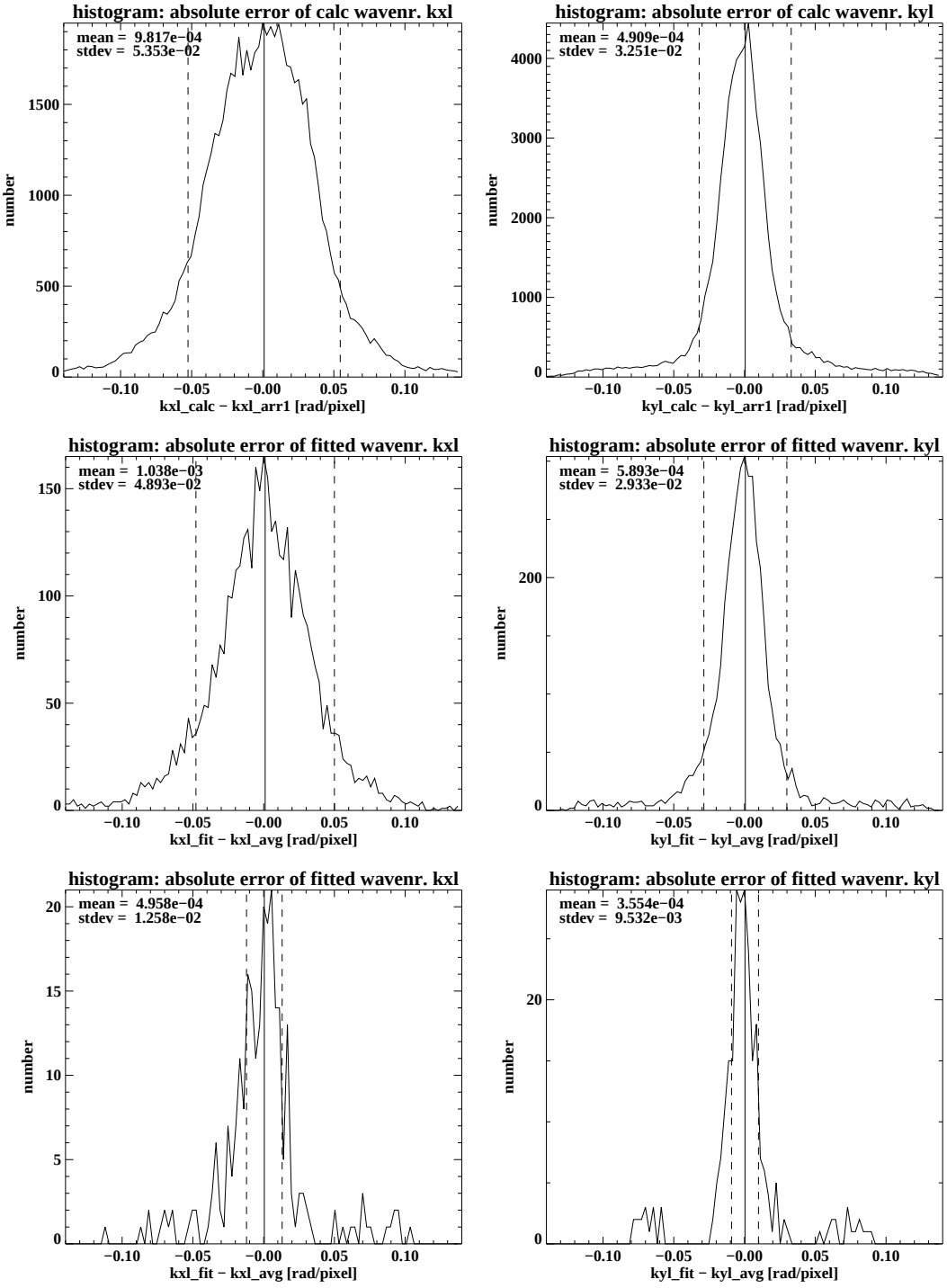

Figure 93: Histograms of the accuracy of local-wavenumber estimation. Left: wavenumber-vector components k_x; right: wavenumber-vector components k_y. Top: pixelwise estimation; center: blockwise estimation with block sizes 4 pixels × 4 pixels; bottom: blockwise estimation with 16 pixels × 16 pixels.

G Linearized Approach to Calibrate Optical Sea-Surface Image Sequences

G.1 Calibration Ansatz

Image spectra and surface-wave spectra are related by the ITF. The ITF can be parametrized by a power law (3.7). To deduce calibrated surface-wave spectra from image spectra, the calibration coefficients of the ITF are to be determined. Assuming tilt modulation (see Sec. 3.2.3), according to (3.11) the coefficient $\beta = 2$ and the magnitude and azimuthal dependency of α can be deduced from the experimental setup, i.e the camera-incidence angle, and radiometric measurements of the illumination.
Alternatively, the coefficients can be determined using in situ sensors. In a hydraulic wave tank, in situ wave gauges are standard equipment for measuring 1D ω spectra of the sea-surface elevation, ζ. The high-frequency part of surface-elevation spectra (beyond the peak frequency) can be described by a power law:

$$E_w(\omega) = \alpha_w \cdot \omega^{\beta_w}. \tag{G.1}$$

The introduction of a power law is motivated due to the fact, that especially for tilt modulation, dominant for optical imaging of sea-surface waves, it can be proved that the MTF follows a power law (see Sec. 3.2.3).
For deep-water waves the high-frequency part of the integrated image ω spectra can be parametrized by the following power law:

$$E_o(\omega) = \alpha_o \cdot \omega^{\beta_o}. \tag{G.2}$$

From (G.1) and (G.2) it follows that the frequency representation of the ITF is

$$\mathrm{ITF}(\omega) = \frac{E_o(\omega)}{E_w(\omega)} = \frac{\alpha_o}{\alpha_w} \cdot \omega^{(\beta_o - \beta_w)}. \tag{G.3}$$

If the deep-water dispersion relation is applied, the exponent β, in the Υ domain, is related to the exponents in the frequency domain by

$$\beta = \sqrt{\beta_o - \beta_w}. \tag{G.4}$$

If that the waves are imaged by tilt modulation ($\beta = 2$), and the high-frequency part of the surface-elevation spectrum shows the frequency dependency $\beta_w = -5$, the frequency dependency of the image spectrum should be $\beta_o = -1$. Parametrizing ω spectra by a power law results in

$$E_{dB}(\omega_{dB}) = \alpha_{dB} + \beta \cdot \omega_{dB}, \tag{G.5}$$

which is a straight line on a log–log scale, with

$$E_{dB} = 10 \cdot \log_{10}(E) \qquad \text{and} \qquad \omega_{dB} = 10 \cdot \log_{10}(\omega). \tag{G.6}$$

The exponent β can be determined by line fitting.
In the field, ocean-wave spectra are deduced from image sequences of the sea surface acquired by nautical radars. For nautical-radar image spectra, the ITF can also be parametrized with a power law. In contrast to optical image sequences, the exponent of wavenumber dependency has the magnitude, given by $\beta = 1$. After a calibration with a buoy, the value of the coefficient α can be deduced from the signal-to-noise ratio of the image spectrum [BHR99]. After calibration period, the in situ sensor can be removed. Using an optical sensor, it is only possible to abandon the in situ wave gauges if the illumination is controlled and held constant because a CCD camera is a passive system.

G.2 Results of Global Calibration

To obtain global empirical calibration, following the power law given in (3.7), 1D optical ω spectra and in situ wave-gauge ω spectra were compared. The the coefficients β calculated from (3.7) were retrieved from the filtered and integrated ω spectra of two image sequences acquired in area B; their accompanying wave-gauge spectra were compared to show the variability of this parameter. This variability prima facie contravenes the theory for linear tilt modulation (3.9) and the results retrieved with the 1D optical model described in Appendix E.
The image sequences were selected for the following parameter sets:

- sequence 1 (area B): $T_p = 1$ s, $s = 1$, $\vartheta_p = 0°$, $\mathrm{H_{max}} = 0.09$ m,
- sequence 2 (area B): $T_p = 2$ s, $s = 1$, $\vartheta_p = 0°$, $\mathrm{H_{max}} = 0.09$ m,

where T_p is the peak period of the wave fields, s is the spread parameter, ϑ_p is the spread parameter (with $\vartheta_p = 0°$: directed normal to the wave generators paddle panel) and $\mathrm{H_{max}}$ is the maximum wave height.
Example images of the sequences are presented in Fig. 94. The wave field with the peak period $T_p = 1$ s on the left-hand side shows shorter waves, and the wave field with the peak period $T_p = 2$ s on the right-hand side contains longer waves.
The 3D FFT was performed on both image sequences , yielding the 3D image Ω_i spectra $\mathcal{G}_1(\Omega_i)$ and $\mathcal{G}_2(\Omega_i)$. After dispersion-filtering of the the 3D spectra, the 1D ω spectra were calculated and compared with the in situ wave gauges of wave-gauge probe $\mathrm{S_4}$ (see Fig. 44).
The optical image sequences, each consisting of 256 images, were acquired within $T_o = 10.24$ s with a temporal sampling resolution of 25 Hz and a shutter time of 1/60 s. The optical 1D ω spectra therefore have 128 frequency bins, a frequency resolution of $\Delta\omega = 0.61$ rad $\mathrm{s^{-1}}$ and a Nyquist frequency of $\omega_{\mathrm{Ny}} = 78.54$ rad $\mathrm{s^{-1}}$. The time series, $\zeta(t)$, of the in situ wave-gauge probe $\mathrm{S_4}$ with a frequency resolution of 25 Hz was separated into 58 chunks of 256 temporal samples each. The time series has a duration of $T_w = 593.92$ s, and each chunk has a duration of $\Delta T_w = T_o = 10.24$ s. From these 58 chunks, 58 1D ω spectra, $\mathcal{S}_{w,n}(\omega)$, are calculated. The averaged ω spectrum, $\bar{\mathcal{S}}_w(\omega)$,

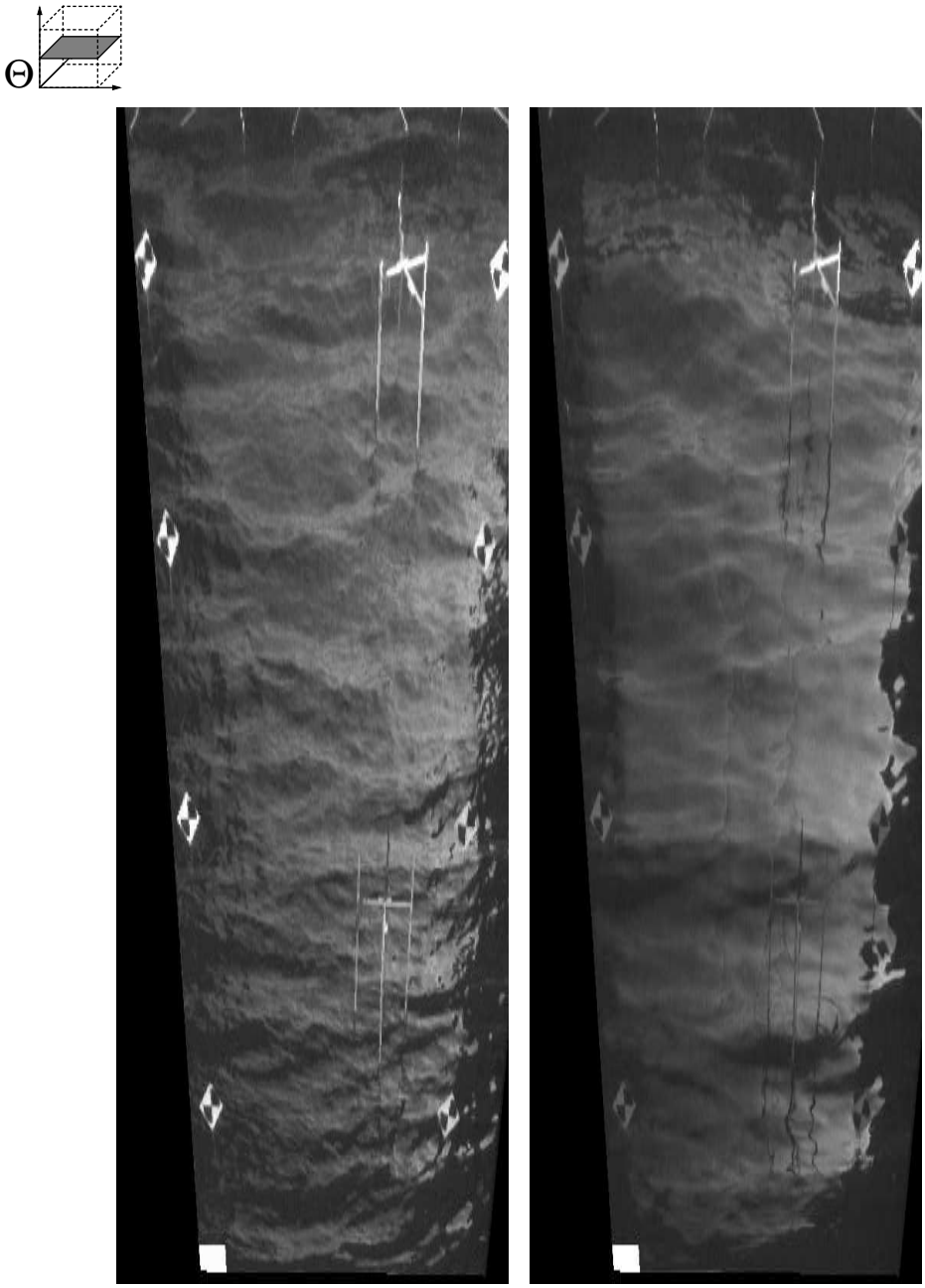

Figure 94: Example images of sequences with peak period $T_p = 1$ s, where shorter waves are dominant (left), and $T_p = 2$ s with longer waves (right). Both image sequences were acquired in CEDEX area B. The pixel resolution of the images in world coordinates is 0.01 m × 0.03 m; the spatial dimensions are 5.12 m × 15.36 m; the number of pixels is 512 × 512.

of these 58 spectra is used for comparison with the optical 1D ω spectrum. The averaging of the chunks is performed because the statistical variability is reduced for the averaged ω spectrum, $\bar{\mathcal{S}}_w(\omega)$.
On the 3D image spectra, $\mathcal{G}_1(\Omega)$ ($T_p = 1$ s) and $\mathcal{G}_2(\Omega)$ ($T_p = 2$ s), the optical transfer function (5.8) is performed, yielding $\mathcal{G}_{1,H}(\Omega)$ and $\mathcal{G}_{2,H}(\Omega)$. The spectral interval between the peak frequencies and the high-frequency

part, where for the optical spectra a cut-off frequency is reached, is fitted by a least-squares algorithm with a straight line as the regression-model function in a log–log coordinate system. The slopes of the curves, β_o and β_w, are calculated by fitting a straight line by a least-squares algorithm. The coefficient β is calculated from the gradients by $(\beta_o - \beta_w)^{0.5}$.
The spectral comparison is presented in Fig. 95. The log–log diagrams show the uncorrected image spectra and the image spectra corrected by the inverse OTF (see Sec. 5.2.4 and Appendix B). Both are compared to averaged wave-gauge spectrum. The performance of the OTF indicates a correction difference of ca. 0.3 for the calibration coefficient β. The coefficient β is not stable nor is it equal to 2 and varies for the cases presented here (and for others not presented). This is not the behaviour expected from the linear tilt-modulation theory; in addition this fact does not follow the results retrieved by the 1D simulation model (see Appendix E). After correction with the inverse OTF, the magnitude of the calibration coefficient β more closely approaches the expected value of 2. For the period $T_p = 1$ s, the waves are steeper than for $T_p = 2$ s, because the wave height was the same. For the wave field with the steeper waves, i.e. with the larger modulation of the images, the magnitude of β is closer to 2, suggesting that a certain modulation strength is necessary to allow the application of the tilt-modulation model.

G.3 Results: Local 1D Frequency Spectra

A local 1D integrated frequency spectrum from the center of the analyzed area is presented in Fig. 96 on a log–log scale. The dotted line represents a line fit of both parameters: $\alpha_{o,dB} = 18.81$ and $\beta_o = -2.65$. The full line is fitted by assuming the theoretically expected slope $\beta_o = -1$ ($\beta = 2$ and $\beta_w = -5$), resulting in the value $\alpha_{t,dB} = 5.573$.
In Fig. 97 spatial maps and histograms of the calibration coefficients of the local frequency spectra are outlined. If both parameters are fitted the pattern is strongly inhomogeneous. The patterns of α_o (left) and β_o (center) are reciprocal to each other: the value of α_o is larger in the upper area and the value of β in the lower area. The scatter of the parameters over the analyzed area is $\alpha_{o,dB} = -1.23 \pm 12.65$ and $\beta_o = -1.24 \pm 1.60$. Performing a line fit assuming the theoretically expected slope $\beta_o = -1$ results in at much more homogeneous distribution of the parameter α: the scatter is $\alpha_{t,dB} = 1.84 \pm 4.63$.
In Fig. 98 the global, 1D integrated frequency spectrum is presented for comparison. The same frequency interval as in the local analysis was used for the line fit. The very-high-frequency part with a stronger spectral decay corresponds to noise of the image spectrum. The regression parameters are $\alpha_{o,dB} = 2.35$, $\beta_o = -0.74$ and $\alpha_{t,dB} = 4.52$.

G.4 Summary

A new technique to calibrate image sequences of the dynamic water surface in reflection on a global and on a local spatial scale has been introduced

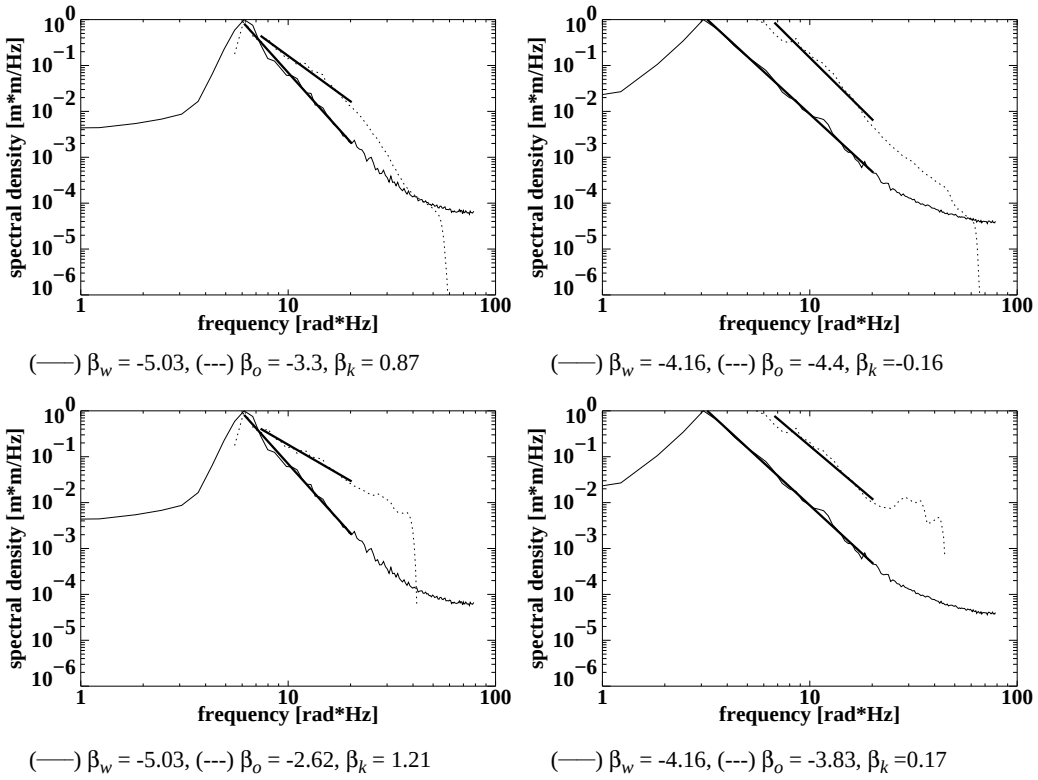

Figure 95: Comparison of the gray-level variance ω spectra and wave-gauge ω spectra acquired in CEDEX area B. The upper row shows the comparison of uncorrected 1D image ω spectra and 1D wave-gauge ω spectra, the lower row shows the comparison of corrected image ω spectra and wave-gauge ω spectra. The left column depicts the case where $T_p = 1$ s, and the right column the case where $T_p = 2$ s.

and has been confirmed with first results. The application of the calibration method to the global image spectra has shown that the magnitude of β is closer to the value expected by tilt modulation for the analyzed data set with the steeper waves, i.e with a stronger modulation signal.
The pattern of the coefficient β is spatially inhomogeneous. The variation of the parametrization exponent β contradicts tilt-modulation theory. The value of β is closer to the value expected by tilt-modulation theory in strongly illuminated areas. This supports the hypothesis that a certain signal strength is necessary to obtain $\beta = 2$. For a weak wave pattern this value hints that the parametrization approach is too simple and is inadequate solving the problem of calibration in the determination of spatial maps of the significant wave height. The tilt-theory approach and the results of the 1D simulation model, for both of which the coefficient β has a value of 2, have been used as a motivation to set β explicitely to this value.
Proposed reasons for the variation of β are

- the absent consideration of the azimuthal dependency of the tilt MTF, which may play a role because of the multidirectionality of the wave field of ca 30° at CEDEX,

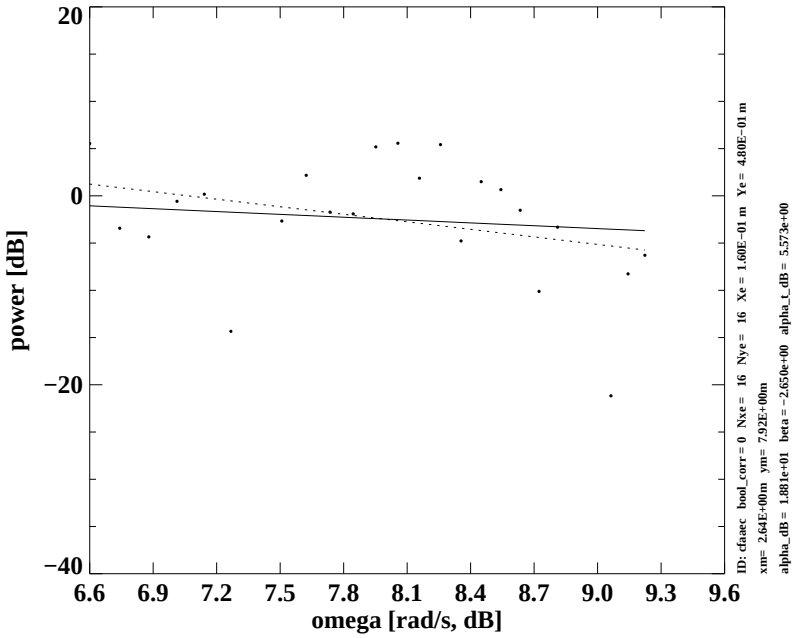

Figure 96: CEDEX Tank, area B: local 1D integrated ω spectrum: dotted line; line fit, solid line: fit with fixed slope $\beta_o = -1$.

- the behaviour of the Gabor-filter bank, which probably is not energy preserving due to the shape of the Gaussian function.

The azimuthal dependency can be overcome by implemenation of a direction-dependent correction term applied to the directed Gabor filters. For the second problem, as a first approach a correction procedure has been implemented, which is performed on a single spectral Gabor filter. Up to now the eventual overlapping of neighbouring Gabor filters has not been considered. For this case a correction procedure should be introduced in the near future. The physically motivated calibration is an open scientific question. On the other hand, apart from this the practical application is ensured if one follows an empirical approach by calibrating the image spectra with independent in situ data sets, which generally are available at hydraulic wave tanks. Because the calibration coefficients, α and β, vary in space very smoothly, these values can be interpolated between in situ wave gauges.

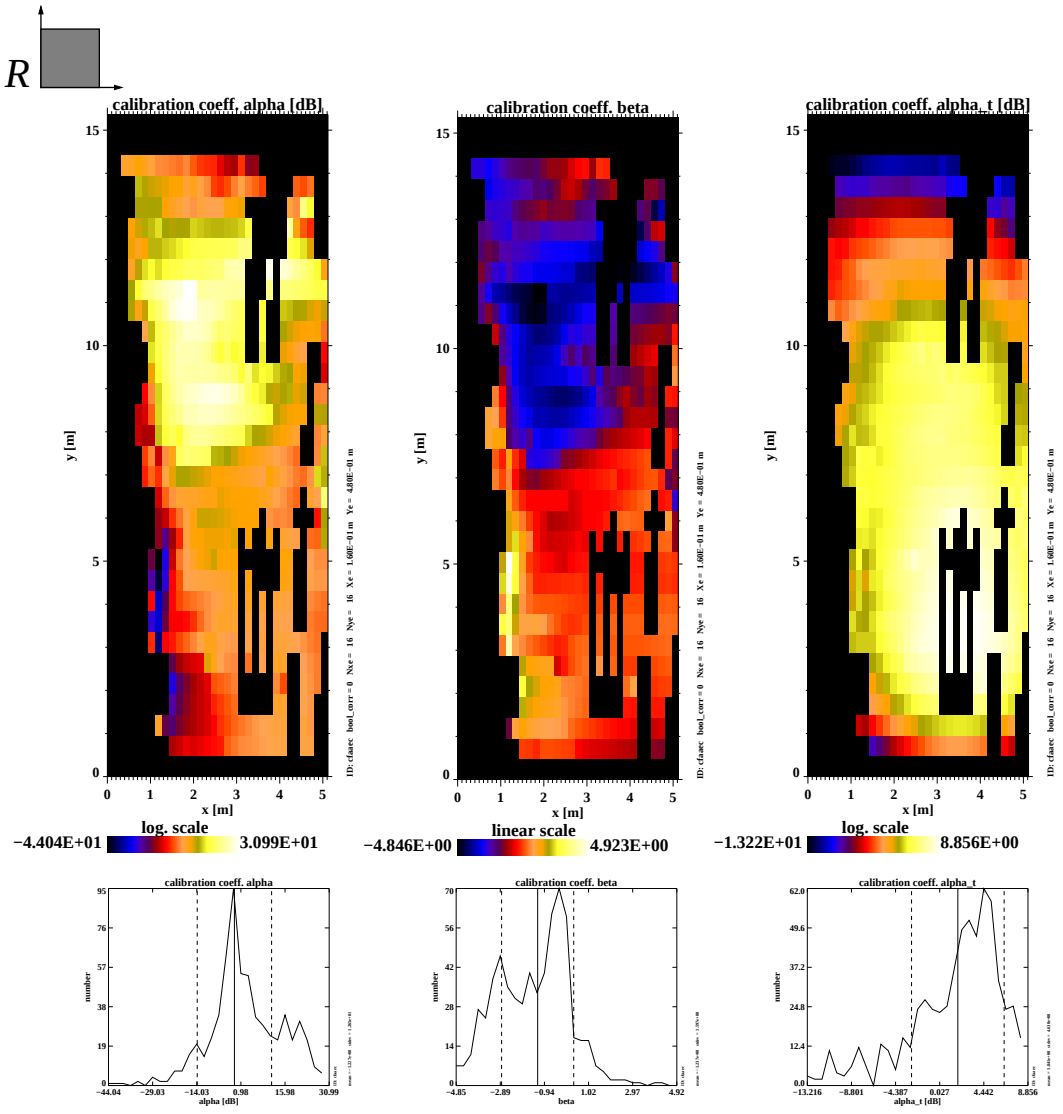

Figure 97: CEDEX Tank, area B: Spatial maps (top) and histograms (bottom) of the parametrization coefficients of the local ω spectra; $\alpha_{o,dB}$ (left), β_o (center), and $\alpha_{t,dB}$ (right).

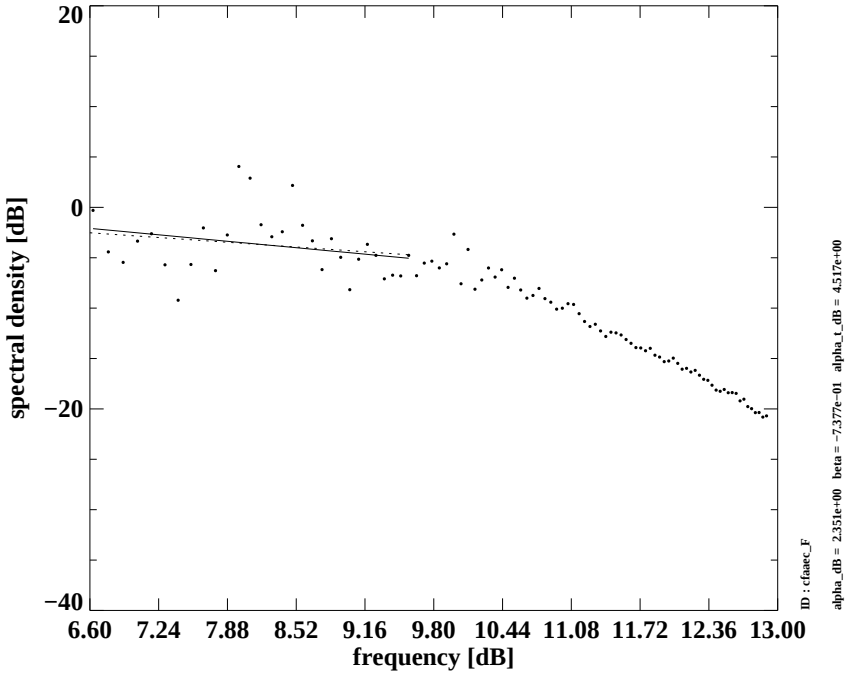

Figure 98: CEDEX Tank, area B: global 1D integrated ω spectrum; dotted line: line fit, solid line: line fit with fixed slope $\beta_o = -1$.

Acknowledgments

Parts of this work have been supported by the Bundesministerium für Bildung und Forschung (BMBF) in the frame of the SARPAK project (project to investigate the spatial resolution marine meteorological and marine biological parameter fields in coastal areas with ERS-SAR images, coordinator: W. Rosenthal) under contract number 03F0165C.
The realization of the optical experiment at the Centro de Estudios de Puertos y Costas (Madrid) has been supported by the European Union in the frame of the European Frame Program 'Large-Scale Facilities' under contract number ERBFMGECT 950075.
An dieser Stelle möchte ich mich bei Frau Prof. Dr.-Ing. Bärbel Mertsching (GET Lab, Universität Paderborn), Herrn Prof. Dr. Bernd Neumann (AG Kognitive Systeme, Universität Hamburg) und Herrn Prof. Dr. Bernd Jähne (AG Digitale Bildverarbeitung, Universität Heidelberg) für die Begutachtung der Arbeit bedanken.
Herrn Dr. Friedwart Ziemer (Radarhydrographie, GKSS-Forschungszentrum Geesthacht GmbH) danke ich für Diskussionen und die begleitende Betreuung der Arbeit.
Bei Herrn Dr. Jörg Seemann (V2T VISION TO TECHNOLOGY GmbH, Geesthacht) bedanke ich mich insbesondere für die gute und substantielle Zusammenarbeit auf dem Gebiet der Bildsequenzverarbeitung, die anregenden Diskussionen und die Betreuung der Arbeit.
Ganz speziell möchte ich mich bei unserem Techniker Herrn Gottfried Schymura (Radarhydrographie, GKSS-Forschungszentrum Geesthacht GmbH) bedanken, ohne dessen technische Erfahrungen, dessen kreativen Erfindungsgeist und unermüdlichen Einsatz die Durchführung der Experimente nicht so erfolgreich hätten durchgeführt werden können. Im weiteren bedanke ich mich bei ihm für die Erinnerungen, die ich mit unseren Experimenten und unseren gemeinsamen Aufenthalt in Madrid verbinde.
Unserer ehemaligen Diplomandin Frau Dipl.-Math. Ulrike Wolff (Agfa-Gevaert AG, München) danke für ihre wertvollen Diskussionsbeiträge und für ihre neue und erfrischende mathematische Sichtweise auf die Probleme der Bildsequenzverarbeitung mit geophysikalischer Anwendung. Im weiteren bedanke ich mich bei unserem ehemaligen Diplomanden Herrn Dr. Heiko Dankert (Gekoppelte Modellsysteme, GKSS-Forschungszentrum Geesthacht GmbH), der in seiner Diplomarbeit gezeigt hat, dass man die Methode DiSC auf wasserbauliche Probleme anwenden kann, sowie seinen Begutachtern und Betreuern Herrn Prof. Sören Kohlhase und Herrn Dr. Peter Fröhle (beide Institutit für Wasserbau, Universität Rostock).
Meinem ehemaligen Zimmerkollegen Herrn Dipl.-Oz. Helge Hatten (Lufthansa Technik, Hamburg) danke ich für die anregenden Diskussionen zu meinen und seinen wissenschaftlichen Arbeiten und aller sonstigen die Welt bewegenden Themen.
Den Herren Dipl.-Phys. Peter Rybaczok (Bürgermeister von Lütau und ehemaliger Kollege) und Dipl.-Math Adolf Krüger (ehemalig Wissenschaftliche Assistenz, GKSS-Forschungszentrum Geesthacht GmbH) danke ich für die

hilfreichen Diskussionen und insbesondere für deren reichen Erfahrungsschatz, an denen sie mich haben teilhaben lassen.
Herrn Dr. Wolfgang Rosenthal, Herrn Dr. Heinz Günther, Herrn Dr. Jochen Horstmann, Herrn Dipl.-Math. Wolfgang Koch, Herrn Dipl.-Oz. Gerhard Gayer (alle Gekoppelte Modellsysteme, GKSS-Forschungszentrum Geesthacht GmbH), Herrn Dr. Thomas Wolf (Institut für Seenforschung, Langenargen) danke ich für deren Diskussionsbeiträge und konstruktive Kritik zum Thema der vorliegenden Arbeit.
Herrn Dr. Hermann Kuhn, dem Systemadministrator des Instituts für Küstenforschung (GKSS-Forschungszentrum Geesthacht GmbH) und einer der nicht ersetzbaren Personen, möchte ich dafür danken, dass er meine SUN Workstation – nun in der vierten Hardware-Generation – am Leben erhalten hat und für die vielen Erläuterungen über die Mysterien der SUN Welt.
Herrn Dr. Roland Doerffer, Herrn Prof. Dr. Helmut Schiller, Herrn Heinrich Siewers und Herrn Wolfgang Cordes (alle Biooptische Fernerkundung, GKSS-Forschungszentrum Geesthacht GmbH) möchte ich für deren Diskussionsbeiträge und technischen Hilfestellungen auf dem Gebiet der optischen Fernerkundung danken.
Danken möchte ich Herrn Prof. Heinrich Hühnerfuß (Institut für Organische Chemie, Universität Hamburg) der Arbeitsgruppe Fernerkundung von Herrn Prof. Werner Alpers, insbesondere Frau Dipl.-Oz. Nicole Braun (jetzt Radarhydrographie, GKSS-Forschungszentrum Geesthacht GmbH), Herrn Dr. Martin Gade und Herrn Dr. Philipp A. Lange (alle Institut für Meereskunde, Universität Hamburg).
Ich danke Herrn Dipl.-Ing. Holger Rahlf, Herrn Dirk Carstens, Herrn Dipl.-Ing. Bernhard Kondziella und Herrn Dr.-Ing Klemens Uliczka (alle Bundesamt für Wasserbau - Dienststelle Hamburg, Referat K2 - Ästuarsysteme I) für die Möglichkeit vorbereitende Experimente am hydraulischen Warnemündemodell des Bundesamtes für Wasserbau durchzuführen. Für die Durchführung des vorbereitenden Freilandexperiments im Oderhaff danke ich der Besatzung der F.S. Ludwig Prandtl Kapitän Helmut Bornhöft, Bootsmann Reinhard Reshöft und Tauchermeister Hans Belau und insbesondere Fischermeister Heiko Gerbatsch (UECK 9, Ückermünde) für deren Einsatz.
Quisiera agradecer a Dr. José C. Nieto Borge (Puertos del Estado, Madrid, DLR, Oberpfaffenhofen) por las discusiones interesantes y el compañerismo, aquí en Alemania y en España, y para corregir el español de la actual sección. Especialmente quisiera agradecer al Director posterior del Centro de Estudios de Puertos y Costas, José M. Grassa Garrido, y los ingenieros José R. Amoros Serret, José M. Berenguer Pérez, José Lozano Pedroche, Miguel A. González Gallego, Juan M. Prada Espada, Ángel Fernández Mozo (también del Centro de Estudios de Puertos y Costas, Madrid) para utilizar el experimento a CEDEX.
Danken möchte ich Herrn Claas-Hinrich Schröder (Stabsstelle Technologietransfer, GKSS-Forschungszentrum Geesthacht GmbH) und Herrn Dipl.-Met. Volker Dzaak (Instituts für Küstenforschung, GKSS-Forschungszentrum Geesthacht GmbH) für die Hilfestellungen und die fachliche Beratung während der Phase der Patentbeantragungen.

Herrn Prof. Dr.-Ing. Dietmar P. F. Möller (Technische Informatiksysteme, Universität Hamburg), Herrn Dr. Martin Lehmann (Telekommunikation und Rechnernetze, Universität Hamburg), Frau Elke Gabriel, Frau Carola Tenge (beide Sekr. Technische Informatiksysteme, Universität Hamburg) danke ich für die freundliche und herzliche Begleitung des Disputationsverfahrens.
Diese Arbeit widme ich meiner Familie.